

https://dspace.org/

Structure and thermoresponsive behaviour of porous and non-porous borophosphates

Mogodi, Mashikoane Wilson

2016

http://hdl.handle.net/10539/21714

Mogodi, Mashikoane Wilson (2016) Structure and thermoresponsive behaviour of porous and non-porous borophosphates, University of the Witwatersrand, Johannesburg, <http://hdl.handle.net/10539/21714>

Downloaded from a DSpace repository. https://dspace.org/

Structure and thermoresponsive behaviour of porous and non-porous borophosphates

A thesis submitted to the Faculty of Science, University of the Witwatersrand, Johannesburg, in fulfilment of the requirements for the degree of Doctor of Philosophy

By

Mashikoane Wilson Mogodi

Declaration

I declare that this thesis is my own, unaided work. It is being submitted for the Degree of Doctor of Philosophy in the University of the Witwatersrand, Johannesburg. It has not been submitted before for any degree or examination in any other University.



Candidate

(Mashikoane Wilson Mogodi)

17 October 2016

Supervisor: Professor David Gordon Billing

Co-supervisor: Professor Manuel Antonio Fernandes

Abstract

In this PhD thesis, the synthesis, crystal chemistry and thermoresponsive behaviour of non-porous borophosphates [$ABPO_5$ (A= Ca, Sr, Ba) and BPO_4] and porous borophosphates [$NH_4Fe(III)[BP_2O_8(OH)]$] and $M^I_xM^{II}_z(H_2O)_2[BP_2O_8].zH_2O$ (M^I = Na, NH_4 and M^{II} = Mn, Co)] phases were investigated. Understanding the crystal structure dynamics as a function of temperature of the selected porous and non-porous borophosphates revealed the thermal stability of the studied compounds, while serving as a predictive measure of the effects of temperature on other materials properties and subsequent applications.

The non-porous borophosphates were synthesized using the solid state method, whereas the porous borophosphates were synthesized using the hydrothermal method. The powder X-ray diffraction (PXRD) technique, along with the application of the Rietveld refinement method, was the principle characterisation technique employed for the non-destructive and non-invasive thermoresponsive characterisation of the studied borophosphate phases.

This thesis consists of seven chapters, four of which are independent papers corresponding to four chapters. Chapter 1 reviews the relevant scientific literature, while chapter 2 describes the methods of characterisation used in this thesis. Concerning the highly thermally stable non-porous borophosphates, chapter 3 presents the thermal expansion behaviour of $ABPO_5$ compounds, which have been determined from the sequential application of the Rietveld refinement method of variable temperature powder X-ray diffraction (VT-PXRD) data. For trigonal $ABPO_5$ compounds, a near linear expansion of the unit cell axes was found for all structures as a function of temperature. The variation of the crystal structure with temperature of $ABPO_5$ compounds was also established.

With the general understanding that borophosphates display intriguing crystal structure architectures, chapter 4 describes the synthesis and characterisation of four metal borophosphate hydrates: $NaM^{II}(H_2O)_2[BP_2O_8](H_2O)$; M^{II} = Co (**I**), Mn (**II**) and $(NH_4)_{0.5}M^{II}_{1.25}(H_2O)_2[BP_2O_8](H_2O)_{0.5}$; M^{II} = Co (**III**), Mn (**IV**). The structures refined at room temperature from PXRD data revealed that isostructural phases **I** and **II** have an ordered arrangement of water molecules in the voids, whereas isostructural phases **III** and **IV** have fractional and disordered distribution of water molecules in the voids. Scanning electron microscope (SEM), fourier transform infrared spectroscopy (FT-IR), variable temperature powder X-ray diffraction (VT-PXRD) and thermogravimetric analysis (TGA) for all

compounds are also presented. Chapter 5 was an investigation into the synthesis, crystal structure and thermal properties of the porous iron borophosphate $NH_4Fe(III)[BP_2O_8(OH)]$. Variable temperature PXRD and thermogravimetric analysis were used to investigate the compounds thermal stability and expansion behaviour. Thermal investigations indicated that the compound is stable up to 470 °C.

Of great importance to the accurate and/or precise measurement of the crystal structures and lattice parameters of the phases investigated using powder diffraction was the correct application of the Rietveld refinement method to the measured diffraction data. Therefore, chapter 6 is an investigation into a number of different Rietveld refinement approaches, which were aimed at modelling the changes in the atomic coordinates of BPO_4 as a function of temperature. Parametric Rietveld refinements and rigid body Rietveld refinements were among the refinement strategies employed.

Acknowledgements

I am thankful to the following people and institutions:

- The University of the Witwatersrand, NRF and DST-CoE for the financial support.
- School of Chemistry including the head of school, academic, administration and cleaning staff for providing an excellent working environment.
- CATOMAT members for being great colleagues and friends.
- My fellow research group members: Michelle, Natsayi and Rob for your friendship and research support.
- To Manuel for the guidance and encouragement during this work.
- To Dave, I am grateful for your mentorship beyond diffraction.
- And lastly, to my family for your continual moral support.

Conference and meeting proceedings resulting from work presented in this thesis

Poster presentations:

Wilson M. Mogodi and David G. Billing, *Thermoresponsive behaviour of $CaBPO_5$ evaluated from Parametric Rietveld refinement*. 13th European Powder Diffraction Conference Grenoble France. (2012).

Wilson M. Mogodi and David G. Billing, Thermoresponsive behaviour of $CaBPO_5$, $SrBPO_5$ and $H_8Mn_5O_{20}P_4$. European Crystallographic Meeting (ECM) Warwick UK. (2013).

Mogodi M.W., Billing D.G., ECM 28, UK, 2013 *Acta Cryst*. (2013). **A69**, 473.

Wilson M. Mogodi and David G. Billing, Thermoresponsive behaviour of $CaBPO_5$, $SrBPO_5$ and $H_8Mn_5O_{20}P_4$. Centre of Excellence in Strong Materials (CoE-SM) Student Presentations, University of the Witwatersrand South Africa (2013).

Wilson M. Mogodi and David G. Billing, *Thermoresponsive behaviour of porous and non-porous borophosphates.* Centre of Excellence in Strong Materials (CoE-SM) Student Presentations, University of the Witwatersrand South Africa (2014).

Wilson M. Mogodi and David G. Billing, *Thermodiffractometry study of a zeolite borophosphate; $NaCo(H_2O)_2[BP_2O_8]H_2O$ with 61 helices* Centre of Excellence in Strong Materials (CoE-SM) Student Presentations, University of the Witwatersrand South Africa (2015).

Wilson M. Mogodi and David G. Billing, *Crystal structure and thermoresponsive behavior of porous and non-porous borophosphates.* African Light Source Conference and Workshop, European Synchrotron Radiation Facility (ESRF), Grenoble, France (2015).

Oral presentations:

Wilson M. Mogodi and David G. Billing, *Parametric Rietveld refinement of $CaBPO_5$ and $SrBPO_5$*. Centre of Excellence in Strong Materials (CoE-SM) Student Presentations, University of the Witwatersrand (2012).

Wilson M. Mogodi and David G. Billing, *Thermoresponsive behaviour of porous and non-porous borophosphates*, Southern African Powder Diffraction Conference and Workshop South Africa (2014).

Wilson M. Mogodi and David G. Billing, *Thermoresponsive studies of porous and non-porous borophosphates*. IUCr 2014, Montréal, Canada (2014).

Wilson M. Mogodi and David G. Billing, *Thermoresponsive studies of porous and non-porous borophosphates.* 6th Wits Cross-Faculty Graduate Symposium, University of the Witwatersrand (2014) (**3rd place oral presentation prize**).

Wilson M. Mogodi and David G. Billing, *Thermoresponsive studies of porous and non-porous borophosphates.* 2014 SACI Young Chemist Symposium, North-West University Potchefstroom (2014) (**Won oral presentation prize**).

Table of Contents

Declaration ..... **I**

Abstract ..... **II**

Acknowledgements ..... **IV**

Conference and meeting proceedings resulting from work presented in this thesis ..... **V**

Table of Contents ..... **VII**

Lists of Figures ..... **XII**

Lists of Tables ..... **XVII**

Chapter 1 Introduction and Literature review **1**

1.1. Overview 1

1.2. Thermal Expansion 1

1.2.1. Measuring and quantifying thermal expansion 3

1.2.2. Microcracking 6

1.3. The origin of thermal expansion 6

1.3.1. Phase transitions 7

1.3.2. Magnetic effect 8

1.3.3. Phonons 9

1.4. Negative and low positive thermal expansion materials 12

1.4.1. Cordierite 12

1.4.2. Lithia-Alumina-Silica (LAS) system 13

1.4.3. AM_2O_8 family 14

1.4.4. Zeolites and Aluminophosphates ($AlPO_4$'s) 16

1.4.5. Other materials 18

1.5. Borophosphates and Metalloborophosphates 23

1.6. Aim of the research 30
1.7. References 32
Chapter 2 Methods of Characterisation 42
2.1. Powder X-ray Diffraction (PXRD) 42
2.2. Structure determination from powder data (SDPD) 44
2.2.1. Whole powder pattern decomposition (WPPD) methods 44
2.2.2. The Rietveld Method 45
2.2.3. Parametric Rietveld refinement 46
2.2.4. Rigid body refinement 47
2.2.5. Quality of fit 49
2.2.6. Considerations when refining the crystal structure 52
2.3. Topas ® 54
2.4. Powder X-ray diffraction instruments 56
2.4.1. Bruker D2 Phaser 56
2.4.2. Bruker D8 Advance 57
2.4.3. Anton Paar XRK 900 non-ambient sample chamber 58
2.5. Supplementary characterization techniques 59
2.5.1. Fourier transform infrared spectroscopy (FTIR) 59
2.5.2. Scanning Electron Microscopy (SEM) 59
2.5.3. Thermogravimetric analysis (TGA) 59
2.6. Synthesis methods 60
2.7. References 61
Chapter 3 Thermoresponsive behaviour of $ABPO_5$ (A = Ca, Sr, Ba) compounds 63
3.1. Introduction 64
3.2. Experimental 65
3.2.1. Synthesis of $ABPO_5$ powders 65
3.2.2. Characterisation 66

3.3. Results and discussion 67

3.4. Conclusion 80

3.5. References 81

Chapter 4 Hydrothermal synthesis, crystal structure and thermodiffractometry study of zeolite borophosphates $M^{I}_{x}M^{II}_{z}(H_2O)_2[BP_2O_8].zH_2O$ (M^{I} = Na, NH_4 and M^{II} = Mn, Co) with CZP topology 83

4.1. Introduction 85

4.2. Experimental 86

4.2.1. Synthesis 86

4.2.2. FTIR Spectroscopy 87

4.2.3. Thermogravimetric analysis (TGA) 88

4.2.4. Scanning electron micrograph (SEM) 88

4.2.5. Powder X-ray diffraction (PXRD) 89

4.3. Results and discussion 93

4.3.1. General description of the anionic unit, $\infty^1[BP_2O_8]^{3-}$ 93

4.3.2. Crystal structure of $NaM^{II}(H_2O)_2[BP_2O_8](H_2O)$; M^{II} = Co (I), Mn (II). 95

4.3.3. Crystal structure of $(NH_4)_{0.5}M^{II}_{1.25}(H_2O)_2[BP_2O_8].(H_2O)_{0.5}$; M^{II} = Co (III), Mn (IV) 99

4.3.4. Borophosphates (I, II, III and IV) analogue of the zincophosphate CZP framework 105

4.3.5. Thermal studies 107

4.3.6. $NaM^{II}(H_2O)_2[BP_2O_8].(H_2O)_2$ M^{II} = Co (I), Mn (II) 113

4.3.7. $(NH_4)_{0.5}M^{II}_{1.25}(H_2O)_2[BP_2O_8].(H_2O)_{0.5}$; M^{II} = Co (III), Mn (IV). 114

4.4. Conclusion 116

4.5. References 117

Chapter 5 Hydrothermal synthesis, crystal structure and thermal behaviour the porous iron borophosphate, $NH_4Fe(III)[BP_2O_8(OH)]$ 119

5.1. Introduction 120

5.2. Experimental 121

5.2.1. Synthesis of $NH_4Fe[BP_2O_8(OH)]$ 121
5.2.2. Chemical analysis 122
5.2.3. FTIR Spectroscopy 122
5.2.4. Thermogravimetric analysis (TGA) 122
5.2.5. Scanning electron micrograph (SEM) 123
5.2.6. Powder X-ray diffraction (PXRD) 123
5.3. Discussion 128
5.3.1. Crystal structure 128
5.3.2. Thermal investigations 132
5.4. Conclusion 137
5.5. References 138
Chapter 6 Merits and pitfalls of Rietveld refinement strategies: the BPO_4 thermoresponsive case 140
6.1. Introduction 142
6.2. Results and discussion 145
6.2.1. Method 1: Free atom refinements 145
6.2.2. Method 2: Low-order polynomials 148
6.2.3. Method 3: Rigid body Rietveld refinements 150
6.3. Conclusion 154
6.4. References 155
Chapter 7 General conclusions 157
Appendix 1: Calibration of the Bruker D2 Advance diffractometer using the NIST LaB_6 line position and profile shape standard (SRM 660a). 162
A1.1: Introduction 162
A1.2: Results 163
A1.2.1: Line position evaluation 164
A1.2.2: Line shape evaluation 166

A1.3: References 167

Appendix 2: Supplementary material 168

A2.1: Chapter 3 168

A2.2: Chapter 4 172

A2.3: Chapter 5 174

A2.4: Chapter 6 176

Appendix 3: Guide to the electronic appendix 177

Lists of Figures

Figure 1.1: a) Engine pistons [5], b) tooth filling [6] and c) bridges are affected by thermal expansion [7]. 2
Figure 1.2: Model of an anharmonic potential energy curve for a pair of atoms in a solid material. 7
Figure 1.3: Variation in the unit cell volume with temperature for $Sc_2Mo_3O_{12}$. Monoclinic to orthorhombic phase change occurs around 178 K. Obtained from [19]. 8
Figure 1.4: Schematic representation of a) longitudinal thermal motion b) transverse thermal motion of oxygen atom in the M-O-M linkage as a function of heat. M = Metal and O = oxygen atoms, respectively. Adapted from [13]. 10
Figure 1.5: 2D square lattices showing the rocking motion of rigid MO_4 RUM's as a consequence of the bending of M-O-M linkages in response to heat. Note the change in unit cell area with increase in temperature. Obtained from [10]. 11
Figure 1.6: The crystal structure of orthorhombic (space group *Cccm*, no. 66) $Mg_2Al_3(Si_5Al)O_{18}$, the parent compound of the cordierite family. AlO_4 tetrahedra (green), Si/Al tetrahedra (blue) and Mg atoms (white spheres). 13
Figure 1.7: Three-dimensional open-framework of (a) β-spodumene (space group $P4_32_12$, no. 96) and (b) β-eucryptite (space group $P6_422$, no. 181) formed from corner-linked AlO_4 and SiO_4 tetrahedra. Li ions (white spheres) are accommodated in the voids. 14
Figure 1.8: Variation of the cubic lattice parameter of ZrW_2O_8 determined using neutron diffraction and dilatometry measurements [38]. ZrW_2O_8 is stable until 1050 K and re-emerges (thermodynamically stable) around 1443 K [55]. The dashed line connects both points. 15
Figure 1.9: Crystal structure of ZrW_2O_8 at room temperature (space group $P2_13$, no. 198). ZrO_6 octahedra (blue) and WO_4 tetrahedra (red). 16
Figure 1.10: Crystal structure of the siliceous zeolite faujasite (dealuminated Y-type zeolite). Reference Code: ICSD- 41394. 17
Figure 1.11: Structure of $AlPO_4$-17 projected along the *c*-axis [32]. 18
Figure 1.12: Variation of the unit cell volume with temperature of ice I*h*, also known as ice-phase-one (space group $P6_3/mmc$). Derived from measurements by Röttger *et al.* [57]. 19
Figure 1.13: Alteration of the relative expansion (%) with temperature of three $Al_{2-x}In_x(WO_4)_3$ materials, representing the $A_2M_3O_{12}$ family. Obtained from [13]. 20
Figure 1.14: Borophosphates; intermediate compounds of the systems M_xO_y-B_2O_3-P_2O_5-(H_2O) (M = main group/transition metal or ammonium). BO_4 tetrahedra (blue), BO_3 trigonal

planar (ball and stick) and PO_4 tetrahedra (red). Boron and phosphorous can be coordinated by either oxygen or OH-species. Adapted from [92]. 24
Figure 1.15: Structure directing organic templates a) 1,2-diaminopropane (1,2-DAP), b) Piperazine (PIP), c) 1,3-diaminopropane (1,3-DAP), which occupy the voids of the porous borophosphate; $[H_2(Templ.)][Mn^{II}\{B_2P_3O_{12}(OH)\}]$. Diagrams obtained from [134]. 30
Figure 2.1: (a) Single crystal (SC) and (b) powder XRD interference patterns. SC-XRD experiments form spots in the reciprocal space. Powder patterns form Debye rings (cones) which can be integrated to a one-dimensional diffraction pattern in reciprocal space made up of step intensities. 43
Figure 2.2: Depiction of an idealised octahedron, with central atom A coordinated by atoms B to G. 48
Figure 2.3: GUI screenshot of the program jEdit used to build the input file for execution in the program Topas. The text (set of instructions) to be executed are shown on the right. The plugins window used to prepare the text is shown on the left. 56
Figure 2.4: Front opening of the Bruker D2 Phaser diffractometer. 57
Figure 2.5: (a) Depicts the front opening of the Bruker D8 Advance diffractometer equipped with the Anton Paar XRK 900 furnace and (b) the Anton Paar XRK 900 in-situ chamber shown with the Macor® sample stage (the sample stage has been removed from the bottom of the chamber). 58
Figure 2.6: Teflon bomb. 61
Figure 3.1: Observed (blue), calculated (red) and difference (grey lower line) PXRD patterns for $CaBPO_5$ (top panel), $SrBPO_5$ (middle panel) and $BaBPO_5$ (lower panel) at 30°C. The vertical blue lines in the $BaBPO_5$ PXRD patterns represent the Topas peaks phase (split-PVII peak function) used to model the unidentified regions. Lower tick marks indicate predicted peak positions. 68
Figure 3.2: (a) Unit cell representation of the stillwellite $ABPO_5$ structure down [001]. Coordination of oxygen atoms around A^{2+} (black sphere) is omitted for clarity. (b) Two translationally identical chains of boron tetrahedra (blue), with 3_1 symmetry, viewed along [010] direction, with phosphorous tetrahedra (red) and A^{2+} polyhedra linking the chains. 69
Figure 3.3: Graphs showing the variation in unit cell parameters, cell volume and figure of merit (χ^2 is the lower set of curves) vs temperature for $CaBPO_5$ (◊), $SrBPO_5$ (□), $BaBPO_5$ (Δ). Solid lines represent polynomial least squares fits to the data. The error bars are smaller than the symbol size. 70

Figure 3.4: Relative changes (relative to the cell parameter at room temperature) of the unit cell parameters expressed as percentage changes as a function of temperature for a) $CaBPO_5$, b) $SrBPO_5$ c) $BaBPO_5$ and d) $ABPO_5$ counterparts. 73
Figure 3.5: Intra-tetrahedral (a) B-O and (b) P-O distances as a function of temperature for $CaBPO_5$ (◊), $SrBPO_5$ (□), $BaBPO_5$ (Δ). Solid lines represent linear least squares fits to the data. 76
Figure 3.6: Representation of B-O-P bridging angle, θ and related nonbonded B-P distances in $ABPO_5$ compounds. 76
Figure 3.7: Variations of non-bonded B-P distances with temperature for $CaBPO_5$ (◊), $SrBPO_5$ (□), $BaBPO_5$ (Δ). Solid lines represent linear least squares fits to the data. 78
Figure 4.1: SEM images of the as-synthesized (a) sample **I**, (b) sample **II** (c) sample **III** and sample **IV**. 89
Figure 4.2: Observed (blue), calculated (red) and difference (grey) PXRD patterns of compound **I** and **II** refined at 30 °C. Lower ticks are the expected Bragg peak position. 92
Figure 4.3: Observed (blue), calculated (red) and difference (grey) PXRD patterns of compound **III** and **IV** refined at 30 °C. Lower ticks are the expected Bragg peak position. ..92
Figure 4.4: One-dimensional infinite loop-branched borophosphate helices (right), $\infty^1[BP_2O_8]^{3-}$, propagating along [001] formed from the FBU, an open-branched chain (left). BO_4 (blue) and PO_4 (red) tetrahedra. 93
Figure 4.5: Two helical borophosphate chains composed of tetrahedral units, $\infty[BP_2O_8]^{3-}$, wound around a six-fold screw axis (black rod) located at the corners of the unit cell. $M^{2+}(O_{PO4})_4(OH_2)_2$ grey octahedra link the helices. BO_4 (blue), PO_4 (red) tetrahedra and a helix of hydrate water ($O6_{H2O}$) yellow spheres. 94
Figure 4.6: The crystal structures of compounds (a) **I**, **II** and (b) **III**, **IV** viewed along the *c*-axis. BO_4 (blue), PO_4 (red) tetrahedra, H_2O (yellow) spheres, M^{2+} (black) octahedra and additional M^{2+} trigonal bipyramidal (turquoise) site in (b). M^{1+} sites as Na^+ (brown) spheres in (a) and NH_4^+ (grey) spheres in (b). 95
Figure 4.7: Polyhedral representation of (a) tetrahedral helix in CZP zincophosphate and (b) tetrahedral helix in CZP borophosphate phases. ZnO_4 (grey), BO_4 (blue) and PO_4 (red) tetrahedra. 106
Figure 4.8: 4-ring building unit of the (a) zincophosphate and (b) borophosphate phases. ZnO_4 (grey), BO_4 (blue) and PO_4 (red) tetrahedra. 106

Figure 4.9: Thermogravimetric analysis of (a) sample **I** and (b) sample **II**. In each plot the blue curve shows the 1st derivative. 108
Figure 4.10: Thermogravimetric analysis of (a) sample **III** and (b) sample **IV**. In each plot the red curve shows the 1st derivative. 109
Figure 4.11: Structural transformation of (a) sample **I** and (b) sample **II** characterised by VT-PXRD. 111
Figure 4.12: Structural transformation of (a) sample **III** and (b) sample **IV** characterised by VT-PXRD. 112
Figure 5.1: SEM images of the crystals of $NH_4Fe[BP_2O_8(OH)]$ with a rod-shaped morphology. 123
Figure 5.2: Observed (blue), calculated (red) and difference (grey) XRD patterns of $NH_4Fe[BP_2O_8(OH)]$ refined at 30 °C. Lower ticks are the refined peak position. 125
Figure 5.3: Ball and stick representation of the Fe, B P and N atom coordination in the asymmetric unit of $NH_4Fe[BP_2O_8(OH)]$. 126
Figure 5.4: Open-branched $_{\infty}^{1}\{[BP_2O_8(OH)]^{4-}\}$ chain (right) formed by corner sharing $BO_3(OH)$ (blue) and PO_4 tetrahedra (red) with another PO_4 group branching off the $BO_3(OH)$ tetrahedra. Its basic building unit (BBU) is also shown (left). 129
Figure 5.5: Polyhedral representation of the crystal structure of $NH_4Fe[BP_2O_8(OH)]$ viewed along the *a*-axis direction. B tetrahedra (blue), P tetrahedra (red), Fe octahedra (grey) and NH_4^+ molecules (wire/stick model). 129
Figure 5.6: Ball and stick representation of the eight-membered ring of $NH_4Fe[BP_2O_8(OH)]$. P2 ⋯ P2 x P1 ⋯ P1 distances (green atoms) are 6.19(1) x 8.94(3) Å^2. 130
Figure 5.7: Void spaces within the crystal structure of (a) **1** and (b) **1** without NH_4^+ ions. The voids in these structures are depicted as gold coloured spheres. 130
Figure 5.8: Thermogravimetric curves of $NH_4Fe[BP_2O_8(OH)]$ under N_2. Red curve is the thermogravimetric curve and the blue curve is the 1st derivative. 133
Figure 5.9: Temperature dependent powder X-ray diffraction patterns of $(NH_4)Fe[BP_2O_8(OH)]$. 134
Figure 5.10: Variation of the unit cell volume as a function of temperature. The error bars are smaller than the symbol size. 136
Figure 6.1: The polyhedral representation of the tetragonal unit cell of BPO_4 with blue BO_4 tetrahedra and red PO_4 tetrahedra. 142

Figure 6.2: Temperature dependence of the *a- and c* unit cell parameters determined by independent and parametric fitting. 146
Figure 6.3: Parametric Rietveld refinement plot for 42 powder patterns collected as a function of temperature. The superimposed observed (blue), calculated (red) and difference (grey) powder patterns for BPO_4. Lower ticks (blue) represent reflections of BPO_4 as a function of temperature.....147
Figure 6.4: (a) B-P non-bonded distances, (b) interpolyhedral B-O-P bond angles and (c) isotropic thermal parameter for oxygen atom as a function of temperature determined by method 2 (red curves) and independent free atom refinements (blue curves). 150
Figure 6.5: Temperature dependence of P-O (red) and B-O (blue) bond lengths for BPO_4 obtained by (a) free atom sequential refinements and (b) rigid body parametric Rietveld refinements.....151
Figure 6.6: Rigid body description using Z-matrix notation of the asymmetric unit of BPO_4 (formulated in Topas).....152
Figure 6.7: Temperature dependence of the (a) x- and (b) z- rotation angles for the asymmetric unit of BPO_4 obtained by sequential and parametric Rietveld refinements. 153
Figure 6.8: (a) B-O-P bond angles and (b) B-P distances with temperature derived from the free atom sequential Rietveld refinement and rigid body parametric Rietveld refinements. 153
Figure 6.9: Rwp values per temperature of the investigated methods of Rietveld refinement. *Values in brackets are the number of parameters refined 154
Figure A1.1: Line broadening effects to the observed profile [2]. 162
Figure A1.2: Observed (blue line with circles), calculated (red line) and difference patterns (grey line) of LaB_6 at ambient temperature. 165
Figure A1.3: Difference in d-spacing from the NIST vs in-house Bruker D2 Phaser data for SRM 660a. 166
Figure A1.4: FWHM vs 2θ for SRM 660a evaluated on the in-house Bruker D2 Phaser.....167
Figure A2.1: Topographical/2 dimensional view (with colour levels) of variable temperature powder X-ray diffraction (VT-PXRD) patterns of (a) $CaBPO_5$, (b) $SrBPO_5$, (c) $BaBPO_5$. In all plots two colour levels were created: Background (turquoise colour) and peaks/reflections (yellow colour).....169
Figure A2.2: FTIR spectra of (a) $CaBPO_5$, (b) $SrBPO_5$, (c) $BaBPO_5$ and (d) BPO_4.....171
Figure A2.3: FTIR spectra of (a) sample **I**, (b) sample **II**, (c) sample **III** and (d) sample **IV**. 173

Figure A2.4: EDS of $NH_4Fe[BP_2O_8(OH)]$.....174
Figure A2.5: FTIR spectrum of $NH_4Fe[BP_2O_8(OH)]$.....175
Figure A2.6: Topographical/2 dimensional view (with colour levels) of the variable temperature powder X-ray diffraction (VT-PXRD) pattern of BPO_4. Two colour levels were created: Background (turquoise colour) and peaks/reflections (yellow colour). 176

Lists of Tables

Table 1.1: Five classes of thermal expansion materials.....5
Table 1.2: Coefficients of thermal expansion for selected framework oxides. 21
Table 1.3: Selected examples of borophophates anions with varying dimensionality (D = 0, 1, 2, 3). B tetrahedra (blue), P tetrahedra (red), O atoms (red spheres) and H atoms (grey spheres). 27
Table 2.1: Refinable parameters.‡ 54
Table 3.1: Cell dimensions as a function of temperature for $ABPO_5$ compounds. 70
Table 3.2: Fractional atomic coordinates obtained at 30 °C and 850 °C for $ABPO_5$ (A = Ca, Sr, Ba). 71
Table 3.3: Thermal expansion characteristics of $ABPO_5$ compounds. 73
Table 3.4: Selected bond lengths (Å) and angles (°) at 30 °C for $ABPO_5$ compounds. 75
Table 3.5: B-O-P bridging angle (θ) and related non-bonded B-P distances as a function of temperature for $ABPO_5$ compounds. 78
Table 3.6: Infrared band wavenumbers (cm^{-1}) and assignments for BPO_4 and $ABPO_5$ (A = Ca, Sr, Ba) compounds. 80
Table 4.1: Selected IR bands for compounds **I**, **II**, **III** and **IV**. 87
Table 4.2: Crystallographic data and Rietveld refinement details for compounds **I**, **II**, **III** and **IV** at 30 °C. 91
Table 4.3: Atomic coordinates (x, y, z), occupancy factors (occ) and isotropic temperature factors (Beq, $Å^2$) for **I**. 96
Table 4.4: Selected interatomic distances (Å) and angles (°) for **I**. 97
Table 4.5: Atomic coordinates, occupancy factors and isotropic temperature factors ($Å^2$) for **II**.....98
Table 4.6: Selected interatomic distances (Å) and angles (°) for **II**. 99
Table 4.7: Atomic coordinates, occupancy factors and isotropic temperature factors ($Å^2$) for **III**. 101

Table 4.8: Selected interatomic distances (Å) and angles (°) for **III**. 102
Table 4.9: Atomic coordinates, occupancy factors and isotropic temperature factors ($Å^2$) for **IV**. 103
Table 4.10: Selected interatomic distances (Å) and angles (°) for **IV**. 104
Table 4.11: Moles of residual species released per formula unit of compound **III** and **IV** as a function of temperature. Peak maximums determined from the differential curves are in brackets. 115
Table 5.1: Details of the Rietveld refinement of **1** at 30 °C. 124
Table 5.2: Fractional atomic coordinates and isotropic temperature parameters ($Å^2$) for $NH_4Fe[BP_2O_8(OH)]$. 126
Table 5.3: Selected interatomic distances (Å) and angles (°) for $NH_4Fe[BP_2O_8(OH)]$. 131
Table 5.4: Refined unit cell parameters of $NH_4Fe[BP_2O_8(OH)]$ at selected temperatures. 135
Table 6.1: The thermal expansion coefficients (TEC) of several cristobalite-type compounds. 143
Table 6.2: Coefficients of equation 6.1, used to describe the variation of cell parameters with respect to temperature for BPO_4. 148
Table A1.1: Instrument settings for the Bruker D2 Phaser 163

Chapter 1 Introduction and Literature review

1.1. Overview

Borophosphates are newly explored materials which demonstrate intriguing structural chemistry, zeolitic and other properties and have many potential applications. However, much of the work published on these materials has focused on investigating the synthetic approaches as well as exploring their fascinating structural chemistry. Little has been reported about their thermal expansion behaviour. This is a critical aspect, considering that this phenomenon can affect other properties and the application of the material. The thermal expansion behaviour of the various borophosphates will be investigated by variable temperature powder X-ray diffraction *(*VT-PXRD*)* experiments. Also, since these measurements give us the opportunity to probe the structural transitions during thermal treatment, information relating to the thermal stability of the open framework borophosphates can be obtained. This chapter contains a brief review of the relevant literature. This includes the basic physical principles that govern the property of thermal expansion; from high positive thermal expansion behaviour to negative thermal expansion behaviour. This is followed by a general overview of scientifically and technologically relevant low thermal expansion and negative thermal expansion materials. Finally, a brief discussion into the structural chemistry of borophosphates follows.

1.2. Thermal Expansion

Thermal expansion can be defined as the susceptibility of materials to change in volume in response to thermal stimulation [1, 2]. This physicochemical phenomenon affects the vast majority of materials, affecting their properties and applications. Examples include engine parts such as pistons, dental ware such as tooth fillings, numerous alloys and building materials such as cements and bricks (figure 1.1 a and b). Furthermore, numerous composites have been tested as possible dental fillers, with the intention of matching the thermal expansion behaviour of the tooth and the dental filling under varying thermal environments [3]. The property of thermal expansion is also considered in zeolites and zeolites-like materials that are used in the fuel industry for petroleum cracking. Since this catalytic process

occurs at high temperature, knowledge of the composition and structure of these materials at high temperature is important in order to improve the process. Thermal expansion serves as a critical aspect in certain engineering applications where, for example, thermal expansion joints are used to separate sections of roadways on bridges, concrete highways and railroad tracks to amend for dimensional changes that result as the temperature changes (figure 1.1c) [4]. Even with such structural features designed to compensate for thermal expansion, materials may experience mechanical failure during their lifetime due to the thermal stress that occurs from continuous thermal expansion and contraction that the material is exposed to. Thus, it has become desirable to manufacture materials that have dimensional integrity and resist forming microcracks when the operational thermal environment changes [1].

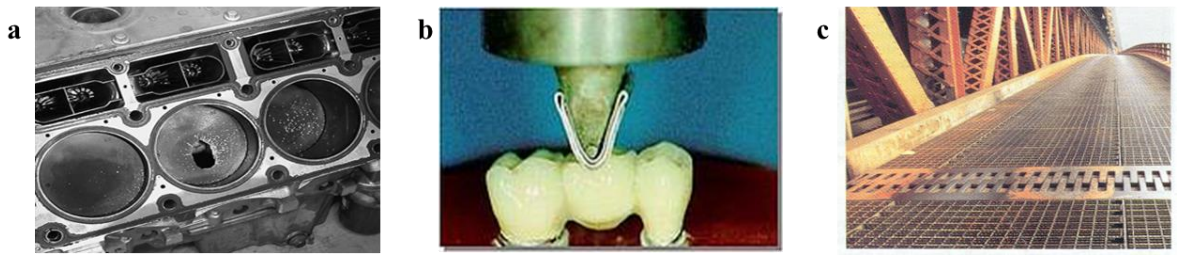


Figure 1.1: a) Engine pistons [5], b) tooth filling [6] and c) bridges are affected by thermal expansion [7].

In general, thermal expansion can be categorised as either intrinsic or extrinsic. The latter occurs as a result of thermally induced changes in crystallites. For example, while the material may have expansion of the unit cell dimensions with increasing temperature, an overall thermal contraction of the material may result from the closing of the microcracks with increasing temperature [8]. Of particular interest is intrinsic thermal expansion because it is possible to adjust the structural features at the atomic level, and hence, engineer materials that have expected thermal behaviour. Intrinsic thermal behaviour is a consequence of changes in the materials unit cell dimensions when heated. Moreover in solids, intrinsic thermal expansion may be categorised into isotropic expansion which occurs by the same magnitude and sign across all of the unit cell axes, and anisotropic thermal expansion occurring disproportionally across the different unit cell axes e.g. expands or contracts only in one or two axes with different magnitude and sign. Hence, materials with a cubic unit cell

or which are amorphous have isotropic thermal expansion behaviour and those with a non-cubic unit cell have anisotropic thermal expansion behaviour.

1.2.1. Measuring and quantifying thermal expansion

Various methods for measuring the coefficient of thermal expansion (CTE), or α, of solids have been devised. Pertaining to the physical principle involved in the measurements, the different methods can be categorised under two general classes [9]:

1. Microscopic (lattice) expansion measurements:

Through the use of X-ray or neutron diffraction experiments of powder or single crystal samples. These measurements are done using *in-situ* heating devices, which vary the temperature while collecting diffraction patterns. Using the appropriate crystal structure solution and refinement methods, a collection of lattice constants at each temperature is obtained and used to calculate the linear and volume coefficients of thermal expansion.

2. Macroscopic measurements:

Various techniques with different degrees of sensitivity have been developed [9]:

- Mirror and optical lever method
- Three-terminal capacitance method
- Optical interferometric techniques
- Dilatometer with grids

Of these macroscopic techniques, the dilatometer with grids is the commonly used measurement. Dilatometry measures α by heating the sample (ceramic pallet or large single crystal) in a furnace and measures the changes in volume through displacement sensors [10].

The microscopic (lattice) diffraction techniques are beneficial in measuring α as opposed to the macroscopic techniques. Whereas macroscopic techniques such as dilatometry fail to measure changes in the respective crystallographic axes with temperature, changes in each crystallographic axis are accounted for using the diffraction techniques. This is important when measuring α in anisotropic materials. Furthermore, since the macroscopic techniques

measure the overall α of bulk samples, this is disadvantageous in multiphase samples, where the expansion or contraction of component phases cannot be distinguished. The lattice changes with temperature of each component in multiphase solids can be distinguished using diffraction measurements.

The coefficient of thermal expansion (α) of a material is defined as the fractional change in length (α_L) or volume (α_v), with per unit change in temperature [10]. Therefore, the coefficient of linear thermal expansion (α_L) and the coefficient of volumetric thermal expansion (α_v) are expressed as:

$$\alpha_L = \frac{\Delta L}{Lo\ \Delta T} \qquad (1.1) \qquad\qquad \alpha_V = \frac{\Delta V}{Vo\ \Delta T} \qquad (1.2)$$

where ΔL and ΔV are the changes in length and volume, respectively, when the temperature is changed by ΔT. Lo and Vo are the initial length and volume, respectively, which are usually measured at room temperature [1, 10]. For isotropic materials (cubic and amorphous solids), α_v is related to α_L by:

$$\alpha_v = 3\ \alpha_L \qquad (1.3)$$

As seen in equations (1.1) and (1.2), α_L and α_v are a function of temperature, therefore it is important to quote the temperature range at which α was measured for the investigated material.

A more useful expression is the Grüneisen equation for the coefficient of volumetric thermal expansion (α_v) obtained from the measurement of γ, Cv, V and K [11, 12]:

$$\alpha_V = \frac{\gamma\ Cv\ K}{V} \qquad (1.4)$$

where γ is the Grüneisen parameter, Cv is the specific heat capacity, K is the isothermal compressibility and V is the molar volume. The various phonon modes present in a crystalline solid at a particular temperature are related to α_v through the Grüneisen parameter γ in equation 1.4. A phonon is defined as a quantized mode of vibration and may possess various sets of frequencies, wavelengths and amplitudes. Different sets of phonons in a solid have a harmonic (in phase) or anharmonic (out of phase) relationship with each other [10]. The equation relating a particular phonon mode to its γ is given by:

$$\gamma = -\frac{\mathrm{d}(\ln \nu)}{\mathrm{d}(\ln V)} \qquad (1.5)$$

where ν is the frequency of the phonon mode. Phonon modes which have a frequency that softens/decreases with a decrease in volume (V) will have a negative Grüneisen parameter (-γ). Therefore the sign of the γ value substituted in equation 1.4 will dictate whether α_v is negative (with $-\gamma$) or positive (with $+\gamma$). The values of Cv, K and V are all greater than 0 [13].

Based on the value of the coefficient of thermal expansion (α) within a particular temperature range, materials can be categorized into five groups, as listed in table 1.1 [1, 14]

Table 1.1: Five classes of thermal expansion materials

Class	CTE (ppm K^{-1})
High positive thermal expansion	$\alpha > 8.0$
Intermediate positive thermal expansion	$2.0 < \alpha < 8.0$
Zero thermal expansion (ZTE)	$\alpha = 0$
Low positive thermal expansion (LTE)	$0 < \alpha < 2.0$
Negative thermal expansion (NTE)	$\alpha < 0$

1.2.2. Microcracking

The α value measured on a single crystal solid is not always identical to the α value measured from a ceramic (polycrystalline) solid. This occurs as the α from a polycrystalline solid will result from averaging the contributions of α from each crystallite [1]. Furthermore, the choice of technique used to measure the α of a material may also result in different magnitudes of α. Generally, macroscopic (bulk) measurements of α are frequently lower in magnitude than α derived from microscopic (lattice) measurements e.g. the material $Sc_2(WO_4)_3$ [15]. The reason for mismatches in the α value is due to microcracks being formed with temperature in the ceramic samples [15]. These microcracks can form as a result of the high degree of anisotropy in the lattice as it expands or contracts (α_a, α_b and α_c are different in magnitude and sign). One would expect fewer microcracks forming from the thermal expansion or contraction of cubic materials. The consequence of these internal microcracks is the lowering of the mechanical strength of the solid, which can have deleterious implications on the materials application. Therefore, for mechanical durability of a material used under varying thermal environments, the material must preferably have a zero to very low average α value and have little degree of anisotropy as a function of temperature. These thermally and therefore mechanically durable materials will typically find applications in composites as buffer materials for thermally induced stress from another material with less thermal and therefore mechanical durability.

1.3. The origin of thermal expansion

In general, the majority of known solids expand upon heating and have a positive coefficient of thermal expansion. The principle by which this positive thermal expansion occurs in materials is well understood, and is related to the dilation of chemical bonds due to the anharmonicity of the potential energy curves [16]. Therefore, it is the nature of the interatomic potential energy curve that governs the positive thermal expansion (PTE) behaviour. Consider figure 1.2, which illustrates the anharmonic potential energy curve relating two atoms in a solid material. As a result of the asymmetry of this curve, the increase in the energy of longitudinal vibrations (phonons) of a pair of atoms along the line linking them causes an increase in the mean distances (R_1 to R_2) between the atoms as the temperature increases (T_1 to T_2) [10, 13]. The asymmetry of this curve is clearly seen as the gradient of the curve is steeper initially on the downward side and shallower on the upward

side. A schematic of these longitudinal vibrations as a function of temperature is shown in figure 1.4a. Generally, materials with stronger chemical bonds will have smaller thermal expansion coefficients [1, 10, 13].

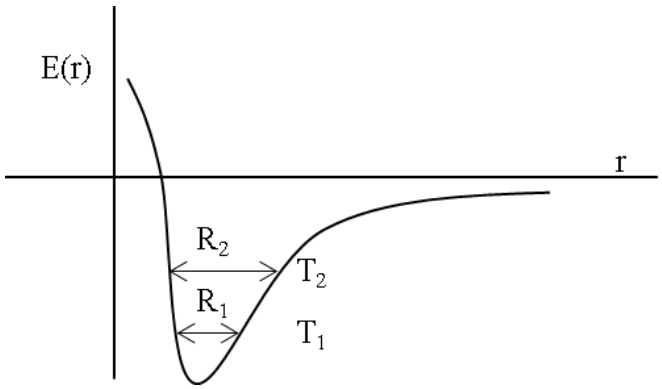


Figure 1.2: Model of an anharmonic potential energy curve for a pair of atoms in a solid material.

The above principles of the anharmonicity of the potential energy curve, longitudinal vibrational modes and chemical bond strength fail to explain the behaviour of materials that display the contrasting effect of having anomalously low thermal expansion (LTE) behaviour and some which contract upon heating (NTE i.e. negative thermal expansion) behaviour. Such anomalous thermal expansion behaviour occurring in a few materials is best explained by the changes of the respective crystal structures with temperature. For such anomalous expansion behaviour to occur, some structural phenomena/mechanism must dominate the factors explained above which lead to the thermal expansion of chemical bonds. The following sections will explain various physical phenomena which have been used to account for the LTE and NTE behaviour of various materials [8, 10, 13].

1.3.1. Phase transitions

NTE behaviour occurs just below the ferroelectric-paraelectric phase transition in perovskite-type solids such as $BaTiO_3$ and $PbTiO_3$ [17]. This phase change signifies a change from the low temperature tetragonal to the high temperature cubic crystal system. Typically, in the tetragonal phase, the TiO_6 and AO_{12} (A = Ba, Pb) polyhedra became less distorted with increasing temperature. For example, in $PbTiO_3$ the average Ti-O bond distance in the TiO_6

octahedra decreases from 2.012 to 1.983 Å. The overall coefficient of thermal expansion in this Ti-O bond distance is α_L = -3 x 10^{-5} K^{-1} [18]. This effect of structural ordering is accompanied by an overall contraction of the unit cell volume with increase in temperature in the tetragonal region (e.g. $PbTiO_3$, α_L = -3.3 x $10^{-6}K^{-1}$ in the temperature range of 30 – 400 °C). Normal PTE behaviour occurs after the phase change to the cubic region (e.g. occurring at 490 °C in $PbTiO_3$).

In other materials such as the $A_2M_3O_{12}$ structural family [19], phase transition often lead to drastic changes in the CTE. For example in $Sc_2Mo_3O_{12}$, the low temperature monoclinic phase shows PTE behaviour (α_v = 2.19 x 10^{-5} K^{-1} between 4 and 170 K), while the high temperature orthorhombic phase shows NTE behaviour (α_v = -6.3 x 10^{-6} K^{-1} between 180 and 300 K; figure 1.3).

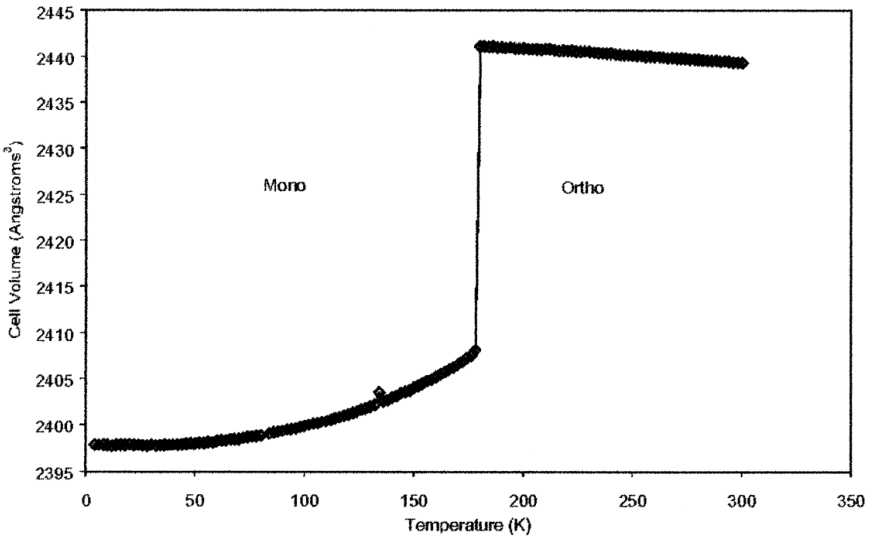


Figure 1.3: Variation in the unit cell volume with temperature for $Sc_2Mo_3O_{12}$. Monoclinic to orthorhombic phase change occurs around 178 K. Obtained from [19].

1.3.2. Magnetic effect

Magnetic effects have been shown to give rise to LTE and NTE behaviour in various solids. One example is the metallic alloy, Invar (FeNi 36 containing 36 % nickel and 64 % iron content), with α of 0.07 x 10^{-6}/°C at 20°C [20]. This anomalous LTE behaviour has been linked to variations in the magnetic structure (via a magnetic phase change) as a function of

temperature, which lead to the formation of magnetic microdomains within the material. Therefore, magnetic order-disorder (ferromagnetic to paramagnetic phase changes) occurs in the material and lead to LTE behaviour. As the temperature increases further, these magnetic microdomains are inhibited, and PTE behaviour is re-established. This magnetic order-disorder mechanism is known as the Invar effect [21]. Other materials which exhibit this magnetostrictive mechanism include metals such as Cr, α-Mn, Lu_2Fe_{17} and Y_2Fe_{17} [22]. Interestingly, the name Invar is derived from the word invariable, due to the materials anomalous thermal expansion behaviour [23].

1.3.3. Phonons

Another mechanism explaining the dependence of NTE behaviour on the crystal structure of oxides, relates to the transverse thermal motion of oxygen in M-O-M linkages. This structural phenomenon has been attributed as the mechanism responsible for NTE behaviour in most materials exhibiting this property. However as will be shown later, since this mechanism can be applied to any crystal structure [8], it has been used to account for LTE behaviour occurring in framework oxides [24-30].

As shown earlier, the origin of PTE behaviour has been linked to longitudinal vibrational modes as a function of temperature in M-O-M linkages (figure 1.4a). These will lead to an increase in the M-O bond length, and subsequently in the non-bonded M-M distances with increase in temperature. Conversely as the temperature elevates, there can be an increase in the mean amplitude of vibration of the oxygen atoms perpendicular to the non-bonding M-M plane (figure 1.4b) [10]. This vibration will lead to the oxygen atoms moving transversely in the M-O-M linkage. The magnitude of the M-O-M tilt angle (θ) will change and compress the metal atoms (M-M distance) together leading to the contraction of the lattice with increase in temperature (NTE behaviour). During these transverse phonons, the individual M-O bonds generally show little thermal expansion due to the strong M-O bonds. Examples of framework structures which have these transverse thermal motions of oxygen atoms leading to NTE behaviour include SiO_2 [8, 10], tungstates and molybdates [19], quartz like materials [25-27, 29, 31], zeolites and zeolite-like materials [32, 33]. Transverse phonons are generally readily activated (over longitudinal phonons) at lower temperatures as they require lower excitation energy. This means that transverse phonons readily populate the overall Grüneisen parameter ($\gamma_{av} = \sum c_i\gamma_i / \sum c_i$, where c_i is the weighting parameter for a particular mode) at

lower temperatures. Interestingly, this phenomenon can also occur in O-M-O linkages with transverse vibrations of the bridging metal atoms with temperature. Examples include compounds such as Cu_2O and Ag_2O [8, 34, 35].

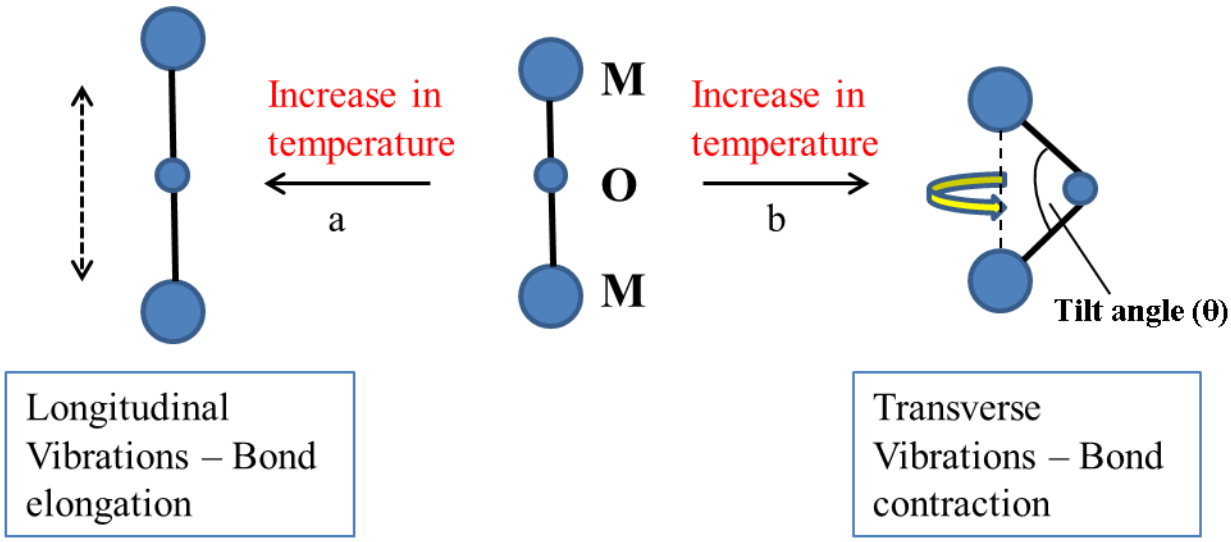


Figure 1.4: Schematic representation of a) longitudinal thermal motion b) transverse thermal motion of oxygen atom in the M-O-M linkage as a function of heat. M = Metal and O = oxygen atoms, respectively. Adapted from [13].

Having discussed transverse motion in M-O-M linkages, and the consequence thereof, the next issue remaining is how these motions are translated over the entire inorganic framework structure. This is readily approached by the rigid unit mode (RUM) model [8, 10, 13, 36-38]. This model has been applied to studies on the crystallographic structures, phase transitions and physical properties of framework silicates [39]. In the RUM model, the MOx polyhedra are treated as rigid bodies i.e. a classic mechanical unit with a moment of inertia, a mass, three translational degrees of freedom, and three vibrational degrees of freedom. The framework structure is treated as a three-dimensional periodic network of corner sharing rigid polyhedra and interstitial spaces. The polyhedra are stiffer (become less distorted due to strong intra-polyhedral M-O bonds) than the flexible M-O-M linkages. The M-O-M linkages connect neighbouring polyhedra. This model postulates that the cooperative back and forth tilting of corner linked polyhedra along the M-O-M linkages give rise to the transverse thermal motion of oxygen atoms. While preventing the distortion of neighbouring polyhedra

and retaining the symmetry of the cell, one polyhedron pulls a neighbouring polyhedron closer, and thus reduces the interstitial volume (figure 1.5). However, some structures have small distortions of the polyhedra. The cooperative back and forth tilting of these polyhedra are known as Quasi-RUMs (QRUMs).

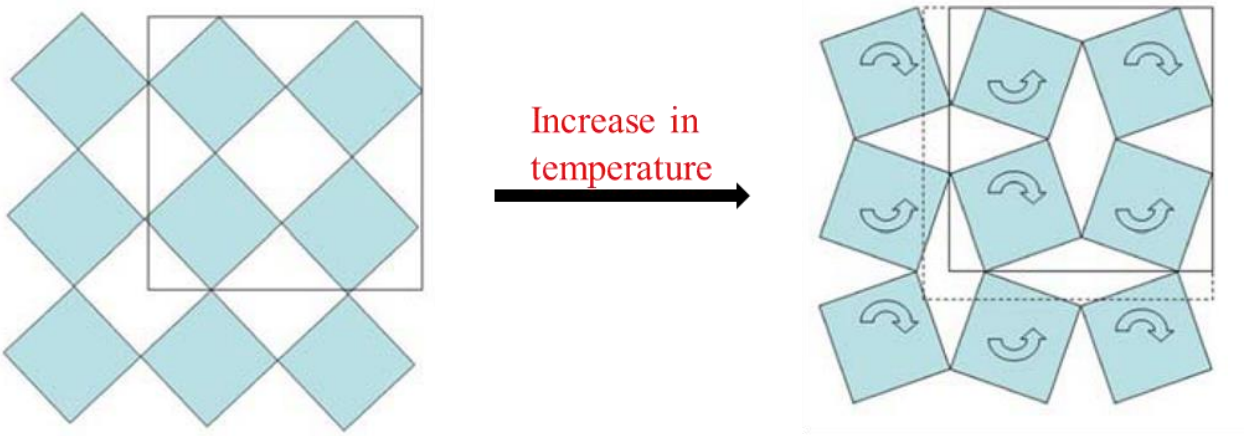


Figure 1.5: 2D square lattices showing the rocking motion of rigid MO_4 RUM's as a consequence of the bending of M-O-M linkages in response to heat. Note the change in unit cell area with increase in temperature. Obtained from [10].

The role of the M-O-M tilt angle (θ) on LTE behaviour has been investigated in quartz-like materials. As with NTE materials, it has been established that the linkage and rotation of constituent rigid polyhedra play a crucial role in determining the thermal expansion behaviour of the material. This finding has also been demonstrated in various cristobalite-type compounds whereby the larger the tilt angle (θ), the smaller the volume thermal expansion coefficient (α_v) [29, 30]. The reason given for this is that the tilt angle will tend to dilate more in order to accommodate the increase in thermal vibration of the bridging oxygen atoms with increase in temperature. However, the degree of variation of the tilt angle (θ) for a particular material is limited by intermolecular forces, the type of framework topology and constraints [10]. Therefore, the distinguishing structural feature for materials with NTE and LTE behaviour are found to be as follows [1, 40]:

- Consists of rigid polyhedra made up of strong metal-oxygen bonds which resist high positive thermal expansion behaviour. The connecting polyhedra must be preferably linked at the corners and be tetrahedral or octahedral units.
- The oxygen atoms are normally found in two-fold coordination in order to form flexible M-O-M linkages connecting the rotating rigid polyhedral units.
- The overall three-dimensional crystal structure should consist of connecting polyhedra and lattice spacing/voids into which the rotating polyhedra can move into. Therefore, the resulting material has low packing density.

As already established, the majority of materials expand on heating and exhibit PTE behaviour. However some remarkable materials display low positive thermal expansion or negative thermal expansion (LTE or NTE, respectively), over certain temperature ranges. The next section is a scope into the structural and thermal characteristics of various families of LTE and NTE materials that have shown valuable scientific and technological interest.

1.4. Negative and low positive thermal expansion materials

Perhaps the most useful application of LTE and NTE materials is their use as components in composites to control the overall CTE (α) of the composite. In certain cases the composite is adjusted to an overall zero thermal expansion (ZTE) coefficient [41]. This will also improve the overall strength of the composites microstructure as a function of temperature. In general, LTE and NTE materials have found widespread applications as catalyst supports, heat-engine components, telescope components, ovenware and low temperature sensing devices.

1.4.1. Cordierite

Three families of low thermal expansion materials, namely, cordierite, zircon and silica glass have been used in ceramic products for several years prior to World War II. The naturally occurring mineral cordierite $(Mg, Fe)_2Al_4Si_5O_{18}.nH_2O$, $0 \leq n < 2$, has the magnesium cordierite $Mg_2Al_3(Si_5Al)O_{18}$ as the parent member of the family [42]. Mg-Cordierite is also the easiest member of the cordierite solid solution to synthesize and is isostructural to the mineral beryl ($Al_2Be_3Si_6O_{18}$). It exists in two polymorphs: a low-temperature orthorhombic phase, and a high temperature hexagonal phase (obtained above 1450 °C) [43]. The crystal

structure of the orthorhombic phase (figure 1.6) features channels running along the *c*-axis formed by stacks of hexagonal rings. Each hexagonal ring is made up of five SiO_4 and one AlO_4 corner-sharing tetrahedra. The three-dimensional open framework is completed by Mg octahedra and additional Al tetrahedra which connect the hexagonal rings. The channel structure can also accommodate various small molecules including H_2O, CO_2 and noble gasses [44]. As far as the thermal expansion behaviour of cordierite solid solutions, the members of this family generally display LTE behaviour along the *a* and *b* axis and NTE behaviour along the *c* axis. This results in an overall LTE behaviour of the material (table 1.2).

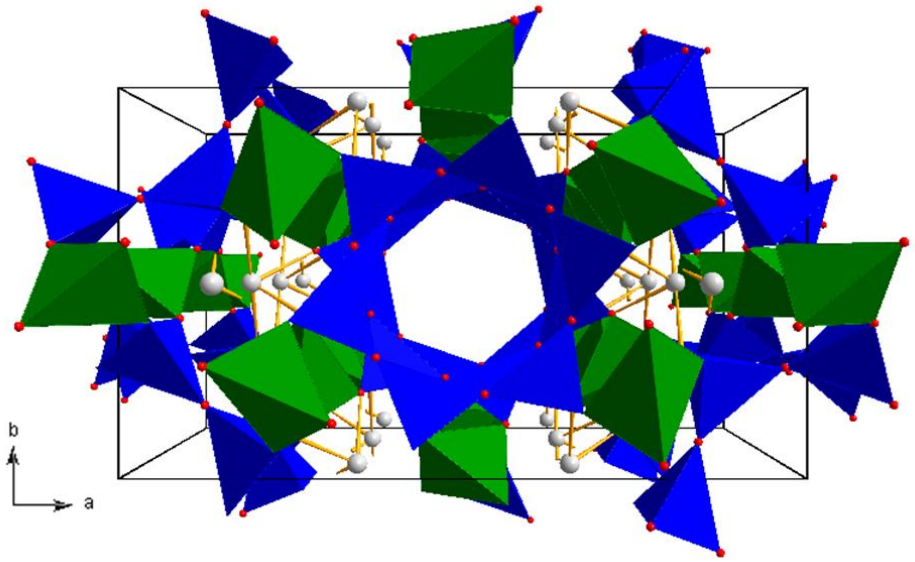


Figure 1.6: The crystal structure of orthorhombic (space group *Cccm*, no. 66) $Mg_2Al_3(Si_5Al)O_{18}$, the parent compound of the cordierite family. AlO_4 tetrahedra (green), Si/Al tetrahedra (blue) and Mg atoms (white spheres).

1.4.2. Lithia-Alumina-Silica (LAS) system

In 1948, Hummel [45] discovered the material β-spodumene and later on other members of the system lithia-alumina-silica. Other members included β-eucryptite and its solid solutions with β-spodumene. These ternary compounds dominated the materials research and ceramic industry almost for four decades. These materials exhibit very low and negative thermal

expansion behaviour (table 1.2). As such these materials have been used in thermal endurance applications from cookware to telescope technologies, with industrial companies such as Owens-Illinois Inc. [46], PPG Industries [47] and Corningware [48] being involved in the research, production and selling of LAS based products. The crystal structure of both β-spodumene and β-eucryptite are closely related to the quartz structure whereby the Al atoms replace the Si atoms in the quartz structure [1, 45]. Additional Li atoms are located in the channels of the structure (figure 1.7).

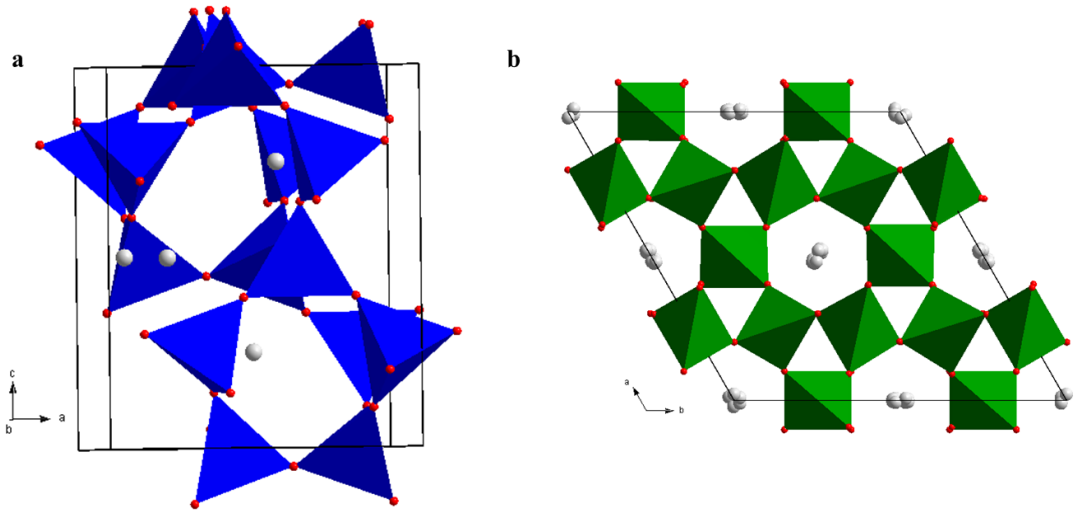


Figure 1.7: Three-dimensional open-framework of (a) β-spodumene (space group $P4_32_12$, no. 96) and (b) β-eucryptite (space group $P6_422$, no. 181) formed from corner-linked AlO_4 and SiO_4 tetrahedra. Li ions (white spheres) are accommodated in the voids.

1.4.3. AM_2O_8 family

Recently, great interest has been shown in the material ZrW_2O_8 because of its extraordinary ability to continuously contract on warming over the exceptional range starting from below 2 K to above 1000 K [49] (figure 1.8 and table 1.2). Cubic zirconium tungstate (ZrW_2O_8) is a member of the AM_2O_8 family (where A is any cation in an octahedral coordination environment and M is W or Mo). Other members of this family include: HfW_2O_8 [38], $Zr_{1-x}Hf_xW_2O_8$ [50], $ZrW_{2-x}Mo_2O_8$ [51], $ZrMo_2O_8$ [52] and $Zr_{1-x}M_xW_2O_8$ (M = Sc, In, Y) [53]. The room temperature crystal structure (figure 1.9) of the AM_2O_8 family is composed of corner sharing MO_4 tetrahedra and AO_6 octahedra whereby each AO_6 octahedron is connected to six

different MO_4 tetrahedra, and each MO_4 tetrahedron is connected to three AO_6 octahedrons. The remaining oxygen atom in each MO_4 tetrahedron is singly coordinated to the central M atom. As with ZrW_2O_8, all of the members of the AM_2O_8 family exhibit NTE behaviour over a broad temperature range (table 1.2). Furthermore, over the NTE temperature range, these materials undergo a phase change (e.g. as α-low temperature to β-high temperature phase change occurs at approximately 423 K in ZrW_2O_8 and HfW_2O_8) which is accompanied by oxygen atom migration. As a result, various oxygen atoms become disordered above the phase transition. It has been shown that the NTE behaviour in AW_2O_8 materials can be attributed to the transverse thermal vibrations of bridging oxygen atoms leading to coupled rotation of rigid bodies (polyhedra). The NTE behaviour of ZrW_2O_8 over a broad temperature has seen the material being used in Cu/ZrW_2O_8 composites which serve as heat sinks in electronic devices [54]. The thermal expansion behaviour of this composite matches that of Si over a broad temperature range.

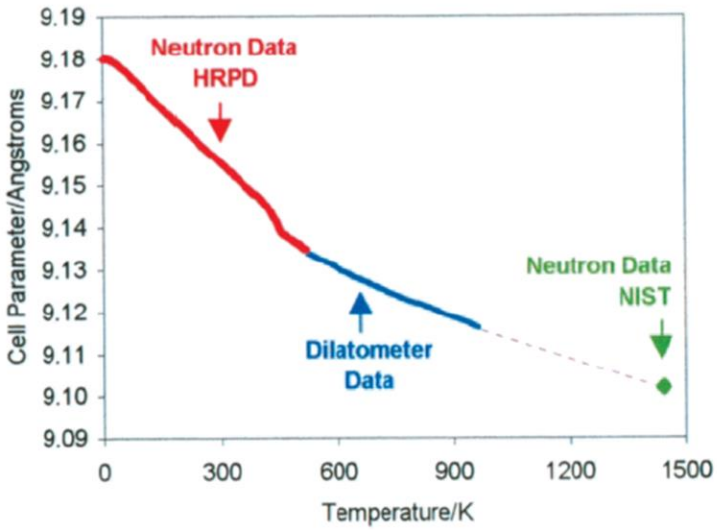


Figure 1.8: Variation of the cubic lattice parameter of ZrW_2O_8 determined using neutron diffraction and dilatometry measurements [38]. ZrW_2O_8 is stable until 1050 K and re-emerges (thermodynamically stable) around 1443 K [55]. The dashed line connects both points.

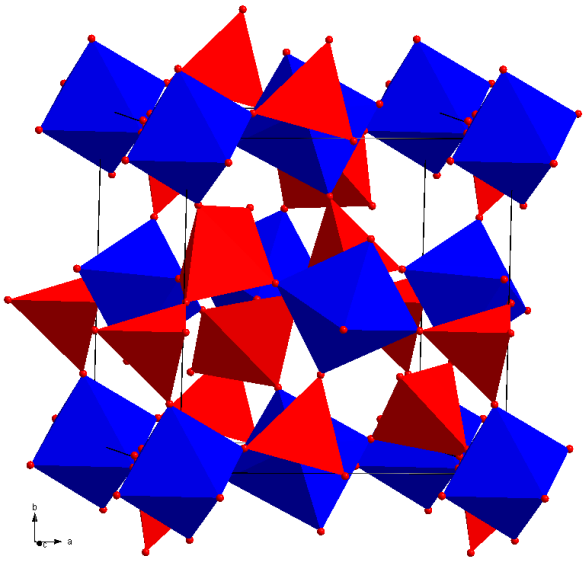


Figure 1.9: Crystal structure of ZrW_2O_8 at room temperature (space group $P2_13$, no. 198). ZrO_6 octahedra (blue) and WO_4 tetrahedra (red).

1.4.4. Zeolites and Aluminophosphates ($AlPO_4$'s)

Zeolites are an established class of microporous materials, each member consisting of a unique framework structure. Currently there are 176 known unique zeolite framework structures indicating that there are 176 ways in which the component polyhedra viz. AlO_4 and (or exclusively) SiO_4 can be connected. The characteristic feature of the zeolite crystal structure having rigid polyhedra and interstitial spaces provides a platform for these materials to exhibit anomalous thermal expansion behaviour. The charge balancing non-framework cations often alter the thermal expansion behaviour in zeolites, by adding a positive contribution to the overall thermal expansion behaviour. This positive contribution arises from the large positive thermal expansion in A-O bonds (where A = alkali or alkaline earth metal cation and O is an oxygen atom) [56]. Despite this, a large number of zeolites exhibit NTE behaviour (table 1.2). In some zeolite materials, the origin of NTE behaviour has been linked to the RUM models [33], whereas computational studies by Tao *et al.* place more emphasis on correlated transverse thermal vibrations of atoms leading to NTE behaviour [37]. The zeolite group faujasite has a framework structure consisting of sodalite cages (figure 1.10). The NTE behaviour in siliceous faujasite (dealuminated Y-type zeolite) has been linked to coupled rotations of corner linked SiO_4 tetrahedra, whereby rotations of these polyhedra causes the sodalite cages to compress and reduce the interstitial volume [56].

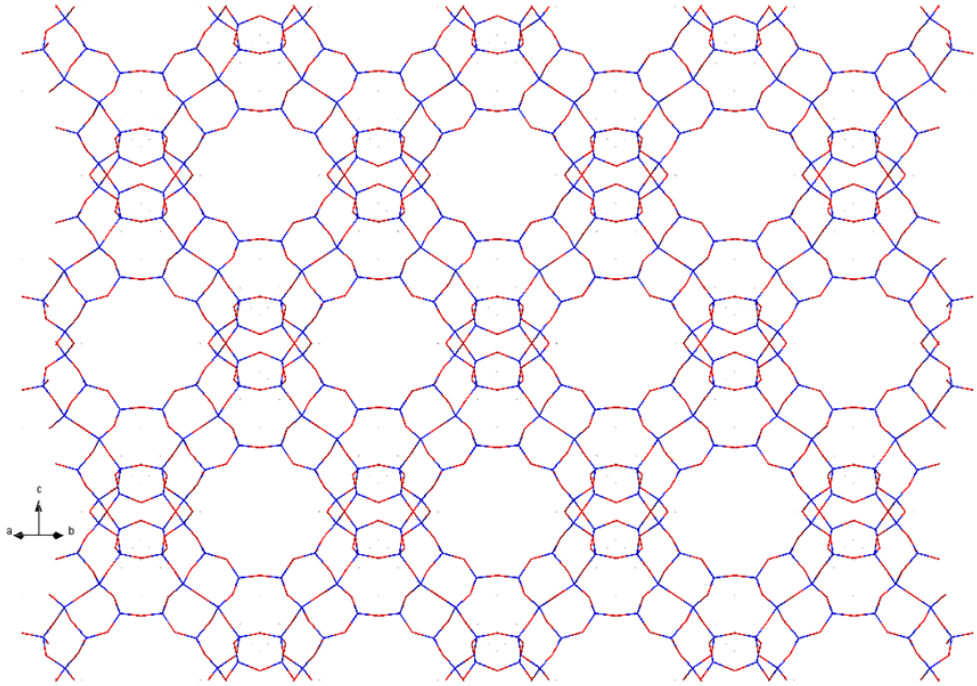


Figure 1.10: Crystal structure of the siliceous zeolite faujasite (dealuminated Y-type zeolite). Reference Code: ICSD- 41394.

The aluminophosphates ($AlPO_4$'s) are porous zeolite-type materials. Therefore, as with zeolites, they possess the essential framework components needed to exhibit LTE and NTE properties. Anhydrous $AlPO_4$-17 has a hexagonal structure (space group: $P6_3/m$) which exhibits strong NTE behaviour of -11.7 x 10^{-6} K^{-1} over the temperature range of 10 – 300 K [32]. This material is devoid of extra framework water molecules and charge balancing cations which would generally add a positive contribution to the thermal expansion behaviour. The crystal structure of $AlPO_4$-17 [32] is composed of alternating, corner-sharing AlO_4 and PO_4 tetrahedra. These link up to form 4- and 6-membered rings which combine to form layers of 6- and 12-membered rings (figure 1.11). The NTE behaviour in this material has been linked to the rotations of rigid polyhedra, arising from transverse thermal motions of bridging oxygen atoms.

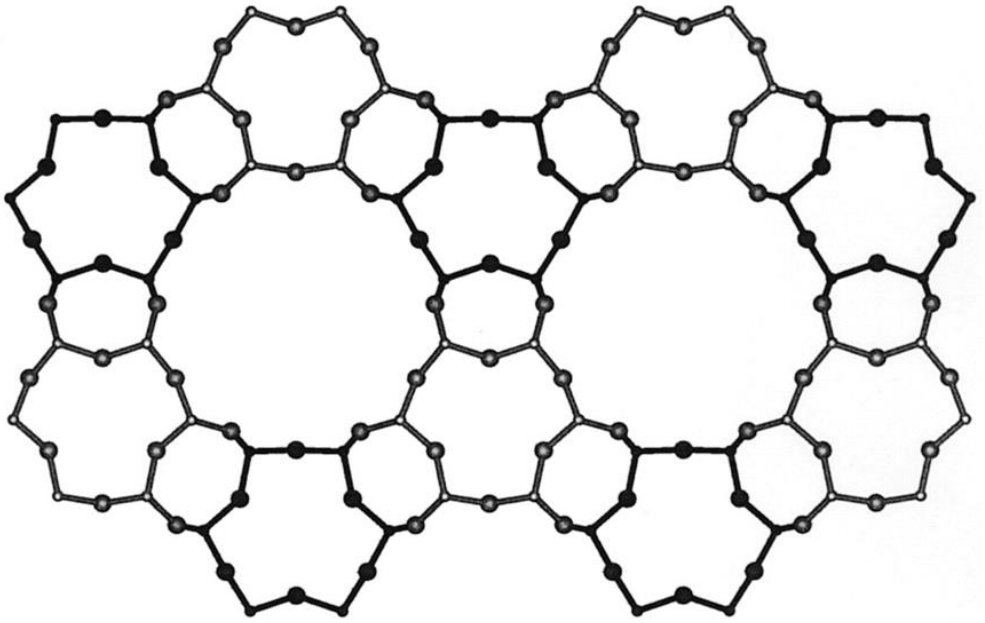


Figure 1.11: Structure of $AlPO_4$-17 projected along the *c*-axis [32].

1.4.5. Other materials

The open-framework type ceramics (as discussed above) are not the only type of materials which exhibit LTE or NTE behaviour. Although exhibiting NTE behaviour over a very narrow temperature window, the hexagonal crystal system of ice (I*h*) reveals this property below 73 K (figure 1.12) [57]. The NTE behaviour in this phase is supposedly related to transverse thermal vibrations of bridging atoms [57-59]. Above this temperature normal PTE behaviour occurs.

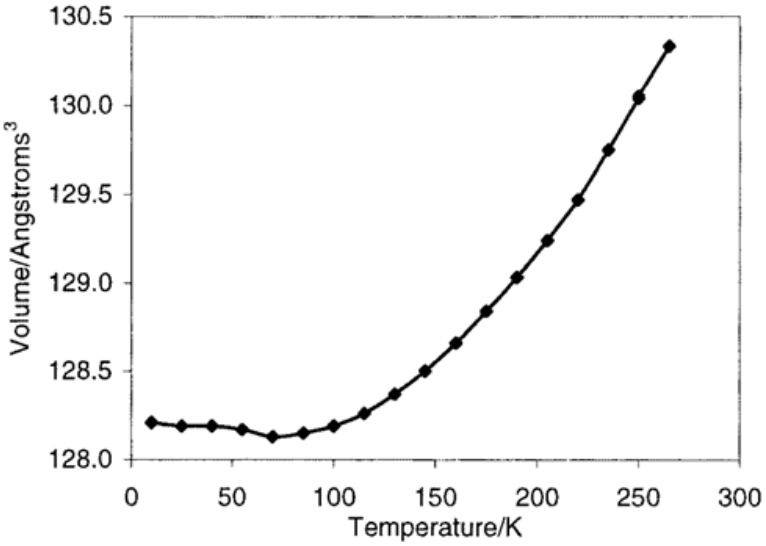


Figure 1.12: Variation of the unit cell volume with temperature of ice I*h*, also known as ice-phase-one (space group $P6_3/mmc$). Derived from measurements by Röttger *et al.* [57].

Another important class of materials that exhibit anomalous thermal expansion behaviour was discovered by Boilot *et al.* in 1979 [60]. While investigating the ionic conductivity of $Na_{1-x}Zr_2P_{3-x}Si_xO_{12}$ (NZP or NASICON) it was reported that the thermal expansion behaviour of this system exhibited controlled LTE and NTE behaviour by varying the ionic substitutions at different lattice sites (x in the chemical formula). This gave a series of materials with various chemical compositions, and owing to the inherent framework topology, varying degrees of superionic conductivity capabilities [61, 62], ability to accommodate certain radioactive waste [63] and substitutions of ionic species at various vacant lattice sites were possible. The average coefficients of thermal expansion (α_L) of various members of the NASICON family are listed in table 1.2. In general, the thermal expansion behaviour of members this family of materials has been related to factors such as migration of cations between various lattice sites [64] and coupled rotations of rigid polyhedra [65, 66].

Several metal oxide mixtures such as the $A_2M_3O_{12}$ family constitute other important materials that display LTE and NTE behaviour over certain temperature ranges (table 1.2). For the $A_2M_3O_{12}$ family, two contrasting framework connectivity's exist. This includes the $ANbP_3O_{12}$ (where A = Ti, Zr or Hf) [67, 68] with rhombohedral symmetry and $A_2M_3O_{12}$ (where A = Sc, Al, Zr, Fe, Lu, Y and others and M = Mo or W) [19] with either monoclinic

(low temperature) and orthorhombic (high temperature) symmetry. Highly anisotropic NTE properties have been observed in the rhombohedral and orthorhombic modifications in several members of this family. Therefore, owing to the compositional diversity in this family, controllable thermal expansion behaviour as a function of composition can be prepared (figure 1.13).

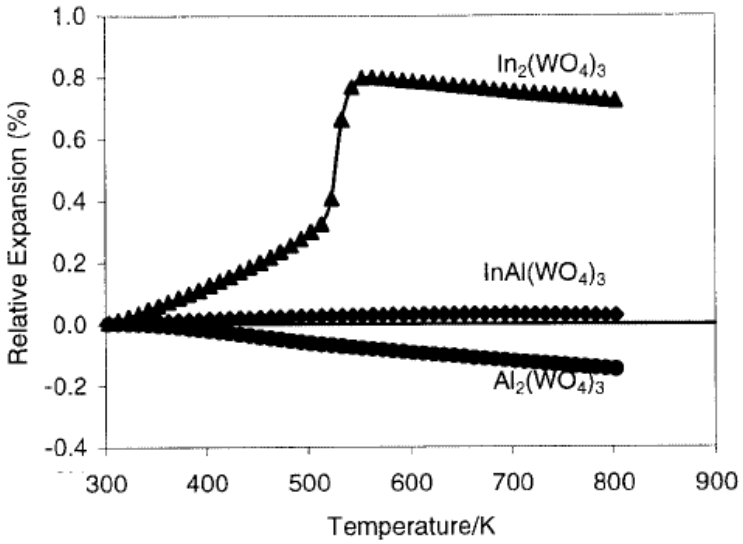


Figure 1.13: Alteration of the relative expansion (%) with temperature of three $Al_{2-x}In_x(WO_4)_3$ materials, representing the $A_2M_3O_{12}$ family. Obtained from [13].

The AM_2O_7 materials (where A = Si, Ge, Sn, Pb, Ti, Hf, U, Th, Mo, W, Re and others; M = P, V) [69] are structurally related to cubic α-ZrW_2O_8. That is, the structure consists of M_2O_7 units (which replace two unlinked WO_4 tetrahedra in ZrW_2O_8). Each M_2O_7 unit is composed of a pair of corner-sharing MO_4 tetrahedra. The network structure is completed by AO_6 octahedral groups, which are corner-linked to six MO_4 tetrahedra. Several members have cubic symmetry, and like ZrW_2O_8 exhibit isotropic NTE behaviour. This NTE behaviour occurs after a phase change from a low-temperature, lower-symmetry cubic phase. The low temperature phase exhibits positive thermal expansion behaviour [69]. However, unlike ZrW_2O_8 the NTE behaviour has its origin from QRUMs, involving coupled three-dimensional rotations of slightly distorted polyhedral units and the bending of non-linear M-O-M linkages with temperature [70].

Lastly, technologically and scientifically interesting materials such as carbon nanotubes (CNTs) [71-73], foams [74] and microporous metal organic frameworks (MOFs) [75-77] have been found to exhibit NTE behaviour over certain temperature ranges.

Table 1.2: Coefficients of thermal expansion for selected framework oxides.

Family	Chemical composition	CTE (x 10^{-6} K^{-1})				Range (*T*/K)	Reference
		α_a	α_b	α_c	α_L*		
Cordierite	$Mg_2Al_4Si_5O_{18}$	2.16	2.16	-1.78		298-873	[78]
	$Mg_{1.546}Fe_{0.454}Al_4Si_5O_{18}$	2.21	2.21	-0.9		298-874	
	$MgMnAl_4Si_5O_{18}$	1.95	1.95	-0.45		298-875	
	$Mg_2Al_{3.4}Ga_{0.6}Si_5O_{18}$	1.27	1.27	-0.28		298-876	
	$Mg_2Al_4Si_4GeO_{18}$	1.34	1.34	-2.17		298-877	
Lithia-Alumina-Silica (LAS) system	β-spodumene (1:1:4)				0.9	Not mentioned	[1]
	β-eucryptite (1:1:2)				-6.2		
	Hercuvit				0 to -0.3		
	Petalite (1:1:8)				0.3		
	Pyroceram (LAS + TiO_2)				-0.07 to 1.3		
AM_2O_8	ZrW_2O_8	-8.7	-8.7	-8.7		20-430	[79]
		-4.9	-4.9	-4.9		430-950	
	HfW_2O_8	-8.8	-8.8	-8.8		90-300	[80]
		-5.5	-5.5	-5.5		500-560	
	$ZrMo_2O_8$	-6.9	-6.9	-6.9		2-200	[52]
		-5.0	-5.0	-5.0		250-502	
	$ZrWMoO_8$	-7.69	-7.69	-7.69		2-200	[51]
	Zeolite MTN	-1.7	-1.7	-1.7		463-1002	[81]
	Zeolite ITQ-3 (ITE)	-0.29	-2.06	-10.1		323-823	[82]
	Zeolite ITQ-1 (ITO)	-4.23	-4.23	-3.21		323-773	[82]

Zeolites and ($AlPO_4$'s)	Zeolite MFI	-5.5	-6.9	-2.8		393-975	[81]
	Zeolite Faujasite (FAU)	-4.2	-4.2	-4.2		25-573	[56]
	Zeolite DOH	-0.6	-0.6	-3.1		573-996	[81]
	Zeolite SSZ-23 (STT)	-6.09	-3.21	-0.73		323-773	[82]
	Zeolite DDR	-2.8	-2.8	-3.1		492-1185	[81]
	Zeolite AFI	-5.1	-5.1	-3.7		424-774	[81]
	AlPO-17 (ERI)	-15.3	-15.3	-4.52		18-300	[32]
	AlPO-31	9.72	9.72	17.3		323-823	[33]
	MAPO-17	-9.16	-9.16	4.66		323-773	[33]
NZP or NASICON	$NaZr_2P_3O_{12}$ (Parent member)				-0.4	298-773	[1]
	$CaTi_4P_6O_{24}$				0.51	298-773	
	$CaTi_2Zr_2P_6O_{24}$				0.435	298-773	
	$Na_{3/2}Zr_{3/2}Cr_{1/2}P_3O_{12}$				0.05	298-773	
	$MgZr_4P_6O_{24}$				0.3	298-773	
$A_2M_3O_{12}$	$Sc_2W_3O_{12}$				-2.2	10-1073	[15]
	$Sc_2Mo_3O_{12}$				7.3	4-170	[83]
					-2.1	180-300	
	$Al_2Mo_3O_{12}$				9.51	150-450	[84]
					2.39	527-923	[85]
	$In_2Mo_3O_{12}$				12.4	373-593	[86]
					-1.85	643-1033	
	$Y_2Mo_3O_{12}$				-9.0	10-449	[87]
	$Er_2Mo_3O_{12}$				-7.6	298-973	[88]
	$Lu_2Mo_3O_{12}$				-6.0	298-973	[88]
	$Cr_2Mo_3O_{12}$				0.7	673-1023	[85]

* $\alpha_L = \alpha$(average)

1.5. Borophosphates and Metalloborophosphates

This section is a general introduction into borophosphate and metalloborophosphate phases - the materials studied in this thesis - and includes a brief overview into the structural chemistry, synthesis and applications of these materials.

Borophosphates are intermediate compounds of the systems M_xO_y-B_2O_3-P_2O_5-(H_2O) (M = main group/transition metal or ammonium), figure 1.14. They exhibit fascinating structural chemistry with a large diversity of connection patterns of the anionic $\infty[B_xP_yO_z]^{n-}$ partial structures [89, 90]. The anionic structural building blocks are related to the aluminosilicates crystal chemistry i.e. tetrahedral arrangements of AlO_4 and SiO_4 [91]. The borophosphate anionic structures are composed of non-protonated and/or protonated borate and phosphate groups. The borate cluster consists of BX_4 (where X = O, OH) tetrahedral groups with sp^3 bonds between the boron (+3 oxidation state) and oxygen atoms and BX_3 groups (trigonal-planar molecular geometry) with sp^2 bonds between the boron (+3 oxidation state) and oxygen atoms. The phosphate cluster consists of phosphorus (+5 oxidation state) bonded to four oxygen atoms by tetrahedral sp^3 bonds forming a PX_4 group. The additional tetrahedral MX_4 units in the anionic structure constitute metalloborophophates (M : B : P). Metal complexes with coordination numbers other than four are not considered as part of the anionic complex. At the minimum one borate and one phosphate component have to be condensed to form a borophosphate. Isolated borate and phosphate anions are classified as borate-phosphates [89, 90].

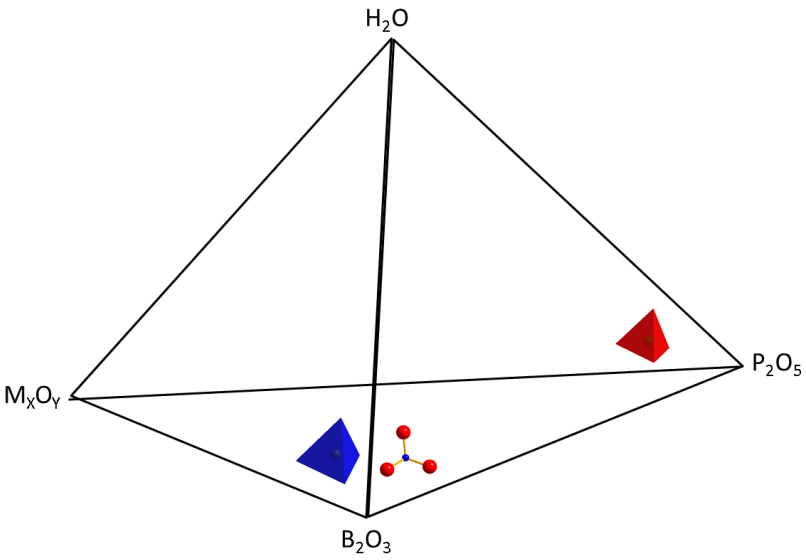


Figure 1.14: Borophosphates; intermediate compounds of the systems M_xO_y-B_2O_3-P_2O_5-(H_2O) (M = main group/transition metal or ammonium). BO_4 tetrahedra (blue), BO_3 trigonal planar (ball and stick) and PO_4 tetrahedra (red). Boron and phosphorous can be coordinated by either oxygen or OH-species. Adapted from [92].

Owing to the increasing number of borophosphate compounds, two papers describing the systematic classification of these compounds have been developed. In both papers, a hierarchical classification of borophosphate anions based on their simple primary building units is suggested [89, 90]. The structural parameters describing these anionic units include the coordination number, branchedness, dimensionality, multiplicity and periodicity. In brief, the coordination number describes the coordination around the respective metals, boron and phosphorus atoms in the anionic structure. The branchedness describes the type of connection sequence within the building units of the anionic structure. These vary from simple linear connections to complex branches (cyclo- and loop-branches). The parameter dimensionality (D = 0, 1, 2, 3) describes the degree of propagation of the anionic structure in space. The multiplicity denotes the number of times (connections) that the same primary polyhedral building units (e.g. oligomers, chains) are connected to one another. The parameter periodicity applies only for linear (therefore excluding branched) chains. In linear chains, periodicity describes the number of constituent polyhedra in the linear motif. These structural parameters and classification principles developed for borophosphates and metalloborophosphates were taken from the structural classification concepts of silicates [91]

and borates [93]. The first systematic approach to the structural chemistry of borophosphates, developed by Kniep and co-workers in 1998 [89], suggested a broad division of borophosphate anionic partial structures into anhydrous and hydrated phases. The anhydrous phases were seen to form either isolated species, oligomers and chains, and the hydrated phases were seen to form either rings, layers or framework structures. Further division of the anionic partial structures in borophosphates is based on molar B : P ratios.

An extension to the first classification was followed by Kniep and co-workers in 2007 [90]. This classification was based on partitioning crystalline (metallo)-borophosphates into five major groups:

1. Tetrahedral borophosphates

This group constitutes borophosphate anionic partial structures which are made up exclusively of tetrahedral environments of corner-sharing borate and phosphate units. The majority of the characterised borophosphate compounds can be classified in this group. All borophosphate phases of this group have molar B : P ratios between 1 : 1 and 1 : 4.

2. Mixed-coordinated borophosphates

Mixed-coordinated borophosphates include anionic structures with tetrahedral groups (BO_4 and/or PO_4) condensed with trigonal-planar borate groups (BO_3). Mixed-coordinated borophosphate anionic units are always boron rich (B : P between 6 : 1 to 1 : 1), as it seems that BO_3 units can only appear at high B : P ratios.

3. Metalloborophosphates

The metalloborophosphate compounds reveal the relationship that exist between chemical composition (molar B : P ratio) and the resulting structural chemistry. All studied metalloborophosphate anionic structures possess the same molar metallate: borate: phosphate ratios of M : B : P = 1 : 1 : 2 or 2 : 1 : 3. The later ratio has only been discovered in the isotypic compounds; $(NH_4)_{16}[M_{16}B_8P_{24}O_{96}]$ (M = Zn, $Zn_{1-x}Co_x$) [94]. Despite the majority of metalloborophosphates possessing the M : B : P = 1 : 1 : 2 ratio, a large diversity of the anionic topologies have been found. These include various zeolite-like topologies with

microporous frameworks formed from four-, six-, and eight-membered ring systems [95-97]. Furthermore, the metalloborophosphate anionic partial structures are built exclusively from BO_4 and PO_4 tetrahedral units. These units link up to form a three-dimensional anionic framework in every case. Thus far, these tetrahedral frameworks are devoid of all linkages between the same tetrahedral groups (i.e. no B-O-B, P-O-P, M-O-M linkages) and there are no M-O-B linkages. In general, the tetrahedral frameworks are formed from alternating metallate and borate tetrahedra linked to branching phosphate tetrahedra or two metallate units linking with a phosphate tetrahedral unit.

4. Anionic-substituted compounds and border-cases

As the term anionic implies, these borophosphate compounds consist of customary borate and phosphate units, but are now linked to other non-borophosphate anion substituted species (sometimes complex anions). Only a handful of these compounds exist including fluorine substituted compounds: $(C_2H_{10}N_2)[BPO_4F_2]$ and $(NH_4)[BPO_4F]$ [98, 99] and the phenyl-substituted heteropolyoxo-compound $(ImH_2)[Mo^{V}_5Mo^{VI}_7O_{30}BPO_4)_2(O_3P\text{-}Ph)_6]$ (Im = imidazole) [100].

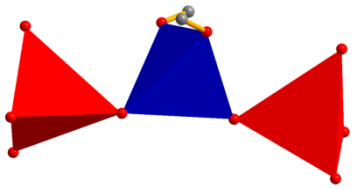
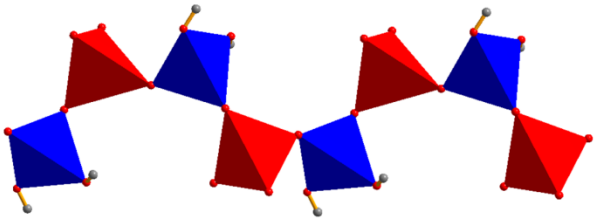
5. Borate-phosphate

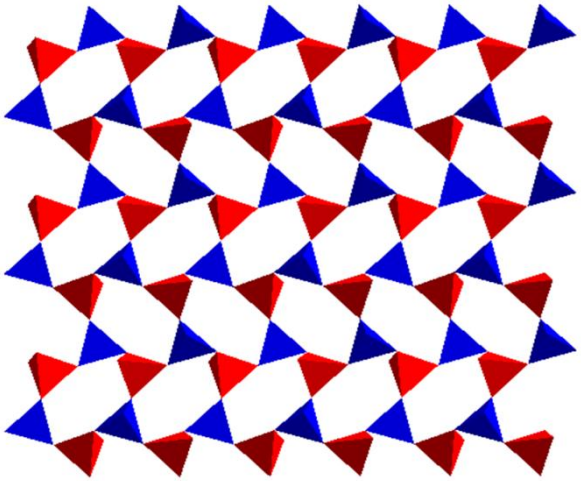
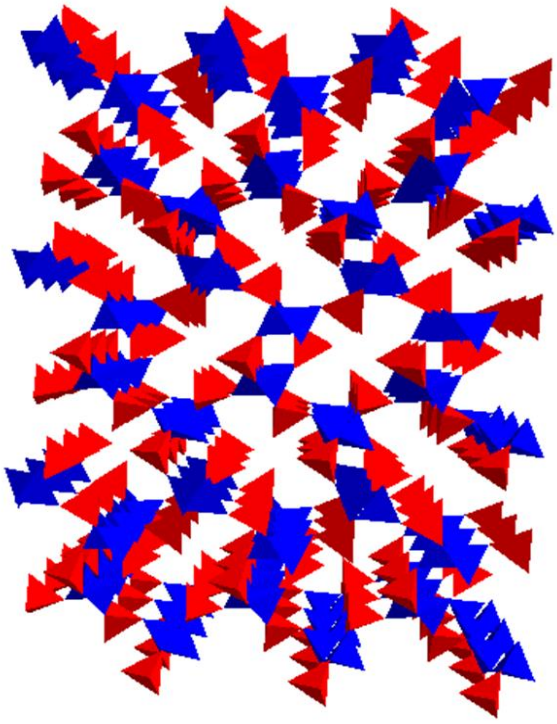
The crystal structure of compounds in this group consists of isolated borate (BX_4, BX_3) and phosphate (PX_4) units. Also, some of the compounds in this group have additional oxide or hydroxide ions in the structure. Examples include the lanthaniod oxo-borate-phosphate compound $Ln_7O_6[BO_3][PO_4]_2$ (Ln = La, Pr, Nd, Sm, Gd, Dy) [101, 102] the mineral Seamanite; $Mn_3(OH)_2[B(OH)_4][PO_4]$ [103, 104] and the metal borate-phosphate; $M^{II}_3[BO_3][PO_4]$ (M^{II} = Zn [105] and Mg [106]).

To date, the structural chemistry of borophosphates have included exceptional diversity of the anionic units including oligomers (formed by at least one borate and phosphate group, D = 0), chains (D = 1), layered (D = 2) and open framework structures (D = 3), table 1.3 [89, 90]. Interestingly, D = 2 layers and D = 3 framework structures are observed with molar B : P ratios between 1 : 1 and 1 : 2. As a result of the diverse ratios of molar B : P units, large varieties of anionic partial structures can be formed. However, the condensation of building

units to form these structural motifs is not random. To date, P-O-P connections and borophosphate anions with B : P ratios lower than 1 : 4 have not been discovered [90]. The lack of P-O-P connections may be correlated to the *Loewenstein* rule for alumosilicates, where Al-O-Al linkages are avoided [107]. The avoidance of P-O-P connections means that to create phosphate rich networks (molar B : P ratio of 1 : 2, 1 : 3, 1 : 4), phosphate tetrahedra have to be exclusively linked to borate units. The B : P ratios are influential on the dimensionality of the anionic partial structures. Thus, phosphates rich anions generally have low dimensionality. The reason for this is that with increasing phosphate content, the phosphate units occupy terminal sites in the borophosphate anion, until a point such that the phosphate species become isolated and form borate-phosphate compounds. In metalloborophosphates and anion-substituted borophosphates, the additional cation also affects (often lowers) the dimensionality of the resulting borophosphate compound. Therefore, structural parameters of the substituted cation such as the charge, size and coordination environment will affect the dimensionality.

Table 1.3: Selected examples of borophophates anions with varying dimensionality (D = 0, 1, 2, 3). B tetrahedra (blue), P tetrahedra (red), O atoms (red spheres) and H atoms (grey spheres).

Compound	Borophosphate anion	Dimensionality (D)
$NaV[B(P_2O_7)(OH)_3]$ [108]		D = 0 (Oligomer)
$Mn[BPO_4(OH)_2]$ [109]		D = 1 (Chain)

$Cu(H_2O)_2[B_2P_2O_8(OH)_2]$ [110]		D = 2 (Layer)
$Rb[B_2P_2O_8(OH)]$ [111]		D = 3 (Framework)

Owing to these materials having diverse crystal structures, a large range of functional materials can be synthesized with a variety of materials properties. Borophosphates have possible applications as magnetic [112], non-linear optical [113-117], electrochemical [118, 119], photoluminescent [120-123] and corrosion resistant [124] materials. Borophosphates which possess microporous (pore diameters < 20Å) apertures have potential separation, ion-exchanging and catalytic aspects such as conversion of organic molecules (particular over the compound, BPO_4) [96, 125-130]. In addition, a patent exists for various borophosphates being used as antioxidant and fire proofing materials [131].

Borophophates have been synthesized under mild hydrothermal conditions, as well as with solid state (high temperature) and microwave methods. Examples of borophosphates synthesized by the more common hydrothermal approach include the open-framework borophosphates with $\infty[BP_2O_8]^{3-}$ and $\infty[B_2P_3O_{12}(OH)]^{4-}$ anionic partial structures. The former anionic structural unit is made up of double helix $\infty\{(M^I[BP_2O_8]^{2-}\}$ of corner-linked borate and phosphate tetrahedra, which are positioned around 6_1 screw axes [132]. Examples include the isostructural $M^IM^{II}(H_2O)_2[BP_2O_8].H_2O$ type compounds where M^I = Na, K; M^{II} = Mg, Mn, Fe, Co, Ni, Zn) and their dehydrated phases $M^I[M^{II}BP_2O_8](H_2O)$ [132, 133]. The $\infty[B_2P_3O_{12}(OH)]^{4-}$ anionic partial framework is characterized by forming templated borophosphates. These include the 'organic templated' $[H_2(Templ.)][Mn^{II}\{B_2P_3O_{12}(OH)\}]$, [templates: 1,3-diaminopropane, $C_3H_{10}N_2$ (DAP); piperazine, $C_4H_{10}N_2$ (PIP); 1,4-diazacyclo-[2.2.2]octane, $C_6H_{12}N_2$ (DABCO)], where the organic template cation plays a role in controlling the pore size and shape distribution (figure 1.15) [134]. $[Co(en)_3][B_2P_3O_{11}(OH)_2]$ is a borophosphate templated by a transition-metal complex (en = ethylenediamine) [135].

Borophoshates synthesized by the solid state method include $M^{II}[BPO_5]$ (M^{II} = Ca, Sr) [136], which possess infinite loop branched chains of BO_4 and PO_4 tetrahedra and $Ba_3[BP_3O_{12}]$ [136], with voids in which the barium ions are located. $Na_5[B_2P_3O_{13}]$ [137] and BPO_4 [138] are examples of borophosphates prepared by the microwave method. $K_3[BP_3O_9(OH)_3]$ and $Rb_3[B_2P_3O_{11}(OH)_2]$ have been synthesized by the solvothermal techniques, in this case ethanol is used as a solvent [139]. Several borophosphates have been synthesized using flux [140, 141] and chemical transport reactions [142].

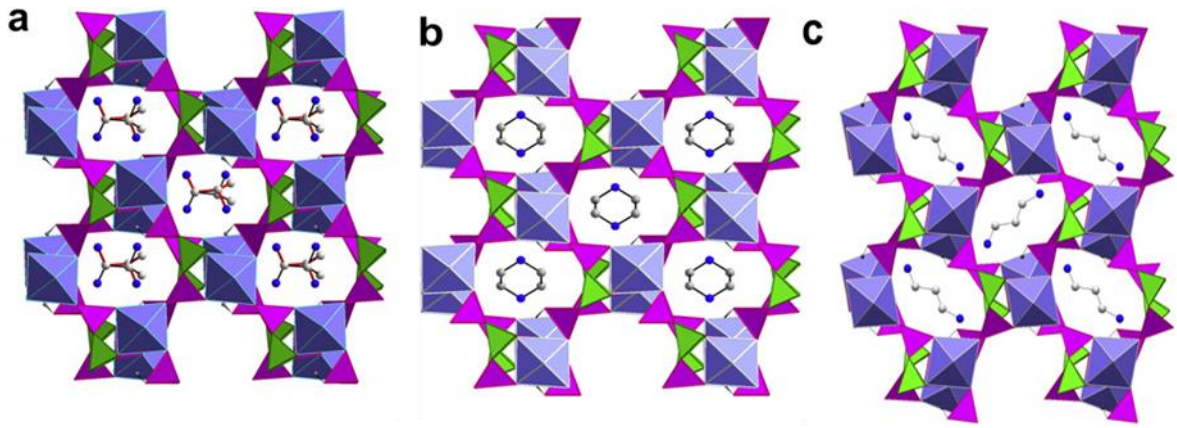


Figure 1.15: Structure directing organic templates a) 1,2-diaminopropane (1,2-DAP), b) Piperazine (PIP), c) 1,3-diaminopropane (1,3-DAP), which occupy the voids of the porous borophosphate; $[H_2(Templ.)][Mn^{II}\{B_2P_3O_{12}(OH)\}]$. Diagrams obtained from [134].

1.6. Aim of the research

The main aim of this thesis was to synthesize and explore the structural diversity and thermal properties offered by various borophosphates. In this regard, four borophosphate phases were selected; two which are anhydrous dense compounds (synthesized by the solid state method) and two which are porous (synthesized by the hydrothermal method). The anhydrous dense compounds were $ABPO_5$ (A = Ca, Sr, Ba) and BPO_4 phases. The porous compounds were $NH_4Fe(III)[BP_2O_8(OH)]$ and $M^I_xM^{II}_z(H_2O)_2[BP_2O_8].zH_2O$ (M^I = Na, NH_4 and M^{II} = Mn, Co) phases.

Objective 1:

The aim is to investigate the thermal expansion behaviour of Stillwellite-type $ABPO_5$ (A = Ca, Sr, Ba) compounds. To date, only the room temperature crystal structures of these compounds have been reported [136]. We therefore attempted to explore the coefficient of thermal expansion of these phases over a large temperature range. As with previous studies on LTE and NTE type materials, attempts will be made to correlate the changes in the $ABPO_5$ crystal structures with temperature to the observed thermal expansion behaviour of the respective compounds.

Objective 2:

Several porous borophosphates with a spiral and chiral $\infty[BP_2O_8]^{3-}$ framework have been characterised, and exhibit fascinating thermal properties [132]. We intend to extend this work by studying the effect of incorporating a small (Na), and a large (NH_4) monovalent cation (M^{1+}) into the $M^{I}_{x}M^{II}_{z}(H_2O)_2[BP_2O_8].zH_2O$ (M^{II} = Mn or Co) open-framework structure. Attention will be focused on elucidating the effect of ion substitution on the crystal structure and thermal properties of the resulting borophosphate compounds. IR, SEM and TGA will be used as complementary techniques to assist the investigation of the title compounds.

Objective 3:

The aim is to study the thermal behaviour of a porous iron borophosphate, $NH_4Fe(III)[BP_2O_8(OH)]$. The crystal structure of this compound has been previously determined using single crystal X-ray diffraction analysis performed at room temperature [143]. In this work we intend to study the structural behaviour of these materials at the atomic level from room temperature up to 860 °C by the Rietveld refinement method. Therefore, we will explore the thermal stability range and the coefficient of thermal expansion of the title compound. Infrared spectroscopy (IR), Scanning Electron Microscope (SEM) and Thermal Gravimetric Analysis (TGA) will be used as supplementary techniques to assist the investigation of the title compound.

Objective 4:

Recently, the thermal expansion behaviour of cristobalite-type BPO_4 has been determined [29]. The thermal stability of this compound has been explained in terms of the variation in the inter-polyhedral angle with temperature. In addition, the temperature dependence of the crystal structure was determined from conventional free isotropic Rietveld refinements. We aim to extend on this refinement strategy, by carrying out Rietveld refinements using two alternative refinement strategies; namely: refinement of atomic coordinates using low-order polynomials and rigid body refinements. Furthermore, to the series of diffraction data collected as a function of temperature, attempts will be made to fit each of the above mentioned refinement models using the parametric Rietveld refinement method and the

conventional sequential Rietveld refinement method. At the end of this study, we aim to elucidate which of the three refinement strategies fits the best and describes the observed structural trends of BPO_4 as a function of temperature.

1.7. References

[1] R. Roy, D.K. Agrawal, H.A. McKinstry, *Annual Review of Materials Science* 19 (1989) 59-81.

[2] P.A. Tipler, G. Mosca, *Physics for scientists and engineers*. Macmillan, 2007.

[3] A. Versluis, W.H. Douglas, R.L. Sakaguchi, *Dental Materials* 12 (1996) 290-294.

[4] R.A. Serway, R.J. Beichner, J.W. Jewett, *Physics for scientists and engineers with modern physics*, (2000).

[5] H.C. Work, 2015/10/16.

[6] C.D. Practice, 2015/10/16.

[7] S.C. Schools, 2015/10/16.

[8] A.W. Sleight, *Current Opinion in Solid State and Materials Science* 3 (1998) 128-131.

[9] R.S. Krishnan, R. Srinivasan, S. Devanarayanan, *Thermal Expansion of Crystals: International Series in The Science of The Solid State*. Elsevier, 2013.

[10] W. Miller, C. Smith, D. Mackenzie, K. Evans, *Journal of materials science* 44 (2009) 5441-5451.

[11] J.S. Evans, W. David, A. Sleight, *Acta Crystallographica Section B: Structural Science* 55 (1999) 333-340.

[12] C. Kittel, *Introduction to solid state physics*. Wiley, 2005.

[13] J.S. Evans, *Journal of the Chemical Society, Dalton Transactions* (1999) 3317-3326.

[14] F. Hummel, Industrial Publications, Chicago, 1958.

[15] J. Evans, T. Mary, A. Sleight, *Journal of Solid State Chemistry* 137 (1998) 148-160.

[16] I.D. Brown, A. Dabkowski, A. McCleary, *Acta Crystallographica Section B: Structural Science* 53 (1997) 750-761.

[17] G.A. Rossetti Jr, J.P. Cline, A. Navrotsky, *Journal of materials research* 13 (1998) 3197-3206.

[18] A. Glazer, S. Mabud, *Acta Crystallographica Section B: Structural Crystallography and Crystal Chemistry* 34 (1978) 1065-1070.

[19] J. Evans, T. Mary, A. Sleight, *Journal of Solid State Chemistry* 133 (1997) 580-583.

[20] W. Schlosser, G. Graham, P. Meincke, *Journal of Physics and Chemistry of Solids* 32 (1971) 927-938.

[21] S. Chikazumi, *Journal of Magnetism and Magnetic Materials* 10 (1979) 113-119.

[22] D. Gignoux, D. Givord, F. Givord, R. Lemaire, *Journal of Magnetism and Magnetic Materials* 10 (1979) 288-293.

[23] J.R. Davis, *Alloying: understanding the basics*. ASM international, 2001.

[24] M. O'keeffe, B. Hyde, *Acta Crystallographica Section B: Structural Crystallography and Crystal Chemistry* 32 (1976) 2923-2936.

[25] E. Philippot, P. Armand, P. Yot, O. Cambon, A. Goiffon, G. McIntyre, P. Bordet, *Journal of solid state chemistry* 146 (1999) 114-123.

[26] J. Haines, O. Cambon, E. Philippot, L. Chapon, S. Hull, *Journal of Solid State Chemistry* 166 (2002) 434-441.

[27] E. Philippot, A. Goiffon, A. Ibanez, M. Pintard, *Journal of Solid State Chemistry* 110 (1994) 356-362.

[28] E. Philippot, D. Palmier, M. Pintard, A. Goiffon, *Journal of Solid State Chemistry* 123 (1996) 1-13.

[29] S. Achary, A. Tyagi, *Journal of Solid State Chemistry* 177 (2004) 3918-3926.

[30] S. Achary, O. Jayakumar, A. Tyagi, S. Kulshresththa, *Journal of Solid State Chemistry* 176 (2003) 37-46.

[31] O. Cambon, J. Haines, G. Fraysse, J. Détaint, B. Capelle, A. Van der Lee, *Journal of applied physics* 97 (2005) 74110-74300.

[32] M.P. Attfield, A.W. Sleight, *Chemistry of materials* 10 (1998) 2013-2019.

[33] P. Lightfoot, D.A. Woodcock, M.J. Maple, L.A. Villaescusa, P.A. Wright, *Journal of materials Chemistry* 11 (2001) 212-216.

[34] W. Tiano, M. Dapiaggi, G. Artioli, *Journal of applied crystallography* 36 (2003) 1461-1463.

[35] S. a Beccara, G. Dalba, P. Fornasini, R. Grisenti, A. Sanson, F. Rocca, *Physical review letters* 89 (2002) 025503.

[36] J.N. Grima, V. Zammit, R. Gatt, *Xjenza* 11 (2006) 17-29.

[37] J. Tao, A. Sleight, *Journal of Solid State Chemistry* 173 (2003) 442-448.

[38] J. Evans, T. Mary, T. Vogt, M. Subramanian, A. Sleight, *Chemistry of materials* 8 (1996) 2809-2823.

[39] D.H. KENTON, T. MARTIN, P.G. ANDREW, *American Mineralogist* 81 (1996) 1057-1079.

[40] J. Evans, T. Mary, A. Sleight, *Physica B: Condensed Matter* 241 (1997) 311-316.

[41] A. Yamanaka, T. Kashima, M. Tsutsumi, K. Ema, Y. Izumi, S. Nishijima, *Journal of composite materials* 41 (2007) 165-174.

[42] B. A., *Arkiv foer Kemi, Mineralogi och Geologi, B* 15 (1942) 1.

[43] W. Schreyer, J. Schairer, *Journal of Petrology* 2 (1961) 324-406.

[44] P. Mirwald, *Physics of the Earth and Planetary Interiors* 29 (1982) 1-5.

[45] F. Hummel, *Foote Prints* 20 (1948) 3-11.

[46] Owens-Illinois Inc, URL: http://www.o-i.com.

[47] PPG Industries, URL: http://corporate.ppg.com/Home.aspx.

[48] Corningware, URL: http://www.corningware.com.

[49] T. Mary, J. Evans, T. Vogt, A. Sleight, *Science* 272 (1996) 90.

[50] N. Nakajima, Y. Yamamura, T. Tsuji, *Journal of thermal analysis and calorimetry* 70 (2002) 337-344.

[51] J. Evans, P. Hanson, R. Ibberson, N. Duan, U. Kameswari, A. Sleight, *Journal of the American Chemical Society* 122 (2000) 8694-8699.

[52] S. Allen, J. Evans, *Physical Review B* 68 (2003) 134101.

[53] N. Nakajima, Y. Yamamura, T. Tsuji, *Solid state communications* 128 (2003) 193-196.

[54] H. Holzer, D. Dunand, 4th Int. Conf. on Composite Engineering, Hawaii, 1997.

[55] N. Duan, U. Kameswari, A. Sleight, *Journal of the American Chemical Society* 121 (1999) 10432-10433.

[56] M.P. Attfield, *Chemical Communications* (1998) 601-602.

[57] K. Röttger, A. Endriss, J. Ihringer, S. Doyle, W. Kuhs, *Acta Crystallographica Section B: Structural Science* 50 (1994) 644-648.

[58] H. Tanaka, *The Journal of chemical physics* 108 (1998) 4887-4893.

[59] S.M. Bennington, J. Li, M.J. Harris, D.K. Ross, *Physica B: Condensed Matter* 263 (1999) 396-399.

[60] J. Boilot, J. Salanie, G. Desplanches, D. Le Potier, *Materials Research Bulletin* 14 (1979) 1469-1477.

[61] J. Goodenough, H.-P. Hong, J. Kafalas, *Materials Research Bulletin* 11 (1976) 203-220.

[62] H.-P. Hong, *Materials Research Bulletin* 11 (1976) 173-182.

[63] R. Roy, E. Vance, J. Alamo, *Materials Research Bulletin* 17 (1982) 585-589.

[64] D. Woodcock, P. Lightfoot, *Journal of Materials Chemistry* 9 (1999) 2907-2911.

[65] G.E. Lenain, H.A. McKinstry, J. Alamo, D. Agrawal, *Journal of materials science* 22 (1987) 17-22.

[66] J. Alamo, *Solid State Ionics* 63 (1993) 547-561.

[67] K.G. Kutty, R. Asuvathraman, C. Mathews, U. Varadaraju, *Materials research bulletin* 29 (1994) 1009-1016.

[68] D. Woodcock, P. Lightfoot, R. Smith, MRS Proceedings, Cambridge Univ Press, 1998, pp. 191.

[69] V. Korthuis, N. Khosrovani, A. Sleight, N. Roberts, R. Dupree, W.J. Warren, *Chemistry of materials* 7 (1995) 412-417.

[70] R. Withers, Y. Tabira, J. Evans, I. King, A. Sleight, *Journal of Solid State Chemistry* 157 (2001) 186-192.

[71] Y. Maniwa, R. Fujiwara, H. Kira, H. Tou, H. Kataura, S. Suzuki, Y. Achiba, E. Nishibori, M. Takata, M. Sakata, *Physical Review B* 64 (2001) 241402.

[72] Y.-K. Kwon, S. Berber, D. Tománek, *Physical review letters* 92 (2004) 015901.

[73] S. Brown, J. Cao, J. Musfeldt, N. Dragoe, F. Cimpoesu, S. Ito, H. Takagi, R. Cross, *Physical Review B* 73 (2006) 125446.

[74] J.N. Grima, A. Alderson, K.E. Evans, *Journal of the Physical Society of Japan* 74 (2005) 1341-1342.

[75] A.L. Goodwin, M. Calleja, M.J. Conterio, M.T. Dove, J.S. Evans, D.A. Keen, L. Peters, M.G. Tucker, *Science* 319 (2008) 794-797.

[76] W. Zhou, H. Wu, T. Yildirim, J.R. Simpson, A.H. Walker, *Physical Review B* 78 (2008) 054114.

[77] D. Dubbeldam, K.S. Walton, D.E. Ellis, R.Q. Snurr, *Angewandte Chemie* 119 (2007) 4580-4583.

[78] S. Nara, K. Yoshimitsu, T. Matsubara, *Progress of Theoretical Physics* 66 (1981) 1143-1159.

[79] A.W. Sleight, *Annual review of materials science* 28 (1998) 29-43.

[80] Y. Yamamura, N. Nakajima, T. Tsuji, *Physical Review B* 64 (2001) 184109.

[81] S. Park, R.-W.G. Kunstleve, H. Graetsch, H. Gies, *Studies in Surface Science and Catalysis* 105 (1997) 1989-1994.

[82] D.A. Woodcock, P. Lightfoot, P.A. Wright, L.A. Villaescusa, M.A. Camblor, *Journal of Materials Chemistry* 9 (1999) 349-351.

[83] J.S. Evans, T. Mary, *International journal of inorganic materials* 2 (2000) 143-151.

[84] K.J. Miller, (2012).

[85] M. Ari, P. Jardim, B. Marinkovic, F. Rizzo, F. Ferreira, *Journal of Solid State Chemistry* 181 (2008) 1472-1479.

[86] B.A. Marinkovic, M. Ari, P.M. Jardim, R.R. De Avillez, F. Rizzo, F.F. Ferreira, *Thermochimica Acta* 499 (2010) 48-53.

[87] B.A. Marinkovic, M. Ari, R.R. de Avillez, F. Rizzo, F.F. Ferreira, K.J. Miller, M.B. Johnson, M.A. White, *Chemistry of Materials* 21 (2009) 2886-2894.

[88] C. Guzmán-Afonso, C. González-Silgo, J. González-Platas, M.E. Torres, A.D. Lozano-Gorrín, N. Sabalisck, V. Sánchez-Fajardo, J. Campo, J. Rodríguez-Carvajal, *Journal of Physics: Condensed Matter* 23 (2011) 325402.

[89] R. Kniep, H. Engelhardt, C. Hauf, *Chemistry of materials* 10 (1998) 2930-2934.

[90] B. Ewald, Y.X. Huang, R. Kniep, *Zeitschrift für anorganische und allgemeine Chemie* 633 (2007) 1517-1540.

[91] F. Liebau, *Structural chemistry of silicates: structure, bonding, and classification*. Springer Science & Business Media, 2012.

[92] P.W. Menezes, 2009.

[93] J.D. Grice, P.C. Burns, F. Hawthorne, *Canadian mineralogist* 37 (1999) 731-762.

[94] M. Yang, J. Yu, P. Chen, J. Li, Q. Fang, R. Xu, *Microporous and mesoporous materials* 87 (2005) 124-132.

[95] R. Kniep, G. Schaefer, H. Engelhardt, I. Boy, *Angewandte Chemie International Edition* 38 (1999) 3641-3644.

[96] G. Schäfer, H. Borrmann, R. Kniep, *Microporous and mesoporous materials* 41 (2000) 161-167.

[97] I. Boy, F. Stowasser, G. Schäfer, R. Kniep, *Chemistry-A European Journal* 7 (2001) 834-839.

[98] Y.X. Huang, G. Schaefer, H. Borrmann, J.T. Zhao, R. Kniep, *Zeitschrift für anorganische und allgemeine Chemie* 629 (2003) 3-5.

[99] M.-R. Li, W. Liu, M.-H. Ge, H.-H. Chen, X.-X. Yang, J.-T. Zhao, *Chemical communications* (2004) 1272-1273.

[100] C. Sassoye, K. Norton, S.C. Sevov, *Inorganic chemistry* 42 (2003) 1652-1655.

[101] Y. Shi, J. Liang, H. Zhang, J. Yang, W. Zhuang, G. Rao, *Journal of Solid State Chemistry* 129 (1997) 45-52.

[102] B. Ewald, Y. Prots, R. Kniep, *Zeitschrift für Kristallographie-New Crystal Structures* 219 (2004) 233-235.

[103] P.B. Moore, S. Ghose, *American Mineralogist* 56 (1971) 1527-&.

[104] E. Kneus, W. Seluex, (1930).

[105] K. Bluhm, C. Park, *Zeitschrift für Naturforschung B* 52 (1997) 102-106.

[106] G. Gözel, A. Baykal, M. Kizilyalli, R. Kniep, *Journal of the European Ceramic Society* 18 (1998) 2241-2246.

[107] W. Loewenstein, *American Mineralogist* 39 (1954) 92-96.

[108] L.-R. Zhang, H. Zhang, H. Borrmann, R. Kniep, *Zeitschrift für Kristallographie-New Crystal Structures* 217 (2002) 477-478.

[109] Y.-X. Huang, B. Ewald, W. Schnelle, Y. Prots, R. Kniep, *Inorganic chemistry* 45 (2006) 7578-7580.

[110] H. Shi, M. Li, H. Tangbo, A. Kong, B. Chen, Y. Shan, *Inorganic chemistry* 44 (2005) 8179-8181.

[111] C. Häuf, R. Kniep, *Zeitschrift für Naturforschung B* 52 (1997) 1432-1435.

[112] W. Yang, J. Li, Q. Pan, H. Xing, Y. Chen, J. Yu, R. Xu, *Journal of Materials Chemistry* 19 (2009) 4523-4528.

[113] V. Nazabal, E. Fargin, C. Labrugere, G. Le Flem, *Journal of non-crystalline solids* 270 (2000) 223-233.

[114] S. Pan, Y. Wu, P. Fu, G. Zhang, Z. Li, C. Du, C. Chen, *Chemistry of materials* 15 (2003) 2218-2221.

[115] G. Wang, Y. Wu, P. Fu, X. Liang, Z. Xu, C. Chen, *Chemistry of materials* 14 (2002) 2044-2047.

[116] G. Wang, Y. Wu, H. Liu, P. Fu, S. Pan, G. Zhang, C. Chen, *Chemistry Letters* (2002) 620-621.

[117] Y. Wu, G. Wang, P. Fu, X. Liang, Z. Xu, C. Chen, *Journal of crystal growth* 229 (2001) 205-207.

[118] L. Tao, G.l. Rousse, M.T. Sougrati, J.-N. Chotard, C. Masquelier, *The Journal of Physical Chemistry C* 119 (2015) 4540-4549.

[119] A. Ahoussou, J. Rogez, A. Kone, *Journal of non-crystalline solids* 353 (2007) 271-275.

[120] I. Berezovskaya, V. Dotsenko, N. Efryushina, A. Voloshinovskii, C. Van Eijk, P. Dorenbos, A. Sidorenko, *Journal of alloys and compounds* 391 (2005) 170-176.

[121] Q. Zeng, N. Kilah, M. Riley, *Journal of luminescence* 101 (2003) 167-174.

[122] H.-B. Liang, Q. Su, Y. Tao, T.-D. Hu, T. Liu, S. Shulin, *Journal of Physics and Chemistry of Solids* 63 (2002) 719-724.

[123] R. Ternane, M.T. Cohen-Adad, G. Panczer, C. Goutaudier, C. Dujardin, G. Boulon, N. Kbir-Ariguib, M. Trabelsi-Ayedi, *Solid state sciences* 4 (2002) 53-59.

[124] M. Zhou, K. Li, D. Shu, B. Sun, J. Wang, *Materials Science and Engineering: A* 346 (2003) 116-121.

[125] G.J. Hutchings, I.D. Hudson, D. Bethell, D.G. Timms, *Journal of Catalysis* 188 (1999) 291-299.

[126] S. Gao, J. Moffat, *Journal of Catalysis* 180 (1998) 142-148.

[127] R. Tartarelli, M. Giorgini, A. Lucchesi, G. Stoppato, F. Morelli, *Journal of Catalysis* 17 (1970) 41-45.

[128] K. Otsuka, Y. Uragami, M. Hatano, *Catalysis today* 13 (1992) 667-672.

[129] Y. Uragami, K. Otsuka, *J. Chem. Soc., Faraday Trans.* 88 (1992) 3605-3610.

[130] S. Imamura, K. Imakubo, S. Furuyoshi, H. Jindai, *Industrial & engineering chemistry research* 30 (1991) 2355-2358.

[131] K. Geotzman, D. Karlheionz, N. Hans-Dieter, G. Talf.

[132] R. Kniep, H.G. Will, I. Boy, C. Röhr, *Angewandte Chemie International Edition in English* 36 (1997) 1013-1014.

[133] A. Baykal, M. Kizilyalli, R. Kniep, *Journal of materials science* 35 (2000) 4621-4626.

[134] Y.X. Huang, O. Hochrein, D. Zahn, Y. Prots, H. Borrmann, R. Kniep, *Chemistry-A European Journal* 13 (2007) 1737-1745.

[135] G.-Y. Yang, S.C. Sevov, *Inorganic chemistry* 40 (2001) 2214-2215.

[136] R. Kniep, G. Gözel, B. Eisenmann, C. Röhr, M. Asbrand, M. Kizilyalli, *Angewandte Chemie International Edition in English* 33 (1994) 749-751.

[137] C. Hauf, A. Yilmaz, M. Kizilyalli, R. Kniep, *Journal of Solid State Chemistry* 140 (1998) 154-156.

[138] A. Baykal, M. Kizilyalli, M. Toprak, R. Kniep, *Turkish Journal of Chemistry* 25 (2001) 425-432.

[139] B. Ewald, Y. Prots, P. Menezes, S. Natarajan, H. Zhang, R. Kniep, *Inorganic chemistry* 44 (2005) 6431-6438.

[140] R.P. Bontchev, S.C. Sevov, *Inorganic chemistry* 35 (1996) 6910-6911.

[141] W. Yang, J. Li, T. Na, J. Xu, L. Wang, J. Yu, R. Xu, *Dalton Transactions* 40 (2011) 2549-2554.

[142] M. Schmidt, B. Ewald, Y. Prots, R. Cardoso-Gil, M. Armbrüster, I. Loa, L. Zhang, Y.X. Huang, U. Schwarz, R. Kniep, *Zeitschrift für anorganische und allgemeine Chemie* 630 (2004) 655-662.

[143] Y.-X. Huang, G. Schäfer, W. Carrillo-Cabrera, R. Cardoso, W. Schnelle, J.-T. Zhao, R. Kniep, *Chemistry of materials* 13 (2001) 4348-4354.

Chapter 2 Methods of Characterisation

2.1. Powder X-ray Diffraction (PXRD)

The phenomenon of X-ray diffraction occurs when parallel-monochromatic electromagnetic waves are scattered by electrons from periodically assembled atoms, resulting in a characteristic interference pattern. The constructive interference of these waves (and therefore a diffraction intensity) occurs when the path difference of two or more of these waves is an integer multiple of the incident wavelength [1, 2]. The interference pattern which is composed of varying magnitudes of intensity as a function of position (scattering angle θ) is best described by Bragg's law (equation 2.1) [3]:

$$n\lambda = 2d_{hkl}\sin\theta \qquad (2.1)$$

where: λ – Incident monochromatic wavelength

θ – Diffraction angle

n – Diffraction order

d_{hkl} – Spacing between the crystallographic planes

hkl – Miller indices

Therefore the above equation describes the angular position (θ) at which constructive diffraction intensity occurs. The position of the diffracted peaks are dictated by the size and shape of the unit cell (unit cell dimensions), while the intensities of the peaks are dictated by the positions of the atoms (atomic coordinates) within the unit cell [1].

While single crystal diffraction offers a three-dimensional interference pattern consisting of easily integratable, isolated reflections (figure 2.1a), the technique suffers from the requirement of growing large enough, high quality single crystals for analysis. In contrast, polycrystalline samples of smaller randomly orientated crystallites, form two-dimensional diffraction patterns made up of a 'suite of shells/rings', which may be condensed to a one-

dimensional interference pattern comprising a series of individual peaks, each with a peak height, peak width and a slowly changing background (figure 2.1b). In reality, the experimental powder pattern is a collection of step intensities (as a function of diffraction angle), which are used in the Rietveld algorithm as the observed intensities. The challenge of analysing powder diffractograms is the inherent loss of information (due to the collapse from three-dimensional to one-dimensional interference pattern) and the systematic overlapping of the measured diffraction peaks e.g. two or more *hkl* reflections with very similar 2θ values.

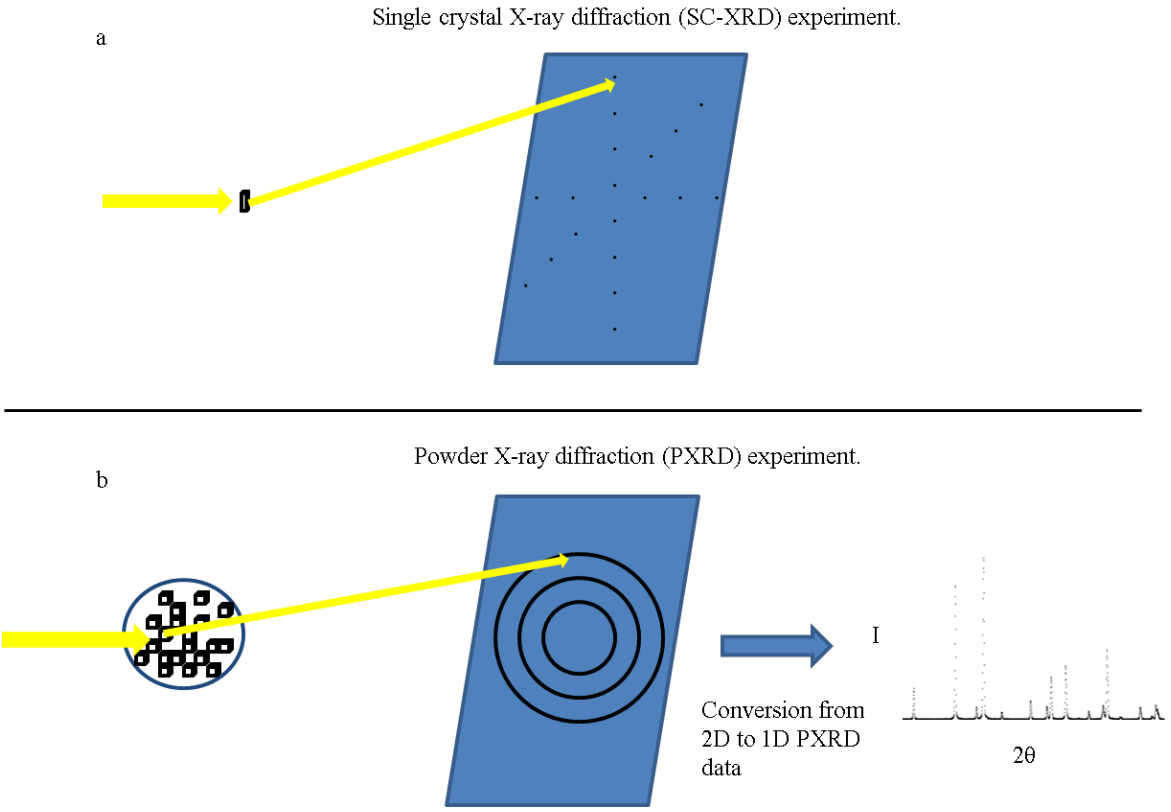


Figure 2.1: (a) Single crystal (SC) and (b) powder XRD interference patterns. SC-XRD experiments form spots in the reciprocal space. Powder patterns form Debye rings (cones) which can be integrated to a one-dimensional diffraction pattern in reciprocal space made up of step intensities.

2.2. Structure determination from powder data (SDPD)

In all X-ray diffraction experiments, the information content carried from each diffracted wave includes the measured intensity (I_{hkl}), the diffraction direction (θ_{hkl}) and their relative phases. Reconstruction of the relative phases of the diffracted waves is a critical aspect for crystal structure solution in crystallography. In powder diffraction, crystal structure determination proceeds via two consecutive approaches; structure solution and structure refinement.

Structure solution is a three-step process which involves generating a crystal structure model. The first step involves indexing the diffraction pattern to obtain lattice parameters. The second step is space group determination from systematically absent reflections. The third step involves determining the crystal structure model (unit cell contents) using either the Patterson method, direct method or real space methods optimised for powder data with a substantially smaller dataset (where the molecular structure connectivity is known and its position and orientation in the unit cell is unknown).

The second approach to SDPD is structure refinement, also known as a whole powder pattern refinement (WPPR) method or Rietveld refinement method. With the Rietveld method, an initial (trial) crystal structure is optimized. The WPPR methods as well as the whole powder pattern decomposition (WPPD) method (Le Bail and Pawley algorithms, see below) form part of the whole powder pattern fitting (WPPF) methods, which in general, use the method of non-linear least squares to fit a calculated pattern to an experimental pattern. WPPR methods are usually used as the last step in SDPD.

2.2.1. Whole powder pattern decomposition (WPPD) methods

For the purpose of systematic partitioning and extraction of Bragg reflection intensities, whole powder pattern decomposition techniques such as the Le Bail [4] and Pawley [5] algorithms have been developed to analyse powder patterns. These algorithms extract the integrated intensities as a set of single crystal like I_{hkl} vs 2θ data by carrying out a least-squares refinement procedure between a calculated powder pattern [based on the space group, lattice parameters, full width at half maximum (FWHM), peak asymmetry, 2θ corrections and background parameters] and the measured powder pattern. The above mentioned model parameters are refined until the differences between the calculated and measured diffraction

patterns are minimized. These pattern decomposition techniques are independent of the crystal structure i.e. crystal structure is not considered in these calculations, and therefore structural information is derived using alternative structure determination procedures using the extracted intensities.

2.2.2. The Rietveld Method

Currently the most widely used refinement technique for the analysis of powder patterns is the Rietveld method [6]. Unlike the decomposition methods, the Rietveld method not only partitions the observed and calculated Bragg reflections but also carries out a crystal structure refinement (of a trial model) using the corresponding Bragg reflections. Furthermore, the Rietveld method does not only refine the integrated intensities (peaks) but considers the entire measured powder pattern in the form of the step-scanned intensities (Yo_i vs $2\theta_i$), as seen in figure 2.1b. This allows for the use of the maximum amount of information relating to the crystal structure and other characteristics of the materials (e.g. crystallite size and lattice strain) to be derived from a 1D powder pattern. In this case the model function (Yc_i) will include preliminary structure parameters (including atomic coordinates, atomic displacement parameters, occupancy factors and unit cell parameters) together with instrumental parameters (incident profile function, zero offset, peak shape parameters) and a background contribution term:

$$Yc_i = s \sum_i L_k |F_K|^2 \Omega(2\theta_i - 2\theta_K) P_K A + Yb_i \quad (2.2)$$

where: Yc_i – Calculated intensity at the ith step of the powder pattern

s – Scale factor

$\sum$ - Sum over all reflections represented by Miller indices, K.

L_k - Lorentz-Polarization and multiplicity factor

F_K – Structure factor

Ω – Reflection profile function

P_K – Preferred orientation factor

A - Absorption factor

Yb_i - Background intensity at the ith step of the powder pattern

Therefore, for each observed step-scan intensity (Yo_i) there is a corresponding calculated step-scan intensity (Yc_i). In the Rietveld algorithm, the method of nonlinear least squares refinement is used to minimize (find the best fit) between the entire experimental powder pattern (with several thousand step intensities Yo_i) and a theoretical powder pattern composed of the same number of points ($\sum Yc_i$). The function that is minimized in the least-squares refinement is the residual, Sy:

$$S_y = \sum_i w_i (Yo_i - Yc_i)^2 \qquad (2.3)$$

where: $w_i = 1/ Yo_i$

Yo_i - Observed intensity at the ith step of the powder pattern

Yc_i - Calculated intensity at the ith step of the powder pattern

While the sum is over the entire data points of the experimental diffraction pattern.

2.2.3. Parametric Rietveld refinement

In-situ and *in-operando* X-ray diffraction are powerful techniques for structural characterisation of crystalline materials as a function of an external variable. Such real-time studies are extremely valuable for knowledge of the crystal structure, chemical and physical properties and behaviour of crystalline materials under varying external conditions. Examples include the use of non-ambient studies in elucidating the reaction mechanisms, kinetics and thermodynamic processes of materials undergoing change due to an external variable.

The use of superior brilliance and collimation at 3rd and 4th generation synchrotron sources have led to ultra-fast time-resolved studies in fractions of seconds as opposed to minutes in home laboratory or neutron sources. After each experiment, the analyst obtains a large body of diffraction data (up to thousands of diffractograms) and applies a fast and robust whole powder pattern fitting (WPPF) procedure as part of the data analysis. Typically WPPF

procedures such as LeBail [4], Pawley [5] (decomposition) codes and Rietveld refinement [6] methods are applied to each pattern separately. In this independent/sequential procedure of WPPF, the structural model of the previous data set forms a starting model to refine the succeeding powder pattern.

One weakness of the sequential analysis method is its susceptibility to lead to refinements finding false minima even with refined crystallographic parameters constrained to lie within sensible minimum and maximum values. This is due to the sequential protocols inability to process parameters which remain fixed or are known to evolve smoothly as a function of the external variable. For example in temperature dependent studies, the 2θ zero point set error of the diffractometer should remain constant throughout the experiment. Additionally as a result of the thermal expansion of the powder sample holder in Bragg-Brentano geometry, an evolving vertical height correction should be applied throughout the diffraction body.

In order to address these issues, the parametric Rietveld refinement method was developed by Evans and Stinton [7]. In this method, a single evolving model is simultaneously refined over all of the data ranges. Therefore, one essentially fits a 2θ, external variable (e.g. temperature) and intensity (I) surface of diffraction data. As opposed to the sequential method, there is a greater data point to parameter ratio e.g. calculating a value from 100 5 minute data sets (parametric Rietveld refinement) versus a single 5 minute data set (sequential Rietveld refinement). The 2θ zero point set error value will be determined with greater accuracy using the parametric method. Furthermore, because crystallographic quantities of a phase are expected to evolve smoothly with changing external variables, models can be introduced to describe or parameterise the variation during these refinements. A quadratic function can be used to parameterise the variation of the powder sample holder vertical height with temperature. Physically realistic models can also be applied during data analysis. Implementing models can also be useful in directing the refinements to avoid false minima, provided that the models are correct. As with the sequential method structural parameters can also be varied independently for each data set (e.g. the lattice parameters).

2.2.4. Rigid body refinement

The successful interpretation and solution of a crystal structure is dependent on the correct selection of chemical and crystallographic variables. Often, due to the limited resolution of

powder X-ray diffractometers, additional chemical information can be included into the refinement process. One alternative solution is to use rigid bodies to describe known molecular fragments during the refinement process. A rigid body is made up of points in space, whereby all or some of the points are oriented or positioned with fixed/adjustable bond lengths and angles within the crystal structure [2, 8]. While maintaining the overall molecular symmetry the motion of the molecule is treated as a rigid body. The rigid body can be formulated using the Cartesian (xyz) coordinate system with new atoms being formulated by bond translations from the origin. The more elaborate 'z-matrix' description includes bond and torsion angles, which describe translations of atoms from the Cartesian origin or from a previously positioned atom.

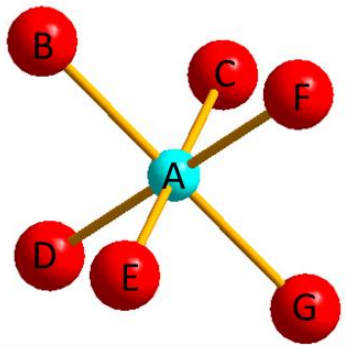


Figure 2.2: Depiction of an idealised octahedron, with central atom A coordinated by atoms B to G.

An example of a typical octahedron is shown in figure 2.2. The z-matrix formulation of this molecule can be described as follows:

z_matrix A..... line 1

z_matrix B A = b_1..... line 2

z_matrix C A = b_2 B 90..... line 3

z_matrix D A = b_3 B 90 C 90..... line 4

z_matrix E A = b_4 B 90 C 180..... line 5

z_matrix F A = b_5 B 90 C 270….. line 6

z_matrix G A = b_6 B 180 C 0……. line 7

Rotate_about_axes (R_X 0, R_Y 0, R_z 0)

Translate (t_x 0.1, t_y 0.2, t_z 0.3)

Line 1 places atom A at the Cartesian origin 0, 0, 0. Line 2 defines atom B at a distance with a value of b_1 from atom A. Line 3 places atom C at a distance b_2 away from A and makes the angle 90° with respect to atom A and B. Line 4 places atom D at a bond distance of b_3 from A, making the angle of 90° with atoms A and B, and at a torsion angle of 90° with respect to atoms A, B, and C. The rest of the atoms making the octahedron are formulated using the same series of distance, angle and torsion statements.

Once the starting rigid model is created, it is included into the unit cell by applying rotation and translation operations about the Cartesian axes (x, y, z). The translation parameters will translate part or the entire rigid body. The rotation parameters will rotate part or the entire rigid body around a point or line. In figure 2.2, the octahedron is oriented with three translational and rotational degrees of freedom, respectively. Finally, the rigid body Cartesian coordinates are converted into crystallographic coordinate system (i.e. fractional atomic coordinates) followed by applying the relevant space group symmetry operations.

The rigid body approach to crystal structure refinement offers improved benefits over the ‘free atom’ refinement approach. As seen in figure 2.2, instead of describing the crystal structure as a function of the position of each atomic coordinate (adjustment of 7 atoms therefore 21 parameters) a smaller set of parameters (3R and 3T) was used to describe the position and orientation of the molecular fragment. Furthermore, physical or empirical equations can be used to describe the rigid body [9].

2.2.5. Quality of fit

The process of iteratively adjusting the refinable parameters until the residual (equation 2.3) is minimised, can be thought of as progressing through a multi-dimensional surface consisting of shallow minima (false minima) and a deep minimum (global minimum). It therefore becomes imperative to constantly monitor the response of the refinement, in terms

of ensuring the crystal model remains chemically and physically sensible and obtaining a best fit between the calculated and observed Bragg reflections. For this, graphical as well as numerical criteria have been developed for judging a Rietveld refinement [1, 2, 10]. Graphical accounts, as either plots of the calculated and observed patterns or a difference profile plot are key, which can be used at every iteration to guide a refinement. Such plots can reveal which refined parameter (or lack of one) leads to the mismatch between the calculated and observed profiles. For example, an intensity mismatch may relate to an inadequate structural model or an impure phase in the sample. A quantitative judgement of the refinement can be given by several R-values found in the literature. Generally, these 'figures of merit' compute the squared difference between the observed and calculated powder profiles, and the lower the value, the more satisfactory the fit. The most useful and highly cited R-value is the residual weighted profile factor, Rwp (equation 2.4), which contains the residual being minimized during a refinement in the numerator:

$$R_{wp} = \sqrt{\frac{\sum w_i (Yo_i - Yc_i)^2}{\sum w_i Yo_i^2}} \qquad (2.4)$$

where: Yo_i = Observed intensity at the ith step of the powder pattern

Yc_i = Calculated intensity at the ith step of the powder pattern

w_i = Weights of the observed intensities

Careful consideration of the experimental background of the measured diffraction pattern must be taken when comparing Rwp values from different experiments. This is because the Rwp will be biased to a low value if the measured diffraction pattern contains a high background, as much of the diffraction pattern will be well described by the background function. Therefore, a background subtracted Rwp should be quoted ('R_wp_dash' in Topas). The Rwp value determined from a whole powder pattern decomposition method (LeBail or Pawley algorithm) is the best Rwp value that can be attained from a fit to a particular dataset. The Rwp from a satisfactory Rietveld refinement protocol should be near this value.

The statistically expected R-value (Rexp) is given by:

$$R_{exp} = \sqrt{\frac{\sum N-P}{\sum w_i Yoi^2}} \qquad (2.5)$$

.

where: N – The number of observations (data points)

P – The number of parameters

Rexp indicates the dominance of the counting errors and therefore the quality of the data collection. The ratio between the Rwp and Rexp (ideally should be 1) is expressed by the goodness-of-fit (χ^2):

$$\chi^2 = \frac{R_{wp}}{R_{exp}} \qquad (2.6)$$

The R_{Bragg} (equation 2.7) and R_F (equation 2.8) are equivalent to the residuals reported for single crystal structure refinements.

$$R_{Bragg} = \frac{\sum |I_{oK} - I_{cK}|}{\sum I_{oK}} \quad (2.7) \qquad R_F = \frac{\sum |(I_{oK})^{1/2} - (I_{cK})^{1/2}|}{\sum (I_{oK})^{1/2}} \qquad (2.8)$$

where: I_{oK} and I_{cK} are the observed and calculated intensity assigned to the K^{th} Bragg reflection.

These R-values (equations 2.7 and 2.8) are calculated by partitioning the intensity of the reflections according to the model and not the observed reflection. Coincidently, these are biased towards the model and can be misleading if an incorrect model is used in the refinement. However if the model is correct, non-structural misfits can be observed and corrected appropriately during the refinement. The Durbin-Watson statistic (d) [11], is given by:

$$d = \sum_{i=2}^{N}(\Delta Y_i - \Delta Y_{i-1})^2 \Big/ \sum_{i=1}^{N}\Delta Y_i^2 \qquad (2.9)$$

where: $\Delta Y_i = Yo_i - Yc_i$

The Durbin-Watson statistic indicates the degree of serial correlation in the series of intensities (Y_i). Ideally this value should be equal to 2, but will shift away from this value if there is a mismatch in the calculated and observed profile intensities.

2.2.6. Considerations when refining the crystal structure

Some of the general strategies before and during a Rietveld structure refinement are considered here. These factors were also considered when refining powder patterns collected for the materials investigated in this thesis. The first aspect to consider is the data collection duration and acceptable diffraction data quality. This includes the accuracy of the instrument alignment, calibration and the sample/specimen quality. In terms of the former aspect, it is important that the peak positions determined from the diffractometer are accurate within 0.01° (2θ) of the correct measurements [10]. This can be certified by using a standard reference material. The 2θ calibration using a NIST LaB_6 660a for the Bruker D2 Phaser used in this project is given in appendix 1. The instrument should also collect powder patterns with good signal-to-noise ratio viz. low background, high peak intensity and narrow peak profile which will provide a larger structural information content to be used in the refinement strategy. Regarding sample quality, narrow particle size distribution is important, meaning a well ground sample with small randomly orientated crystallites. This ensures that there is a fair relative intensity distribution of the reflections, avoiding a case where too few crystallites in the specimen produce too few measured intensities, or too large measured intensities are collected from the large crystallites, a 'rock and dust' scenario [10].

Concerning performing a Rietveld refinement, table 1.1 lists the relevant profile and structural refinable parameters in the Rietveld method. It is important that good initial values for all these parameters are fed into the first refinement iteration, which can usually reduce the number of subsequent iterations and the computation time. Good initial 2θ zero set point error can be derived from the diffractometer calibration using an external standard. Reliable

initial unit cell parameters can also be derived from a preliminary LeBail or Pawley refinement.

Approximate parameters of the original structural model, which include a full or almost complete account of the atomic coordinates, need to be fed in the first iteration in order to model the electron density within the unit cell, otherwise the refinement protocol will produce chemically unrealistic crystal structures. Ways to approach this issue is to perform a Fourier analysis (which will locate the missing atoms), to introduce minimum or maximum constraints to the structural model or to introduce a known chemical connectivity model. The latter approach can entail a geometric constraint of bond length and angles via building a rigid body model of the crystal framework. This mode of analysis has been explored in chapter 6 for the high temperature behaviour of the compound BPO_4.

During the refinement procedure, it is important to constantly monitor the refined parameters to ensure that the residual has refined to a global rather than local false minimum. Indicators of global minimum include monitoring the figures of merit, the graphical difference profile plot, crystal structure drawings and the Rietveld error or estimated standard deviation (e.s.d) for a refined parameter. The precision of the refined parameter should be less than 0.01 between successive refined parameters in the final iteration [12]. Finally, a smooth variance (with little oscillations) of a refined parameter as a function of an external variable (e.g. temperature), within a materials stability range, is an indication that the refinement converged to a global minimum.

Table 2.1: Refinable parameters.‡

Refinable parameters for each phase present	
Xj Yj Zj Bj Nj *	
Scale Factor	
Specimen-Profile breadth parameters	
Lattice Parameters	
Overall temperature factor	
Individual anisotropic thermal parameters	
Preferred Orientation	
Crystallite Size and Microstrain	
Extinction	
Overall refineable parameters	
2θ Zero set point error	Wavelength
Instrumental profile	Specimen Displacement
Profile Asymmetry	Specimen Transparency
Background	Absorption

‡ Adapted from Young *et al.* [10].

* (Xj, Yj and Zj are position coordinates, Bj is an isotropic thermal parameter and Nj is the site occupancy multiplier, all for the jth atom in the unit cell.)

2.3. Topas ®

Various computer software for performing Rietveld refinements have been made available without charge while others have an associated fee for purchase. Some widely used refinement software include GSAS (General Structure Analysis System) developed by A. C.

Larson and R. B. Von dreele [13], Jana developed by V. Petricek, M. Dusek and L. Palatinus [14], FULLPROF developed by J. Rodriguez-Carvajal [15] and Topas (Total Pattern Analysis System) developed by A. A Coelho [16]. All of the powder patterns reported in this thesis have been analysed using Topas version 4.2. Topas allows refinement of PXRD data through two platforms including graphical user interface (GUI) or Launch mode operation accessed by an input file consisting of a unique scripting language. In this work, room temperature diffraction patterns were analysed using the GUI interface while variable-temperature diffraction data were analysed using the Launch mode (kernel) operation.

The Launch mode kernel was used for performing fast and robust refinements of the many diffraction patterns analysed by the consecutive/sequential Rietveld refinement method. This mode of operation included compiling a batch file (for automated sequential refinement) with instructions of using the refined parameters of a previous refined model pattern as staring values to calculate the powder pattern of the next temperature. The batch file processing capabilities of Topas was also used to extract the refined structural parameters at each of the temperatures. The Launch mode operation was also used to perform rigid body and parametric Rietveld refinement of the diffraction data of the compound BPO_4 changing as a function of temperature (chapter 6). For example, parameterization of the lattice parameters of BPO_4 with temperature using a user defined equation was made possible in the Launch mode operation.

The program jEdit [17] was configured to interact with the Launch mode kernel of Topas and was used to compile the keywords and macro commands (contained in the input file) necessary to perform the automated sequential and parametric Rietveld refinements (figure 2.3).

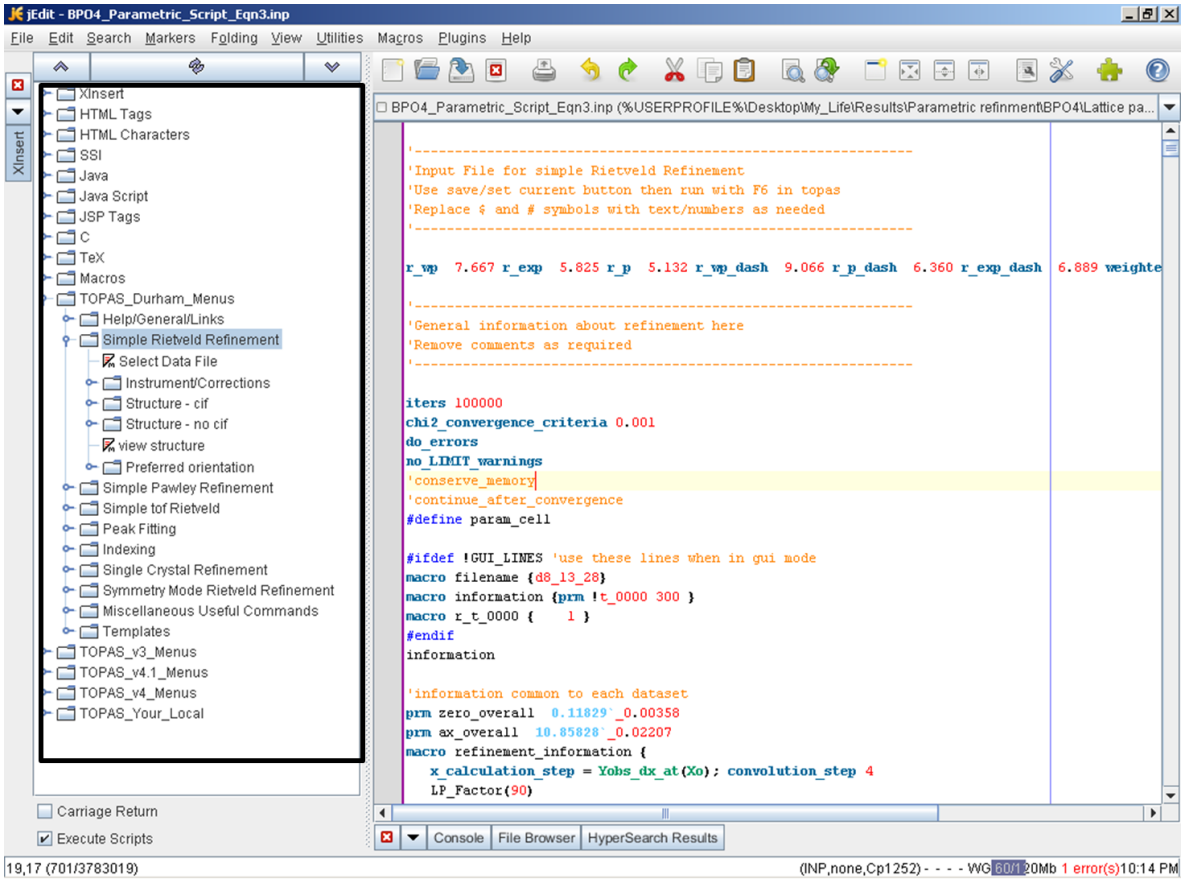


Figure 2.3: GUI screenshot of the program jEdit used to build the input file for execution in the program Topas. The text (set of instructions) to be executed are shown on the right. The plugins window used to prepare the text is shown on the left.

2.4. Powder X-ray diffraction instruments

Two in-house flat stage reflection geometry diffractometers - a Bruker D2 Phaser and Bruker D8 Advance diffractometer - were used to measure the powder diffraction patterns discussed in this work.

2.4.1. Bruker D2 Phaser

The θ – θ Bruker D2 Phaser desktop diffractometer, shown in figure 2.4, was primarily used for phase identification, purity confirmation and performing diffraction experiments under ambient conditions. This instrument is equipped with a sealed tube Co $K\alpha_1$/ $K\alpha_2$ X-ray source; λ = 1.78897/1.79285 Å, a Bruker Lynxeye PSD detector (set to measure a 5° 2θ

angular range) and 2.5° primary and secondary beam soller slits and a motorized sample stage is capable of 360° rotation of the sample during data collection. The goniometer radius of the diffractometer is 70.7 mm. The instrument is also fitted with a secondary beam Ni filter to attenuate K_β radiation and a 3 mm air-scatter slit. The X-ray generator was operated at 30 KV and 10 mA. The powdered samples were packed onto plastic sample holders. The instrument was operated using the Bruker Diffrac.Commander software with an auto-repeat scan function, which adds together multiple diffraction patterns for improved signal to noise data.



Figure 2.4: Front opening of the Bruker D2 Phaser diffractometer.

2.4.2. Bruker D8 Advance

The Bruker D8, shown in figure 2.5a, was employed to measure the variable-temperature PXRD measurements of the materials reported in this work. As such, it was fitted with the Anton Paar XRK 900 furnace (discussed below). The Bruker D8 uses a sealed Cu $K\alpha_1$/ $K\alpha_2$ X-ray source; λ = 1.5406/1.54439 Å and a Bruker VÅNTEC-1 PSD detector (set to measure a 12° 2θ angular range). The goniometer radius is 250 mm. The incident beam passes through a primary beam Göbel mirror and a primary soller slit with 2.5° opening. After interacting with the sample the beam passes through a secondary soller slit of 2.5° opening and a secondary beam Ni filter. The X-ray generator was operated at 40 KV and 40 mA. The Bruker D8 was operated with the Bruker Diffrac plus XRD Commander software, version

2.6.1 (discussed above) which also allowed hardware control features such as height and detector scans necessary for alignment tasks.

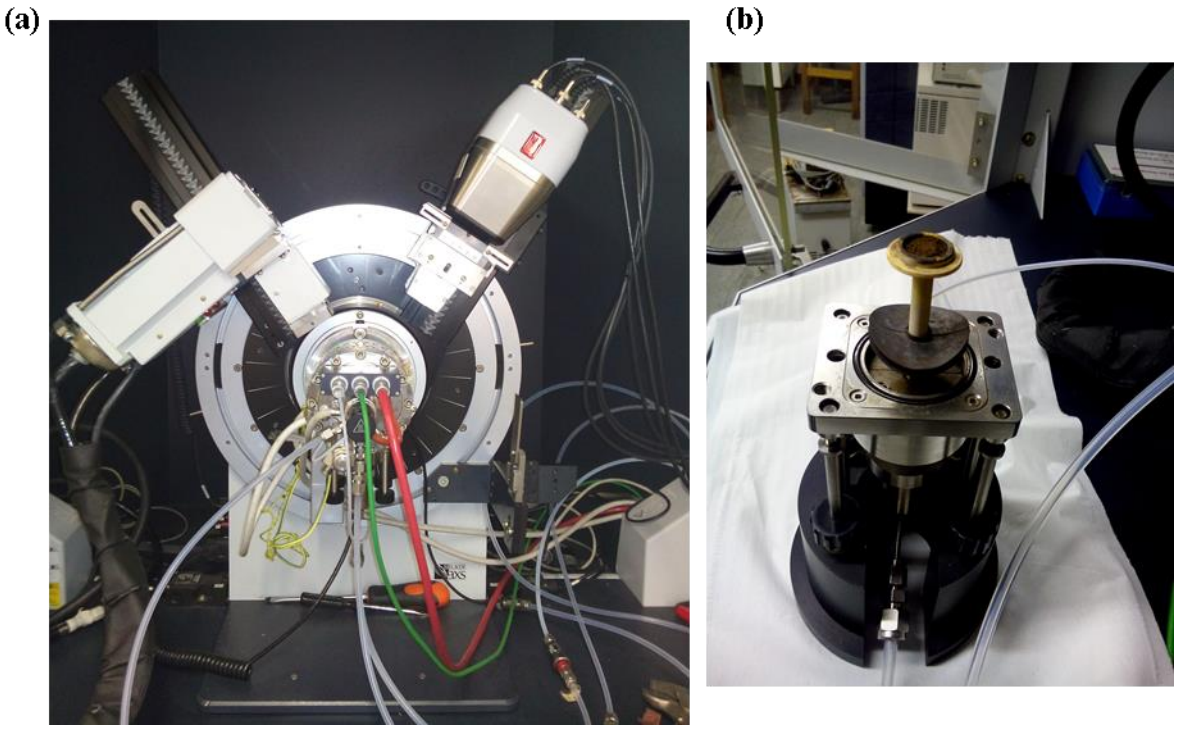


Figure 2.5: (a) Depicts the front opening of the Bruker D8 Advance diffractometer equipped with the Anton Paar XRK 900 furnace and (b) the Anton Paar XRK 900 in-situ chamber shown with the Macor® sample stage (the sample stage has been removed from the bottom of the chamber).

2.4.3. Anton Paar XRK 900 non-ambient sample chamber

The Anton Paar XRK 900 (figure 2.5a and b) [18] is a state-of-the-art sample stage for *in-situ* powder X-ray diffraction experiments. It has the capability of investigating materials at controlled temperatures from 30 °C up to 900 °C (maximum heating of 0.3 °C/sec) and pressure conditions of up to 10 bar. This reaction chamber features two thermocouples, one positioned next to the sample holder (approximately 2 to 3 mm away) and the other inside the chamber. In this work, powdered samples were packed either on a closed ceramic (Macor ®) or open ceramic (Macor ®) sample holder fitted with a piece of circular platinum foil. These sample holders have an internal diameter of approximately 11 mm. The Bruker software

XRD Wizard version 2.9.0.22 was used to control the workings of the reaction chamber. Diffraction data were collected in a step-wise temperature regime, after the chamber had equilibrated at the desired temperature. Therefore, the Anton Paar XRK 900 compliments the experimental aim of measuring the structural changes, thermal stability and expansion properties of the investigated porous and non-porous borophosphates as a function of temperature.

2.5. Supplementary characterization techniques

The characterization techniques described in this section were used in conjunction with the primary analytical technique (variable temperature powder X-ray diffraction) VT-PXRD to analyse the porous and non-porous borophosphates investigated in this thesis.

2.5.1. Fourier transform infrared spectroscopy (FTIR)

This technique was used to confirm the presence of inorganic functional groups contained in the studied materials. Frequencies at which particular atoms in the functional groups vibrate were recorded and correlated with spectra known from the literature. All FTIR experiments were performed on a Bruker Tensor 27 Fourier Transform Infrared spectrometer in the range of 550 – 4000 cm^{-1}.

2.5.2. Scanning Electron Microscopy (SEM)

All SEM images of the compounds investigated in chapters 4 and 5 were performed on a FEI Nova Nanolab 600 FIB/SEM.

2.5.3. Thermogravimetric analysis (TGA)

Thermogravimetric analyses of the compounds investigated in chapters 4 and 5 were performed on a Perkin Elmer STA 6000. Typical measurements were conducted from room temperature up to 900 °C. All TGA experiments were conducted under nitrogen atmospheric conditions. These measurements entail determining physical or chemical changes of a material (with known mass) as a function of temperature. From the changes in mass as a

function of increase in temperature, these measurements were useful in determining the decomposition and dehydration temperatures and subsequently determining the identity and amount of the volatile species in the investigated materials.

2.6. Synthesis methods

This section describes the synthetic techniques used to prepare the porous and non-porous borophosphates investigated in this thesis. All of the non-porous borophosphates were prepared using the solid state method, whereas the porous borophosphates were prepared using the hydrothermal method. The specific details regarding the syntheses of the investigated compounds are comprehensively reported in chapters 3, 4, 5 and 6.

The solid state reaction or shake ‘n bake methods involves initially forming an intimate mixture of solid reactants, either by grinding using an agate and mortar or using a mill. The solid mixture of reactants are then reacted with each other in a quartz boat or alumina crucible and heated to high temperatures. At these elevated temperatures, the solid state reaction may proceed via gaseous or liquid (melt) intermediates which facilitate the transport of atoms or ions.

The hydrothermal method has been used to form both anhydrous and hydrated powders. The chemical reactions occurring by the hydrothermal method occur at high temperatures and pressure. These reactions occur in the presence of water which acts as both a solvent and a pressure-transmitting medium. Therefore under these conditions, the formation of the desired crystalline powders can be controlled by adjusting the temperature, volume [degree of fill (%)] and pressure. For the porous borophosphate powders synthesised by the hydrothermal method, the reactants were initially placed into a Teflon bomb (figure 2.6), which was then placed into an oven and heated.

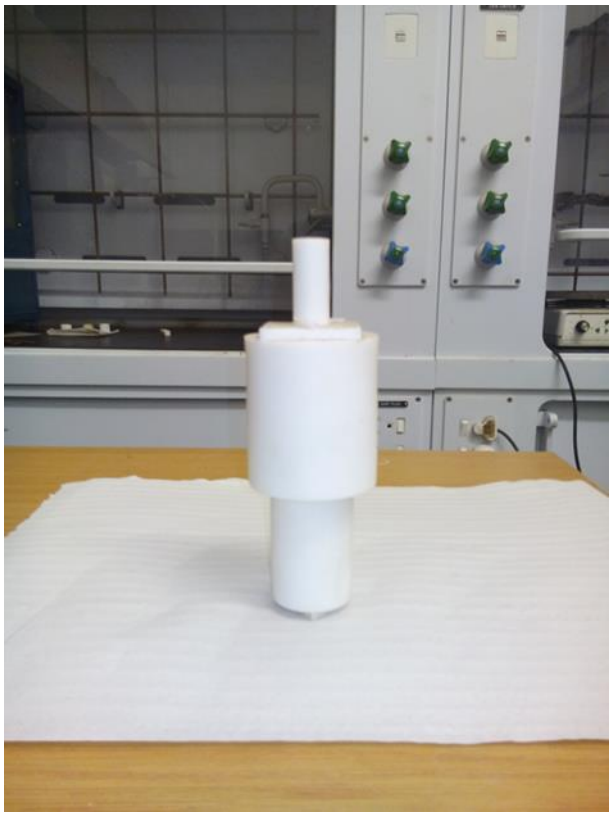


Figure 2.6: Teflon bomb.

2.7. References

[1] V.K. Pecharsky, P.Y. Zavalij, *Fundamentals of powder diffraction and structural characterization of materials*. Springer, 2009.

[2] R.E. Dinnebier, S.J. Billinge, *Powder diffraction: theory and practice. Royal society of chemistry*, 2008.

[3] W.L. Bragg, *Proceedings of the Cambridge Philosophical Society*, 1913, pp. 4.

[4] A. Le Bail, H. Duroy, J. Fourquet, *Materials Research Bulletin* 23 (1988) 447-452.

[5] G. Pawley, *Journal of Applied Crystallography* 14 (1981) 357-361.

[6] H. Rietveld, *Journal of applied Crystallography* 2 (1969) 65-71.

[7] G.W. Stinton, J.S.O. Evans, *Journal of Applied Crystallography* 40 (2007) 87-95.

[8] R.E. Dinnebier, *Powder Diffraction* 14 (1999) 84-92.

[9] M. Etter, M. Mueller, M. Hanfland, R.E. Dinnebier, *Zeitschrift für Kristallographie. Crystalline materials* 229 (2014) 246-258.

[10] R.A. Young, *The Rietveld method* Oxford university press, New York, 1991.

[11] J. Durbin, G. Watson, *Biometrika* 58 (1971) 1-19.

[12] L. McCusker, R. Von Dreele, D. Cox, D. Louer, P. Scardi, *Journal of Applied Crystallography* 32 (1999) 36-50.

[13] A.C. Larson, R.B. Von Dreele, *General Structure Analysis System*. LANSCE, MS-H805, Los Alamos, New Mexico (1994).

[14] V. Petříček, M. Dušek, L. Palatinus, *Zeitschrift für Kristallographie-Crystalline Materials* 229 (2014) 345-352.

[15] J. Rodriguez-Carvajal, *Satellite Meeting on Powder Diffraction of the XV Congress of the IUCr.*, Toulouse, France, 1990, pp. 127.

[16] C.A. A., *Bruker AXS*, Karlsruhe, 2007.

[17] P. S., Ottawa, Canada, 1998.

[18] A.P.X. 900, http://www.anton-paar.com/corp-en/products/details/reactor-chamber-xrk-900/xrd/.

Chapter 3 Thermoresponsive behaviour of $ABPO_5$ (A = Ca, Sr, Ba) compounds

M. W. Mogodi[a], M. A. Fernandes[b], D. G. Billing[a]*

[a]School of Chemistry and DST/NRF Centre of Excellence in Strong Materials, University of the Witwatersrand, Private Bag 3, WITS, 2050, South Africa.

[b]Molecular Sciences Institute, School of Chemistry, University of the Witwatersrand, PO Wits, 2050, South Africa.

*Corresponding author: Professor David Billing

School of Chemistry,

University of the Witwatersrand,

Private Bag 3, WITS, 2050, South Africa

Email: dave.billing@wits.ac.za

Tel no : +27 11 717 6759

Fax no: +27 11 717 6749

This chapter has been submitted to the Journal of Solid State Chemistry and has been structured according to the journal's format.

Abstract

The thermal expansion behaviour of the stillwellite type structures $ABPO_5$ (A = Ca, Sr, Ba) were determined from variable-temperature powder X-ray diffraction (VT-PXRD) data, in the temperature range of 30 to 850°C. These materials were prepared by traditional solid state synthesis methods. The Rietveld refinement method was applied to the VT-PXRD data to determine the crystallographic parameters of interest. All compounds crystallize in the space group $P3_121$ (No.152) with Z = 3. In the reported temperature range, a non-linear expansion of the unit cell axes is found for all structures, with volume expansion coefficients (α_V) being $CaBPO_5$ = 32.9 x 10^{-6}/°C; $SrBPO_5$ = 32.5 x 10^{-6}/°C; $BaBPO_5$ = 29.9 x 10^{-6}/°C. This positive thermal expansion behaviour is correlated to changes in the crystal structures as a function of temperature. Variations in the inter-tetrahedral bridging angle θ, non-bonded B-P distance and average A^{2+}-O distances as a function of temperature, and the influence of the cationic A^{2+} radii are discussed. Infrared spectra of all of the $ABPO_5$ compounds were recorded to confirm the presence of the inorganic anion borate and phosphate groups.

Keywords: Stillwellite, Thermal expansion, VT-PXRD

3.1. Introduction

Borophosphates are intermediate compounds of the systems M_xO_y-B_2O_3-P_2O_5-(H_2O) (M = main group/transition metal or ammonium). They exhibit exciting structural chemistry with a large variety of structural motifs possible with the anionic unit $\infty[B_xP_yO_z]^{n-}$ [1, 2]. From this, three-dimensional open framework/porous structures of metal borophosphates have been synthesised. These materials have proven to be of technological importance in shape-selective catalysis and ion exchange applications. However, only a handful of low-porosity anhydrous borophosphates have previously been synthesised. These include α – $Zn_3[BPO_7]$ [3], $Co_5[BP_3O_{14}]$ [4], $ABPO_5$ A = Ca [5], Sr [6], Ba [7], Pb [8], $Na_2[B_2P_3O_{13}]$ [9], $A_3[BP_3O_{12}]$ A = Ba [10] phases, which are composed of tetrahedral BO_4 or trigonal BO_3 sharing corners with tetrahedral PO_4 groups. Of this, the stillwellite ($CeBSiO_5$) [11] like structures of $ABPO_5$ A = Ca, Sr, Ba, Pb exhibit piezoelectricity. The piezoelectric property in these borophosphates is also supported by the structure being non-centrosymmetric and space group $P3_121$; the same space group as α-quartz which is currently the most used piezoelectric material. $SrBPO_5$ [6] and $BaBPO_5$ [12] have been used in laser and nonlinear optic

technologies. $ABPO_5$ borophosphates have an isoelectronic relationship with silicates and are therefore biocompatible with the living body [5]. More recently, Eu^{2+} doped $ABPO_5$ borophosphates have been shown to be efficient photoluminescence materials [13]. The first advancement to the crystal structures of $ABPO_5$ family was reported in 1966 by Bauer *et. al* [14] and later in 1994 by Kniep *et al.* [15] who published the synthesis and Rietveld refinement analysis of X-ray diffraction patterns of the $ABPO_5$ phases.

The crystal structures of the $ABPO_5$ isostructural phases have only been reported at room temperature, with no information regarding their thermal expansion behaviour. This thermoresponsive behaviour is an important property, noting that the material may lose its favourable piezoelectric function via a phase transformation or thermal decomposition process. To compute this physical behaviour, the linear thermal expansion coefficient must be determined from high-temperature X-ray diffraction data. This often involves collecting a plethora of diffraction data and using the sequential Rietveld structural refinement method to evaluate individual data sets independently. In this work, we report the synthesis, structural and thermal characterisation of low-porosity anhydrous $ABPO_5$, A = Ca, Sr, Ba phases studied by variable temperature powder X-ray diffraction (VT-PXRD). The thermal expansion behaviour of these materials is evaluated and correlated to changes in the crystal structure i.e. variations in bond lengths and inter-tetrahedral (B-O-P) bridging angles, θ. This approach to understand the thermal expansion of a material is synonymous with the explanation that the cooperative bending of M-O-M angles as a function of temperature gives rise to negative thermal expansion behaviour in several molybdates [16], tungstates [17], phosphates [18] and vanadates [19]. This structural change originates from the transverse thermal vibration of bridging oxygen atoms in M-O-M bonds. Therefore concerning $ABPO_5$ compounds, a comparison in the thermal expansion behaviour and structural variation will also be described.

3.2. Experimental

3.2.1. Synthesis of $ABPO_5$ powders

$CaBPO_5$, $SrBPO_5$ and $BaBPO_5$ were synthesized by solid state synthesis methodology according to equations (3.1), (3.2) and (3.3) respectively.

$$CaHPO_4.2H_2O(s) + H_3BO_3(s) \rightarrow CaBPO_5(s) + 4\ H_2O(g) \quad (3.1)$$

$$SrCO_3(s) + H_3BO_3(s) + NH_4H_2PO_4(s) \rightarrow SrBPO_5(s) + NH_3(g) + CO_2(g) + 3\ H_2O(g) \quad (3.2)$$

$$BaCO_3(s) + BPO_4(s) \rightarrow BaBPO_5(s) + CO_2(g) \quad (3.3)$$

For $CaBPO_5$ synthesis, $CaHPO_4.2H_2O$ and H_3BO_3 were ground together in an agate mortar. The resulting mixture was transferred into a quartz boat and heated at 600 ˚C for 6 h and then at 900 ˚C for 3 days. $SrBPO_5$ was synthesized by slowly heating the well ground reaction mixture to 500 ˚C over 10 hours, in order to allow for the gradual evolution of NH_3 and CO_2. The reaction mixture was then cooled to room temperature, ground up again and then heated at 900 ˚C for 24 hours. $BaBPO_5$ was synthesized from $BaCO_3$ and BPO_4 according to equation 3.3. Stoichiometric amounts of each reagent were weighed separately, ground thoroughly in an agate mortar and transferred into a quartz boat. The resulting mixture was initially heated at 400 °C for 12 hours to allow for the removal of CO_2. The reaction mixture was then heated at 1000 ˚C for 72 hours and then cooled to room temperature. The preparation of the three materials were repeated a number of times to verify that they would be prepared reproducibly.

3.2.2. Characterisation

The powder X-ray diffraction data for the $CaBPO_5$, $SrBPO_5$ and $BaBPO_5$ samples were collected on a Bruker D8 Advance diffractometer equipped with a sealed Cu tube X-ray source ($CuK_{\alpha1}/K_{\alpha2}$ with λ = 1.5406/1.54439 Å) operated at 40 kV and 40 mA. The variable temperature experiments were carried out in an Anton Paar XRK900 reaction chamber. The data were collected in the continuous mode in the °2θ range of 10–120 °2θ with a step size of 0.028 ° and count rate of 0.5 sec/step. A complete diffractogram was collected every 50 °C at temperatures ranging from 30 to 850 °C and then cooled to room temperature. The total collection time per experiment was 2 days. Prior to each variable temperature PXRD

experiment, the National Institute of Standards Technology (NIST) Standard Reference Material (SRM), SRM LaB_6 660a was used for peak position calibration and alignment checking.

A Bruker Tensor 27 Fourier Transform Infrared spectrometer was used to obtain IR spectra of the as synthesized $ABPO_5$ powders. All the samples were analysed in powder form. The spectra were recorded in the range of 550-4000 cm^{-1}.

3.3. Results and discussion

The phase purity of the prepared samples were evaluated using the Bruker-AXS Evaluation Package (EVA), release 2008 software using ICDD PDF 4+ release 2009 as a reference database. A single phase sample was prepared for $SrBPO_5$, whereas a $(P_4O_6)O_2$ impurity was identified for $CaBPO_5$ and amorphous impurity was identified for $BaBPO_5$. Rietveld refinement of the PXRD patterns was performed using the Topas (Total pattern analysis solution) version 4.2 package [20]. A two phase refinement was performed for $CaBPO_5$ while a split-PVII peak function was used to model the two amorphous regions for the $BaBPO_5$ patterns. The starting models for the three materials were taken from the room temperature phases (space group $P3_121$) reported by Kniep *et. al* [10]. For the higher temperature datasets, the refined parameters obtained at the end of the refinement of the preceding temperature formed the starting model to the refinement against powder patterns that correspond to the next temperature step. Each sequence of these sequential Rietveld refinement runs was done in an automated manner using the batch file processing capabilities of Topas. In a typical refinement, $CuK_{\alpha1}/K_{\alpha2}$ emission profile taken from Hölzer *et al.* (1997) [21] were used, one histogram scale factor, 4^{th} order Chebychev background polynomial terms and lattice parameters were initially varied. Four profile variables of the pseudo-Voigt profile function were refined. The specimen displacement, LP factor and crystallite size broadening terms of a Lorentzian profile were also included into the refinement. The preferred orientation was modeled by a Spherical Harmonics function, followed by the fractional atomic coordinates and thermal parameters being refined. Figure 3.1 shows the observed, calculated and difference profiles for the Rietveld refinements of $CaBPO_5$, $SrBPO_5$ and $BaBPO_5$ collected at 30 °C.

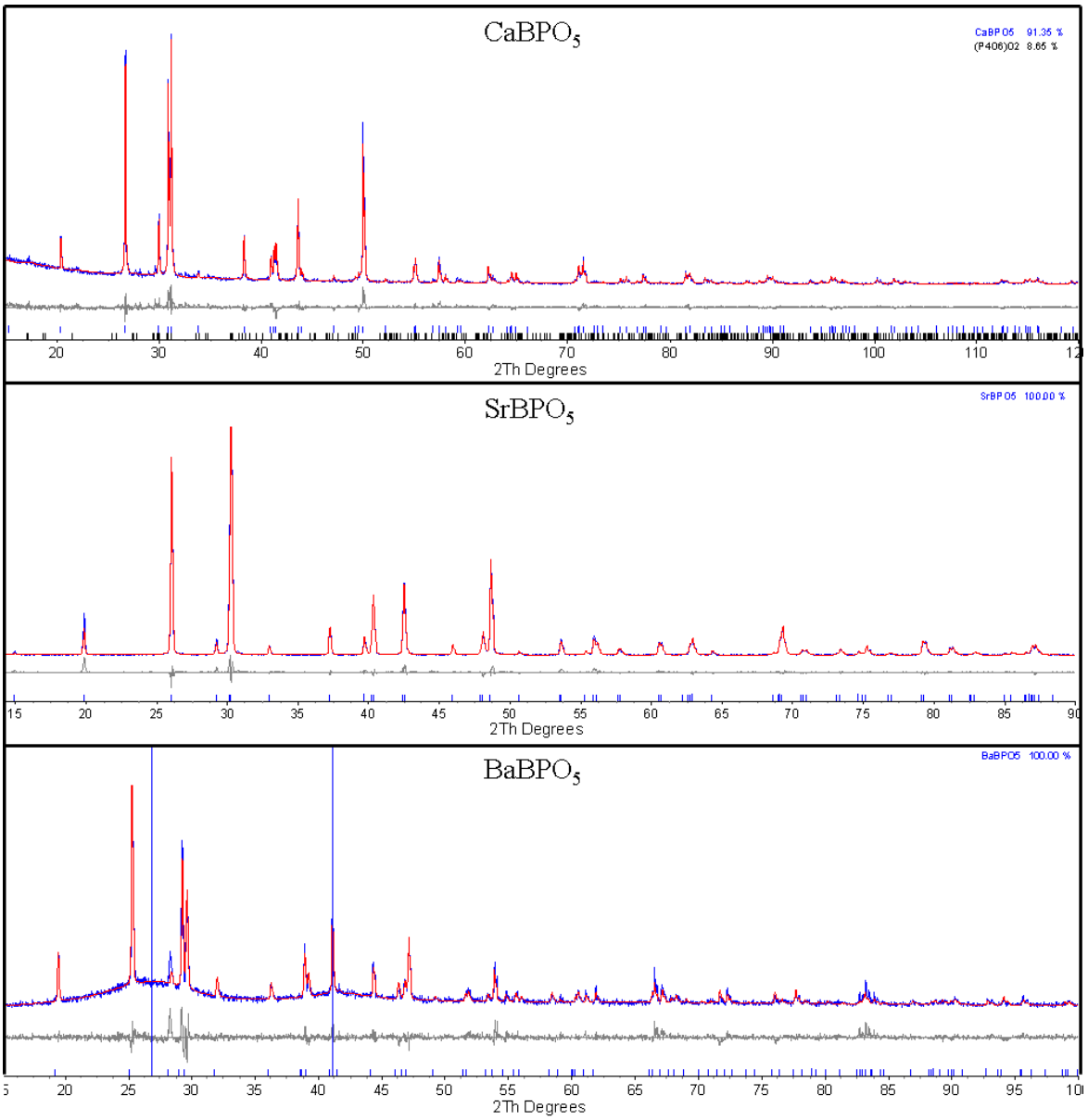


Figure 3.1: Observed (blue), calculated (red) and difference (grey lower line) PXRD patterns for $CaBPO_5$ (top panel), $SrBPO_5$ (middle panel) and $BaBPO_5$ (lower panel) at 30°C. The vertical blue lines in the $BaBPO_5$ PXRD patterns represent the Topas peaks phase (split-PVII peak function) used to model the unidentified regions. Lower tick marks indicate predicted peak positions.

Figure 3.2a shows the projection of the $ABPO_5$ unit cell viewed down the [001] direction. The crystal structure consists of vertical columns, each column built of alternating phosphate tetrahedra and irregular A^{2+} nine coordinated polyhedra in the [001] direction. The alternating columns are linked to four other surrounding columns creating an open framework. These

open spaces are occupied by infinite helical boron tetrahedra at the corners of the unit cell with 3_1 axis (figure 3.2b). All of the polyhedra of the structure are connected by oxygen atoms; with oxygen atoms from the borate tetrahedra sharing its vertices with two phosphate polyhedra and the remaining two corners with A^{2+}polyhedra.

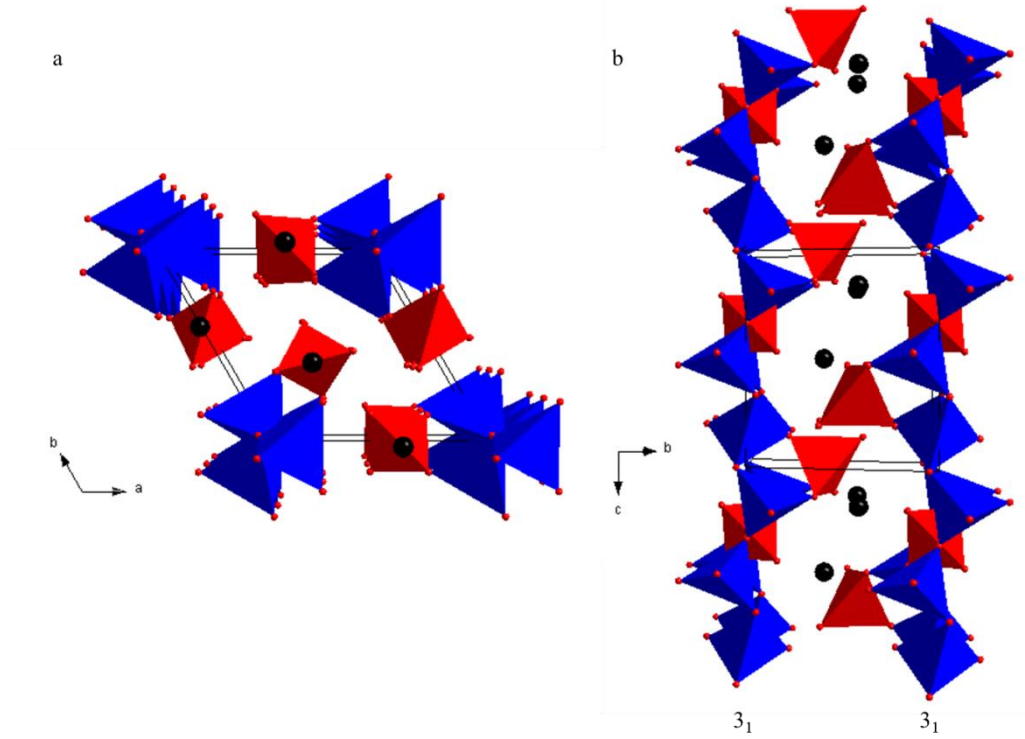


Figure 3.2: (a) Unit cell representation of the stillwellite $ABPO_5$ structure down [001]. Coordination of oxygen atoms around A^{2+} (black sphere) is omitted for clarity. (b) Two translationally identical chains of boron tetrahedra (blue), with 3_1 symmetry, viewed along [010] direction, with phosphorous tetrahedra (red) and A^{2+} polyhedra linking the chains.

Table 3.1 and figure 3.3 show the variation of the unit cell parameters as well as the agreement factors of the Rietveld refinements (Rwp values are between 12 – 17% and χ^2 values are between 1.32 – 2.31) as a function of temperature. Table 3.2 shows the fractional atomic coordinates at 30 and 850 °C.

Table 3.1: Cell dimensions as a function of temperature for $ABPO_5$ compounds.

Temperature (°C)	$CaBPO_5$			$SrBPO_5$			$BaBPO_5$		
	a (Å)	c (Å)	V(Å)^3	a (Å)	c (Å)	V(Å)^3	a (Å)	c (Å)	V(Å)^3
30	6.6805(5)	6.6082(4)	255.41(2)	6.8452(2)	6.8137(7)	276.49(9)	7.1104(9)	6.9926(8)	306.17(8)
100	6.6827(8)	6.6129(9)	255.76(6)	6.8477(8)	6.8201(3)	276.96(4)	7.1140(6)	6.9951(4)	306.59(3)
200	6.6874(1)	6.6222(9)	256.48(1)	6.8540(1)	6.8271(9)	277.75(5)	7.1197(2)	7.0015(4)	307.36(2)
300	6.6918(7)	6.6310(9)	257.16(5)	6.8604(6)	6.8335(5)	278.53(8)	7.1264(1)	7.0075(1)	308.20(2)
400	6.6961(8)	6.6400(7)	257.84(5)	6.8676(5)	6.8404(9)	279.40(5)	7.1327(1)	7.0117(1)	308.93(1)
500	6.7019(5)	6.6505(8)	258.69(8)	6.8746(6)	6.8470(8)	280.24(6)	7.1401(8)	7.0184(4)	309.87(8)
600	6.7083(5)	6.6621(1)	259.64(1)	6.8820(8)	6.8542(6)	281.14(6)	7.1468(7)	7.0249(1)	310.74(5)
700	6.7133(9)	6.6722(1)	260.42(6)	6.8911(1)	6.8622(6)	282.21(3)	7.1566(3)	7.0339(3)	311.99(4)
800	6.7205(7)	6.6851(1)	261.48(9)	6.9000(7)	6.8703(2)	283.27(9)	7.1631(8)	7.0443(5)	313.02(8)
850	6.7243(3)	6.6930(7)	262.09(2)	6.9052(2)	6.8745(2)	283.87(6)	7.1685(1)	7.0490(1)	313.70(2)

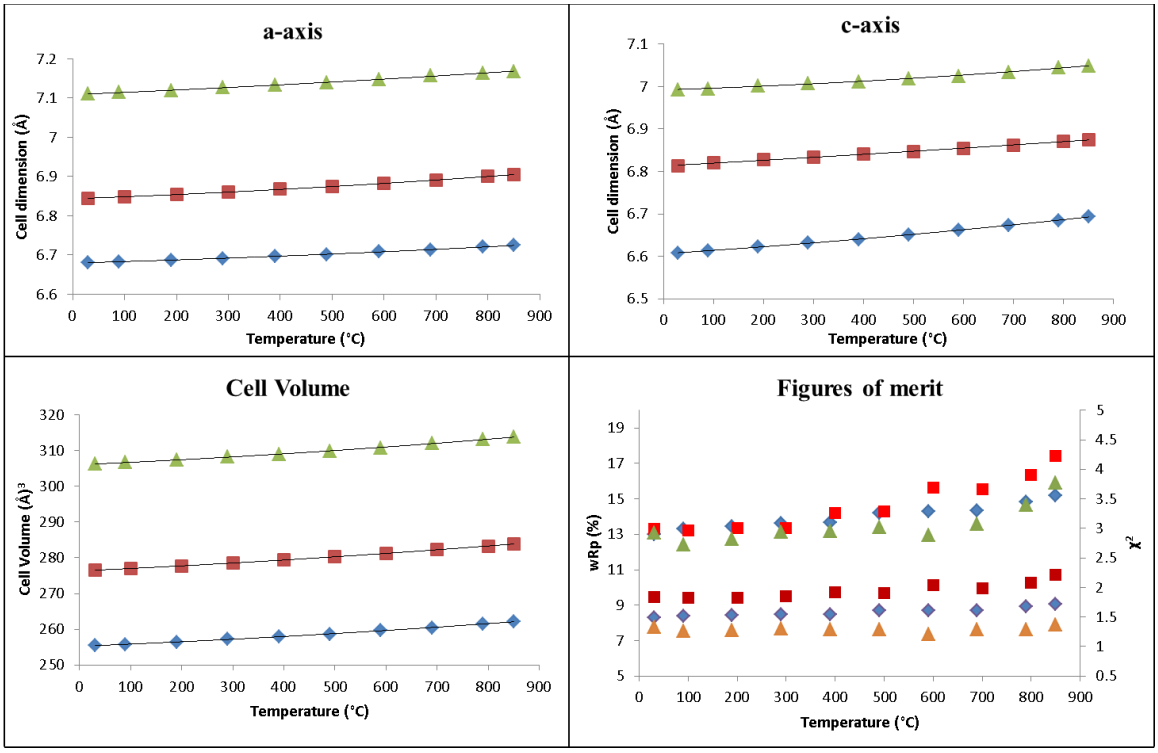


Figure 3.3: Graphs showing the variation in unit cell parameters, cell volume and figure of merit (χ^2 is the lower set of curves) vs temperature for $CaBPO_5$ (◊), $SrBPO_5$ (□), $BaBPO_5$ (Δ). Solid lines represent polynomial least squares fits to the data. The error bars are smaller than the symbol size.

Table 3.2: Fractional atomic coordinates obtained at 30 °C and 850 °C for $ABPO_5$ (A = Ca, Sr, Ba).

Compound	30 °C				850 °C			
	x	y	z	B (Å^2)	x	y	z	B (Å^2)
Ca	0.3913(5)	0.4081(9)	0.50000	0.04(3)	0.4232(2)	0.3792(7)	0.50000	2.631(3)
B	0.9217(7)	1.0120(5)	0.50000	0.5(1)	1.1462(6)	1.1033(1)	0.50000	9.605(3)
P	0.4420(6)	0.4180(1)	0.00000	0.05(7)	0.4476(9)	0.4067(4)	0.00000	1.506(9)
O1	0.3594(2)	0.1903(9)	0.8408(1)	0.06(1)	0.3547(3)	0.1885(6)	0.8243(2)	1.055(3
O2	0.5837(7)	0.4464(6)	0.1273(3)	0.03(8)	0.5870(4)	0.5255(4)	0.1064(1)	2.495(1)
O3	-0.051(1)	-0.051(1)	0.00000	0.29(1)	-0.0114(5)	-0.0762(8)	0.00000	4.255(2)
Sr	0.3981(2)	0.3981(2)	0.50000	0.04(4)	0.4003(3)	0.4003(3)	0.50000	2.714(8)
B	0.9192(5)	0.8929(1)	0.50000	0.7(9)	1.2129(5)	0.8996(6)	0.50000	-3.064(6)
P	0.3985(8)	0.3985(8)	0.00000	0.04(1)	0.3968(3)	0.3968(3)	0.00000	1.473(4)
O1	0.3616(4)	0.1969(1)	0.8824(5)	0.06(9)	0.3339(8)	0.1936(6)	0.877(1)	6.139(8)
O2	0.5801(0)	0.4359(1)	0.1468(6)	0.039(1)	0.5869(7)	0.4387(5)	0.139(1)	4.198(7)
O3	-0.051(1)	-0.0574(9)	0.00000	0.081(9)	-0.0360(9)	-0.0357(7)	0.00000	3.367(0)
Ba	0.3949(1)	0.00000	0.3333	0.31(1)	0.3939(9)	0.00000	0.3333	0.662(1)
B	-0.0816(1)	0.00000	0.3333	0.51(9)	-0.1514(0)	0.00000	0.3333	5.758(2)
P	0.3922(1)	0.00000	0.8333	1.4(1)	0.3837(5)	0.00000	0.8333	0.656(4)
O1	0.3274(1)	0.1414(1)	-0.0392(1)	1.0(4)	0.3790(7)	0.1399(1)	-0.0861(5)	2.253(5)
O2	0.4279(1)	0.8606(1)	-0.0323(1)	1.2(8)	0.4292(2)	0.8413(5)	-0.0225(1)	1.298(8)
O3	-0.0355(1)	0.00000	0.8333	1.1(1)	-0.0605(7)	0.00000	0.8333	7.264(1)

For all three $ABPO_5$ compounds studied, a slightly non-linear expansion is observed over the entire temperature range along the *a*- and *c*- axis. Therefore a second-order polynomial approximation is used to describe the temperature dependence of the unit cell parameters. A linear approximation was also used to describe the temperature dependence of the unit cell parameters. However the measure used to evaluate satisfactory fit, the correlation coefficient or R^2 (R-squared), had better fits (close to unity) for the polynomial approximations. An overall positive thermal expansion in the unit cell volume of the respective $ABPO_5$ compounds results from the corresponding positive expansion behaviour along the unit cell edges. The variation of the unit cell volume as a function of temperature can be represented in a second-order polynomial of the form: $CaBPO_5$, V (Å)^3 = 3 x $10^{-6}(T)^2$ + 0.0057(T) +

255.25 (R^2 = 0.9997); $SrBPO_5$, V $(Å)^3$ = 3 x $10^{-6}(T)^2$ + 0.0065(T) + 276.31 (R^2 = 0.9998); $BaBPO_5$, V $(Å)^3$ = 3 x $10^{-6}(T)^2$ + 0.0063(T) + 306.01 (R^2 = 0.9995).

More useful information concerning thermoresponsive behaviour of $ABPO_5$ compounds is provided by re-drawing the respective unit cell evolutions with temperature as normalised plots (with respect to the experimental cell dimension at room temperature), as shown in figure 3.4. The benefits of these plots (especially over the plots in figure 3.3) are that they assist in identifying and comparing trends between the respective compounds. This will also lead to a more detailed understanding of the thermoresponsive nature of the studied compounds. The results of these plots reveal that the volume expansion is almost identical for all compounds (figure 3.4d). Table 3.3 lists the thermal expansion coefficients of $ABPO_5$ compounds in the temperature range of 30 to 850 °C, along with the anisotropy of thermal expansion for all compounds. The anisotropy of thermal expansion for all compounds has been evaluated using two distinct approaches. The first approach compares the *a/c* ratio at 30 and 850 °C. This approach reveals that the thermal expansion of the $ABPO_5$ have a small anisotropy along the *a*- and *c*- axis. This is reflected by the *a/c* value which does not vary much across the temperature range and remains essentially unity for all compounds. A more in-depth approach to analysing the degree of anisotropy of thermal expansion is the structure-controlled anisotropy factor *A* [22, 23], which is a summation of the differences of the coefficients α(a), α(b) and α(c):

$$A = (|\alpha(b) - \alpha(c)| + |\alpha(b) - \alpha(a)| + |\alpha(c) - \alpha(a)|)(10^{-6}) \qquad (3.4)$$

The value of the anisotropy factor *A* approaches zero for isotopically expanding materials. Therefore, from these values it is seen that the expansion of the unit cell is highly anisotropic for the compound $CaBPO_5$ as opposed to its $SrBPO_5$ and $BaBPO_5$ counterparts. Furthermore, from the normalised plots in figure 3.4, it is observed that for the $CaBPO_5$ compound, the *c*-axis expands almost twice as much as the *a*- and *b*- axes. However, in the $SrBPO_5$ and $BaBPO_5$ compounds, essentially identical thermal expansion of the *a*-, *b*-, *c*- axes is observed. Additional evidence that the *c*-axis in the $CaBPO_5$ compounds is behaving differently from the rest of the studied compounds is that the thermal expansion coefficient of this compound along the *c*-axis is almost two times that along the *a*-axis (table 3.3). Essentially identical

thermal expansion coefficients are observed along the *a*-, *b*-, and *c*- axes in the $SrBPO_5$ and $BaBPO_5$ compounds.

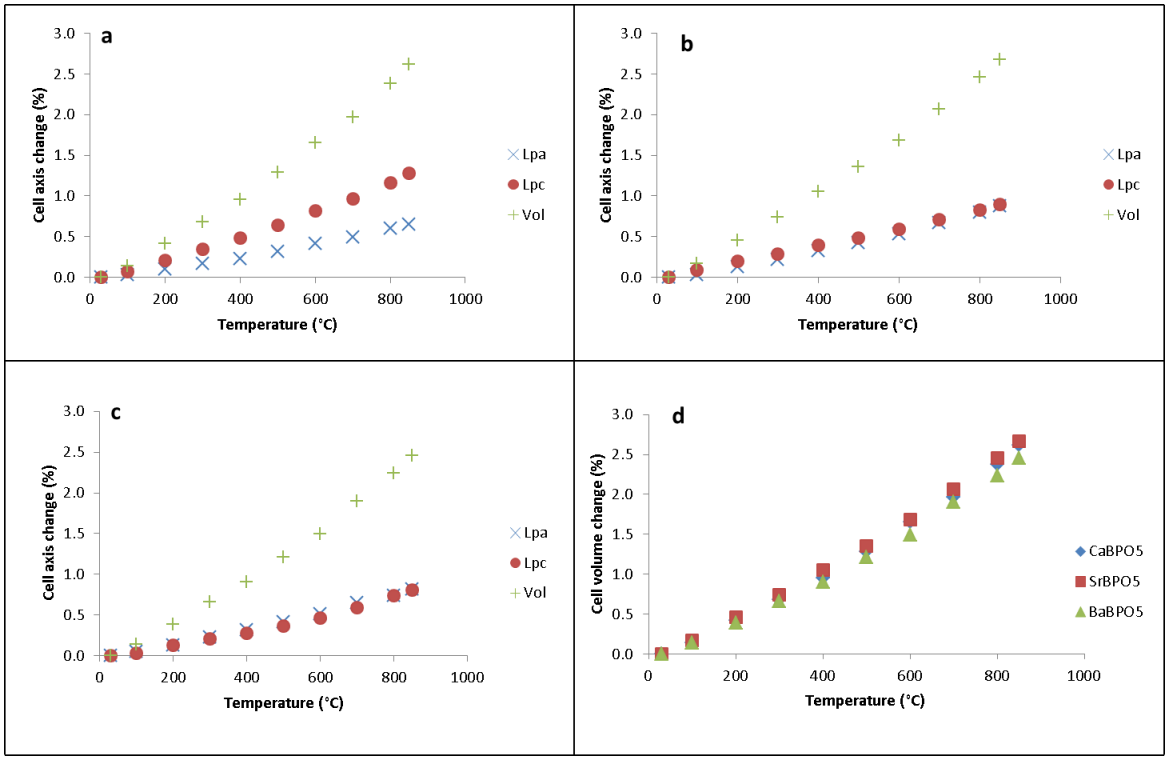


Figure 3.4: Relative changes (relative to the cell parameter at room temperature) of the unit cell parameters expressed as percentage changes as a function of temperature for a) $CaBPO_5$, b) $SrBPO_5$ c) $BaBPO_5$ and d) $ABPO_5$ counterparts.

Table 3.3: Thermal expansion characteristics of $ABPO_5$ compounds.

Compound	α_a x 10^{-6}/°C	α_c x 10^{-6}/°C	α_v x 10^{-6}/°C	Anisotropy of thermal expansion	
				a/c*	Anisotropy factor *A*
$CaBPO_5$	8.27	16.1	32.9	1.01 (1.00)	15.7
$SrBPO_5$	10.7	10.9	32.5	1.00 (1.00)	0.367
$BaBPO_5$	9.95	9.82	29.9	1.02 (1.02)	0.254

* *a/c* value at 30 °C and 850 °C (in brackets).

The reason for this different behaviour for $CaBPO_5$ as opposed to its other $ABPO_5$ compounds can be explained by the difference in the ionic radii of the investigated alkaline earth metal ions. For the $ABPO_5$ compounds, the ionic radii of the corresponding alkaline earth metal ions for nine coordination are: Ca^{2+} = 1.18 Å, Sr^{2+} = 1.31 Å, Ba^{2+} = 1.47 Å [24]. This represents an ionic size percentage increase of 11.0 % (Ca^{2+} to Sr^{2+}) and 24.6 % (Ca^{2+} to Ba^{2+}). It is also important to keep in mind that the A^{2+} ions in the $ABPO_5$ crystal structure are stacked along the *c*-axis (alternating with phosphate tetrahedra). Therefore we rationalize that the incorporation of the smaller Ca^{2+} over Sr^{2+} and Ba^{2+} into the lattice has the effect of causing the *c*-axis to expand twice as fast as the *a*-axis. Furthermore, the incorporation of the smaller Ca^{2+} ion into the lattice can also explain $CaBPO_5$ having the highest volume thermal expansion coefficient among the studied $ABPO_5$ compounds (table 3.3). The volume thermal expansion coefficient for the $ABPO_5$ compounds was shown to increase with a decrease in A^{2+} radii (α_v: $CaBPO_5$ > $SrBPO_5$ > $BaBPO_5$). Nonetheless, the differences in the respective α_v values are marginal. The larger cationic A^{2+} size comes into effect as the increase in ionic radii from Ca^{2+} to Ba^{2+} has the influence of increasing the unit cell dimensions at all temperatures.

Table 3.4 lists the selected bond lengths and angles of $ABPO_5$ compounds at 30 °C. As discussed, each respective crystal structure is composed of irregular/distorted 10 membered A (Ca, Sr, Ba) polyhedra, along with BO_4 and PO_4 tetrahedra. Also listed in table 3.4 are the average A-O, B-O and P-O distances for the respective $ABPO_5$ compounds. The B-O and P-O distances are in good agreement with previously reported results of the crystal structures of borate and phosphate compounds [25, 26]. It is evident that as the alkaline earth metal cation size increases, the average A-O distance increases. The opposite effect is observed for average B-O distances. For P-O distances, the larger Ba cation in $BaBPO_5$ results in the largest P-O distance among the $ABPO_5$ materials. The temperature dependence of the average tetrahedral B-O and P-O distances are shown in figure 3.5. For all of the compounds, there is a linear increase in average B-O and P-O distances as a function of temperature.

Table 3.4: Selected bond lengths (Å) and angles (°) at 30 °C for $ABPO_5$ compounds.

	O1	O2	O3	Average
Ca	2.6105(8) 2x, 2.6497(7) 2x	2.2715(6) 2x, 2.7174(7) 2x	2.8103(7)	2.61195
B	1.583(1) 2x		1.4641(9) 2x	1.52359
P	1.4896(1) 2x	1.4926(6) 2x		1.49113
B-O1-P	125.76(8)			
Sr	2.7709(1) 2x, 2.8382(1) 2x	2.5557(5) 2x, 2.6985(7) 2x	2.7828(0)	2.72925
B	1.5124(5) 2x		1.4886(8) 2x	1.50056
P	1.5020(5) 2x	1.4314(1) 2x		1.46676
B-O1-P	128.53(4)			
Ba	2.8869(9) 2x, 2.9171(7) 2x	2.6885(1) 2x, 2.7941(2) 2x	2.9321(8)	2.84379
B	1.6023(2) 2x		1.3802(5) 2x	1.49128
P	1.5750(9) 2x	1.4769(4) 2x		1.52601
B-O1-P	123.76(6)			

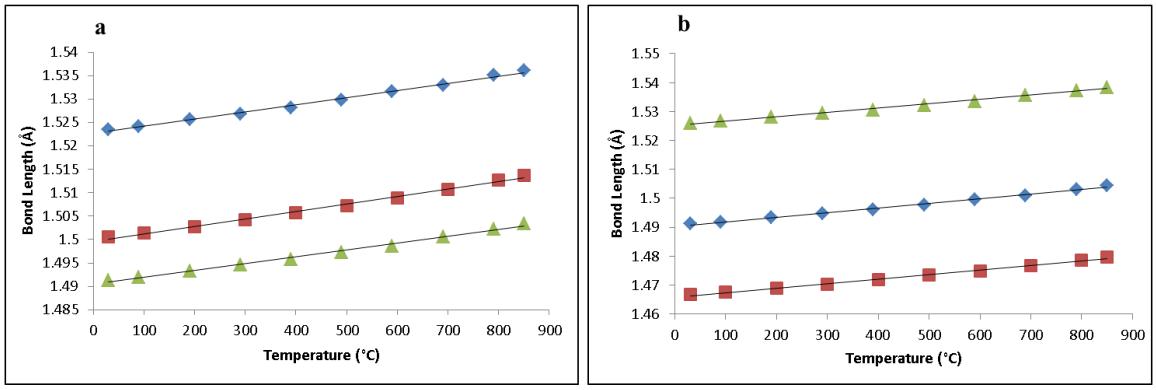


Figure 3.5: Intra-tetrahedral (a) B-O and (b) P-O distances as a function of temperature for $CaBPO_5$ (◊), $SrBPO_5$ (□), $BaBPO_5$ (Δ). Solid lines represent linear least squares fits to the data.

The temperature dependence of the inter-tetrahedral B-O-P bridging angle, θ and B-P nonbonded distances (figure 3.6) are shown in table 3.5 and figure 3.7.

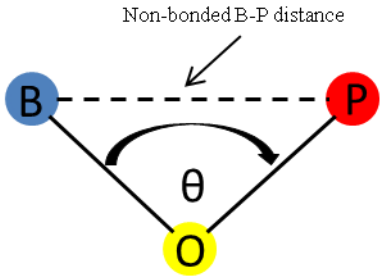


Figure 3.6: Representation of B-O-P bridging angle, θ and related nonbonded B-P distances in $ABPO_5$ compounds.

For all $ABPO_5$ compounds, the B-O-P bridging angle, θ shows little change with temperature, particularly for $SrBPO_5$ and $BaBPO_5$. Maximum variation of 0.035(59) ° was observed in $CaBPO_5$ over the entire temperature range. Furthermore, θ in $CaBPO_5$ is seen to decrease as a function of temperature from 125.76(84) ° (25 °C) to 125.73(65) ° (850 °C). The non-bonded B-P distances for all $ABPO_5$ materials are found to significantly increase respectively as a function of temperature. The coefficient of expansion in non-bonded B-P separations are:

$CaBPO_5$; 9.23 x 10^{-6}/°C, $SrBPO_5$; 10.7 x 10^{-6}/°C, $BaBPO_5$; 9.93 x 10^{-6}/°C. Therefore, the overall linear thermal expansion in each $ABPO_5$ material originates mainly from the increase in this non-bonded B-P distance as a function of temperature. For each compound, this B-P distance expansion extends uniformly along each crystallographic axis of the unit cell leading to the observed low anisotropic expansion.

It is concerning that for all $ABPO_5$ compounds; the B-O-P bridging angles remained largely unchanged as a function of temperature. It therefore follows that for all $ABPO_5$ compounds the B-O-P bridging angle should increase with temperature, this being accompanied by the corresponding increase in non-bonded B-P distance as a function of temperature (figure 3.6). In fact, the dilation of this B-O-P bond should be driven by the thermal vibration of the bridging oxygen atom. As the thermal vibration of the oxygen atom increases with an increase in temperature, this forces the B and P atoms to move further apart in order to adapt to the thermal motion of this atom. On this regard, the unexpected physical evolution of the B-O-P bridging angles in all investigated $ABPO_5$ compounds may be due to the false estimation of the thermal parameters in the refinement protocol. The refinement of a surface-roughness correction (using Suortti intensity correction) was attempted to correct for negative thermal parameters. However, these did not yield any improvement in the refinement of thermal parameters. Improvement of these parameters would probably require anisotropic displacement parameters from single-crystal diffraction. This analysis is beyond the scope of this work, and will be considered in future $ABPO_5$ family thermoresponsive investigations.

Table 3.5: B-O-P bridging angle (θ) and related non-bonded B-P distances as a function of temperature for $ABPO_5$ compounds.

	$CaBPO_5$		**$SrBPO_5$**		**$BaBPO_5$**	
Temperature (°C)	B···P (Å)	B-O-P (°)	B···P (Å)	B-O-P (°)	B···P (Å)	B-O-P (°)
30	2.735(21)	125.76(84)	2.715(54)	128.53(44)	2.802(48)	123.766(91)
100	2.736(29)	125.76(62)	2.716(82)	128.53(42)	2.803(81)	123.766(91)
200	2.738(51)	125.76(21)	2.719(35)	128.53(42)	2.806(11)	123.766(91)
300	2.740(63)	125.75(84)	2.721(91)	128.53(42)	2.808(69)	123.766(91)
400	2.742(71)	125.75(43)	2.724(74)	128.53(42)	2.811(04)	123.766(91)
500	2.745(39)	125.75(02)	2.727(49)	128.53(42)	2.813(94)	123.766(92)
600	2.748(36)	125.74(58)	2.730(42)	128.53(42)	2.816(57)	123.766(92)
700	2.750(77)	125.74(14)	2.733(94)	128.53(41)	2.820(38)	123.766(92)
800	2.754(11)	125.73(65)	2.737(43)	128.53(41)	2.823(23)	123.766(93)

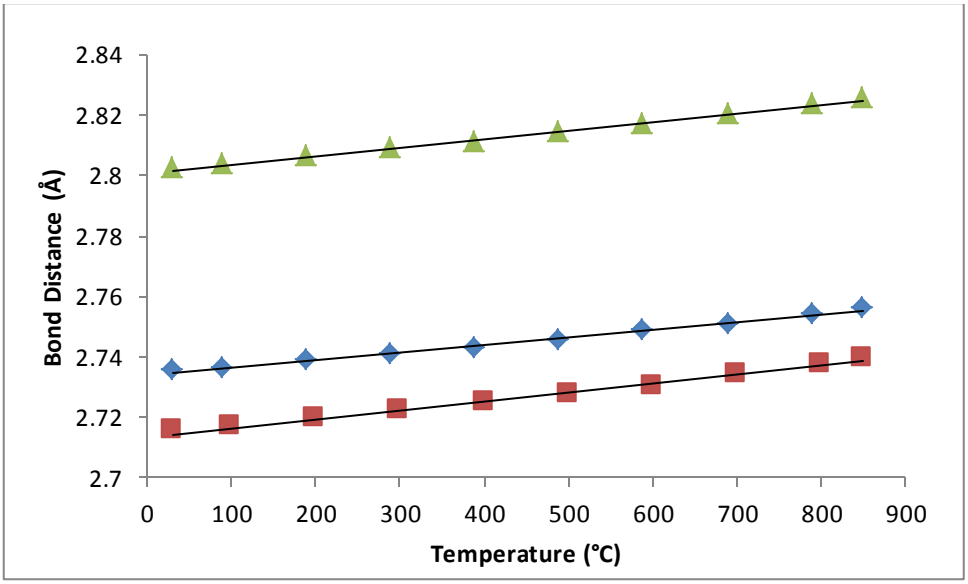


Figure 3.7: Variations of non-bonded B-P distances with temperature for $CaBPO_5$ (◊), $SrBPO_5$ (□), $BaBPO_5$ (Δ). Solid lines represent linear least squares fits to the data.

A close relationship exists between the interpolyhedral angle θ and thermal expansion behaviour of framework solids. For materials that have negative thermal expansion, the interpolyhedral angle θ varies between 150° to 170° [17, 27]. Materials with interpolyhedral angles lower than 150° [28] have low positive thermal expansion behaviour (as seen in the $ABPO_5$ materials). Generally, the smaller the interpolyhedral angle, the greater the values of thermal expansion coefficients.

IR study of ABPO5 (A = Ca, Sr, Ba) compounds.

FT-IR of the BPO_4 starting material and $ABPO_5$ compounds were recorded to confirm the presence of the inorganic anions (table 3.6). Results of previous vibrational spectra measurements published for borate, phosphate and $ABPO_5$ compounds were used to assign the measured spectra. PXRD analysis confirms that the $ABPO_5$ structure is composed of BO_4 and PO_4 units. The spectra of $ABPO_5$ compounds show the presence of absorption bands which can be assigned to the vibrational modes of these borate and phosphate units. The bands are found in two regions of the $ABPO_5$ spectra (1200 - 800 cm^{-1} and 800 - 550cm^{-1}). Generally, bands in the 1200 - 800 cm^{-1} region are characteristic of the tetrahedral borate and phosphate anion. Bands between 800-550 cm^{-1} regions were assigned to bending (B-O-P and O-P-O) and stretching (ν_{as} BOP and ν_s BOP) motions of the tetrahedral groups. Similarly for BPO_4, diffraction measurements showed that the structure of this material is composed of infinite BPO_7^{6-} units [28]. Therefore, the IR spectrum bands of this compound can be assigned to the vibrational modes of the BPO_7 group as labelled in table 3.6.

Table 3.6: Infrared band wavenumbers (cm^{-1}) and assignments for BPO_4 and $ABPO_5$ (A = Ca, Sr, Ba) compounds.

Assignment	BPO_4	$CaBPO_5$	$SrBPO_5$	$BaBPO_5$
ν P=O		1230, 1213	1216	
ν_3 (BO_4)		1185, 1120, 1100	1117	1197, 1022
ν_3 (PO_4)		1068	1051	1095
ν (BPO_7)	1091			
ν_1 (PO_4)		971	972	970
ν_1 (BO_4)		899	882	805, 748
ν_{as} (BOP)		841, 796	850, 800	
ν_s (BOP)		750, 700	749	750
δ (BOP)		673	655	653
δ (OPO)		588	561	570
ν (BPO_7)	630, 608, 560			
ν_4 (BO_4)		627, 517, 439	519, 466	614

3.4. Conclusion

From the results of this study, the observed low thermal expansion behaviour of the $ABPO_5$ compounds originates from changes in the crystal structure as a function of temperature. Of importance was the contribution of the bridging inter-tetrahedral bond angles and distances. Small changes in intra-tetrahedral B-O and P-O distances as a function of temperature suggest that BO_4 and PO_4 groups remain rigid with temperature. Cation size influence is seen as there is a sequential decrease in the volume thermal expansion coefficient as the size of the alkaline earth metal ionic radii size increased; $CaBPO_5$ α_v = 32.9 x 10^{-6}/°C, $SrBPO_5$ α_v = 32.5 x 10^{-6}/°C $BaBPO_5$ α_v = 29.9 x 10^{-6}/°C in the temperature range of 30 - 850 °C. Reliable refinement strategies applied to the $ABPO_5$ dataset are justified by smooth variation of the crystallographic parameters as a function of temperature together with low Rietveld estimated standard deviations.

3.5. References

[1] R. Kniep, H. Engelhardt, C. Hauf, *Chemistry of materials* 10 (1998) 2930-2934.

[2] B. Ewald, Y.X. Huang, R. Kniep, *Zeitschrift für anorganische und allgemeine Chemie* 633 (2007) 1517-1540.

[3] C.H. Park, Bluhm, K., *Z. Naturforsch.* 52b (1997) 102.

[4] R.P. Bontchev, S.C. Sevov, *Inorganic chemistry* 35 (1996) 6910-6911.

[5] A. Baykal, G. Gozel, M. Kizilyalli, M. Toprak, R. Kniep, *Turkish Journal of Chemistry* 24 (2000) 381-388.

[6] S. Pan, Y. Wu, P. Fu, G. Zhang, Z. Li, C. Du, C. Chen, *Chemistry of materials* 15 (2003) 2218-2221.

[7] Y. Shi, J. Liang, H. Zhang, Q. Liu, X. Chen, J. Yang, W. Zhuang, G. Rao, *Journal of Solid State Chemistry* 135 (1998) 43-51.

[8] A.B. Ali, E. Antic-Fidancev, B. Viana, P. Aschehoug, M. Taibi, J. Aride, A. Boukhari, *Journal of Physics: Condensed Matter* 13 (2001) 9663.

[9] C. Hauf, T. Friedrich, R. Kniep, *Zeitschrift für Kristallographie* (1995) pp. 446.

[10] R. Kniep, G. Gözel, B. Eisenmann, C. Röhr, M. Asbrand, M. Kizilyalli, *Angewandte Chemie* 106 (1994) 791-793.

[11] A. Callegari, G. Giuseppetti, F. Mazzi, C. Tadini, *NEUES JAHRBUCH FUR MINERALOGIE-MONATSHEFTE* (1992) 49-57.

[12] C.-J. Duan, W.-F. Li, X.-Y. Wu, H.-H. Chen, X.-X. Yang, J.-T. Zhao, *Journal of luminescence* 117 (2006) 83-89.

[13] A. Karthikeyani, R. Jagannathan, *Journal of luminescence* 86 (2000) 79-85.

[14] H. Bauer, *Zeitschrift für anorganische und allgemeine Chemie* 345 (1966) 225-229.

[15] R. Kniep, G. Gözel, B. Eisenmann, C. Röhr, M. Asbrand, M. Kizilyalli, *Angewandte Chemie* 106 (1994) 791-793.

[16] J.S. Evans, T. Mary, *International journal of inorganic materials* 2 (2000) 143-151.

[17] J. Evans, T. Mary, A. Sleight, *Journal of Solid State Chemistry* 137 (1998) 148-160.

[18] N. Khosrovani, V. Korthuis, A. Sleight, T. Vogt, *Inorganic chemistry* 35 (1996) 485-489.

[19] V. Korthuis, N. Khosrovani, A. Sleight, N. Roberts, R. Dupree, W.J. Warren, *Chemistry of materials* 7 (1995) 412-417.

[20] C.A. A., *Bruker AXS, Karlsruhe* (2007).

[21] G. Hölzer, M. Fritsch, M. Deutsch, J. Härtwig, E. Förster, *Physical Review A* 56 (1997) 4554.

[22] H. Schneider, E. Eberhard, *Journal of the American Ceramic Society* 73 (1990) 2073-2076.

[23] W. Dreyer, *Materialverhalten anisotroper Festkorper: thermische und elektrische Eigenschaften. Ein Beitrag zur Angewandten Mineralogie*. Springer, 1974.

[24] R.t. Shannon, *Acta Crystallographica Section A: Crystal Physics, Diffraction, Theoretical and General Crystallography* 32 (1976) 751-767.

[25] R. Diehl, G. Brandt, *Acta Crystallographica Section B* 31 (1975) 1662-1665.

[26] P. Moore, *American Mineralogist* 57 (1972) 1333-&.

[27] J.S.O. Evans, T.A. Mary, A.W. Sleight, *Journal of Solid State Chemistry* 133 (1997) 580-583.

[28] S. Achary, A. Tyagi, *Journal of Solid State Chemistry* 177 (2004) 3918-3926.

Chapter 4 Hydrothermal synthesis, crystal structure and thermodiffractometry study of zeolite borophosphates $M^{I}_{x}M^{II}_{z}(H_2O)_2[BP_2O_8].zH_2O$ (M^{I} = Na, NH_4 and M^{II} = Mn, Co) with CZP topology

M. W. Mogodi[a], M. A. Fernandes[b], D. G. Billing[a]*

[a]School of Chemistry and DST/NRF Centre of Excellence in Strong Materials, University of the Witwatersrand, Private Bag 3, WITS, 2050, South Africa.

[b]Molecular Sciences Institute, School of Chemistry, University of the Witwatersrand, PO Wits, 2050, South Africa.

*Corresponding author: Professor David Billing

School of Chemistry,

University of the Witwatersrand,

Private Bag 3, WITS, 2050, South Africa

Email: dave.billing@wits.ac.za

Tel no : +27 11 717 6759

Fax no: +27 11 717 6749

This chapter has been submitted to Inorganic Chemistry and has been structured according to the journal's format.

Abstract

Open framework compounds; sodium-metal borophosphate hydrate $NaM^{II}(H_2O)_2[BP_2O_8](H_2O)$; M^{II} = Co (**I**), Mn (**II**) and ammonium-metal borophosphate hydrate $(NH_4)_{0.5}M^{II}_{1.25}(H_2O)_2[BP_2O_8].(H_2O)_{0.5}$; M^{II} = Co (**III**), Mn (**IV**) have been prepared under mild hydrothermal conditions (at 180 °C). Rietveld refinement of laboratory powder X-ray diffraction (PXRD) data and supplementary Fourier Transform Infrared Spectroscopy (FTIR) data collected at room temperature have been used to determine the crystal structures of the investigated compounds. Compounds **I** and **II** crystallize in the $P6_122$ (No. 178) space group with Z = 4 belong to the hexagonal system, whereas compounds **III** and **IV** crystallize in the $P6_5$ (No. 170) space group with Z = 4 also belong to the hexagonal system. The unit cell parameters obtained were: for **I**; a = 9.4565(2) Å, b = 15.8406(9) Å, V = 1226.78(2) $Å^3$, for **II**; a = 9.5915(9) Å, c = 15.9619(8) Å, V = 1271.74(1) $Å^3$, for **III**; a = 9.4970(3) Å, c = 15.6079(7) Å, V = 1219.13(9) $Å^3$, for **IV**; a = 9.6360(2) Å, c = 15.8647(1) Å, V = 1275.73(1) $Å^3$. The influence of the ionic radii of the M^{II} cations on the unit cell parameters of the isostructural (and overall) phases was also established. The crystal structure of the four phases consists of an anionic framework structure $\infty[BP_2O_8]^{3-}$, composed of corner sharing BO_4 and PO_4 tetrahedra. The water molecules in all compounds are found within the helical channels running along [001] direction. Differences in the coordination number and geometry, occupancy and positioning of the charge balancing M^I and M^{II} species within the respective crystal framework structure are presented. The thermoresponsive behaviour of the phases was characterised by variable temperature PXRD and TGA experiments. The title compounds each undergo a series of dehydration steps (and deammoniation for compounds **III** and **IV**) with similar dehydration behaviour being observed among the isostructural phases. The high temperature dehydration products were identified by the powder diffraction measurements.

4.1. Introduction

The synthesis of crystalline open framework and microporous materials has attracted great attention due to the possibility of obtaining a large diversity of aesthetically interesting crystal structures with varied potential applications in fields such as catalysis, storage, separation and ion-exchange. The characteristic size and shape of the internal pores as well as interactions of the host structure and guest molecules are important factors in microporous materials. Aluminosilicate zeolites are an established class of microporous materials consisting of 176 unique zeolite framework structures [1]. These 176 framework structures form the basis of a three letter code systematic description of zeolite framework structures which have been approved by the Structure Commission of the International Zeolite Association IZA (IZA-SC).

The CZP (chiral zincophosphate) zeolite framework topology is characterised by tetrahedral groups forming one-dimensional chiral helical chains, in which all tetrahedral vertices are shared. The building unit of this framework is 4-ring repeat 'squares' which link up to form spirals of 4-rings [1, 2]. This chiral anionic helical network reveals porous openings running parallel to the spiral axis. Extra framework cations and water molecules are often located in these channels and function to stabilise the framework and provide charge balance. A characteristic feature of materials with CZP framework type is that they crystallize in one of the hexagonal space groups. Examples of materials with the CZP framework are the sodium zincophosphates $NaZnPO_4.H_2O$ [2] and its cobalt substituted phase [3, 4], amine-templated metal gallophosphate $(H_3DETA)_2(H_2O)_{12}[Mn_6Ga_6P_{12}O_{48}]$ [5] and a large series of borophosphates and metalloborophosphates with a B : P = 1:2 ratio with the general formula: $M^I_xM^{II}_z(H_2O)_2[BP_2O_8].zH_2O$ (M^I = Li, Na, K, NH_4; M^{II} = Mn, Fe, Co, Ni, Zn, Cd; x = 0.5 – 1.0) [6-10] as well as $M^{III}(H_2O)_2[BP_2O_8].H_2O$ (M^{III} = Sc, Fe, In) [11-13]. Due to the chiral topology of these materials, one can envision possible uses in enantioselective separations and synthesis and various catalytic roles.

The variety of cations in the borophosphate hydrate phases mentioned above include acting to charge balance the negative charge of the $[BP_2O_8^{3-}]$ anion and control the channel size created by the helices. The latter effect results from varying the ionic radii of the M^I cations. The dehydration of the chiral open framework borophosphate structures has displayed some very interesting observations. For example, $NaZn(H_2O)_2[BP_2O_8].H_2O$ reversibly dehydrates to form a microporous $Na[ZnBP_2O_8].H_2O$ phase which also has CZP topology [7]. Moreover,

the dehydration process in these spiral compounds is further complicated by the presence of two chemically distinct types of water in the crystal structures. Here we report on the hydrothermal synthesis, crystal structure and variable temperature X-ray powder investigations of the borophosphates $NaM^{II}(H_2O)_2[BP_2O_8].(H_2O)$; M^{II} = Co (**I**), Mn (**II**) and $(NH_4)_{0.5}M^{II}_{1.25}(H_2O)_2[BP_2O_8].(H_2O)_{0.5}$; M^{II} = Co (**III**), Mn (**IV**).

4.2. Experimental

4.2.1. Synthesis

All reagents were purchased from Merck/Sigma-Aldrich and were used as received.

$NaM^{II}(H_2O)_2[BP_2O_8].(H_2O)$; M^{II} = Co (**I**), Mn (**II**).

The compounds **I** and **II** were synthesized under mild hydrothermal conditions. A starting mixture of 0.0285 mol $M^{II}Cl_2.6H_2O$ (M^{II} = Co (6.781 g), Mn (7.173 g)), 3.524 g (0.00924 mol) of $Na_2B_4O_7.10H_2O$, 4.0 ml (0.00791 mol) of 80 % H_3PO_4 and 10 ml of H_2O was prepared under stirring. With continuous stirring and applying heat at approximately 80 °C, the mixture was eventually homogenous. The resulting homogenous gel was transferred into an 18 ml Teflon digestion bomb (degree of filling ≈ 70 %) and heated at 180 °C under autogenous pressure for 3 days. After cooling to room temperature, the solid products were recovered by vacuum filtration, washed with water and dried in air for 1 day at 50 °C. For compound **I** a purple coloured powder was formed. For compound **II** a white coloured powder sample was formed.

$(NH_4)_{0.5}M_{1.25}(H_2O)_2[BP_2O_8].(H_2O)_{0.5}$; M^{II} = Co (**III**), Mn (**IV**).

In a typical experiment a mixture of 0.0285 mol of $M^{II}Cl_2.6H_2O$ (M^{II} = Co (6.781 g), Mn (7.173 g), 7.550g (0.0570 mol) of $(NH_4)_2HPO_4$, 3.524g (0.0570 mol) of H_3BO_3 and 4.6 ml (0.0791 mol) of 80 % H_3PO_4 were added to 10 ml of water with stirring. The mixture was heated at approximately 80 °C to allow water to evaporate until a viscous gel was obtained. The resulting homogenous gel was transferred into an 18 ml Teflon digestion bomb (degree of filling ≈ 70 %) and heated at 180 °C under autogenous pressure for 3 days. Following

cooling to room temperature, the solid products were recovered by filtration, washed with water and dried in air for 1 day at 50 °C. For compound **III** a purple coloured powder was obtained. For compound **IV** a white coloured powder sample was obtained.

4.2.2. FTIR Spectroscopy

FTIR spectra (appendix A2.2) were recorded on a Bruker Tensor 27 Fourier Transform Infrared spectrometer in the range of 4000 to 600 cm^{-1}. FTIR spectra of the compounds were recorded to confirm the presence of the inorganic borate and phosphate groups, water molecules and the framework charge balancing NH_4^+ (found exclusively in compounds **III** and **IV**). The spectra of the studied compounds show similar absorption bands (with the exception of bands arising from NH_4^+ in compounds **III** and **IV**) and can be divided into three regions:

(1) High frequency bands observed in the region 3600 – 1200 cm^{-1}. These confirm the presence of O-H and N-H moieties.
(2) Bands in the 1200 – 954 cm^{-1} region which are related to internal modes of phosphate and borate ions.
(3) Below 954 cm^{-1} attributed to additional borate internal modes.

These important bands are listed in table 4.1.

Table 4.1: Selected IR bands for compounds **I**, **II**, **III** and **IV**.

Assignments	I	II	III	IV
O – H stretches	3357	3375	3469	3452
ν_3 (N – H)	-	-	3233	3215
ν_4 (N – H)	-	-	1432	1419
O – H deformation	1652	1656	1629	1637

ν_3 (BO_4)	1143	1141	1143	1130
ν_1 (PO_4)	945	945	945	947
ν_1 (BO_4)	858	840	848	837
ν_4 (BO_4)	686, 644	678, 642	675, 634	669, 630

4.2.3. Thermogravimetric analysis (TGA)

Thermogravimetric analysis (TGA) experiments were conducted under N_2 in a Perkin Elmer STA 6000 instrument. Samples of approximate weight 10 mg were placed in aluminium crucibles. The thermal behaviour of the materials were investigated between room temperature and 900 °C at heating rates of 10 °C min^{-1}.

4.2.4. Scanning electron micrograph (SEM)

SEM images of compound **I**, **II**, **III** and **IV** were performed on a FEI Nova Nanolab 600 FIB/SEM. The compounds have hexagonal bipyrimidal shaped single crystals which were about 5 to 10 μm in size (figure 4.1).

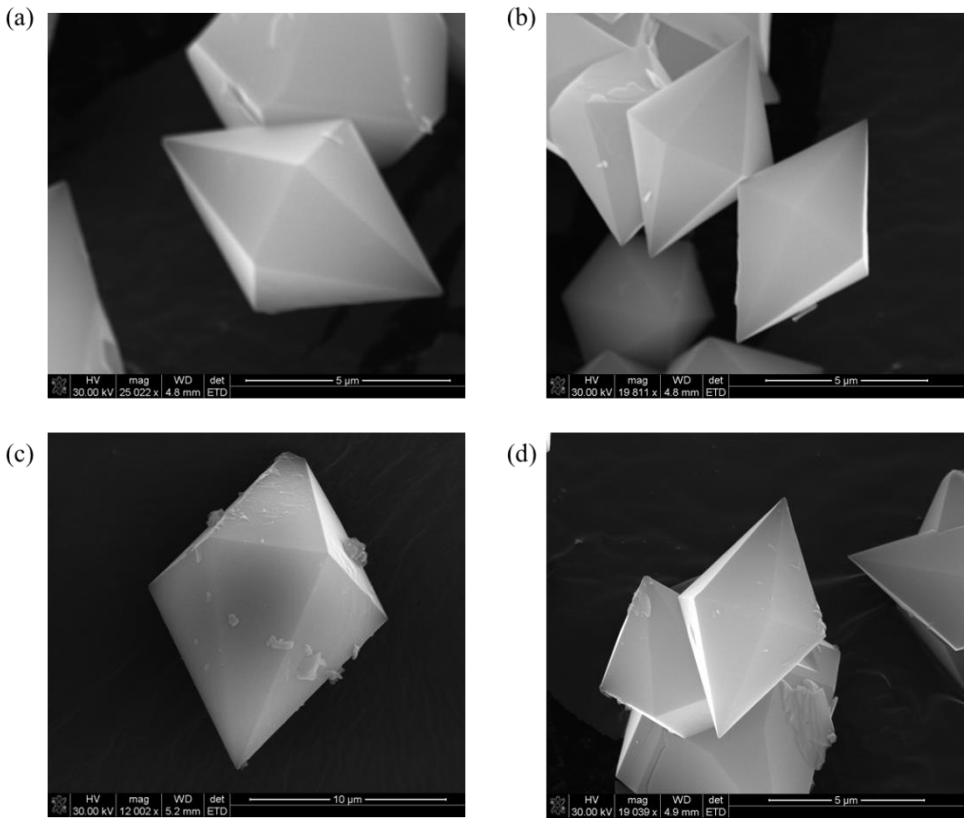


Figure 4.1: SEM images of the as-synthesized (a) sample **I**, (b) sample **II** (c) sample **III** and sample **IV**.

4.2.5. Powder X-ray diffraction (PXRD)

The crystal structures of the obtained products were confirmed by the Rietveld refinement of powder X-ray diffraction (PXRD) data collected at room temperature. The powder X-ray diffraction data of compound **I**, **II**, **III** and **IV** were collected on a Bruker D8 Advance diffractometer equipped with a Cu $K_{\alpha1}/K_{\alpha2}$ X-ray source; λ = 1.5406/1.54439 Å (operated at 40 kV and 40 mA) and a Bruker VÅNTEC-1 PSD detector. The Rietveld refinement protocol was performed using the program TOPAS (Total pattern analysis solution) version 4.2 package [14]. The starting models for the Rietveld refinements for compound **I** were retrieved from structures by Kniep *et al.* [6], compound **II** from Kniep *et al.* [6] and Boy *et al.* [7], compound **III** from Schafer *et al.* [9] and compound **IV** from Schafer *et al.* [9]. In a typical Rietveld refinement of the title compounds, $CuK_{\alpha1}/K_{\alpha2}$ emission profile taken from Hölzer *et al.* (1997) [15] were used, one histogram scale factor, Chebychev background polynomial terms and lattice parameters were initially varied. Four profile variables of the

pseudo-Voigt profile function were refined. The specimen displacement, LP factor and crystallite size broadening terms of a Lorentzian profile were also included into the refinement. The preferred orientation was modeled by a Spherical Harmonics function, followed by the fractional atomic coordinates and thermal parameters being refined. Details concerning the data collection and structure refinement for the title compounds are shown table 4.2. Graphical outputs of the structure refinement are shown in figure 4.2 (compounds **I** and **II**) and figure 4.3 (compound **III** and **IV**). The challenge with refining the crystal structure of the investigated compounds included the unambiguous assignment of the configuration on the enantiomeric space group. That is, compounds **I** and **II** can be refined in either the enantiomeric space groups $P6_122$ or $P6_522$, and compounds **III** and **IV** can be refined in either the enantiomeric space groups $P6_1$ or $P6_5$. The difference between the enantiomeric space groups is the handedness of the six fold screw axis. Resolution of this would require the refinement of the Flack parameter of a single crystal dataset. Since this work was restricted to powder diffraction, due to lack of having grown large enough, high quality single crystals, the crystal structures were refined from models obtained in literature. Therefore, discerning the space groups for the respective compounds was accomplished by monitoring the figures of merit and observing which space group configuration resulted in a better fit to the powder diffraction raw data. Therefore when space group $P6_522$ was adopted, compound **I** had Rwp and χ^2 values of 8.79 and 2.53, whereas compound **II** had Rwp and χ^2 values of 7.30 and 4.80. When space group $P6_1$ was adopted, compound **III** had Rwp χ^2 values 15.7 and 6.67, whereas compound **IV** had Rwp and χ^2 values of 4.90 and 3.04. It is also noted that the refined isotropic thermal parameters for Na and O_{6H2O} in the crystal structures of **I** and **II** were unusually large. Similarly large thermal parameters were obtained in the Rietveld refinement of the $NaZn(H_2O)_2[BP_2O_8]H_2O$ structure [7] of PXRD data. In the paper of the $NaZn(H_2O)_2[BP_2O_8]H_2O$ structure, the authors point out that the observed large displacement parameters (which were also obtained in the SCXRD data), resulted from weak bonding interactions among the coordination environments. During the Rietveld refinement conducted for this work, the isotropic thermal parameters for compounds **III** and **IV** were fixed.

The thermal behaviour of the samples was also studied using variable-temperature powder X-ray diffraction (VT-PXRD) in the temperature range of room temperature to 860 °C. These high temperature experiments were carried out in an Anton Paar XRK 900 furnace with a Macor® ceramic sample holder. Unfortunately detailed structural information of each

compound as a function of temperature could not be retrieved due to the low-quality individual datasets collected for each sample. However, the data quality was sufficient to provide reliable estimation of the lattice changes (unit cell parameters), and qualitative information of the evolved phases as a function of temperature.

The crystal structure drawings were generated using the Diamond Version 3.2g program [16].

Table 4.2: Crystallographic data and Rietveld refinement details for compounds **I**, **II**, **III** and **IV** at 30 °C.

Compound	**I**	**II**	**III**	**IV**
Formula	$NaCo(H_2O)_2[BP_2O_8](H_2O)$	$NaMn(H_2O)_2[BP_2O_8](H_2O)$	$(NH_4)_{0.5}Co_{1.25}(H_2O)_2[BP_2O_8](H_2O)_{0.5}$	$(NH_4)_{0.5}Mn_{1.25}(H_2O)_2[BP_2O_8](H_2O)_{0.5}$
Molecular Weight (g mol^{-1})	336.72	332.73	328.48	323.48
Crystalline system	Hexagonal	Hexagonal	Hexagonal	Hexagonal
Space group (No.)	$P6_122$ (No. 178)	$P6_122$(No. 178)	$P6_5$ (No. 170)	$P6_5$ (No. 170)
a (Å)	9.4565(2)	9.5915(9)	9.4970(3)	9.6360(2)
c (Å)	15.8406(9)	15.9619(8)	15.6079(7)	15.8647(1)
V ($Å^3$)	1226.78(2)	1271.74(1)	1219.13(9)	1275.73(1)
Z	4	4	4	4
Calc. density p (g cm^{-3})	2.691	2.560	2.619	2.467
Data range θ (°)	10 - 100	10 - 100	10 - 100	10 - 100
Rexp (%)	3.47	1.52	2.34	1.60
Rwp (%)	4.24	2.22	5.87	2.37
χ^2 - GOF	1.22	1.46	2.51	1.48

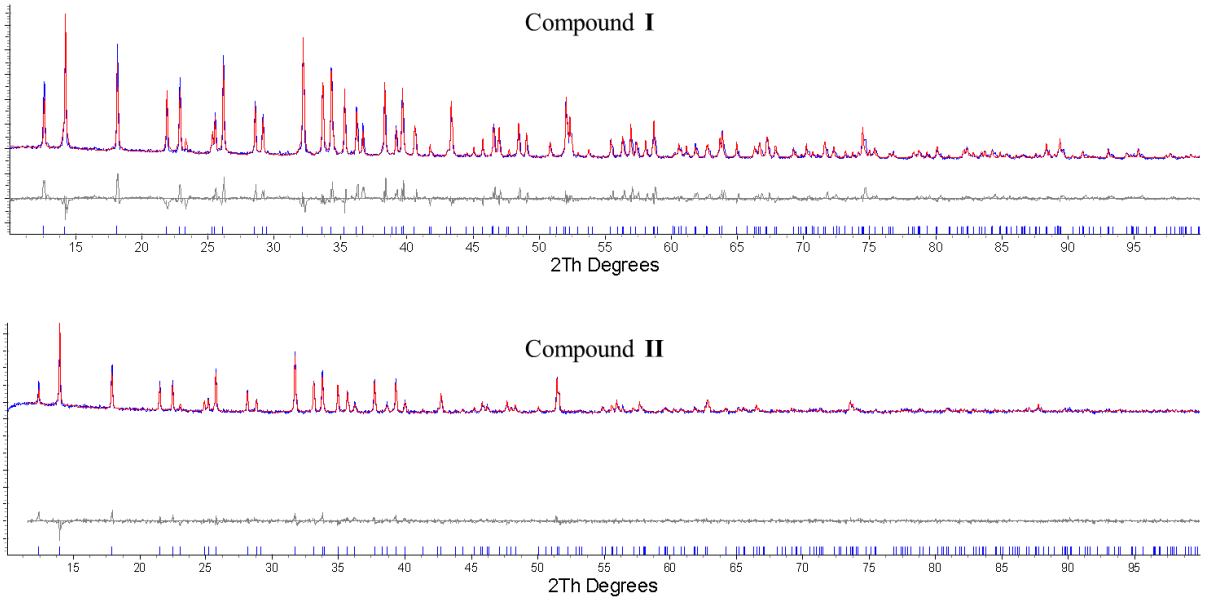


Figure 4.2: Observed (blue), calculated (red) and difference (grey) PXRD patterns of compound **I** and **II** refined at 30 °C. Lower ticks are the expected Bragg peak position.

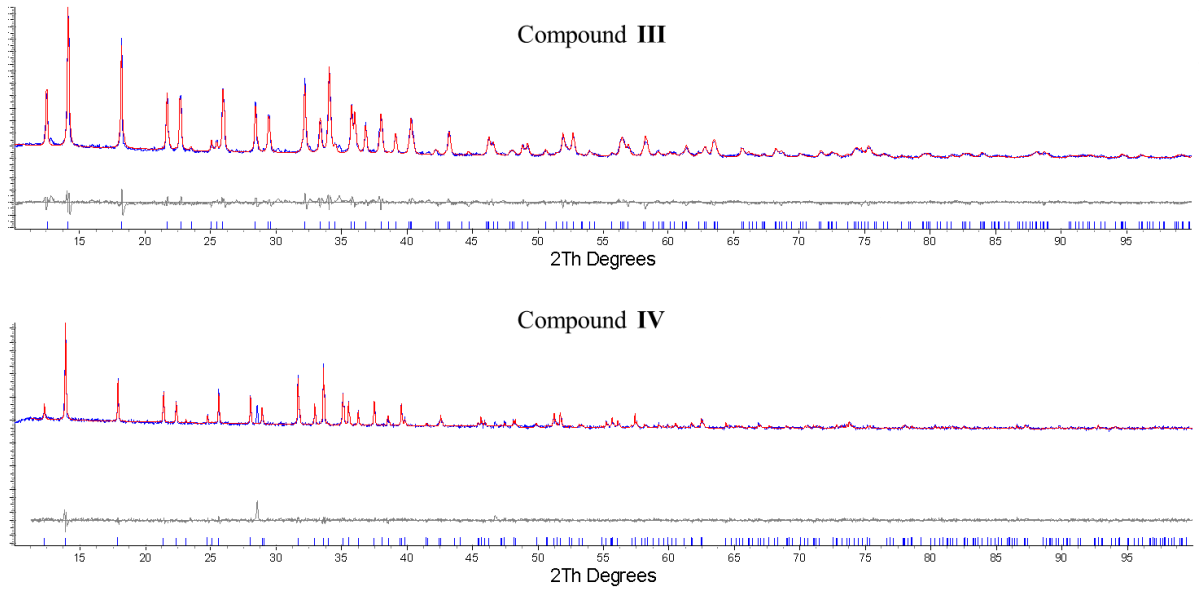


Figure 4.3: Observed (blue), calculated (red) and difference (grey) PXRD patterns of compound **III** and **IV** refined at 30 °C. Lower ticks are the expected Bragg peak position.

4.3. Results and discussion

4.3.1. General description of the anionic unit, $\infty^1[BP_2O_8]^{3-}$.

The crystal structures of the chiral compounds (**I-IV**) is composed of single borophosphate helical chains $\infty[BP_2O_8]^{3-}$ which have a left- or right- handed six fold screw-axis (6_1 or 6_5 helix), and therefore crystallize in chiral space groups $P6_122$ or $P6_5$. The anionic partial structure, $\infty[BP_2O_8]^{3-}$, is made up from corner-sharing alternating boron $[BO_4]^{3-}$ and phosphorous $[PO_4]^{3-}$ tetrahedra. The chains can be further broken down into their fundamental building unit (FBU), a hexameric open-branched chain of alternating BO_4 and PO_4 groups (figure 4.4). The spiral chain has each boron tetrahedron sharing all bridging oxygen atoms with phosphorous tetrahedra. In turn, the phosphate tetrahedra which occupy the edge of the ribbon, share only two oxygen atoms with the borate tetrahedra and the remaining two terminal oxygen atoms serve as ligands to coordinate the M^{2+} metal ions.

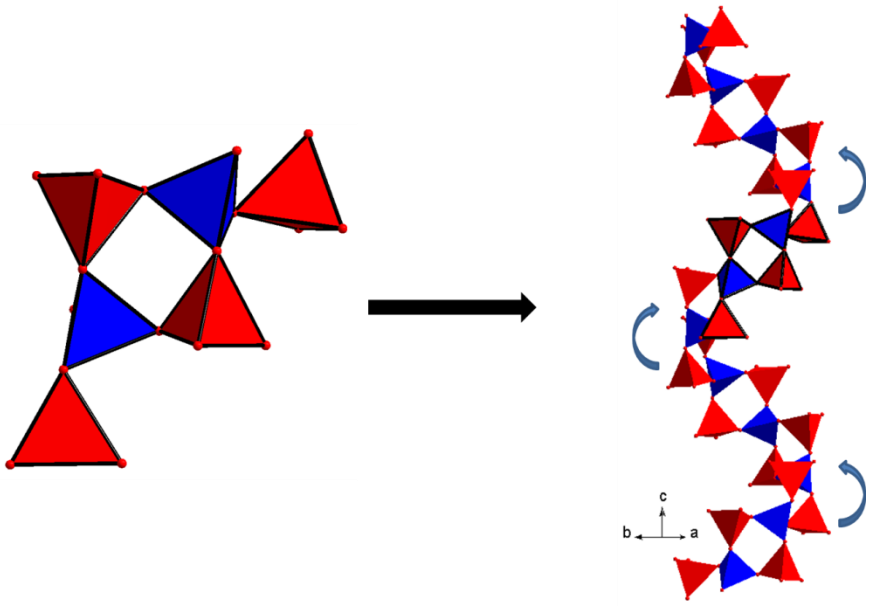


Figure 4.4: One-dimensional infinite loop-branched borophosphate helices (right), $\infty^1[BP_2O_8]^{3-}$, propagating along [001] formed from the FBU, an open-branched chain (left). BO_4 (blue) and PO_4 (red) tetrahedra.

The $M^{2+}(O_{PO4})_4(OH_2)_2$ coordination octahedra has four oxygen atoms from phosphate units and two from coordinating water molecules. The $M^{2+}(O_{PO4})_4(OH_2)_2$ octahedra interconnect the borophosphate helices to form a three-dimensional helix, $\infty^1\{M^{II}(H_2O)_2[BP_2O_8]^{3-}\}$ (figure 4.5). The central pores of the helix are filled with hydrate water molecules ($O6_{H2O}$) which hydrogen bond to each other.

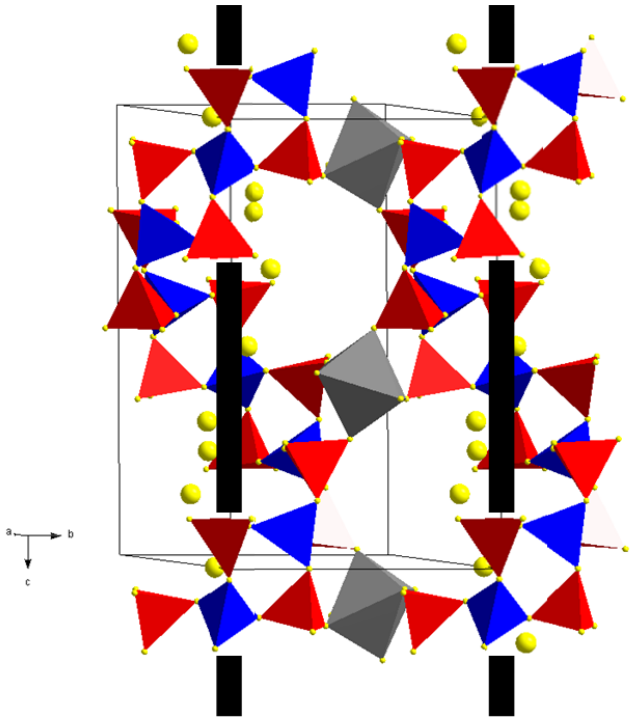


Figure 4.5: Two helical borophosphate chains composed of tetrahedral units, $\infty[BP_2O_8]^{3-}$, wound around a six-fold screw axis (black rod) located at the corners of the unit cell. $M^{2+}(O_{PO4})_4(OH_2)_2$ grey octahedra link the helices. BO_4 (blue), PO_4 (red) tetrahedra and a helix of hydrate water ($O6_{H2O}$) yellow spheres.

The crystal structures of the borophosphate hydrate structural family discussed above - $M^IM^{II}(H_2O)[BP_2O_8].zH_2O$ (M^I = Li, Na, K, NH_4; M^{II} = Mn, Fe, Co, Ni, Zn, Cd; x = 0.5 – 1.0) [6-10] - show structural similarity. Deviations in this structural family arise with the influence of the size of the monovalent M^I positive charge and its occupancy within the thread of the borophosphate spiral. The small M^I metals (Li^+ and Na^+ in compound **I** and **II**) which are structurally similar to the aristotype structure, $NaZn(H_2O)_2[BP_2O_8].H_2O$ [7], have the free loops of the borophosphate helices being fully occupied by the M^I cations (coordinated by

eight O_2 atoms, $M^{I}(O_{PO4})_6(OH_2)_2$) and have a fully ordered arrangement of water molecules within the helical channels (figure 4.6a). However, both positional and occupational disorder of the M^{I}, M^{II} and hydrated H_2O species is manifested in the crystal structures of the larger ionic radii of NH_4^+. In the crystal structure of compounds **III** and **IV**, the larger NH_4^+ ions are pushed within the spiral channels, with fractional occupancy at the sites of these species. Therefore, additional trigonal bipyramidal $M^{2+}(O_{PO4})_2(OH_2)_3$ units are included for charge stability within the borophosphate spirals, in order to compensate for the compromised charge stability from occupationally limited NH_4^+ species (figure 4.6b). The occupancy at the sites of these species has been fixed to 0.5 (H_2O), 0.5 (NH_4^+) and 0.25 (Co2) during the Rietveld refinement protocol.

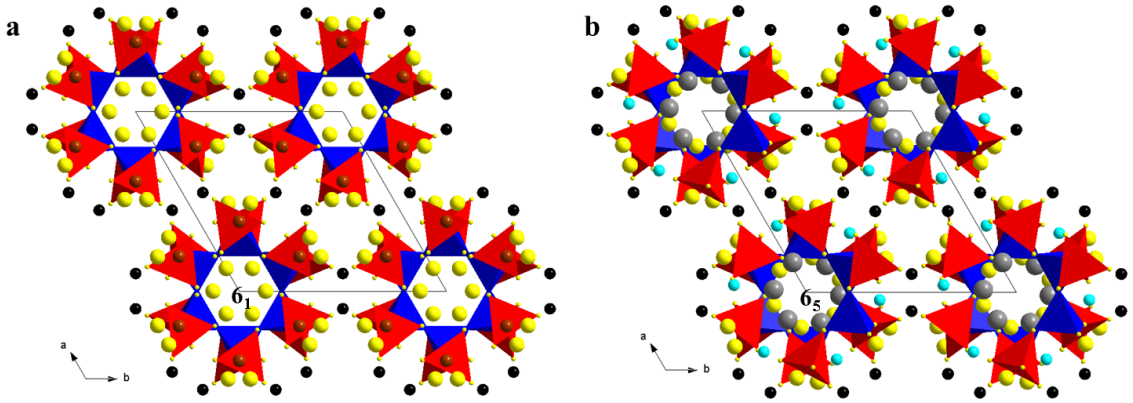


Figure 4.6: The crystal structures of compounds (a) **I**, **II** and (b) **III**, **IV** viewed along the *c*-axis. BO_4 (blue), PO_4 (red) tetrahedra, H_2O (yellow) spheres, M^{2+} (black) octahedra and additional M^{2+} trigonal bipyramidal (turquoise) site in (b). M^{1+} sites as Na^+ (brown) spheres in (a) and NH_4^+ (grey) spheres in (b).

4.3.2. Crystal structure of $NaM^{II}(H_2O)_2[BP_2O_8](H_2O)$; M^{II} = Co (I), Mn (II).

The compounds (**I**, *sodium-cobalt borophosphate hydrate and* **II**, *sodium-manganese borophosphate hydrate*) are isostructural to each other, and crystallize in the hexagonal space group $P6_122$. The asymmetric unit contains 10 independent atoms including one unique M^{2+} (Co or Mn) atom, one P atom, one B atom and five O atoms as well as one O_{H2O} (O6) non-framework atom. The results are listed in table 4.3 and 4.5, with the selected bond lengths and angles given in table 4.4 and 4.6, for compounds **I** and **II**, respectively. In both

compounds, the BO_4 and PO_4 interatomic distances and angles of the tetrahedral spiral $\infty^1[BP_2O_8]^{3-}$ lie within the expected values for borophosphates [6, 17]. The mean M^{2+}-O bond lengths in the metal octahedral coordination environment are 2.1686 Å (**I**-Co) and 2.1960 Å (**II**-Mn). The mean bond distances correlate with the relative sizes of the respective metal ionic radius in octahedral environment viz. Co^{2+} (0.65 Å) and Mn^{2+} (0.67 Å) [18]. The water molecules within each compound form hydrogen bonds with each other along the helix ($O6_{H2O}\cdots O6_{H2O}$ 2.8976 Å (**I**) and $O6_{H2O}\cdots O6_{H2O}$ 2.9247 Å (**II**)).

Table 4.3: Atomic coordinates (x, y, z), occupancy factors (occ) and isotropic temperature factors (Beq, $Å^2$) for **I**.

Atom	x	y	z	Occ	Beq
Na	0.1939	0.3878	0.25	1	0.249
Co	0.5569	0.1039	0.25	1	0.0392
P	0.38594	0.16389	0.41712	1	0.0392
B	0.8493	0.6986	0.25	1	0.067
O1	0.21501	0.02064	0.40423	1	0.035
O2	0.47561	0.12825	0.39029	1	0.044
O3	0.37929	0.26628	0.37946	1	0.054
O4	0.4159	0.18307	0.52167	1	0.036
O5	0.30935	0.48808	0.11525	1	0.064
O6	0.12395	0	0	1	0.471

Table 4.4: Selected interatomic distances (Å) and angles (°) for **I**.

Co	O3	2.1068(1)	(2x)	O2	Co	O5	84.310(5)	(4x)
	O2	2.1286(1)	(2x)	O3	Co	O5	131.969(5)	(4x)
	O5	2.2705(1)	(2x)	O3	Co	O2	95.359(5)	(4x)
Average	Co-O	2.1686		O3	Co	O3	95.253(1)	
				O2	Co	O2	164.133(2)	
Na	O5	2.3826(1)	(2x)	O5	Co	O5	88.280(1)	
P	O2	1.4436(0)		O5	Na1	O5	136.746(2)	
	O3	1.4643(0)						
	O4	1.5684(1)		O2	P	O3	117.684(2)	
	O1	1.5704(0)		O2	P	O4	107.521(2)	
				O2	P	O1	110.803(2)	
B	O4	1.3821(0)	(2x)	O3	P	O4	111.401(2)	
	O1	1.5407(0)	(2x)	O3	P	O1	104.387(2)	
				O4	P	O1	104.243(2)	
O4	B	O4	111.947(2)					
O1	B	O1	112.051(2)	(4x)				
O1	B	O1	95.238(2)					

Table 4.5: Atomic coordinates, occupancy factors and isotropic temperature factors ($Å^2$) for **II**.

Atom	x	y	z	Occ	Beq
Na	0.1913	0.3826	0.25	1	0.248
Mn	0.5497	0.0994	0.25	1	0.0394
P	0.3917	0.1694	0.4144	1	0.0395
B	0.8395	0.679	0.25	1	0.067
O1	0.2147	0.0206	0.4013	1	0.035
O2	0.5123	0.1353	0.379	1	0.044
O3	0.3837	0.3096	0.3808	1	0.054
O4	0.4155	0.1815	0.5127	1	0.037
O5	0.2985	0.4899	0.1138	1	0.065
O6	0.1267	0	0	1	0.476

Table 4.6: Selected interatomic distances (Å) and angles (°) for **II**.

Mn	O3	2.1312(1)	(2x)	O2	Mn	O5	84.096(5) (4x)
	O2	2.1483(1)	(2x)	O3	Mn	O5	131.855(5) (4x)
	O5	2.3097(1)	(2x)	O3	Mn	O2	95.528(5) (4x)
Average	Mn-O	2.1960		O3	Mn	O3	95.546(1)
				O2	Mn	O2	163.580(2)
Na	O5	2.3893(1)	(2x)	O5	Mn	O5	87.947(1)
P	O2	1.4847(0)					
	O3	1.5084(1)		O5	Na	O5	138.425(2)
	O4	1.5555(0)					
	O1	1.5676(1)		O2	P	O3	115.071(2)
				O2	P	O4	107.013(2)
B	O4	1.4941(0)	(2x)	O2	P	O1	111.847(2)
	O1	1.4585(1)	(2x)	O3	P	O4	110.765(2)
				O3	P	O1	105.177(2)
O4	B	O4	101.273(2)	O4	P	O1	106.714(2)
O4	B	O1	112.801(2) (4x)				
O1	B	O1	104.677(2)				

4.3.3. Crystal structure of $(NH_4)_{0.5}M^{II}_{1.25}(H_2O)_2[BP_2O_8].(H_2O)_{0.5}$; M^{II} = Co (III), Mn (IV)

The borophosphates **III** (*ammonium-cobalt borophosphate hydrate* and **IV**, *ammonium-manganese borophosphate hydrate*) are isostructural to each other, and crystallize in the hexagonal space group $P6_5$. The atomic coordinates of the independent atoms in the crystal structures are given in table 4.7 and 4.9, and selected bond lengths and angles are listed in table 4.8 and 4.10, for compounds **III** and **IV**, respectively. In contrast to the crystal structures of compounds **I** and **II**, the borophosphate helix $\infty^1[BP_2O_8]^{3-}$ has slightly distorted BO_4 and PO_4 tetrahedra, as evidenced by the broader spread of interatomic bond lengths and angles i.e. **I**: B-O: 1.3821(0) – 1.5407(0) Å; P-O: 1.4436(0) – 1.5704(0) Å and O-B-O: 95.238(2) - 112.051(2) ° vs **III** B-O: 1.4411(8) – 1.7695(1) Å, P-O: 1.4166(3) – 1.6177(5) Å and O-B-O: 93.843(6) - 118.628(6) °. Another distinct difference in the crystal structures of compounds **I** and **II** vs **III** and **IV** is the arrangement in and around the spiral framework. When the spiral framework is viewed along the [001] direction (figure 4.6), differences in the polyhedral layers propagating radially from the central screw axis are observed. The crystal

structures extend as follows (e.g. for compounds **I** vs **III**): central hydrate O_{H2O} helix (**I**, diameter ≈ 8.2702 Å) vs hydrate O_{H2O} helix (**III**, diameter ≈ 8.2732 Å) and statistically occupied N_{NH4+} (**III**, diameter ≈ 8.3536 Å). Therefore, the hydrate O_{H2O} helix in compound **III** extends slightly further from the channel axis than the hydrate O_{H2O} helix in compound **I.** Next is the borate helix (**I**, diameter ≈ 9.500(9) Å and **III**, diameter ≈ 9.113(0) Å) then the phosphate helix (**I**, diameter ≈ 10.198(8) Å vs **III**, diameter ≈ 10.098(6) Å), followed by eight coordinated M^{1+} polyhedra (exclusive to **I** and **II**, diameter ≈ 10.093(5) Å) and the additional trigonal bipyramidal $M^{2+}(O_{PO4})_2(OH_2)_3$ layer (exclusive to compounds **III** and **IV**, diameter ≈ 10.104(7) Å). Lastly is the $M^{2+}(O_P)_4(O_{H2O})_2$ layer (**I**, diameter ≈ 12.4343 Å and **III**, diameter ≈ 12.2369 Å). These values were calculated by measuring the interatomic distances between the central atoms of each of the respective polyhedra.

Table 4.7: Atomic coordinates, occupancy factors and isotropic temperature factors ($Å^2$) for **III**.

Atom	x	y	z	Occ	Beq
B	0.8637(9)	1.1506(9)	0.0838(7)	1	0.0113
Co1	0.5398(1)	0.4348(1)	0.0817(1)	1	0.038
P1	0.1669(2)	0.3937(3)	0.0885(1)	1	0.034
P2	0.6159(2)	0.8241(2)	0.0980(1)	1	0.034
O1	0.5753(3)	0.8177(3)	0.0031(1)	1	0.0157
O2	0.1828	0.4128	0.1888	1	0.0122
O3	0.792	0.9776	0.1155	1	0.0209
O4	0.0376(2)	0.2337(3)	0.0746(1)	1	0.0082
O5	0.3206(3)	0.3993(2)	0.0584(1)	1	0.0224
O6	0.6254	0.6861	0.1328	1	0.0143
O7	0.4979(4)	0.8839(5)	0.1382(2)	1	0.0213
O8	0.1486(4)	0.5304(4)	0.0473(2)	1	0.0155
O9	0.4807(2)	0.1917(2)	0.0614(1)	1	0.0324
O10	0.8125	0.5289	0.1368	1	0.0331
Co2	1.0766(2)	0.7066(3)	0.1026(2)	0.25	0.038
O11	0.1018(7)	-0.0660(79)	0.1138(3)	0.5	0.124
N	0.166	0.016	0.0236	0.5	0.098

Table 4.8: Selected interatomic distances (Å) and angles (°) for **III**.

Co1	O7	1.8386(3)		O7	Co1	O5	94.866(1)
	O5	1.9734(3)		O7	Co1	O8	162.151(1)
	O8	2.1125(3)		O7	Co1	O9	93.811(1)
	O9	2.1141(2)		O7	Co1	O6	96.147(1)
	O6	2.2517(1)		O7	Co1	O10	92.524(1)
	O10	2.4396(1)		O5	Co1	O8	102.92(1)
Average	Co1-O	2.1216		O5	Co1	O9	96.035(1)
				O5	Co1	O6	92.117(8)
Co2	O11	2.0625(8)		O5	Co1	O10	165.318(1)
	O9	2.2307(3)		O8	Co1	O9	85.882(1)
	O8	2.2747(6)		O8	Co1	O6	81.866(1)
	O10	2.2830(2)		O8	Co1	O10	69.804(1)
	O6	2.4113(3)		O9	Co1	O6	166.546(8)
Average	Co2-O	2.2524		O9	Co1	O10	96.112(8)
				O6	Co1	O10	74.464(4)
P1	O4	1.4166(3)					
	O5	1.5117(4)		O11	Co2	O9	96.193(2)
	O8	1.5369(6)		O11	Co2	O8	152.377(2)
	O2	1.5715(2)		O11	Co2	O10	105.366(2)
				O11	Co2	O6	99.844(1)
P2	O6	1.4650(2)		O9	Co2	O8	91.114(1)
	O1	1.5215(3)		O9	Co2	O10	99.090(1)
	O3	1.6030(1)		O9	Co2	O6	163.911(1)
	O7	1.6177(5)		O8	Co2	O10	99.682(1)
				O8	Co2	O6	75.203(1)
B1	O4	1.4411(8)		O10	Co2	O6	75.446(9)
	O2	1.4442(1)					
	O3	1.5157(8)		O4	P1	O5	107.205(2)
	O1	1.7695(1)		O4	P1	O8	116.172(2)
				O4	P1	O2	104.951(1)
O4	B1	O2	118.628(6)	O5	P1	O8	110.978(2)
O4	B1	O3	113.477(5)	O5	P1	O2	105.592(1)
O4	B1	O1	107.705(6)	O8	P1	O2	111.245(2)
O2	B1	O3	117.187(6)				
O2	B1	O1	93.843(6)	O6	P2	O1	116.868(2)
O3	B1	O1	101.640(4)	O6	P2	O3	104.425(1)
				O6	P2	O7	122.495(2)
				O1	P2	O3	109.307(1)
				O1	P2	O7	100.548(2)
				O3	P2	O7	101.948(2)

Table 4.9: Atomic coordinates, occupancy factors and isotropic temperature factors ($Å^2$) for **IV**.

Atom	x	y	z	Occ	Beq
B	0.8419	1.13903	0.0921	1	0.0113
Mn1	0.5486	0.44329	0.0896	1	0.038
P1	0.16132	0.37567	0.09326	1	0.034
P2	0.60344	0.82911	0.10162	1	0.034
O1	0.58103	0.82075	0.00894	1	0.0157
O2	0.1828	0.4128	0.1888	1	0.0122
O3	0.792	0.9776	0.1155	1	0.0209
O4	0.04595	0.23332	0.08359	1	0.0082
O5	0.28255	0.38081	0.0647	1	0.0224
O6	0.6254	0.6861	0.1328	1	0.0143
O7	0.48244	0.87789	0.12948	1	0.0213
O8	0.1394	0.50581	0.04701	1	0.0155
O9	0.47999	0.17572	0.06047	1	0.0324
O10	0.8125	0.5289	0.1368	1	0.0331
Mn2	1.06466	0.70899	0.11896	0.25	0.038
O11	0.13426	-0.04642	0.0814	0.5	0.124
N	0.13727	0.03012	0.02373	0.5	0.098

Table 4.10: Selected interatomic distances (Å) and angles (°) for **IV**.

Mn1	O8	2.0679(8)		O8	Mn1	O7	167.669(3)
	O7	2.0719(8)		O8	Mn1	O6	101.079(2)
	O6	2.1833(3)		O8	Mn1	O5	91.977(3)
	O5	2.3567(8)		O8	Mn1	O9	85.083(2)
	O9	2.3672(5)		O8	Mn1	O10	96.158(2)
	O10	2.3704(3)		O7	Mn1	O6	89.252(2)
Average	Mn1-O	2.2362		O7	Mn1	O5	94.022(3)
				O7	Mn1	O9	84.074(2)
Mn2	O9	2.0606(7)		O7	Mn1	O10	79.213(3)
	O11	2.1887(1)		O6	Mn1	O5	93.967(1)
	O10	2.1880(3)		O6	Mn1	O9	172.079(1)
	O6	2.6499(6)		O6	Mn1	O10	78.339(1)
	O8	2.6637(1)		O5	Mn1	O9	90.762(2)
Average	Mn2-O	2.3521		O5	Mn1	O10	169.724(2)
				O9	Mn1	O10	96.169(1)
P1	O5	1.2326(6)					
	O4	1.2727(9)		O11	Mn1	O6	85.717(4)
	O8	1.5471(5)		O11	Mn1	O8	128.907(3)
	O2	1.5534(1)		O11	Mn1	O10	68.924(3)
				O10	Mn1	O11	120.659(3)
P2	O1	1.4832(6)		O10	Mn1	O8	94.200(2)
	O7	1.5259(1)		O10	Mn1	O11	73.671(2)
	O6	1.5762(4)		O10	Mn1	O10	133.358(2)
	O3	1.6742(3)		O9	Mn1	O11	113.953(4)
				O9	Mn1	O6	156.332(3)
B1	O2	1.4296(2)		O9	Mn1	O8	88.350(3)
	O3	1.4779(2)					
	O4	1.7098(2)		O5	P1	O4	107.393(4)
	O1	1.7158(2)		O5	P1	O8	109.675(4)
				O5	P1	O2	107.585(5)
O2	B1	O3	123.784(1)	O4	P1	O8	108.167(4)
O2	B1	O4	105.762(1)	O4	P1	O2	114.459(6)
O2	B1	O1	110.143(1)	O8	P1	O2	109.485(4)
O3	B1	O4	111.652(1)				
O3	B1	O1	102.242(1)	O1	P2	O7	101.024(4)
O4	B1	O1	100.970(1)	O1	P2	O6	110.121(3)
				O1	P2	O3	104.091(3)
				O7	P2	O6	129.563(4)
				O7	P2	O3	111.666(4)
				O6	P2	O3	98.228(1)

Table 4.2 shows the lattice parameters and volume for compounds – **I, II, III** and **IV** refined at room temperature, respectively. The influence of the M^{2+} ions on the parameters of the studied compounds is observed. For the isostructural compounds, the lattice parameters and volume of each material increase with the increase in ionic radii of the M^{2+} cations with **I** < **II** and **III** < **IV**. The overall trend in the unit cell volume among all compounds is as follows: **III** < **I** < **II** < **IV**. In an interesting manner, the mean B-O bond distances increase with the

increase in the combined M^{1+} and M^{2+} ionic radius, despite B not sharing bridging oxygen atoms with M^{1+} and M^{2+} species. The combined M^{1+} (Na^{1+} = 1.18 Å and NH_4^{2+} = 1.43 Å [18, 19]) and M^{2+} ionic radius can be ranked as follows: NaCo (**I**) < NaMn (**II**) < NH_4Co (**III**) < NH_4Mn (**IV**), and following the same trend the mean B-O bond distances increase as a function of these ionic radius: 1.4614 (**I**) < 1.4763 (**II**) < 1.5427 (**III**) < 1.5790 (**IV**).

4.3.4. Borophosphates (I, II, III and IV) analogue of the zincophosphate CZP framework

As mentioned earlier the crystal structure of the phases: $NaM^{II}(H_2O)_2[BP_2O_8].(H_2O)$ and $(NH_4)_{0.5}M^{II}_{1.25}(H_2O)_2[BP_2O_8].(H_2O)_{0.5}$ with M = Co, Mn possess a chiral octahedral-tetrahedral framework related to the CZP topology which is found in the crystal framework of the zincophosphate: $NaZnPO_4.H_2O$ and the isomorphous cobalt substituted phase [3, 4]. In detail, the anionic framework structure of the borophosphate ($\infty^1[BP_2O_8]^{3-}$ with corner sharing BO_4 and PO_4 tetrahedra) and zincophosphate ($\infty^1[ZnPO_4]^-$ with corner sharing ZnO_4 and PO_4 tetrahedra) have an analogous chiral helical network (figure 4.7) with pores orientated along the [001] direction. Each helix is made up of 4-ring repeat squares (figure 4.8). The B atoms in the borophosphate phases occupy the Zn1 sites of the sodium zincophosphate phases. Comparing the 4-ring building unit in both crystal structures (figure 4.8), the zincophosphate building unit is severely twisted out of shape as a result of the distorted ZnO_4 tetrahedral units with mean Zn-O bond distances of 1.9449 Å and a large variance in O-Zn-O bond angles of 96.38 to 121.65 °. Ideal average distances and narrower variance is found in the corresponding B-O bond distances of 1.4614 Å and O-B-O bond angles of 95.22 to 112.26 ° (e.g. in structure **I)**. Hence, the borophosphate 4-ring building unit is more regular. Under thermal treatment, the crystal structures of these materials behave distinctly different. It has been previously noted that the dehydration of the zincophosphate hydrate phases causes the collapse of the hexagonal structure into unknown crystal phases [4]. Conversely helical borophosphates such as $NaZn(H_2O)_2[BP_2O_8].H_2O$ reversibly dehydrate to $Na[ZnBP_2O_8].H_2O$, while retaining the CZP topology. This process in borophosphates is also reversible, meaning that the dehydrated phase will re-hydrate and revert to the parent structure when exposed to moisture which indicates that the water molecules found in the zincophosphates have an important structural stability role. This is not

as crucial in porous borophosphates. Further thermoresponsive behaviour of helical borophosphates, **I** – **IV** will be reported in the following thermal analysis sections.

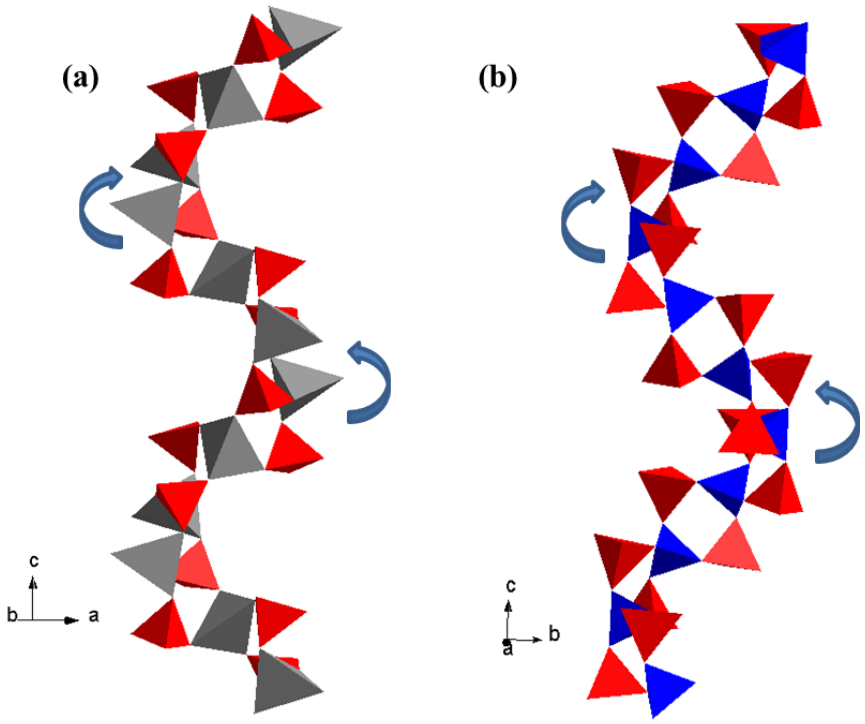


Figure 4.7: Polyhedral representation of (a) tetrahedral helix in CZP zincophosphate and (b) tetrahedral helix in CZP borophosphate phases. ZnO_4 (grey), BO_4 (blue) and PO_4 (red) tetrahedra.

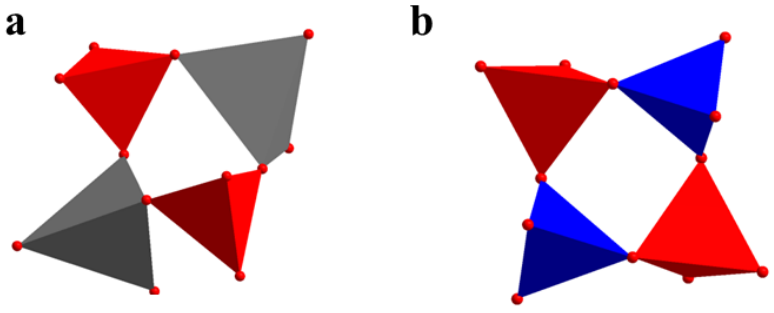


Figure 4.8: 4-ring building unit of the (a) zincophosphate and (b) borophosphate phases. ZnO_4 (grey), BO_4 (blue) and PO_4 (red) tetrahedra.

4.3.5. Thermal studies

TGA curves of samples **I** and **II** are given in figure 4.9 and for sample **III** and **IV** are given in figure 4.10. From the TGA curves, it is observed that samples **I** and **II** exhibit the same thermal behaviour which include a two-step weight loss process. However, samples **III** and **IV** have a much more complex and different thermal decomposition process, with sample **III** exhibiting a four step weight loss process and sample **IV** exhibiting a three step weight loss process. The differences in the thermal evolution between samples **I** and **II** vs samples **III** and **IV** can be attributed to the fact that water molecules are the only non-framework species that can be released in samples **I** and **II**, whereas water and additionally ammonia molecules are the only non-framework species that can be released in sample **III** and **IV** as a function of temperature.

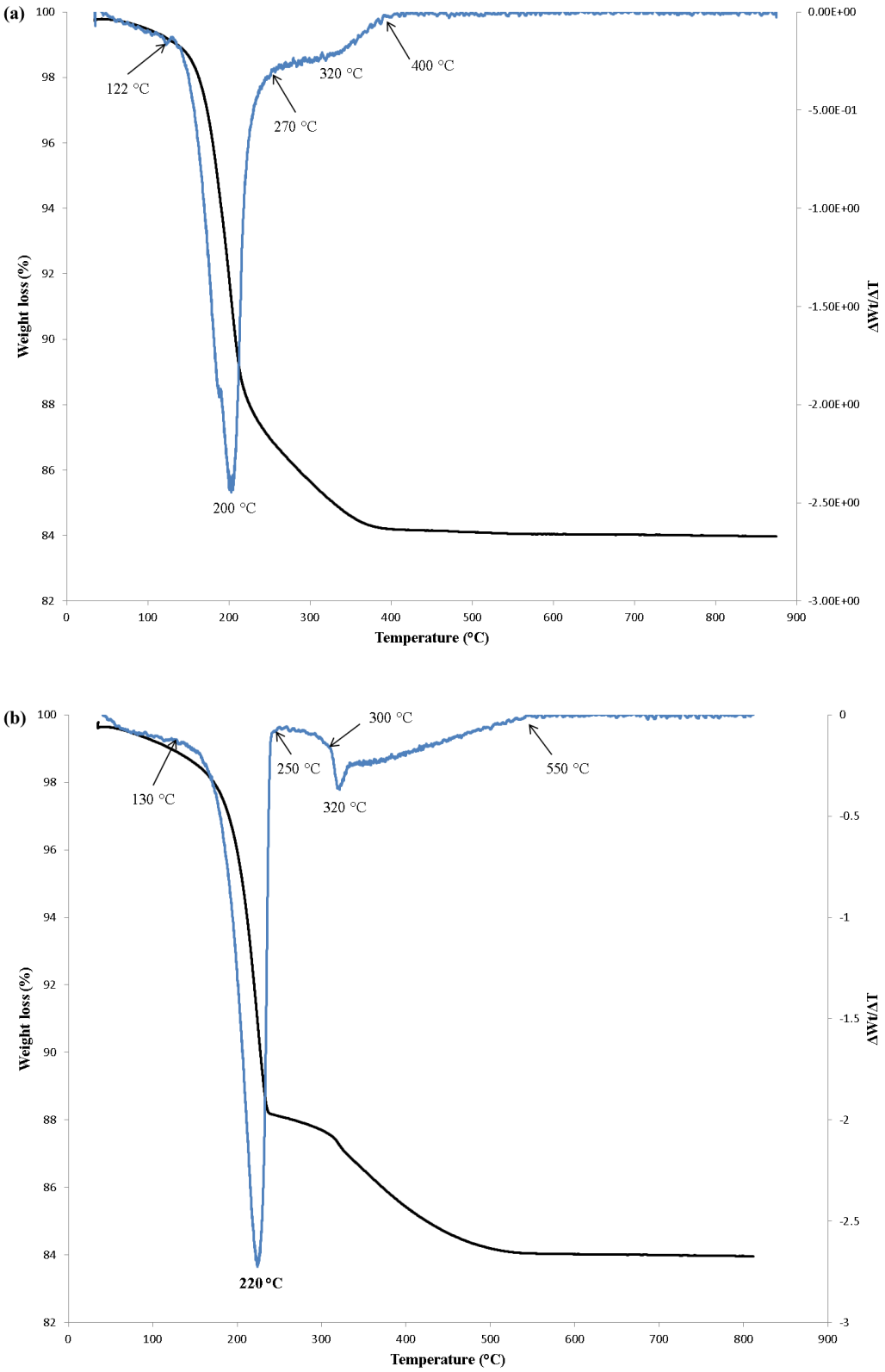


Figure 4.9: Thermogravimetric analysis of (a) sample **I** and (b) sample **II**. In each plot the blue curve shows the 1st derivative.

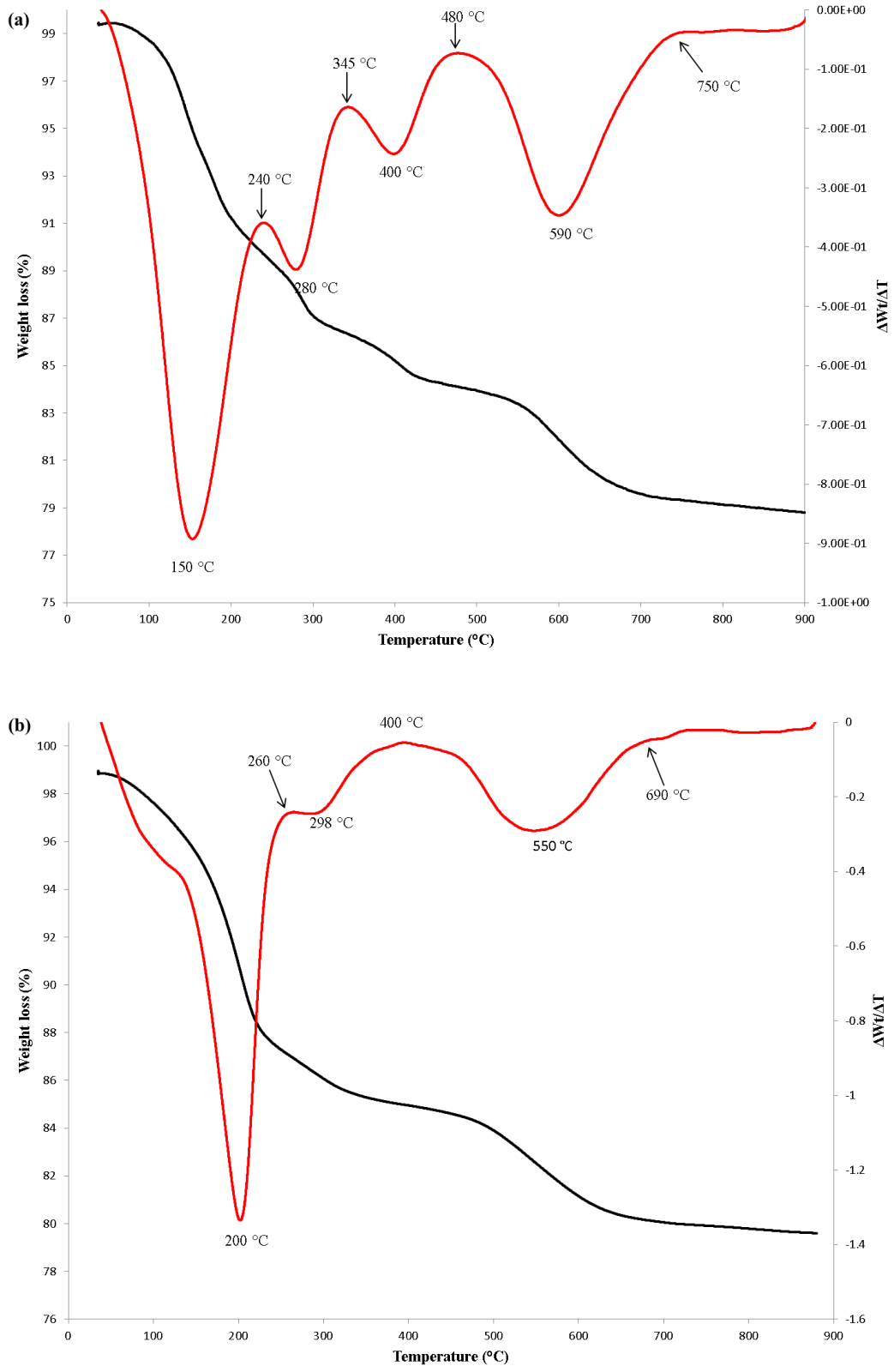


Figure 4.10: Thermogravimetric analysis of (a) sample **III** and (b) sample **IV**. In each plot the red curve shows the 1st derivative.

Selected VT-PXRD patterns measured as a function of temperature for samples **I** and **II** are given in figure 4.11 and for sample **III** and **IV** are given in figure 4.12. VT-PXRD patterns of samples **I**, **II**, **III** and **IV** are similar due to the fact that the diffraction patterns hardly change until the beginning of the first decomposition process. This is evident as the powder patterns collected at higher temperatures (within this first region) are similar to the patterns collected at room temperature. Minor changes in the temperature-dependent diffraction patterns within this first region include slight shifting of the diffraction peaks due to changes in the unit cell volumes. In each dataset, this first region corresponds to the thermal stability region of the title compounds. VT-PXRD results show that compound **I** is stable up to 140 °C, compound **II** is stable up to 200 °C, compound **III** is stable up to 110 °C and compound **IV** is stable up to 170 °C. The unit cell volume expands from 1226.78(1) $Å^3$ to 1228.52(1) $Å^3$ (0.14 % expansion) for **I** and from 1271.74(1) $Å^3$ to 1273.53(1) $Å^3$ (0.14 % expansion) for **II**. The unit cell volume contracts from 1219.13(9) $Å^3$ to 1212.74(2) $Å^3$ (-0.52 % contraction) for **III** and from 1275.73(1) $Å^3$ to 1240.50(2) $Å^3$ (-2.76 %) for **IV**. Furthermore, VT-PXRD analysis reveal that a common feature in all of the samples is that the inorganic residues BPO_4 and a metal phosphate are formed in the last decomposition step and are maintained until the end of each experiment at approximately 860 °C.

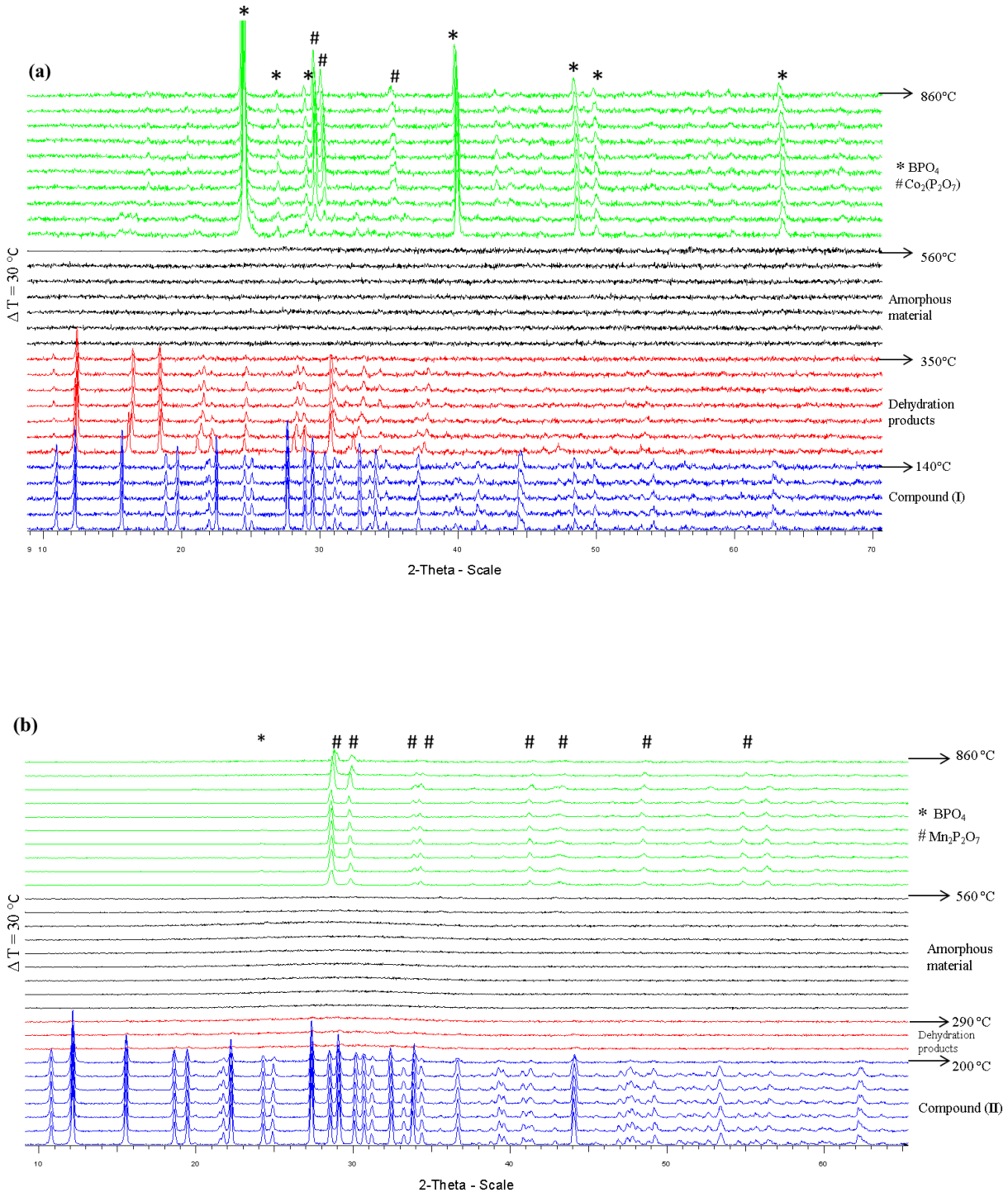


Figure 4.11: Structural transformation of (a) sample **I** and (b) sample **II** characterised by VT-PXRD.

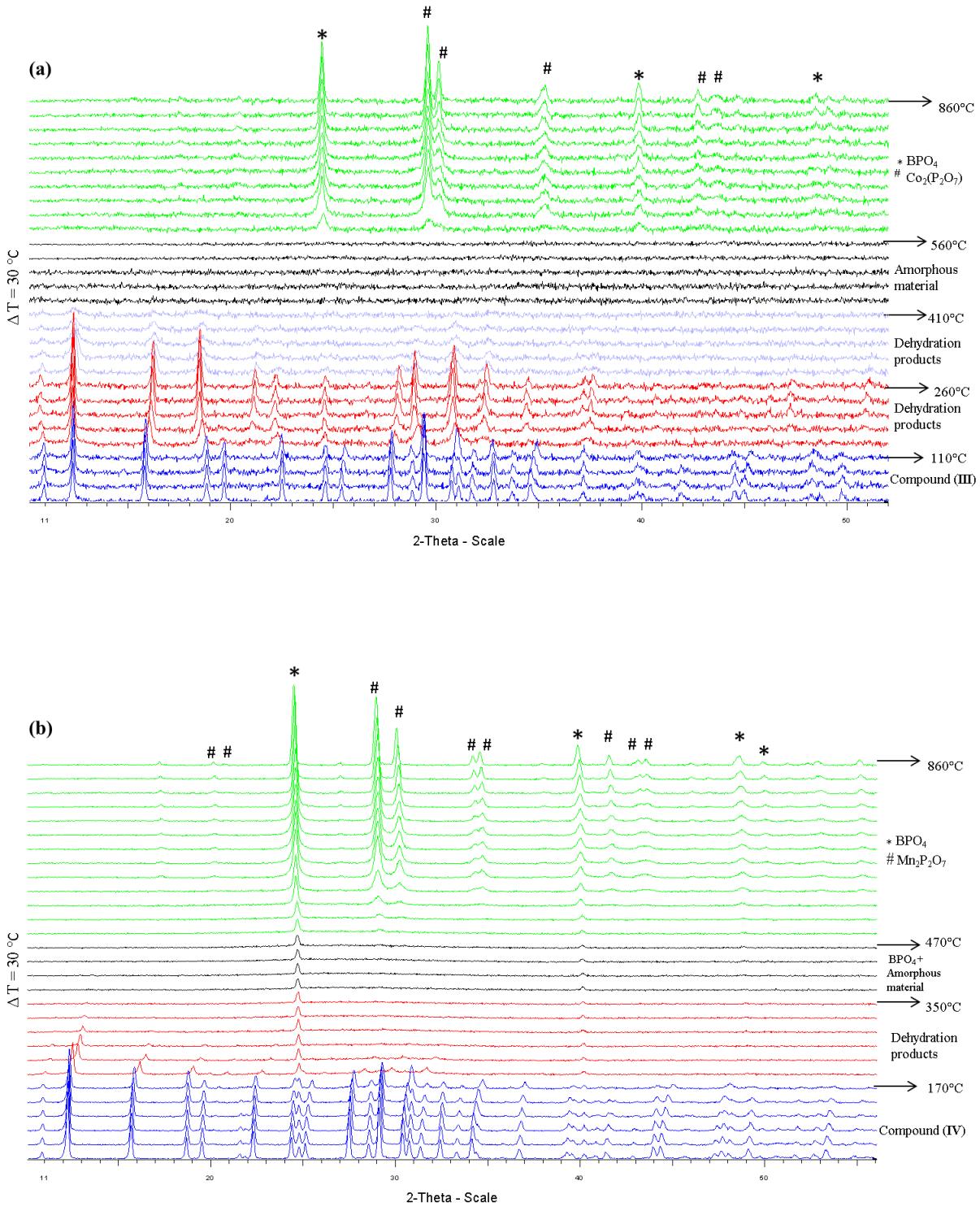


Figure 4.12: Structural transformation of (a) sample **III** and (b) sample **IV** characterised by VT-PXRD.

4.3.6. $NaM^{II}(H_2O)_2[BP_2O_8].(H_2O)_2$ M^{II} = Co (I), Mn (II)

TGA measurements reveal a total weight loss recorded for sample **I** of 16.0 % (calc. 16.7 %) and sample **II** 15.8 % (calc. 16.9 %). As already mentioned, sample **I** and **II** both have a two-step weight loss process. In the first weight loss step, the following percentages were recorded for **I:** 12.8 % (calc. 10.7 %) in the temperature range of 122 - 270 °C; for **II**: 12.0 % (calc. 10.8 %) in the temperature range of 130 – 250 °C. For both compounds, this weight loss corresponds to the release of two moles of H_2O molecules per formula unit. The peak maxima (seen on the derivative curves) for this weight loss step is recorded at 200 °C for compound **I**, and at a slightly higher temperature of 220 °C for compound **II**. In the second weight loss step, the following percentages were recorded for **I**: 3.2 % (calc. 5.9 %) in the temperature range of 278 – 400 °C; for **II**: 3.8 % (calc. 6.0 %) in the temperature range of 300 – 550 °C. This matches the release of one mole of H_2O molecule per formula unit. From the derivative curves, identical peak maximums at 320 °C for this decomposition step were recorded for sample **I** and **II**. Since quite a small temperature difference of 20 °C and 0 °C is seen in the first and second peak maximums for TGA's of sample **I** and **II**, respectively, we can conclude that the incorporation of Co or Mn bears minimal effect to the thermal behaviour of the sodium borophosphate hydrate framework $\{Na(H_2O)_2[BP_2O_8]^{2-}(H_2O)\}$.

According to the VT-PXRD data of sample **I** and **II**, four temperature dependent regions are observed, respectively. Each region is characterised by identified crystalline phases and in some regions unidentified phases, which are amorphous. As shown above, the first region signifies the thermal stability field of the compounds. After this, both materials form crystalline phases which are stable until 350 °C in sample **I** and 290 °C in sample **II**. Unfortunately due to the compromised data quality within these second regions, appropriate crystal structure analysis methods could not be applied to this data. However, inferring from previous temperature dependent diffraction studies of the material $NaZn(H_2O)_2[BP_2O_8].H_2O$ by Kniep and co-workers [6, 7], we suggest that upon losing two moles of water (as confirmed by TGA analysis), the structural changes that accompany this process include the change in coordination of the $M^{2+}(O_{PO4})_4(OH_2)_2$ (M^{2+} = Co, Mn) octahedral environment to a $M^{2+}(O_{PO4})_4$ (M^{2+} = Co, Mn) tetrahedral environment. Additionally, the coordination number around Na^+ changes from 8 ($Na(O_{PO4})_6(OH_2)_2$) to 6 ($Na(O_{PO4})_6$). The predicted chemical formula described by Kniep and co-workers accompanying this dehydration step is described as

$$NaZn(H_2O)_2[BP_2O_8]H_2O \rightarrow Na[ZnBP_2O_8].H_2O + 2H_2O$$

Therefore, conforming to this description we predict that the title compounds will dehydrate to form the microporous compound: $Na[M^{2+}BP_2O_8].H_2O$ (where M^{2+} = Co, Mn). At elevated temperatures above the second decomposition step, an amorphous phase is identified in sample **I** and **II**, respectively. Finally at temperatures above 560 to 860 °C, α-BPO_4 (ICSD number: 026890) and $Co_2(P_2O_7)$ (ICSD number: 203161) are formed in sample **I** while α-BPO_4 and $Mn_2P_2O_7$ (PDF number: 00-035-1497) are formed in sample **II**.

4.3.7. $(NH_4)_{0.5}M^{II}_{1.25}(H_2O)_2[BP_2O_8].(H_2O)_{0.5}$; M^{II} = Co (III), Mn (IV).

TGA curves for samples **III** and **IV** display different thermal behaviour. In the measured temperature range of 30 – 900 °C, the total weight loss of 20 % (calc. 17.3 %) and 18.5 % (calc. 17.3 %) was determined for samples **III** and **IV**, respectively. Furthermore, four and three step decomposition behaviour is observed for sample **III** and **IV**, respectively. The major weight losses for samples **III** and **IV** are summarised in table 4.11. These measurements reveal that the differences in the number of decomposition steps arise from the number of temperature steps required to liberate the water molecules from the structure. The ammonium borophosphate hydrate framework $\{(NH_4)_{0.5}(H_2O)_2[BP_2O_8]^{2-}(H_2O)_{0.5}\}$ can accommodate a total of 2.5 moles of H_2O molecules per formula unit. These H_2O molecules are released in three-steps in compound **III** as opposed to two steps in compound **IV**. That is, in the first step of dehydration, 1.5 moles of H_2O are released in sample **III**: 10.2 % (calc. 8.23 %) whereas 2 moles of H_2O are released in sample **IV**: 11.5 % (calc. 11.1 %). 0.5 moles of H_2O per formula unit are released for the second step for both compounds viz. in sample **III**: 3.30 % (calc. 2.99 %) and in sample **IV**: 2.20 % (calc. 3.13 %). Therefore an additional temperature step between 345 – 450 °C is required to liberate the remaining 0.5 moles of H_2O in the framework of sample **III**: 2.00 % (calc. 3.08 %).. The final decomposition step in both samples relates to the release of 0.5 moles of NH_3 per formula unit viz. peak maxima of 590 °C in sample **III**: 4.50 % (calc. 3.00 %) and 550 °C in sample **IV**: 4.80 % (calc. 3.06 %).

Table 4.11: Moles of residual species released per formula unit of compound **III** and **IV** as a function of temperature. Peak maximums determined from the differential curves are in brackets.

Weight loss	Compound III	Compound IV
Step 1	1.5 H_2O (150 °C)	2 H_2O (200 °C)
Step 2	0.5 H_2O (280 °C)	0.5 H_2O (298 °C)
Step 3	0.5 H_2O (400 °C)	0.5 NH_3 (550 °C)
Step 4	0.5 NH_3 (590 °C)	-

Selected powder XRD patterns as a function of temperature of samples **III** and **IV** display similar phase evolution behaviour as with samples **I** and **II**. The quality of the diffraction data collected with temperature for samples **III** and **IV** is not sufficient to extract information relating to changes in the crystal structures with temperature. As with samples **I** and **II**, we predict that the second (and third for sample **III**) phase stability region in the VT-PXRD data for samples **III** and **IV** consists of dehydrated phases of the title compounds. This postulation is supported by the liberated water detected using thermogravimetry analysis. The borophosphate framework structure is seen to collapse quite early in sample **IV** i.e. at approximately 290 °C whereas a gradual collapse of the framework structure is observed in sample **III** i.e. at approximately 380 °C. The collapse of the framework structure in both samples lead to a purely amorphous phase being formed in sample **III**, whereas α-BPO_4 and an amorphous phase are identified in sample **IV**. The formation of crystalline material between 560 to 860 °C in sample **III** and 500 to 860 °C in sample **IV** corresponds to the release of NH_3 molecules (as supported by data from thermogravimetry analysis). Within this temperature region, the crystalline phases identified are a combination of α-BPO_4 and $Co_2(P_2O_7)$ in sample **III**; α-BPO_4 and $Mn_2P_2O_7$ in sample **IV**.

4.4. Conclusion

In this work, we have successfully synthesized the metal borophosphate hydrates: $NaCo(H_2O)_2[BP_2O_8].(H_2O)$ (**I**), $NaMn(H_2O)_2[BP_2O_8].(H_2O)$ (**II**), $(NH_4)_{0.5}Co_{1.25}(H_2O)_2[BP_2O_8].(H_2O)_{0.5}$ (**III**) and $(NH_4)_{0.5}Mn_{1.25}(H_2O)_2[BP_2O_8].(H_2O)_{0.5}$ (**IV**) under hydrothermal conditions. The crystal structures of all phases were refined by the Rietveld method of powder X-ray diffraction data collected at room temperature. The common feature in the crystal structure of all phases is the one-dimensional helical anionic unit $\infty^1[BP_2O_8]^{3-}$, which is built from alternating BO_4 and PO_4 tetrahedra. This anionic chain is either wound around left- or right handed six fold screw axis (6_1 or 6_5), and form channels orientated along the [001] direction. $M^{2+}O_6$ octahedrons interconnect the chains. Isostructural phases **I** and **II** have an ordered arrangement of water molecules in the voids and have sites around the borophosphate helix which are fully occupied by Na cations. Isostructural phases **III** and **IV** have water molecules and ammonium ions being fractionally distributed within the voids and require an additional $M^{2+}O_2(H_2O)_3$ trigonal bipyrimidal polyhedra. Based on the crystal structures of the title compounds, one would attribute the variety of these structures to the flexibility of the $\infty^1[BP_2O_8]^{3-}$ framework in accommodating a diversity of metals (with different sizes), which are essential in providing charge balance of the resulting material.

Thermogravimetric analysis showed that the investigated compounds can be completely dehydrated at: (**I**) = 400 °C, (**II**) = 550 °C, (**III**) = 450 °C and (**IV**) = 400 °C. Thermal analysis by VT-PXRD methods showed that the crystal structures of the title compounds gradually collapsed and were ultimately transformed into new materials as a function of temperature during the dehydration processes. Therefore, the presence of water molecules in all of the studied phases has a role in maintaining the integrity of the crystal structures.

The porosity of the studies materials may owe themselves to future interesting applications. Already materials with $\infty^1[BP_2O_8]^{3-}$ framework such as $Sc(H_2O)_2[BP_2O_8](H_2O)$ [11] has been shown to absorb NH_3 atmosphere, while the helical channels in $(NH_4)_{0.75}Fe(H_2O)_2[BP_2O_8]\cdot 0.25H_2O$ [20] have provided a possible diffusion tunnel for Li^+ or Na^+, and can be used as a battery cathode material. Therefore, future investigations into the electrochemical and small molecule absorption activity of the title compounds are highly encouraged.

4.5. References

[1] C. Baerlocher, L.B. McCusker, D.H. Olson, *Atlas of zeolite framework types*. Elsevier, 2007.

[2] W.T. Harrison, T.E. Gier, G.D. Stucky, R.W. Broach, R.A. Bedard, *Chemistry of materials* 8 (1996) 145-151.

[3] M. Helliwell, J. Helliwell, V. Kaucic, N. Zabukovec Logar, L. Barba, E. Busetto, A. Lausi, *Acta Crystallographica Section B: Structural Science* 55 (1999) 327-332.

[4] N.Z. Logar, N. Rajic, V. Kaucic, L. Golic, *Journal of the Chemical Society. Chemical communications* (1995) 1681-1682.

[5] C.-H. Lin, S.-L. Wang, *Chemistry of materials* 14 (2002) 96-102.

[6] R. Kniep, H.G. Will, I. Boy, C. Röhr, *Angewandte Chemie International Edition in English* 36 (1997) 1013-1014.

[7] I. Boy, F. Stowasser, G. Schäfer, R. Kniep, *Chemistry-A European Journal* 7 (2001) 834-839.

[8] Y.-X. Huang, G. Schäfer, W. Carrillo-Cabrera, R. Cardoso, W. Schnelle, J.-T. Zhao, R. Kniep, *Chemistry of materials* 13 (2001) 4348-4354.

[9] G. Schaefer, W. Carrillo-Cabrera, W. Schnelle, H. Borrmann, R. Kniep, *Zeitschrift für anorganische und allgemeine Chemie* 628 (2002) 289-294.

[10] B. Birsöz, A. Baykal, M. Toprak, Y. Köseoglu, *Central European Journal of Chemistry* 5 (2007) 536-545.

[11] B. Ewald, Y. Prots, C. Kudla, D. Grüner, R. Cardoso-Gil, R. Kniep, *Chemistry of materials* 18 (2006) 673-679.

[12] A. Yilmaz, X. Bu, M. Kizilyalli, G.D. Stucky, *Chemistry of materials* 12 (2000) 3243-3245.

[13] B. Ewald, Y. Prots, P. Menezes, R. Kniep, *Zeitschrift für Kristallographie-New Crystal Structures* 219 (2004) 351-352.

[14] C.A. A., Bruker AXS, Karlsruhe, 2007.

[15] G. Hölzer, M. Fritsch, M. Deutsch, J. Härtwig, E. Förster, *Physical Review A* 56 (1997) 4554.

[16] K. Brandenburg, Crystal Impact, Bonn, Germany, URL: http://www.crystalimpact.com/company.htm.

[17] S. Achary, A. Tyagi, *Journal of Solid State Chemistry* 177 (2004) 3918-3926.

[18] R.t. Shannon, *Acta Crystallographica Section A: Crystal Physics, Diffraction, Theoretical and General Crystallography* 32 (1976) 751-767.

[19] W. Masterton, D. Bolocofsky, T.P. Lee, *The Journal of Physical Chemistry* 75 (1971) 2809-2815.

[20] L. Tao, G.l. Rousse, M.T. Sougrati, J.-N. Chotard, C. Masquelier, *The Journal of Physical Chemistry C* 119 (2015) 4540-4549.

Chapter 5 Hydrothermal synthesis, crystal structure and thermal behaviour the porous iron borophosphate, $NH_4Fe(III)[BP_2O_8(OH)]$

M. W. Mogodi[a], M. A. Fernandes[b], D. G. Billing[a]*

[a]School of Chemistry and DST/NRF Centre of Excellence in Strong Materials, University of the Witwatersrand, Private Bag 3, WITS, 2050, South Africa.

[b]Molecular Sciences Institute, School of Chemistry, University of the Witwatersrand, PO Wits, 2050, South Africa.

*Corresponding author: Professor David Billing

School of Chemistry,

University of the Witwatersrand,

Private Bag 3, WITS, 2050, South Africa

Email: dave.billing@wits.ac.za

Tel no : +27 11 717 6759

Fax no: +27 11 717 6749

This chapter has been submitted to Acta Crystallographica Section B and has been structured according to the journal's format.

Abstract

The open framework borophosphate $NH_4Fe(III)[BP_2O_8(OH)]$ (**1**) has been synthesized under mild hydrothermal conditions and autogenous pressure. The crystal structure was refined at room temperature by the Rietveld method of powder X-ray diffraction data. **1** crystallizes in the monoclinic space group $P2_1/c$ (No. 14) with Z = 4 and the unit cell parameters a = 9.352(4) Å, b = 8.286(7) Å, c = 9.671(8) Å, β = 101.98(5) ° and V = 733.2(2) $Å^3$. The structure consists of a three-dimensional network of $BO_3(OH)$ and PO_4 tetrahedra, and $FeO_5(OH)$ octahedra forming the porous framework. Charge balancing NH_4^+ ions are trapped in the elliptical pores. Thermogravimetric analysis (TGA) reveals that **1** is stable up to 495 °C. The thermal expansion coefficients of **1** determined using variable temperature PXRD are: α_a = -13.6 x 10^{-6}/°C, α_b = 34.1 x 10^{-6}/°C and α_c = 1.15 x 10^{-6}/°C in the temperature range of 30 to 470 °C. In this temperature range the volume expansion coefficient of the lattice is 21.1 x 10^{-6}/°C.

borophosphate; hydrothermal synthesis; crystal structure; thermal study

5.1. Introduction

Materials with open-framework structures such as aluminosilicate zeolites, silicates, aluminophosphates, metallosilicates and phosphates are of interest in the field of materials science and chemistry. This is due to their fascinating structures which have diverse compositions, a wide range of structural dimensionalities, mixed valencies and bonding as well as tunable porosity. The most important of these porous frameworks are the aluminosilicate zeolites which are composed of silicon and aluminium tetrahedral building units forming structures with compositions of $A_{x/n}[Si_{1-x}Al_xO_2].mH_2O$, where A is a metal cation of valence n and $0 \leq x \leq 0.5$ [1]. A subsequent systematic description of the structural chemistry of aluminosilicates which focuses on the chemical structure, bonding and classification of these materials has been developed [2]. Like-wise a similar structural classification has been adapted for the newly studied borophophates [3]. The borophosphate phases include anionic partial structures ($_\infty[B_xP_yO_z]^{n-}$) with isolated units, oligomers, chains, ribbons, layers and three-dimensional frameworks [3, 4]. The diverse structural dimensionality of the borophosphate phases is interlinked with the rich stoichiometries found in these materials with B : P ratios of 6:1, 5:1, 3:1, 3:2, 1:1, 3:4, 2:3, 1:2, 2:5, 1:3 and 1:4 [3-

5]. Of these, the 1:2 ratio seems to be prevalent in the structural architectures synthesized so far. This includes the microporous borophosphate: ammonium iron (III) (monophosphate-hydrogen-monoborate-monophosphate), $NH_4Fe(III)[BP_2O_8(OH)]$, which is related to the series of compounds with the general composition: $AM^{III}[BP_2O_8(OH)]$ (A= NH_4, Rb, Cs; M = V, Fe, ($Fe_{0.53}V_{0.47}$), Al, Ga) [3, 5-9]. The room temperature structure of $NH_4Fe(III)[BP_2O_8(OH)]$ has previously been determined using single crystal X-ray diffraction analysis and described [7, 10]. The above materials crystallize in either a triclinic or a monoclinic crystal system. In general, the hydrothermal method has been used to prepare these compounds.

In view of the recent synthesis of borophosphates containing template cations, organic amines and other molecules within their voids [11-15], in this work we report the hydrothermal synthesis, crystal structure and thermal behaviour of a microporous transition metal borophosphate, $NH_4Fe(III)[BP_2O_8(OH)]$, with quaternary ammonium cations within its voids. With the presence of the transition metal and intrinsic microporosity, the title compound may have potential magnetic, sorption and catalytic properties. However the optimum functioning of these properties are reliant on the materials thermal stability. This is an important aspect as the material may lose its beneficial property due to a thermal decomposition, phase transition or excessive expansion or contraction of the lattice with temperature. In this regard, a comprehensive thermal investigation including quantitative analysis of the thermal expansion behaviour by variable temperature powder X-ray crystallography was carried out.

5.2. Experimental

5.2.1. Synthesis of $NH_4Fe[BP_2O_8(OH)]$

5.68 g of $FeCl_2.4H_2O$ (28.5 mmol), 7.55 g of $(NH_4)_2HPO_4$ (57 mmol), 3.52 g of H_3BO_3 (57 mmol) and 7.75 g of 85 % of H_3PO_4 (7.91 mmol) were added to 10 ml of water with stirring. The mixture was heated (approximately 80°C) to allow slow evaporation of the water until a viscous homogeneous brown gel was obtained. The resulting gel was transferred into an 18 ml Teflon bomb (degree of filling ~70 %) and heated at 180 °C and autogenous pressure for three days. Following cooling to room temperature, the solid product was isolated by

filtration, washed with water and dried in air at 80 °C. A pale pink powdered material was recovered for full characterisation.

5.2.2. Chemical analysis

Elemental analysis of $NH_4Fe[BP_2O_8(OH)]$ was investigated with ICP-AES (SPECTRO Genesis ICP-OES). Elemental analysis found: molar ratio Fe:P as 1:1.58(4). Energy-dispersive X-ray spectroscopy (EDS) analysis (FEI Nova Nanolab 600 FIB/SEM) was also conducted, with the results shown in figure A2.4 (Appendix 2: Supplementary material). EDS analysis confirms the presence of Fe, P, O and C. The signal for C is attributed to the carbon grid onto which the powdered material was mounted during the EDS analysis.

5.2.3. FTIR Spectroscopy

FTIR spectra analysis was conducted using a Bruker Tensor 27 Fourier Transform Infrared spectrometer with the spectrum recorded in the range of 550-4000 cm^{-1}. The result of the study is shown in figure A2.5. The spectrum confirms the presence of the inorganic groups (PO_4 and $BO_3(OH)$ units), and the framework charge balancing NH_4^+ group. The bands at 3246, 3043, 2860 and 1431 cm^{-1} represent the bending and stretching vibrations of the N-H moieties of the NH_4 group. Bands in the 1200 – 954 cm^{-1} region are related to the internal modes of phosphate and borate groups including 1089, 859 and 642 cm^{-1} **(**BO_4) and 966 cm^{-1} (PO_4). The bands at 3588 cm^{-1} (O – H stretches) and 1676 cm^{-1} (O – H deformation) signify the presence of the O-H groups of the $BO_3(OH)$ coordination environment.

5.2.4. Thermogravimetric analysis (TGA)

Thermogravimetric analysis (TGA) was carried out on a Perkin Elmer STA 6000. The sample weight was approximately 10 mg. The sample was heated at 10 °C min^{-1} under a nitrogen atmosphere.

5.2.5. Scanning electron micrograph (SEM)

SEM images of the studied material were collected on a FEI Nova Nanolab 600 FIB/SEM. Figure 5.1 show that rod shaped crystals of $NH_4Fe[BP_2O_8(OH)]$ were grown.

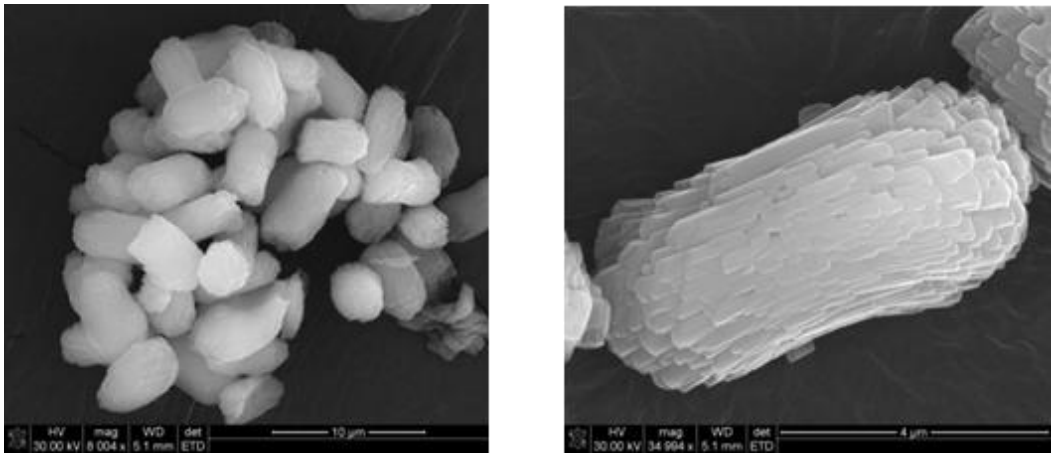


Figure 5.1: SEM images of the crystals of $NH_4Fe[BP_2O_8(OH)]$ with a rod-shaped morphology.

5.2.6. Powder X-ray diffraction (PXRD)

Powder X-ray diffraction data were collected on a Bruker D8 Advance diffractometer equipped with a sealed tube X-ray Cu source ($Cuk_{\alpha1}/k_{\alpha2}$) operated at 40kV and 40 mA, a Göbel mirror and a Bruker VÅntec-1 linear position sensitive detector (PSD). The variable temperature (VT) measurements were carried out in an Anton Paar XRK 900 furnace using a Macor® ceramic sample holder. The diffraction patterns were collected in the continuous scan mode between the 2θ range of 8 – 75 ° with a step-size of 0.027 ° and counting for 1 sec/step. The data was collected every 30 °C ranging from 30 to 860 °C. Before the VT-PXRD experiment, the National Institute of Standards Technology (NIST) Standard Reference Material (SRM), SRM LaB_6 660a standard was used for peak position calibration and alignment checking.

Rietveld refinement [16] on the measured diffraction patterns were performed using the TOPAS (Total pattern analysis solution) version 4.2 package [17]. The starting model for refining the room temperature phase was obtained from the structure reported by Huang and co-workers [10]. Details of the structure refinement at 30 °C are given in table 1 and figure

5.2. For refining the diffraction data of the $NH_4Fe[BP_2O_8(OH)]$ phase within the temperature range of its stability, which includes 16 temperatures between 30 and 470 °C (see figure 5.8 below), the following parameters were adjusted for each pattern:

5 emission profile variables (fixed), 6 background polynomials, 1 overall scale factor, 4 unit cell parameters, 6 Pearson VII profile variables, 4^{th} order spherical Harmonics preferred orientation factor, fractional coordinates and isotropic displacement parameters for all atoms.

Crystal structure drawings were generated using the Diamond Version 3.2g program [18].

Table 5.1: Details of the Rietveld refinement of **1** at 30 °C.

Compound	This work	[10]
space group	$P2_1/c$ (no. 14)	$P2_1/c$ (no. 14)
formula weight ($gmol^{-1}$)	291.64	291.64
a (Å)	9.352(4)	9.369(8)
b (Å)	8.286(7)	8.309(2)
c (Å)	9.671(8)	9.680(1)
β (Å)	101.98(5)	102.04(9)
Vol ($Å^3$)	733.2(2)	737.0(4)
Z	4	4
Crystal Density ρ, ($g\ cm^{-3}$)	2.642(1)	2.628
Data range (°)	8 - 75	3.3 – 52.1

X^2	1.11	-
wRp(%)	3.66	-
Rexp (%)	3.29	-

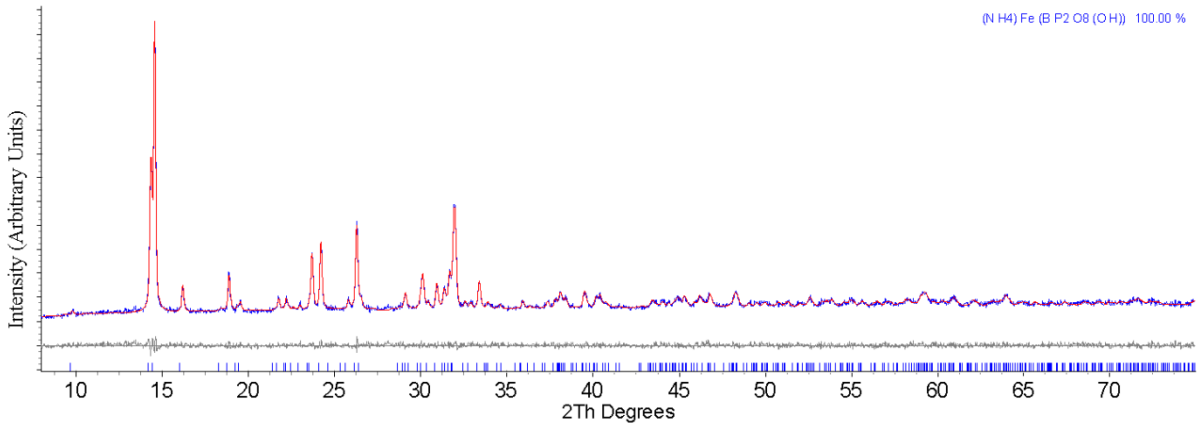


Figure 5.2: Observed (blue), calculated (red) and difference (grey) XRD patterns of $NH_4Fe[BP_2O_8(OH)]$ refined at 30 °C. Lower ticks are the refined peak position.

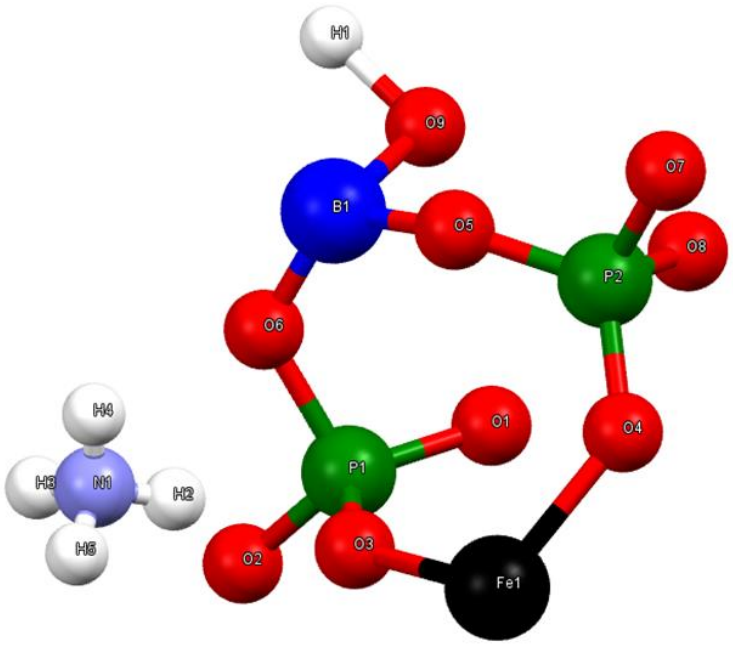


Figure 5.3: Ball and stick representation of the Fe, B P and N atom coordination in the asymmetric unit of $NH_4Fe[BP_2O_8(OH)]$.

Table 5.2: Fractional atomic coordinates and isotropic temperature parameters ($Å^2$) for $NH_4Fe[BP_2O_8(OH)]$.

atom	x	y	z	B ($Å^2$)
Fe1	0.7903(11)	0.1525(11)	0.5743(13)	2.50(1)
B1	0.6750(78)	0.5683(85)	0.7959(73)	2.32(3)
P1	0.9285(18)	0.4302(23)	0.8003(22)	2.31(8)
P2	0.5796(19)	0.2391(24)	0.7819(21)	1.99(8)
O1	0.8973(26)	0.3351(36)	0.9299(33)	1.38(6)
O2	1.0796(31)	0.5022(42)	0.8017(32)	2.88(4)

O3	0.8965(35)	0.3485(42)	0.6601(41)	4.29(1)
O4	0.6578(25)	0.1253(31)	0.6989(37)	1.08(1)
O5	0.5920(34)	0.4163(45)	0.7516(34)	3.69(8)
O6	0.8224(32)	0.5838(35)	0.7831(33)	2.09(3)
O7	0.4142(36)	0.2165(34)	0.7518(33)	1.99(9)
O8	0.6311(34)	0.2121(49)	0.9539(44)	7.18(7)
O9	0.6737(33)	0.5596(35)	0.9761(36)	2.46(8)
H1	0.649(38)	0.707(44)	0.991(38)	0.013(1)
N1	0.8184(31)	0.5955(43)	0.4386(36)	1.53(2)
H2	0.827(3)	0.52(3)	0.495(3)	0.025(1)
H3	0.875(3)	0.666(3)	0.47(3)	0.025(1)
H4	0.734(2)	0.625(4)	0.421(3)	0.025(1)
H5	0.84(3)	0.562(4)	0.365(3)	0.025(1)

5.3. Discussion

5.3.1. Crystal structure

The asymmetric unit (figure 5.3 and table 2) of $NH_4Fe[BP_2O_8(OH)]$ consists of one crystallographically unique Fe^{3+} site, two crystallographically unique P^{5+} sites, one B^{3+} site, one N^{3-} site and five H^{1+} sites. Nine O atoms coordinate to the Fe, B, and P atoms. The B(1) atoms are involved in forming distorted tetrahedral $[BO_4]^{5-}$complexes, the two phosphorous atom sites P(1) and P(2) form distorted $[PO_4]^{3-}$ tetrahedra. The $[BO_4]$ tetrahedra share three of their four oxygen atoms with the phosphate tetrahedra (i.e. one oxygen atom with P(1) atoms and two oxygen atoms to P(2) atoms), while the remaining hydrogen-bond donating oxygen atoms (O(9)H) are shared with the Fe(1) atoms. Concerning the phosphate tetrahedra, the P(1) tetrahedra share one corner with the $[BO_4]$ groups, while the P(2) tetrahedra share two of their corners with the $[BO_4]$ groups. The resulting open-branched borophosphate chain $_\infty^1\{[BP_2O_8(OH)]^{4-}\}$ constitutes the fundamental building unit (FBU) of the structure (figure 5.4). This infinite-one-dimensional borophosphate chain is orientated along the [010] direction. Additionally, the 6-coordinate Fe(1) atoms share the hydrogen donating O(9)H atom with B(1), three O atoms with three P(1) atoms and two O atoms with two P(2) atoms. The resulting $Fe(III)O_5(OH)$ octahedra connect to the anionic FBU, by linking the atoms O(3), O(4) and O(2) in one chain to atoms O(1), O(8) and O(9) in the adjacent chain. A three-dimensional open framework structure, $\{Fe[BP_2O_8(OH)]^-_\infty\}$ is formed (figure 5.5). The structure is composed of voids occupied by charge balancing NH_4^+ cations which are connected to the anionic framework $\{Fe[BP_2O_8(OH)]^-_\infty\}$ via hydrogen bonds to atoms O(2), O(3), O(6) and O(7) (N-H···O hydrogen bond are between 2.8086 – 3.0577 Å). The elliptical voids are composed of 8-corner-sharing polyhedral viz. two $BO_3(OH)$ and four PO_4 tetrahedra and two $FeO_5(OH)$ octahedra (figure 5.6). Using the voids visualisation function within the program Mercury [19], the void sizes for this crystal structure have been calculated (figure 5.7). The calculation considers the atomic Van Der Waals radii as the regions where the molecule(s) are present. The voids were calculated by finding any empty space within the structure that can accommodate a spherical probe with a particular radius. During the calculation, the radius of the spherical probe was adjusted until the spherical probes are exclusively isolated within the largest cavities of the structure. Using this program, the crystal structure of **1** could accommodate a spherical probe of radius 0.63 Å, which corresponds to a

void volume of 3.13 $Å^3$ which occupies 0.4 % of the unit cell volume (figure 5.7a). When the NH_4^+ molecules were removed/deleted from the cavities, the resulting crystal structure could accommodate a spherical probe of radius 1.1 $Å^3$, which corresponds to a void volume of 29.46 $Å^3$ which occupies 4.0 % of the unit cell volume (figure 5.7b).

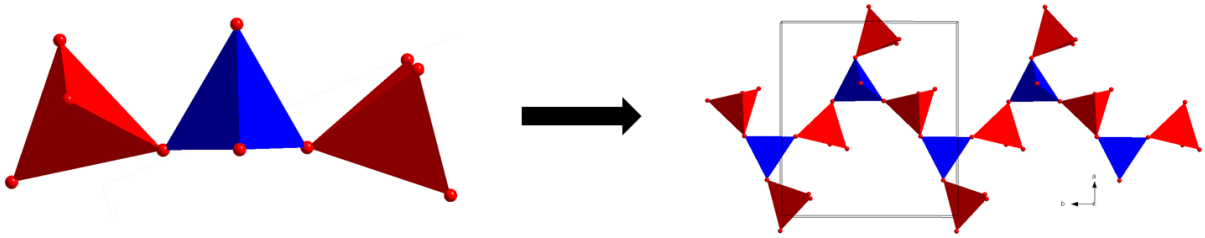


Figure 5.4: Open-branched $_\infty^1\{[BP_2O_8(OH)]^{4-}\}$ chain (right) formed by corner sharing $BO_3(OH)$ (blue) and PO_4 tetrahedra (red) with another PO_4 group branching off the $BO_3(OH)$ tetrahedra. Its basic building unit (BBU) is also shown (left).

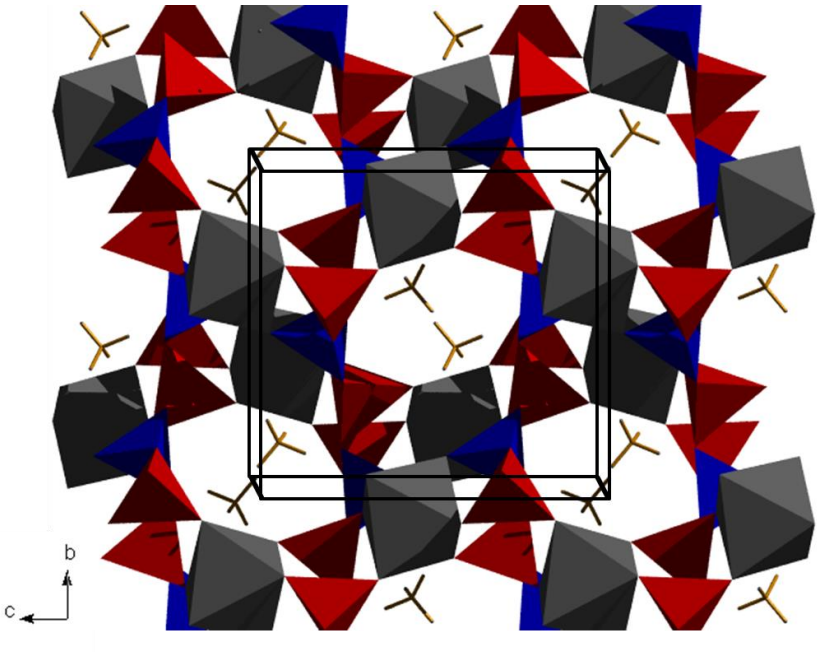


Figure 5.5: Polyhedral representation of the crystal structure of $NH_4Fe[BP_2O_8(OH)]$ viewed along the *a*-axis direction. B tetrahedra (blue), P tetrahedra (red), Fe octahedra (grey) and NH_4^+ molecules (wire/stick model).

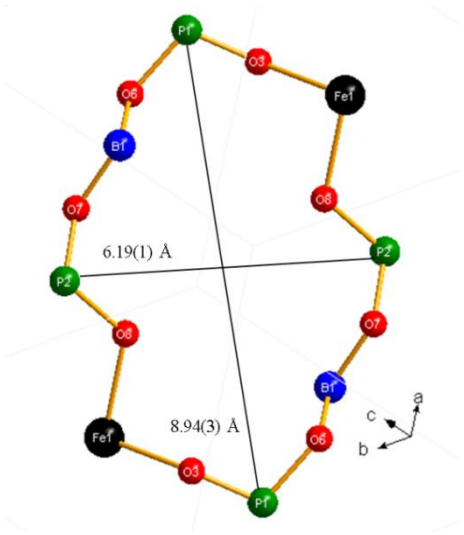


Figure 5.6: Ball and stick representation of the eight-membered ring of $NH_4Fe[BP_2O_8(OH)]$. P2 ⋯ P2 x P1 ⋯ P1 distances (green atoms) are 6.19(1) x 8.94(3) $Å^2$.

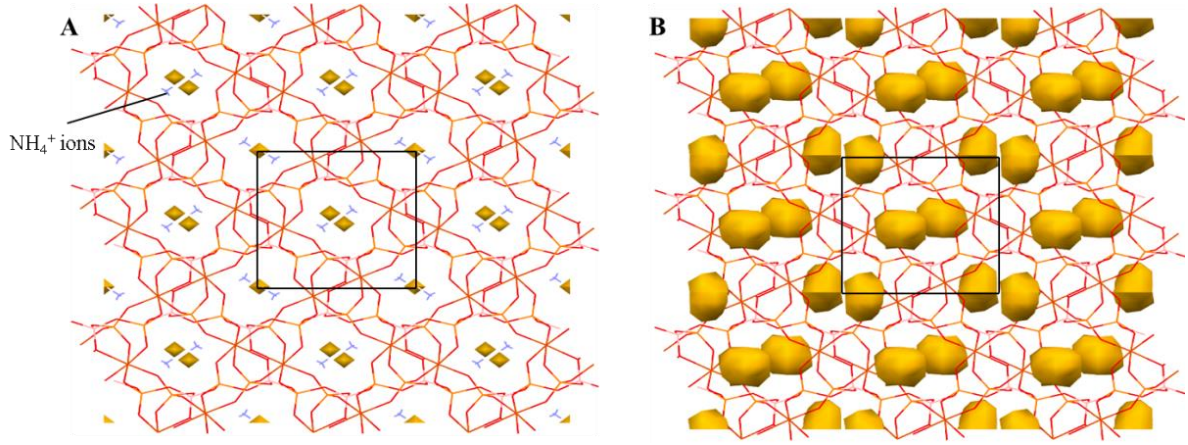


Figure 5.7: Void spaces within the crystal structure of (a) **1** and (b) **1** without NH_4^+ ions. The voids in these structures are depicted as gold coloured spheres.

Selected bond lengths and angles are given in table 3. The boron, phosphorous tetrahedra as well as the iron octahedra are all slightly distorted. The B-O bond lengths range between 1.415 to 1.746 Å (ave 1.539 Å) and the O-B-O angles range from 98.07 to 121.8° (ave 98.88°). The P1 tetrahedra are slightly less distorted than the P2 tetrahedra as seen by the respective average distances in table 3. The overall P-O bond distances change from 1.489 to 1.648 Å (ave 1.547 Å) and O-P-O angles change from 101.3 to 121.1° (ave 109.2 °). The

inter-tetrahedral B-O-P angles range between 120.8 (B1-O6-P1) and 145.3 ° (B1-O5-P2). The Fe-O distances range from 1.882 to 2.179 Å, with the Fe-O(9)H bond being the longest in the Fe octahedra. The degree of distortion of the Fe, B and P coordination environment are comparable with previously investigated borates [20, 21], phosphates [21, 22] and iron environments [23].

Table 5.3: Selected interatomic distances (Å) and angles (°) for $NH_4Fe[BP_2O_8(OH)]$.

Fe octahedron			Angle		Angle	
Fe1	O1	1.882(3)	O1-Fe-O4	170.9(9)	O6-B1-O5	120.5(7)
	O4	1.912(9)	O1-Fe-O2	97.4(8)	O6-B1-O7	112.8(1)
	O2	1.965(7)	O1-Fe-O3	88.2(1)	O6-B1-O9	107.4(4)
	O3	1.992(7)	O1-Fe-O8	89.0(7)	O6-B1-H1	107.5(6)
	O8	2.027(7)	O1-Fe-O9	90.8(9)	O5-B1-O7	112.2(4)
	O9	2.179(5)	O4-Fe-O2	86.6(1)	O5-B1-O9	98.0(7)
	$Fe-O_{AVE}$	1.9934	O4-Fe-O3	99.5(4)	O5-B1-H1	121.8(1)
B tetrahedron			O4-Fe-O8	86.1(3)	O7-B1-O9	102.8(1)
B1	O6	1.415(3)	O4-Fe-O9	81.2(8)	O7-B1-H1	72.0(7)
	O5	1.494(8)	O2-Fe-O3	94.0(4)	O9-B1-H1	33.4(5)
	O7	1.502(4)	O2-Fe-O8	171.3(5)		
	O9	1.746(9)	O2-Fe-O9	86.8(5)	O3-P1-O2	101.2(8)
	$B-O_{AVE}$	1.5398	O3-Fe-O8	91.7(8)	O3-P1-O1	117.8(1)
P1 tetrahedron			O3-Fe-O9	178.8(1)	O3-P1-O6	105.2(9)
P1	O3	1.489(3)	O8-Fe-O9	87.4(1)	O2-P1-O1	121.0(9)
	O2	1.531(4)			O2-P1-O6	104.0(1)
	O1	1.558(6)	O5-P2-O4	115.9(1)	O1-P1-O6	105.6(6)
	O6	1.601(2)	O5-P2-O7	101.4(5)		

	P1 – O_{AVE}	1.5451	O5-P2-O8	108.0(8)
P2 tetrahedron			O4-P2-O7	113.7(7)
P2	O5	1.506(5)	O4-P2-O8	112.1(3)
	O4	1.520(7)	O7-P2-O8	104.3(7)
	O7	1.525(1)		
	O8	1.648(2)		
	P2 – O_{AVE}	1.5501		

Hydrogen bond lengths (Å) and angles (°)

D···H		H···A		D···A		D-H···A			
N···H3	0.8043	H5···O2	1.988	N···O2	2.8086	N1-H2-O2	109.034	N1-H4-O2	113.378
N···H4	0.8099	H2···O3	2.136	N···O3	2.9432	N1-H2-O7	139.916	N1-H4-O3	116.524
N···H2	0.8229	H3···O6	2.727	N···O6	3.0577	N1-H3-O2	102.228	N1-H5-O3	108.961
N···H5	0.8272	H4···O7	2.340	N···O7	2.9810	N1-H3-O3	100.715	N1-H5-O7	85.475

5.3.2. Thermal investigations

Thermogravimetric analysis (TGA) curves are presented in figure 5.8. This measurement reveals a three-step weight loss occurring around temperatures 110, 495, 550 °C. The first weight loss corresponds to the release of unreacted H_3BO_3, which was used in the synthesis of the title compound. The second weight loss process corresponds to the elimination of one NH_3 molecule per formula unit (6.60 % observed / 5.84 % calculated). This indicates that $NH_4Fe[BP_2O_8(OH)]$ is stable up to a temperature of 495 °C. The third decomposition with weight loss of 6.20 % observed / 6.56 % calculated corresponds to the liberation of one H_2O molecule.

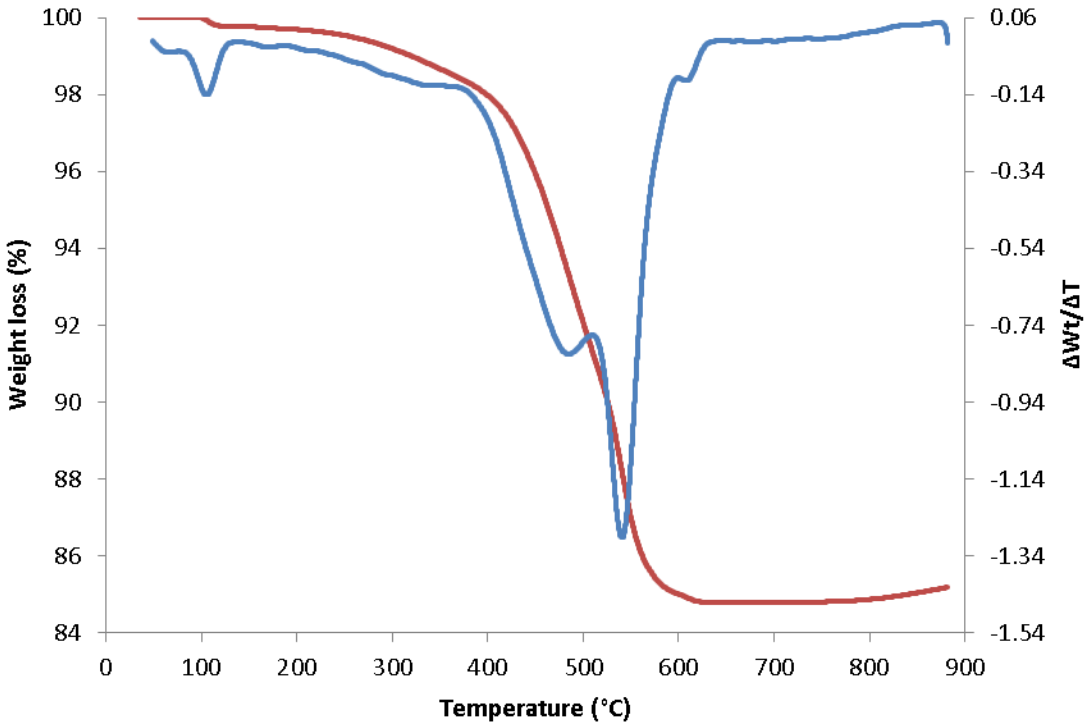


Figure 5.8: Thermogravimetric curves of $NH_4Fe[BP_2O_8(OH)]$ under N_2. Red curve is the thermogravimetric curve and the blue curve is the 1st derivative.

The thermal behaviour was also investigated by variable temperature PXRD under N_2. Figure 5.9 shows the results of this analysis. From the VT-PXRD study, a three-stage temperature dependent structure evolution is observed. The first stage, which signifies the temperature stability region of $NH_4Fe[BP_2O_8(OH)]$, takes place in the 30 – 470 °C range. Changes in the temperature dependent diffraction patterns in this region include slight lateral shifting in various peak positions due to the expansion/contraction of the lattice and a decrease in the intensity of the diffraction peaks particularly at higher temperatures due to the progressive collapse of the material. The decomposition of $NH_4Fe[BP_2O_8(OH)]$ occurs around 470 °C and leads to a short lived amorphous phase which is stable until 530 °C. This amorphous phase corresponds to the third weight loss process observed by TGA analysis at 550 °C. The decomposition of this unknown amorphous phase leads to the crystalline materials; α-BPO_4 (ICSD number: 026890), iron phosphate ($Fe_3P_6O_{18}$) which is isostructural to manganese phosphate ($Mn_3P_6O_{18}$: PDF number: 00-039-0-164) and an unidentified phase. The abundance and crystallinity of these residual phases increase (as indicated by an increase in

the intensity of the reflections of these phases) and are maintained until the end of the data collection at 860 °C. Using the results from the thermal analysis techniques and chemical knowledge, we propose the decomposition reaction of the title compound to be:

$$NH_4^+ + Fe^{3+}[BP_2O_8(OH)]^{4-} \rightarrow Fe^{3+}[BP_2O_8]^{3-} + NH_3 + H_2O$$

This process proceeds via the helical borophosphate framework [21], $\infty[BP_2O_8]^{3-}$. However X-ray analysis shows an amorphous material being formed upon the decomposition of $NH_4Fe[BP_2O_8(OH)]$ viz. 470 to 530 °C. A similar speculative decomposition pathway has been postulated for the isostructural ammonium vanadium (III) (monophosphate-hydrogen-monoborate-monophosphate) material, $NH_4V(III)[BP_2O_8(OH)]$ [7].

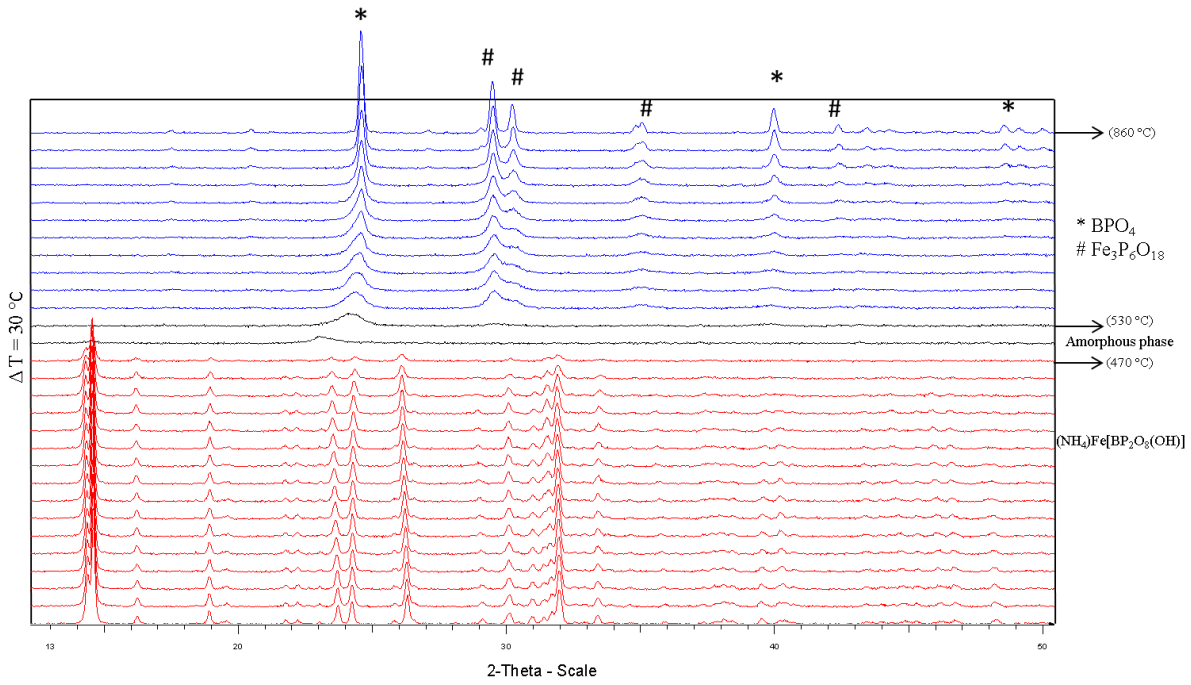


Figure 5.9: Temperature dependent powder X-ray diffraction patterns of $(NH_4)Fe[BP_2O_8(OH)]$.

In relation to the quantitative analysis of the thermal stability region of $NH_4Fe[BP_2O_8(OH)]$, the structure was refined from 30 – 470 °C by the Rietveld method of the observed diffraction data. The refined unit cell parameters are given in table 5.4 and the unit cell volume with temperature is plotted in figure 5.10. The results in table 5.4 reveal a strong anisotropic expansion of the lattice, with a negative thermal coefficient (contraction with increasing temperature) along the *a* of -13.6 x 10^{-6}/°C and positive thermal expansion coefficient along the *b*- and *c*-axis of 34.1 x 10^{-6}/°C and 1.15 x 10^{-6}/°C, respectively. This anisotropic thermal behaviour along the crystallographic axes results in the overall expansion of 0.93 % in the unit cell volume, and a volume thermal coefficient of 21.1 x 10^{-6}/°C in the temperature range of 30 – 470 °C. The levelling off of the unit cell volume between temperatures 410 and 470 °C (figure 5.10) signifies the onset of the structural decomposition. Therefore, an essentially linear expansion of the unit cell volume is observed from 30 to 380 °C.

Table 5.4: Refined unit cell parameters of $NH_4Fe[BP_2O_8(OH)]$ at selected temperatures.

Temp. (°C)	**a (Å)**	**b (Å)**	**c (Å)**	**Vol (Å^3)**	**χ^2**	**Rexp**	**Rwp**
30	9.352(4)	8.286(7)	9.671(8)	733.2(2)	1.11	3.29	3.65
50	9.353(2)	8.293(9)	9.672(4)	733.9(9)	1.08	3.29	3.58
80	9.350(1)	8.303(1)	9.673(4)	734.6(7)	1.10	3.28	3.61
110	9.348(7)	8.314(2)	9.672(7)	735.4(9)	1.08	3.28	3.56
140	9.346(7)	8.323(6)	9.674(6)	736.2(9)	1.12	3.28	3.69
170	9.345(9)	8.335(5)	9.678(1)	737.5(2)	1.08	3.28	3.56
200	9.344(8)	8.344(8)	9.678(0)	738.2(3)	1.10	3.29	3.63
230	9.343(6)	8.357(7)	9.678(4)	739.2(9)	1.08	3.30	3.59
260	9.341(3)	8.366(5)	9.679(7)	739.9(5)	1.06	3.30	3.52

290	9.337(8)	8.376(7)	9.681(2)	740.6(8)	1.10	3.31	3.64
320	9.337(4)	8.388(3)	9.684(4)	741.9(2)	1.10	3.31	3.66
350	9.334(3)	8.397(6)	9.686(0)	742.5(8)	1.09	3.32	3.64
380	9.329(6)	8.406(6)	9.686(5)	743.0(3)	1.09	3.33	3.66
410	9.316(1)	8.413(4)	9.685(4)	742.4(9)	1.06	3.34	3.54
440	9.298(8)	8.414(7)	9.676(2)	740.4(7)	1.05	3.33	3.52
470	9.297(2)	8.411(7)	9.677(3)	740.1(9)	1.06	3.31	3.51

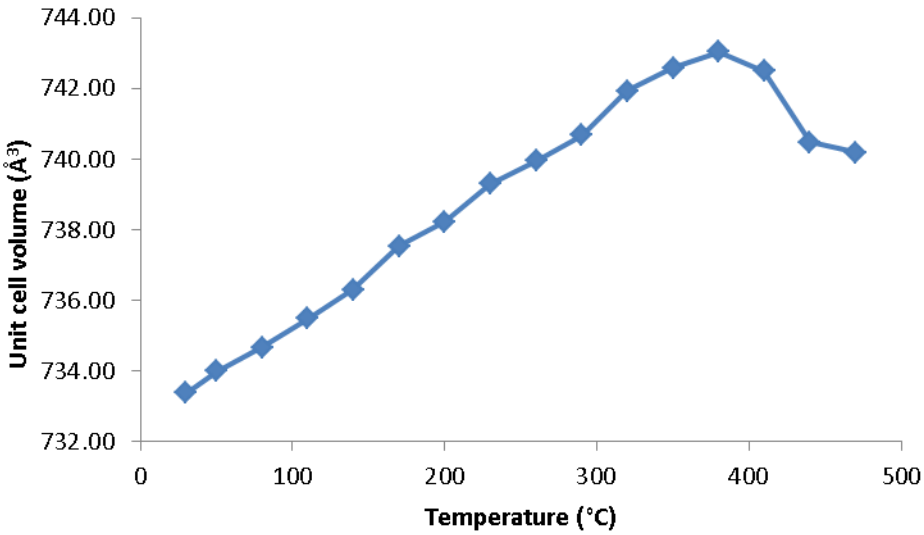


Figure 5.10: Variation of the unit cell volume as a function of temperature. The error bars are smaller than the symbol size.

For comparison, it is worth considering the thermal expansion behaviour of several porous open framework solids that have been reported in literature. This includes the thermal stability of zeolites, zeolite-like structures such as aluminophosphates ($AlPO_4$'s) and metal-organic frameworks (MOFs). A large number of zeolites and $AlPO_4$'s contract on heating, thus exhibiting negative thermal expansion (NTE) behaviour. However, this NTE behaviour is observed only in the high symmetry (high temperature) forms of the structure, after a

displacive phase transition from the low symmetry (low temperature) forms. Examples include zeolites MFI, DOH, DDR, MTN and the aluminium phosphate AFR which display a positive volume expansion coefficient of around + 10 x 10^{-6}/°C in the low symmetry form of the structure [24]. Volume coefficients of - 10 x 10^{-6}/°C are reported in the high temperature forms of these structures [24]. For MOF's the majority of these materials have low thermal stability with the structures decomposing at temperatures around 377 °C [25]. However, one exception is MOF-5 (Zn_4O_{13}-$(C_8H_4)_3$), which displays NTE behaviour of $\alpha_v \approx$ - 16 x 10^{-6}/°C to - 10 x 10^{-6}/°C in the temperature range of 269 to 327 °C.

5.4. Conclusion

In this study, we have prepared $NH_4Fe[BP_2O_8(OH)]$ from low temperature hydrothermal methods forming a powdered material. The structure was refined by the Rietveld refinement method of powder X-ray diffraction data. The crystal structure contains anionic $_{\infty}^{1}\{[BP_2O_8(OH)]^{4-}\}$ chains which are built by alternating $BO_3(OH)$ and PO_4 tetrahedra linked through common corner oxygen atoms. $FeO_5(OH)$ octahedra link these anionic units to form the three dimensional open-framework,$\{Fe[BP_2O_8(OH)]^{-}_{\infty}\}$, consisting of elliptical voids. Charge balancing NH_4^+ species reside within the voids. The resulting structure can be formulated by the following expression:

$$\{Fe[BP_2O_8(OH)]^{-}_{\infty}\} + NH_4^+ = NH_4Fe[BP_2O_8(OH)]$$

Thermal analysis has revealed that the material is stable up to 470 °C. The volume expansion coefficient of this material was found to be α_v = 21.1 x 10^{-6}/°C in the temperature range of 30 - 470 °C. This material displays improved thermal stability as compared to competitive open-framework solids such as the metal–organic frameworks (MOFs). This thermal stability can be attributed to strong covalency within the $BO_3(OH)$ and PO_4 units, creating a rigid framework.

5.5. References

[1] D.W. Breck, *Zeolite molecular sieves: structure, chemistry, and use*. Wiley, New York, 1973

[2] F. Liebau, *Structural chemistry of silicates*. Springer Berlin, 1985.

[3] B. Ewald, Y.X. Huang, R. Kniep, *Zeitschrift für anorganische und allgemeine Chemie* 633 (2007) 1517-1540.

[4] R. Kniep, H. Engelhardt, C. Hauf, *Chemistry of materials* 10 (1998) 2930-2934.

[5] G. Wang, A.-V. Mudring, *Crystals* 1 (2011) 22-27.

[6] O. Yakubovich, I. Steele, O. Dimitrova, *Crystallography Reports* 55 (2010) 760-768.

[7] M. Kritikos, E. Wikstad, K. Walldén, *Solid state sciences* 3 (2001) 649-658.

[8] R. Kniep, I. Boy, H. Engelhardt, *Zeitschrift für anorganische und allgemeine Chemie* 625 (1999) 1512-1516.

[9] J.-X. Mi, H. Borrmann, Y.-X. Huang, S.-Y. Mao, J.-T. Zhao, R. Kniep, *Zeitschrift für Kristallographie-New Crystal Structures* 218 (2003) 171-172.

[10] Y.-X. Huang, G. Schäfer, W. Carrillo-Cabrera, R. Cardoso, W. Schnelle, J.-T. Zhao, R. Kniep, *Chemistry of materials* 13 (2001) 4348-4354.

[11] G.-Y. Yang, S.C. Sevov, *Inorganic chemistry* 40 (2001) 2214-2215.

[12] M. Wiebcke, A. Bögershausen, H. Koller, *Microporous and mesoporous materials* 78 (2005) 97-102.

[13] W. Liu, M. Ge, X. Yang, H. Chen, M. Li, J. Zhao, *Inorganic chemistry* 43 (2004) 3910-3914.

[14] Y.X. Huang, O. Hochrein, D. Zahn, Y. Prots, H. Borrmann, R. Kniep, *Chemistry-A European Journal* 13 (2007) 1737-1745.

[15] W. Liu, M.-R. Li, H.-H. Chen, X.-X. Yang, J.-T. Zhao, *Dalton Transactions* (2004) 2847-2849.

[16] H. Rietveld, *Journal of applied Crystallography* 2 (1969) 65-71.

[17] T.G. Profile, *Bruker AXS*, Karlsruhe, Germany (2009).

[18] K. Brandenburg, *Crystal Impact*, Bonn, Germany, URL: http://www.crystalimpact.com/company.htm.

[19] C.F. Macrae, I.J. Bruno, J.A. Chisholm, P.R. Edgington, P. McCabe, E. Pidcock, L. Rodriguez-Monge, R. Taylor, J.v. Streek, P.A. Wood, *Journal of Applied Crystallography* 41 (2008) 466-470.

[20] S. Filatov, R. Bubnova, *Physics and Chemistry of Glasses-European Journal of Glass Science and Technology Part B* 41 (2000) 216-224.

[21] R. Kniep, H.G. Will, I. Boy, C. Röhr, *Angewandte Chemie International Edition in English* 36 (1997) 1013-1014.

[22] H.-M. Yuan, J.-S. Chen, G.-S. Zhu, J.-Y. Li, J.-H. Yu, G.-D. Yang, R.-R. Xu, *Inorganic chemistry* 39 (2000) 1476-1479.

[23] K.-H. Lii, Y.-F. Huang, V. Zima, C.-Y. Huang, H.-M. Lin, Y.-C. Jiang, F.-L. Liao, S.-L. Wang, *Chemistry of materials* 10 (1998) 2599-2609.

[24] S. Park, R.-W.G. Kunstleve, H. Graetsch, H. Gies, *Studies in Surface Science and Catalysis* 105 (1997) 1989-1994.

[25] W. Zhou, H. Wu, T. Yildirim, J.R. Simpson, A.H. Walker, *Physical Review B* 78 (2008) 054114.

Chapter 6 Merits and pitfalls of Rietveld refinement strategies: the BPO_4 thermoresponsive case

M. W. Mogodi[a], M. A. Fernandes[b], D. G. Billing[a]*

[a]School of Chemistry and DST/NRF Centre of Excellence in Strong Materials, University of the Witwatersrand, Private Bag 3, WITS, 2050, South Africa.

[b]Molecular Sciences Institute, School of Chemistry, University of the Witwatersrand, PO Wits, 2050, South Africa.

*Corresponding author: Professor David Billing

School of Chemistry,

University of the Witwatersrand,

Private Bag 3, WITS, 2050, South Africa

Email: dave.billing@wits.ac.za

Tel no : +27 11 717 6759

Fax no: +27 11 717 6749

This chapter has been submitted to the Journal of Powder Diffraction and has been structured according to the journal's format.

Abstract

The thermal expansion behaviour and crystal structure investigations of tetragonal BPO_4 as a function of temperature has been described by three distinct Rietveld refinement methods using variable temperature powder X-ray diffraction (VT-PXRD) data, collected from room temperature up to 850 °C. Method 1 was the conventional Rietveld refinement of atomic coordinates (free atom), with the focus on comparing the sequentially refined unit cell parameters to parameterization of the unit cell parameters using an empirical equation with respect to temperature. Method 2 concerns the parameterization of the independent atomic coordinates by low-order polynomials with respect to temperature. Method 3 involved applying the rigid body method in the Rietveld refinement procedure, which described the collective movement of atoms in the asymmetric unit as a function of temperature. Both sequential and parametric Rietveld refinements were carried out for the rigid body method. In general, the application of an empirical equation for the description of the unit cell parameters with increasing temperature using the parametric Rietveld method (method 1) was able to reproduce similar physical variations of these parameters with temperature, and provide comparable estimations of the thermal expansion coefficients as compared to parameters derived by the sequential Rietveld protocols. The application of methods 2 and 3 in describing the variation of the crystal structure parameters with increasing temperature were also explained, and were compared to results obtained by the traditional sequential Rietveld refinement protocol. All parametric Rietveld refinement protocols were able to reduce the total number of parameters refined. The application of sequential and parametric Rietveld refinement protocols in all of the methods were processed in the launch mode of Topas version 4.2 software.

6.1. Introduction

Boron phosphate (BPO_4) is a silica (SiO_2) analogous compound and its structure is obtained by replacing half of the silicon atoms by boron atoms and the other half by phosphorous atoms (where BPO_4 = $SiSiO_4$) [1] [2] [3-8]. BPO_4 crystallizes in the high-cristobalite-type structure (space group $I\bar{4}$, Z = 4) and can be obtained in the α-quartz-type structure (space group $P3_121$ and $P3_221$, Z = 3) when subjected to high-pressure and high-temperature conditions. Both polymorphs of BPO_4 consist of corner-sharing boron and phosphorous tetrahedra (figure 6.1).

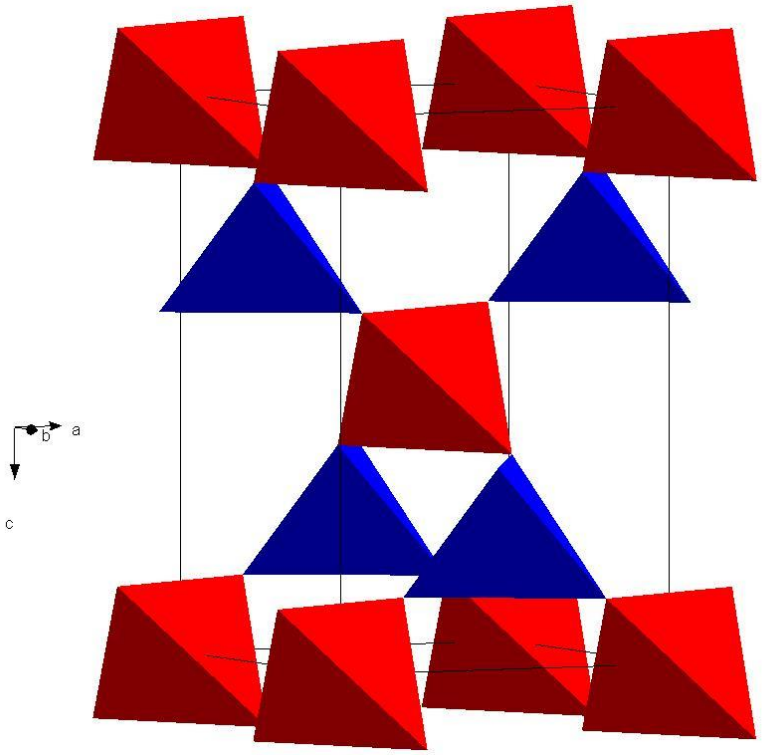


Figure 6.1: The polyhedral representation of the tetragonal unit cell of BPO_4 with blue BO_4 tetrahedra and red PO_4 tetrahedra.

Previous studies for SiO_2-derivative structures such as ternary $A^{III}B^{V}O_4$ (A = B, Al, Ga, Fe; B = P, As) isotypes include detailed high-temperature and high-pressure-crystal structure investigations [2] [9-11]. These studies relate changes in the interpolyhedral (A-O-B) angle and polyhedral tilt angle with changes in temperature and pressure. In general, the crystal

structures displayed contrasting effects as a function of these external conditions. With increase in temperature, there is an increase in A-O-B angle and a decrease in the polyhedral tilt angle. The opposite effects in these structural parameters were observed as a function of pressure. Literature values for the thermal expansion coefficients of BPO_4 and other cristobalite-type isostructural compounds are listed in table 6.1 [1].

Table 6.1: The thermal expansion coefficients (TEC) of several cristobalite-type compounds.

Phase	Crystal system	TEC (ppm. °C)				Reference
		α_a	α_b	α_c	α_v	
SiO_2	Cubic	3.44	-	-	10.35	[12]
BPO_4	Tetrahedral	2.1		12.9	28.2	[1]
$AlPO_4$	Orthorhombic	27.4	27.2	44.5	99.8	[3]
	Cubic	1.93	-	-	5.75	[3]
	-	-	-	-	67.5	[3]
	Cubic	2.02			6.08	[3]
$Al_{0.5}Ga_{0.5}\ PO_4$	Orthorhombic	18.7	22.4	30.4	71.9	[3]
	Cubic	5.52	-	-	16.6	[3]
	-	-	-	-	86.1	[3]
$GaPO_4$	Orthorhombic	18.5	19.8	23.2	62.2	[3]
	Cubic	7.17	-	-	21.4	[3]
	-	-	-	-	105.8	[3]

Silica analogous compounds have been of interest due to their potential use as piezoelectric and some as negative thermal expansion materials. Currently, α-quartz is the most used piezoelectric material [13]. Applications of BPO_4 include its use as a catalyst for organic reactions including isomerisation [14], oligomerisation and the breakdown of dichlorodifluoromethane (Froen-12) [15], [16]. BPO_4 has also shown potential application for non-linear optical (NLO) uses. It has also shown potential use as a blueish-white luminescent material (Ba^{2+} doped and SiO_2/Al_2O_3-doped BPO_4) [17].

The solid state method utilizing H_3BO_3 or B_2O_3 and $(NH_4)_2HPO_4$ as reagent is the common approach for the synthesis of BPO_4. Other methods include sol-gel [17], microwave and hydrothermal synthesis [18]. Recently, nano-sized BPO_4 and nano-BPO_4-based core-shell spheres have been hydrothermally synthesized from H_3BO_3, H_3PO_4 and short-chain n-alkylamines (n = 3, 4) [19]. These nanostructured materials were prepared to improve BPO_4 functional properties such as catalysis.

In this work the tetragonal (high-cristalobite) modification of BPO_4 was synthesized by the solid state method and characterised by variable-temperature powder X-ray diffraction (VT-PXRD). Although investigations into the thermal expansion behaviour and role of the inter-polyhedral angle have been well reported by Achary *et al.* [1], this present study deals with modelling over the entire temperature range the changes in atomic coordinates (including bond distances and angles) of BPO_4 derived using three distinct Rietveld refinement strategies:

Method 1: Free atom Rietveld refinements (conventional refinement)

Method 2: Parametrisation of independent atomic coordinates by low-order polynomials,

Method 3: Rigid body Rietveld refinements (section 2.2.4.)

In all of these methods, both the sequential and parametric Rietveld refinements (chapter 2) were carried out. The changes in cell parameters of BPO_4 were determined using the sequential and parametric Rietveld refinement methods. The sequential and parametric Rietveld refinement processing of the three methods was performed using the Launch mode kernel of the program Topas (Total pattern analysis solution) [20]. The Launch mode kernel allows features such as user-defined constraints and models to be introduced into the refinements. Similar parametric approaches have been conducted in high pressure case studies of As_2O_5 [21] and $LaFeO_3$ [22]. This work focuses on similar parametric approaches to crystal structure refinement, however on high temperature powder X-ray diffraction data of BPO_4.

6.2. Results and discussion

6.2.1. Method 1: Free atom refinements

The conventional sequential Rietveld refinement protocol whereby each powder pattern is refined independently was performed to determine the structural evolution of BPO_4 as a function of temperature. This analysis was also conducted to provide a good indication of the types of changes of structural parameters and figures of merit with temperature, and compare results from this approach to the other approaches. In particular, this method was used to determine the changes in unit cell parameters from the temperature dependent powder X-ray diffractograms. The initial Rietveld refinement was conducted on the lowest temperature dataset i.e. T = 298 K. The structure reported by Schulze [23] was used as a starting model for the refinement. The following parameters were adjusted: scale factor, 6^{th} order Chebychev background polynomial terms and 2 lattice parameters were initially varied. Six profile variables of the PearsonVII profile function were refined. The specimen displacement, zero error and crystallite size broadening terms of a Lorentzian profile were also included into the refinement. The preferred orientation was modeled by a Spherical Harmonics function, followed by the fractional atomic coordinates (oxygen atom) and thermal parameters of each atom being refined. For the higher temperature datasets, the refined parameters of the model resulting from the refinement of the previous temperature formed the starting model to calculate the 'trial' powder patterns that correspond to the next temperature step. Furthermore, the value of the zero error refined at 298 K was fixed for all of the higher temperature datasets. Using this protocol 29 independent parameters were refined in each of the 42 data sets resulting in 1218 parameters in total. Figure 6.2 shows variation of the *a* and *c* unit cell parameters of BPO_4 with temperature determined by independent refinements. A relatively smooth variation for the agreement factors was also obtained, with individual weighted profile R-factor (Rwp) values varying from approximately 7.67 % to 9.11 %, with the average Rwp value of 8.11 %. From figure 6.2, it is also observed that the plot for the temperature dependence of the *c* cell parameters reveal noisy (non-smooth) changes occurring, particularly between 400 and 600 K, due to the finding of false minima during the refinements. The origins of this "non-physical" evolution in the cell parameters can be traced back to the correct calibration of the diffractometer. The accuracy at which the physical

misalignment of the instrument or zero point error of the diffractometer is determined from the refinements is a crucial factor affecting unit cell parameter determination.

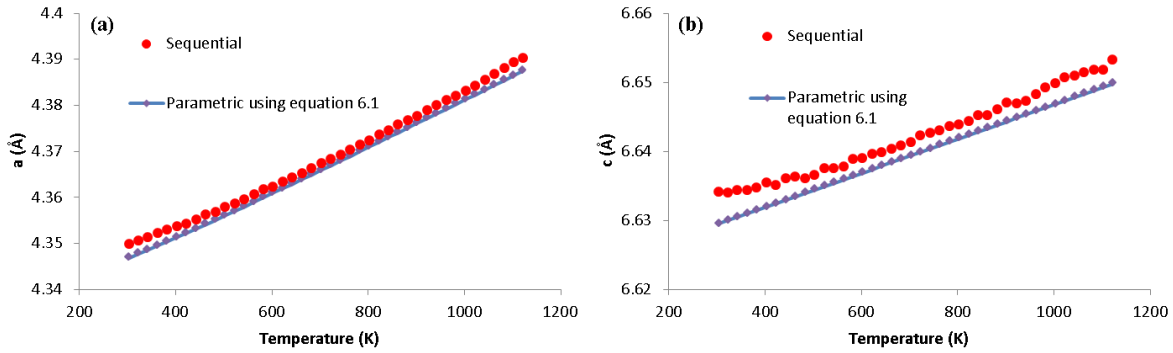


Figure 6.2: Temperature dependence of the *a- and c* unit cell parameters determined by independent and parametric fitting.

To improve the precision and accuracy at which the zero point error parameter is determined, one overall Rietveld refinement was performed to the many powder patterns (parametric Rietveld refinement). Figure 6.3 shows the observed, calculated and difference plots of a typical parametric Rietveld refinement. Using the benefits of the parametric Rietveld refinement method, the zero point error was determined from the entire 21 hour data simultaneously rather than from a single 30 minute data set independently. This methodology resulted in lower Rietveld standard uncertainty (ESD) in the zero error of 0.00358 versus the uncertainty of 0.0892 determined from the independent protocol at 298 K. Utilizing another beneficial feature to parametric Rietveld refinement approach, the BPO_4 unit cell parameters were parameterized with respect to temperature using the expression [24-26] :

$$\ln a = \ln a_0 + \sum_n \frac{c_n \theta_n}{\left[\exp\left(\frac{\theta_n}{T}\right) - 1\right]} \qquad (6.1)$$

where a_0 is the cell parameter at 0 K, θ_n is an Einstein temperature and c_n an empirically derived coefficient. These coefficients were refined simultaneously from the large diffraction

body and fed back as constants into the expression. Table 6.2 shows the coefficients used to determine the temperature dependence of the cell parameters for BPO_4. Using the parametric approach to data analysis, a total of 683 parameters were refined. This is a substantial reduction in the number of adjusted parameters as opposed to the sequential approach. The parameters which were refined simultaneously included the zero error and the coefficients defined in equation 6.1. Parameters adjusted per individual data set were the same as those used for independent refinements. Figure 6.2 shows the dependence of the unit cell parameters of BPO_4 on temperature determined using the parametric method. The effect of imposing the cell parameters using equation 6.1 results in a smooth variation with temperature. The estimation of the linear thermal expansion coefficient can be deduced from the temperature dependence lattice parameters determined by equation 6.1. This includes an expansion along *a*- and *c*- of 11.4 x 10^{-6} K^{-1} and 3.73 x 10^{-6} K^{-1}, respectively and an overall volume expansion of 26.7 x 10^{-6} K^{-1}. These values are comparable to those determined by Achery *et al.*: α_a (12.9 x 10^{-6} K^{-1}), α_c (2.1 x 10^{-6} K^{-1}) and α_v (28.2 x 10^{-6} K^{-1}).

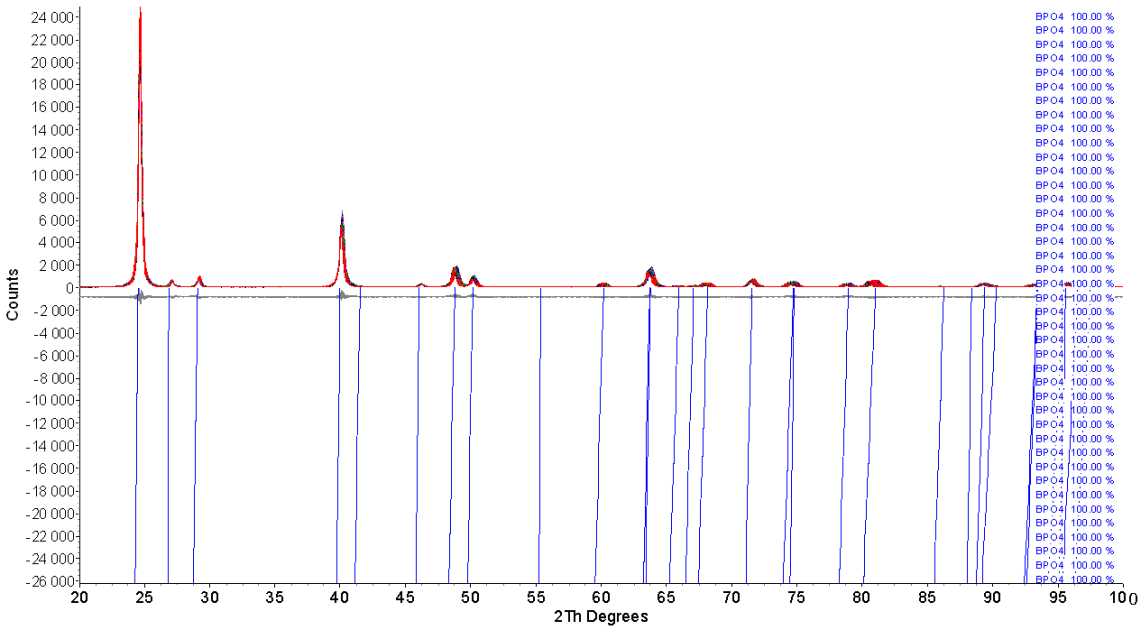


Figure 6.3: Parametric Rietveld refinement plot for 42 powder patterns collected as a function of temperature. The superimposed observed (blue), calculated (red) and difference (grey) powder patterns for BPO_4. Lower ticks (blue) represent reflections of BPO_4 as a function of temperature.

Table 6.2: Coefficients of equation 6.1, used to describe the variation of cell parameters with respect to temperature for BPO_4.

Coefficients	a	c
a_0^*, c_0^{**}	4.34067	6.62311
c_n	0.02645	0.00243
θ_n	500	98

* a_0 is used when describing lattice parameter a, ** c_0 is used when describing cell parameter. These values were determined in a single Rietveld refinement of 42 powder patterns

The possible justification of this parametric approach over the sequential approach is further revealed by the evolution of the R-factor with temperature. An improvement in the overall Rwp of 7.65 % (min = 7.11% max = 8.90%) and a smooth variation with temperature was obtained using the parametric method. Furthermore, slightly lower average standard deviations of the unit cell parameters were obtained using the parametric approach. For the 42 values of the *c*-unit cell parameter the average standard deviation of 0.00594 Å was obtained from sequential fitting and 0.00574 Å from parametric fitting. The Rietveld refinement standard uncertainties were marginal with values of 0.000347 Å from sequential fitting and 0.000342 Å from parametric fitting. Therefore, parametrization of the unit cell parameters of BPO_4 with equation 6.1 and determination of the diffractometer zero error using the many powder patterns measured in the experiment has afforded improved precision and reliability of determined cell parameters as a function of temperature.

6.2.2. Method 2: Low-order polynomials

As can be seen in figure 6.4, the structural evolution of bond lengths, angles and isotropic temperature factors with temperature derived from free atom sequential Rietveld refinement protocol reveal slight deviations from a smooth physically realistic variation, particularly at high temperatures due to the limited data quality. In this section, the evolution of the crystal structure of BPO_4 as a function of temperature is modelled using low order polynomials. This involves fitting a 2^{nd} order polynomial for parameterization of crystallographically-independent fractional atomic coordinates (general positions). The BPO_4 framework consists

of 3 crystallographically independent sites of the x, y and z coordinates of the oxygen atom. For example, the polynomial function used to describe the temperature dependence of the *x*-coordinate of the oxygen site is as follows:

$$Ox(T) = c_o + c_1T + c_2T^2 \qquad (6.2)$$

where c_o, c_1 and c_2 are the parameters refined simultaneously from the entire data set and are fed back into the expression. This approach leads to 3 new parameters per fractional atomic coordinate. However, using the parametric Rietveld refinement this parameterization reduces the number of parameters required to describe the crystal structure evolution with temperature to a total of 935. Parameterization of the oxygen coordinates also leads to an improvement in the figures of merit with an overall Rwp of 7.63 % obtained by this method whereas an overall Rwp of 8.11 % was obtained with the free atom Rietveld refinement method. Furthermore as shown in figure 6.4, parameterization of oxygen atomic coordinates with equation 6.2 is suitable to describe the variation of key structural parameters which contribute to low positive thermal expansion behaviour i.e. B-O-P and B-P changes with temperature. Another key structural parameter is the increase in the thermal motion of oxygen atoms with temperature which lead to an "apparent decrease" in the P-O distance as a function of temperature [1]. Using this parametric method, improved average Rietveld refinement standard uncertainties of the oxygen thermal parameters were obtained as a function of temperature: 0.0536 $Å^2$ (method 2) and 0.0922 $Å^2$ (independent refinements). The variation in this parameter also has a smoother increase with temperature and therefore lower standard deviations of all individual values i.e. 0.00561 $Å^2$ (method 2) versus 0.0105 $Å^2$ (independent refinements). These results justify the choice of parameterization. These results also reveal that the refinement by free atom methods leads to the structure being trapped in a minimum.

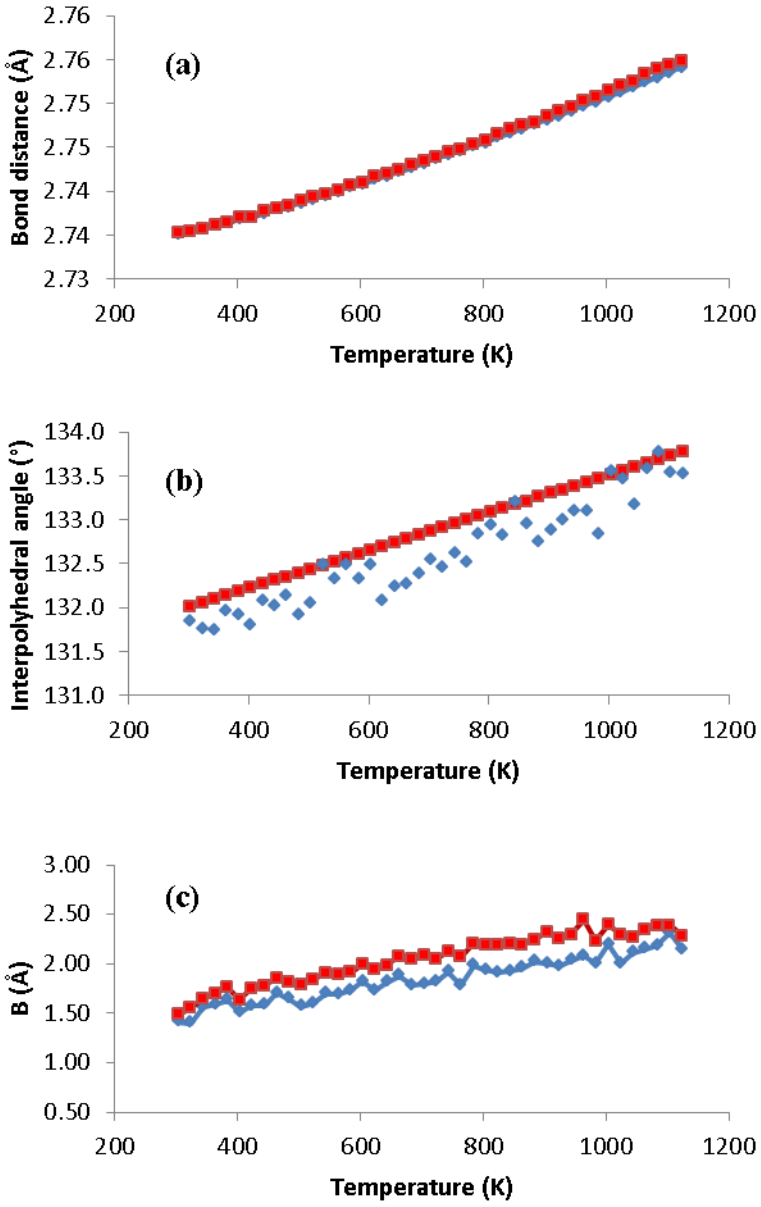


Figure 6.4: (a) B-P non-bonded distances, (b) interpolyhedral B-O-P bond angles and (c) isotropic thermal parameter for oxygen atom as a function of temperature determined by method 2 (red curves) and independent free atom refinements (blue curves).

6.2.3. Method 3: Rigid body Rietveld refinements

In this section the rigid body approach in the Rietveld refinement was performed to model the dependence of the crystal structure of BPO_4 on temperature. This approach is aimed at minimizing the fluctuations in the structural parameters refined by the traditional sequential refinement. It can be shown from the free atom refinements that P-O and B-O bonds showed

very little change with changing temperature (figure 6.5a). This supports the assumption of a rigid body description of the asymmetric unit of BPO_4. Figure 6.6 show a rigid body of all atoms in the asymmetric unit formulated using the z-matrix description. The sequence of lines which follow after the z-matrix statements describe the structural changes with temperature of this material in terms of modelling the internal (orientation) and external (location) degrees of freedom of the rigid body. The external variations with temperature include rotation angles viz. Rx, Ry, Rz and translation viz. Tx, Ty, Tz along the x, y, z Cartesian coordinates of the rigid body which is collinear with the crystallographic axes. Furthermore internal variations of the rigid body include refining the B-O, P-O bond length and B-O-P bond angle. Therefore 9 parameters are used to model the orientation and positional location of the asymmetric unit with temperature.

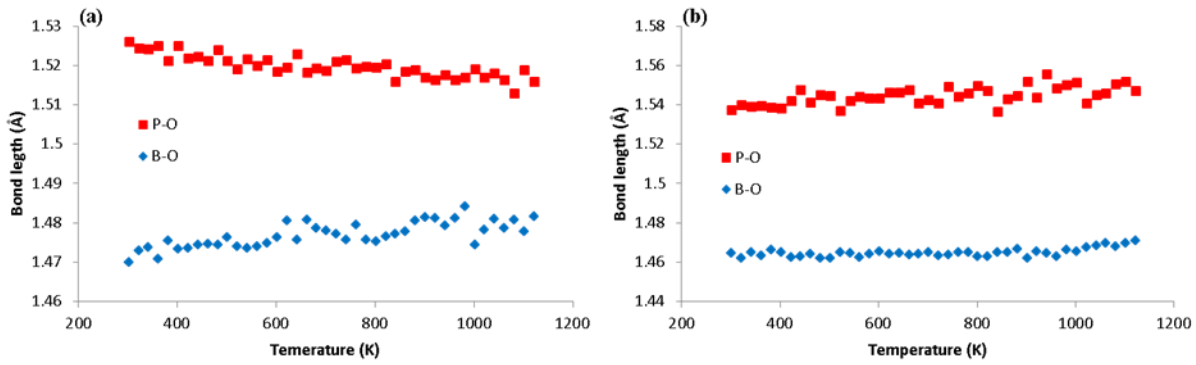
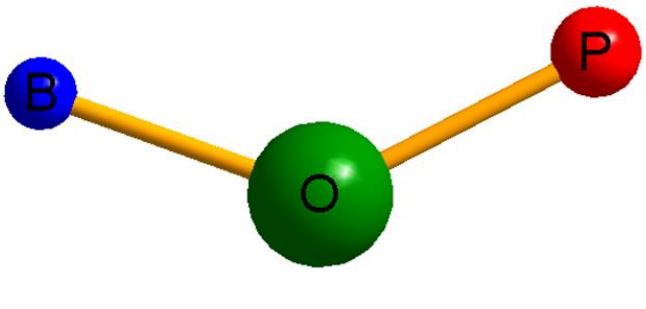


Figure 6.5: Temperature dependence of P-O (red) and B-O (blue) bond lengths for BPO_4 obtained by (a) free atom sequential refinements and (b) rigid body parametric Rietveld refinements.




```
rigid

   z_matrix P1
   z_matrix O1 P1  1.5327
   z_matrix O1 B1  1.4580  P1 132.326

Rotate_about_axes
(xrot -44.15446`, yrot  40.16148`, zrot  3.60089`)
Translate
(xtrans -0.00831`, ytrans  0.00084`, ztrans -0.00212`)
```

Figure 6.6: Rigid body description using Z-matrix notation of the asymmetric unit of BPO_4 (formulated in Topas).

Using this rigid body approach to Rietveld refinements, both sequential and parametric Rietveld refinements were carried out. The expected structural changes (bond lengths and angles) with temperature were obtained using both the sequential and parametric approaches. Figure 6.7 shows the variation of the x- and z- rotation angles for the asymmetric unit with temperature derived by sequential and parametric refinements. Large oscillations in these refined parameters were observed with temperature when following the sequential approach. Using the parametric protocol, the rotation parameters of the z-matrix were constrained through the use of a function similar to equation 6.1. This parameterisation reduced the oscillations in these parameters as a function of temperature. Furthermore, due to the reduction in the total number of refined parameters obtained via the parametric protocol (1011 parameters), the results of this protocol has been chosen for the remainder of this report. Figure 6.8 shows a comparison of the variation of the key structural parameters with temperature derived from the free atom independent Rietveld refinement and rigid body parametric Rietveld protocol. In comparison, the parameterisation of the rigid body did not improve the precision in the derived B-P non-bonded distance and the corresponding B-O-P angle between these separations. However, the description of the asymmetric unit of BPO_4 as a function of temperature by the rigid body approach led to slightly improved figures of merit

compared to independent atom refinements (figure 6.9). Average Rwp of 7.85 % (overall χ^2 of 1.35) and a smooth trend in the Rwp was obtained from all powder patterns using this approach. The temperature dependence of the B-O, P-O bond length are shown in figure 6.5b. This model leads to slightly higher values in average B-O, P-O bond distances compared to free atom derived values. Little oscillations in the individual bond distance were observed, with average standard deviations on the B-O, P-O bond distances of 0.0022 Å and 0.0039 Å were obtained, respectively. Rietveld refinement based on rigid PO_4 tetrahedra and having the internal and external degrees of freedom description was also attempted. This refinement led to essentially the same variations in B-O, P-O bond lengths and B-O-P bond angle, similarly as above. The overall benefits in reduced Rwp and number of parameters refined remained.

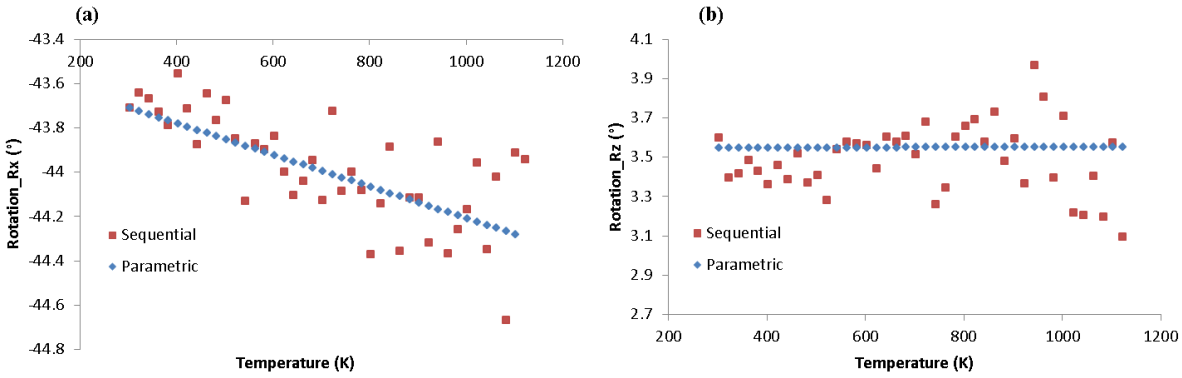


Figure 6.7: Temperature dependence of the (a) x- and (b) z- rotation angles for the asymmetric unit of BPO_4 obtained by sequential and parametric Rietveld refinements.

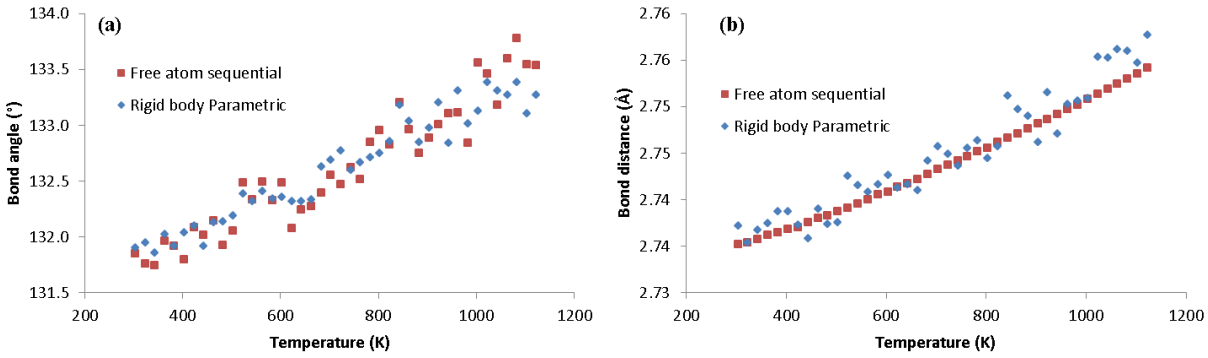


Figure 6.8: (a) B-O-P bond angles and (b) B-P distances with temperature derived from the free atom sequential Rietveld refinement and rigid body parametric Rietveld refinements.

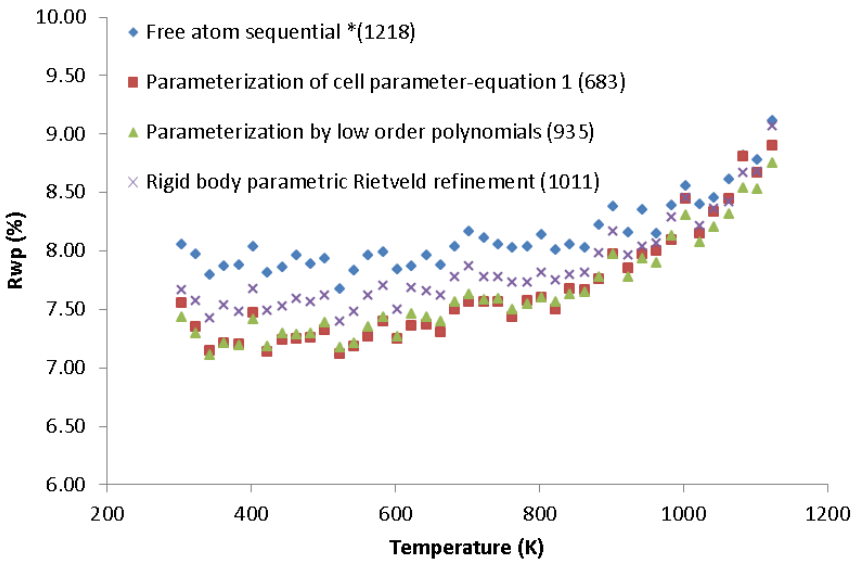


Figure 6.9: Rwp values per temperature of the investigated methods of Rietveld refinement. *Values in brackets are the number of parameters refined

6.3. Conclusion

A number of different Rietveld refinement approaches were investigated with the objective of improving the precision and accuracy at which temperature dependent crystal structure variables can be determined. All of the refinement strategies were able to confirm the thermal expansion behaviour of BPO_4 and the role of the bond lengths and angles with changing temperature. In comparison to the conventional free atom Rietveld analysis, the 3 methods of parameterizing the temperature dependence of the unit cell parameters or crystal structure parameters generally led to smooth physically realistic variations of refined and calculated parameters as well as lower Rwp values with increase in temperature. This provides evidence that the applied parametric models were reliable. The ability to apply empirical functions to the refinement of temperature-dependent diffraction data was critical in reducing the number of free variables. Furthermore, certain free parameters e.g. zero error were determined from the entire datasets which resulted in lower statistical errors and uncertainties. Method 2 involving parameterizing the atomic coordinates using low order polynomials showed the best quality refinements of the powder data. The rigid body description for the collective movement of atoms of the asymmetric unit of BPO_4 was able to reduce the number of

degrees of freedom. This reduces the independent movement of atoms with temperature and therefore reduces the ability for each atom to distort in a non-physical way to fit the diffraction data. The parametrically fitted lattice parameters were able to reduce spontaneous fluctuations in the lattice parameters with temperature and were also able to calculate coefficients of expansions which agreed well to those derived elsewhere in literature [1].

6.4. References

[1] S. Achary, A. Tyagi, *Journal of Solid State Chemistry* 177 (2004) 3918-3926.

[2] J. Haines, O. Cambon, E. Philippot, L. Chapon, S. Hull, *Journal of Solid State Chemistry* 166 (2002) 434-441.

[3] S. Achary, O. Jayakumar, A. Tyagi, S. Kulshresththa, *Journal of Solid State Chemistry* 176 (2003) 37-46.

[4] G.E.R. Schulze, *Z. Phys. Chem*. 24 (1934) 215.

[5] Y. Muraoka, K. Kihara, *Physics and Chemistry of Minerals* 24 (1997) 243-253.

[6] P. Worsch, B. Koppelhuber-Bitschnau, F. Mautner, P. Krempl, W. Wallnöfer, P. Doppler, J. Gautsch, *Materials Science Forum, Trans Tech Publ* (2000) pp. 914-917.

[7] H.N. Ng, C. Calvo, *Canadian Journal of Physics* 55 (1977) 677-683.

[8] P. Worsch, B. Koppelhuber-Bitschnau, F.A. Mautner, P.W. Krempl, W. Wallnöfer, *Materials Science Forum* (1998) pp. 600-605.

[9] E. Philippot, P. Armand, P. Yot, O. Cambon, A. Goiffon, G. McIntyre, P. Bordet, *Journal of solid state chemistry* 146 (1999) 114-123.

[10] E. Philippot, D. Palmier, M. Pintard, A. Goiffon, *Journal of Solid State Chemistry* 123 (1996) 1-13.

[11] J. Haines, C. Chateau, J.M. Léger, C. Bogicevic, S. Hull, D.D. Klug, J.S. Tse, *Physical Review Letters* 91 (2003) 015503.

[12] G.A. Lager, J.D. Jorgensen, F.J. Rotella, *Journal of Applied Physics* 53 (1982) 6751-6756.

[13] H. Ogi, T. Ohmori, N. Nakamura, M. Hirao, *Journal of Applied Physics* 100 (2006) 053511-053517.

[14] S. Gao, J.B. Moffat, *Journal of Catalysis* 180 (1998) 142-148.

[15] S. Imamura, T. Higashihara, K. Utani, *Industrial & Engineering Chemistry Research* 34 (1995) 967-970.

[16] S. Imamura, K. Imakubo, S. Furuyoshi, H. Jindai, *Industrial & Engineering Chemistry Research* 30 (1991) 2355-2358.

[17] C.K. Lin, Y. Luo, H. You, Z. Quan, J. Zhang, J. Fang, J. Lin, *Chemistry of Materials* 18 (2005) 458-464.

[18] A. Baykal, M. Kizilyalli, M. Toprak, R. Kniep, *Turkish Journal of Chemistry* 25 (2001) 425-432.

[19] S. Chen, M. Ye, H.-H. Chen, X.-X. Yang, J.-T. Zhao, *Journal of Inorganic and Organometallic Polymers and Materials* 19 (2009) 139-142.

[20] C.A. A., Bruker AXS, Karlsruhe, 2007.

[21] I. Halasz, R.E. Dinnebier, R. Angel, *Journal of Applied Crystallography* 43 (2010) 504-510.

[22] M. Etter, M. Mueller, M. Hanfland, R.E. Dinnebier, *Zeitschrift für Kristallographie. Crystalline materials* 229 (2014) 246-258.

[23] G.E. Schulze, *Naturwissenschaften* 21 (1933) 562-562.

[24] G.W. Stinton, J.S.O. Evans, *Journal of Applied Crystallography* 40 (2007) 87-95.

[25] J.S. Evans, T. Mary, *International journal of inorganic materials* 2 (2000) 143-151.

[26] R.R. Reeber, *physica status solidi (a)* 32 (1975) 321-331.

Chapter 7 General conclusions

In this thesis, variable-temperature powder X-ray diffraction (VT-PXRD) was used to study the crystallographic structure, thermal expansion properties and phase stability of various borophosphates. The necessity of this study is justified by the lack of literature concerning the thermoresponsive analysis of these newly discovered materials. Special emphasis was placed on designating the studied borophosphates as porous and non-porous borophosphates. Additional characterisation techniques of these materials were also conducted in order to facilitate better understanding of the crystal structure, thermal properties and crystal morphology.

In chapter 3, an investigation into the thermal expansion behaviour of non-porous borophosphates $ABPO_5$ (A = Ca, Sr, Ba) was conducted using VT-PXRD measurements. The aim was to determine the coefficients of thermal expansion and probe the crystal structure (arrangement of atoms in the unit cell) variation with temperature. The most important findings were:

- The order of volume expansion coefficient (α_v) of the studied compounds was found to be: $CaBPO_5 > SrBPO_5 > BaBPO_5$.
- From these isostructural phases, it was also shown that the lattice parameters of the respective compounds had a direct dependence on the alkali earth metal ionic radii (A^{2+}), with the lattice parameters of the respective phases increasing with the increase in A^{2+} radii.
- It was also found that upon heating, the bond lengths and angles of the $ABPO_5$ compounds displayed similar structural behaviour.
- A linear increase in the average B-O and P-O distances with increasing temperature was observed.
- B-O-P bridging angles, θ, displayed small changes with temperature, whereas, significant increases were observed in the non-bonded B-P distances with temperature for all $ABPO_5$ compounds.
- For each compound, these non-bonded B-P distances also had correspondingly large coefficients of expansion, and thus was concluded that the positive thermal expansion behaviour in all $ABPO_5$ compounds was driven by increases in B-P distances as a function of temperature.

- Thermal changes in the B-O and P-O distances were also believed to contribute to the observed thermal expansion behaviour in the respective $ABPO_5$ compounds.

In chapter 4 and 5 VT-PXRD experiments were performed on porous borophosphates, $NaM^{II}(H_2O)_2[BP_2O_8](H_2O)$; M^{II} = Co (**I**), Mn (**II**) and $(NH_4)_{0.5}M^{II}_{1.25}(H_2O)_2[BP_2O_8](H_2O)_{0.5}$; M^{II} = Co (**III**), Mn (**IV**) and $NH_4Fe(III)[BP_2O_8(OH)]$, respectively. Rietveld refinement method was used to determine the fluctuations of the crystal structure of $NH_4Fe(III)[BP_2O_8(OH)]$ up to its decomposition temperature; however, the work was restricted to room temperature crystal structures of $NaM^{II}(H_2O)_2[BP_2O_8](H_2O)$; M^{II} = Co (**I**), Mn (**II**) and $(NH_4)_{0.5}M^{II}_{1.25}(H_2O)_2[BP_2O_8](H_2O)_{0.5}$; M^{II} = Co (**III**), Mn (**IV**) due to low diffraction data quality of the powder patterns collected at the higher temperatures. This was considering that for the $NaM^{II}(H_2O)_2[BP_2O_8](H_2O)$; M^{II} = Co (**I**), Mn (**II**) and $(NH_4)_{0.5}M^{II}_{1.25}(H_2O)_2[BP_2O_8](H_2O)_{0.5}$; M^{II} = Co (**III**), Mn (**IV**) phases, each diffraction pattern was measured for a relatively long time span (approximately 45 minutes per pattern). Therefore for these phases, the higher temperature crystal structure variations were identified by comparing the crystal structure changes of the compound $NaZn(H_2O)_2[BP_2O_8].(H_2O)$ (which possess the same framework topology as the studied compounds) investigated by earlier researchers. The most important findings were:

- With the use of high temperature diffraction methods, the decomposition temperature and the subsequent decomposition products formed for all of the studied porous borophosphates were identified.
- Changes to the powder diffraction line positions and intensities as a function of temperature were important features in the respective VT-PXRD patterns in relaying the structural changes of the studied compounds.
- For these porous compounds, $NH_4Fe(III)[BP_2O_8(OH)]$ displayed the highest thermal stability as compared to the $NaM^{II}(H_2O)_2[BP_2O_8](H_2O)$; M^{II} = Co (**I**), Mn (**II**) and $(NH_4)_{0.5}M^{II}_{1.25}(H_2O)_2[BP_2O_8](H_2O)_{0.5}$; M^{II} = Co (**III**), Mn (**IV**) phases.
- However, it was observed that the crystal structures of $NaM^{II}(H_2O)_2[BP_2O_8](H_2O)$; M^{II} = Co (**I**), Mn (**II**) and $(NH_4)_{0.5}M^{II}_{1.25}(H_2O)_2[BP_2O_8](H_2O)_{0.5}$; M^{II} = Co (**III**), Mn (**IV**) phases undergo a series of dehydration (and additionally deammoniation for $(NH_4)_{0.5}M^{II}_{1.25}(H_2O)_2[BP_2O_8](H_2O)_{0.5}$; M^{II} = Co (**III**), Mn (**IV**) phases) processes whereas, $NH_4Fe(III)[BP_2O_8(OH)]$ undergoes a single deammoniation process at

temperatures exceeding 450 °C which led to the disintegration of the framework and formation of unidentified amorphous phases.

- TGA analysis of each compound, which measured the weight loss as a function of temperature, was able to compliment the VT-PXRD analysis by confirming the decomposition temperatures and identifying the decomposition species.
- Even more critically, by measuring the heights at each decomposition step, TGA analysis was able to determine the relative amounts of the volatile species present in the as-synthesized compounds, which provided a way of confirming the correct chemical formulae of the respective studied compounds, in particular for $(NH_4)_{0.5}M^{II}_{1.25}(H_2O)_2[BP_2O_8](H_2O)_{0.5}$; M^{II} = Co (**III**), Mn (**IV**) phases.

While VT-PXRD and TGA experiments were able to characterise the thermal properties of the investigated porous compounds, one issue identified was the mismatch in the temperatures recorded by the respective techniques which correspond to the respective thermal processes. This mismatch was identified as being due to the temperature scanning mode conducted by the respective thermal analysis techniques. VT-PXRD procedure of constantly heating and then holding at a particular temperature created an apparent thermal lag (and therefore lower temperatures recorded for the decomposition process) as compared to the continuous temperature mode of analysis offered by TGA.

In chapter 6, the merits and pitfalls of various Rietveld refinement methods were investigated that can be used in the analysis of non-ambient PXRD data. More specifically, the different methods were used in the quantitative analysis of the evolution of the crystal structure and lattice parameters of the non-porous borophosphate BPO_4. The structural models included the traditional sequential refinement of "free" atomic coordinates, determination of the diffractometer zero error during the parametric Rietveld refinement approach to data analysis, modelling the evolution of the lattice parameters as a function of temperature with an empirically derived equation during the parametric Rietveld refinement approach to data analysis, modelling the variation of independent atomic coordinates as a function of temperature by low-order polynomials performed during the parametric Rietveld refinement approach and modelling the variation of a group of atoms as a function of temperature using the rigid body method performed during the parametric approaches. The most important findings were:

- With the implementation of the parametric approach to data analysis it was shown that it is possible to impose a particular physical variation to the various parameterised crystallographic variables.

- The various approaches investigated were shown to provide satisfactory variations of the crystal structure and lattice parameters, respectively, which were also comparatively similar to these parameters determined from earlier thermoresponsive studies of BPO_4. Perhaps the one concern was the slight underestimation of the lattice parameter variation with temperature produced from the parametric modeling of the lattice parameters using an empirically derived function compared to the sequentially derived lattice parameters (section 6.2.1). However, these parametrically derived lattice parameters had fewer fluctuations (therefore smooth evolution) as a function of temperature.

- In fact the parametric modelling of the crystal structure with low order polynomials and rigid body models (sections 6.2.2 and 6.2.3, respectively) also generated smooth variations of the crystal structure parameters as a function of temperature.

- It was also shown that performing a single Rietveld refinement of all the powder patterns via the parametric method substantially reduced the total number of refined parameters and generally produced improved fits of the models to the evolving diffraction body.

The validity of implementing the above approaches to data analysis was further supported by the observation that the studied material (BPO_4) did not show abrupt changes in its physical properties (e.g. a decomposition process) and that the models were applied on diffraction data of sufficient quality.

A relationship between the synthetic approach and the resulting crystal structure of the borophosphate compounds was also established. It was seen that the hydrothermal methodology afforded less dense, porous structural architectures, whereas the high-temperature solid state methodology afforded dense, non-porous structural architectures. In general, the investigated porous borophosphates had lower thermal stability. A critical finding was that the small volatile molecules within the pores of the porous borophosphates dictated the thermal stability range of the material.

Therefore, future improvements into the investigation of the "Structure and thermoresponsive behaviour of porous and non-porous borophosphates" would be:

- Optimise the current or explore new, synthetic avenues for forming new porous and non-porous borophosphates. This will be aimed at expanding on the exiting structural diversity of borophosphates.
- For better understanding of the crystal structures of the investigated porous and non-porous borophosphates, alternative crystal structure refinement models can be implemented during the Rietveld refinement procedure, including implementing physically realistic models.

- It is beneficial to perform combined and simultaneous VT-PXRD and TGA experiments of the porous compounds. This would ensure more cohesive recorded temperature measurement results of the various thermal processes.

- The use of extremely powerful synchrotron radiation sources can be pursued. This would be particularly beneficial for the porous borophosphates; to collect better quality powder diffraction patterns as a function of temperature (particularly for $NaM^{II}(H_2O)_2[BP_2O_8](H_2O)$; M^{II} = Co (**I**), Mn (**II**) and $(NH_4)_{0.5}M^{II}_{1.25}(H_2O)_2[BP_2O_8](H_2O)_{0.5}$; M^{II} = Co (**III**), Mn (**IV**) phases) for better crystal structure characterisation at elevated temperatures.

- Alternative synchrotron techniques such as the pair distribution function (PDF) and X-ray absorption spectroscopy techniques which probe the short-range structural information would be beneficial to characterise the amorphous materials formed at high temperatures by the porous borophosphates.

Appendix 1: Calibration of the Bruker D2 Advance diffractometer using the NIST LaB_6 line position and profile shape standard (SRM 660a).

A1.1: Introduction

The purpose of this section is to evaluate the accuracy of the alignment of the in-house Bruker D2 phaser diffractometer. The Standard Reference Material (SRM), SRM LaB_6 660a, issued by The National Institute of Standard and Technology (NIST) was used to evaluate the instruments performance. Typically, the overall peak profile depends on the sample microstructure and instrumental contributions (figure A1.1) such as [1]:

- Size broadening resulting from the size and shape of the crystallites
- Stress broadening resulting from atomic dislocations (vacancies, dislocations substitutional defects)
- Misalignment of the diffractometer goniometer.

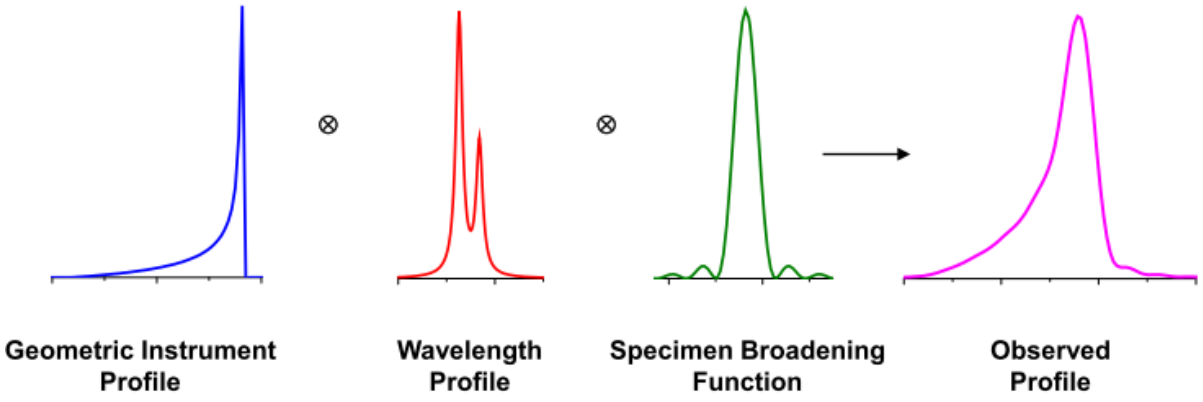


Figure A1.1: Line broadening effects to the observed profile [2].

The first two effects discussed above can be reduced. This is done by using the material LaB_6, which is synthesized with the lattice strain broadening being minimized and a crystallite size which is larger than the typical size which leads to size broadening (2 to 5 µm range) [3]. However, the random orientation of crystallites is still maintained. With the separation of specimen contributions (first two points above), it is possible to evaluate the

Instrumental Profile Function (IPF). The components of the IPF include the geometric instrument profile and the wavelength profile (figure A1.1). Therefore using the NIST SRM 660a standard, the peak positions and peak shapes or full width at half maximum (FWHM) recorded by the Bruker D2 Phaser were evaluated. Profile fitting techniques were used to determine the peak positions and peak widths (FWHM) of the observed diffraction pattern of LaB_6. A well calibrated instrument ensures applications such as correct identification and quantification of phases, stress analysis and unit cell indexing (dependent on correct peak positions), as well as particle size and microstructure analysis (dependent on correct peak widths) are correctly determined.

A1.2: Results

In order to evaluate the performance of the in-house D2 diffractometer in determining precise and accurate profile positions, the certified lattice parameter and the (hkl) values for the sample LaB_6 were obtained from the NIST Certificate of analysis [3]. The in-house Bruker D2 Phaser diffractometer measures data using a locked coupled 2theta configuration and includes a sealed tube Co X-ray source, Bruker Lynxeye PSD detector with primary and secondary beam Soller slits. More details about this instrument are discussed in section 2.4.1 and given in table A1.1.

Table A1.1: Instrument settings for the Bruker D2 Phaser

X-ray source	$CoK_{\alpha1}/K_{\alpha2}$ with λ = 1.78897/1.79285 Å
Goniometer	Primary radius (70.7 mm) Secondary radius (70.7 mm)
Detector	Bruker Lynxeye PSD (Detector opening 5 °)
Slits	Primary Soller Slits (2.5 °) Secondary Soller Slits (2.5 °)
Temperature	Ambient

A1.2.1: Line position evaluation

The peak positions of the measured diffraction pattern were found using the fundamental parameters approach proposed by Cheery and Coelho in 1992 [4]. The fundamental parameters approach is a profile fitting method, which is a function of the X-ray emission profile from the target, the physical dimensions of the diffractometer and the physical variables of the sample. The physical variables of the diffractometer that can be convoluted in the fundamental parameter equation include:

- The receiving-slit width
- The receiving-slit length
- The X-ray source size
- The flat-specimen error function
- The absorption function
- The specimen tilt
- The defocusing function

Therefore as opposed to other profile fitting methods, the line profiles are fitted using physically meaningful parameters (instrumental functions) instead of ordinary numerical profiles. The benefit of such an analysis is that a misaligned diffractometer or sample can be identified as the refined diffractometer or sample variables will differ from the physically realistic (measured) diffractometer or sample variables. For this analysis the $CoK_{\alpha 1}/K_{\alpha 2}$ emission profile was used. A total of sixteen independent parameters were refined: one histogram scale factor, 2^{nd} order Chebychev background polynomial terms, one cubic lattice parameter, terms including the position and intensity of the "X-ray tube tails" described by Bergmann and co-worker in 2000 [5], Soller slit value in the "full" axial divergence model, specimen displacement, LP factor, sample absorption correction term, crystallite size broadening terms of a Lorentzian profile. Figure A1.2 shows the observed, calculated and difference profiles together with figures of merit for the refinement.

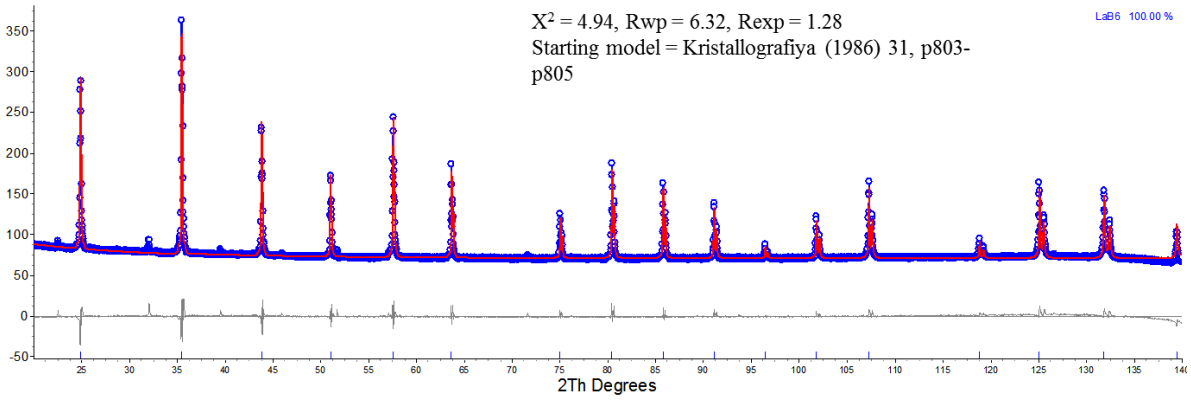


Figure A1.2: Observed (blue line with circles), calculated (red line) and difference patterns (grey line) of LaB_6 at ambient temperature.

The difference between the d-spacing of NIST LaB_6 vs ($h^2 + k^2 + l^2$) reported by NIST and the in-house data are shown in figure A1.3. For comparative purposes, line profile differences are expressed in d-spacing (interplanar spacing) as the in-house diffractometer uses Co-radiation (1.78897/1.79285 Å) while the NIST diffractometer uses a Cu-source radiation (1.5405929 Å). A second order polynomial can be fitted to the differences in the d-spacing. There is an increase in the dependence of the interplanar separation at low d-spacing's ($h^2 + k^2 + l^2 \leq 4$). Overall, there is a very small difference between the d-spacing of the reported datasets, with the largest deviation being 0.0003 Å for the (1 0 0) reflection. The certified lattice parameter for LaB_6 determined by NIST is 4.1569162 Å ± 0.0000097 Å. The lattice parameter measured using the in-house diffractometer is 4.1566518 Å ± 0.0000184 Å. This represents a small difference of 0.026 %. From this we can conclude that the alignment of the in-house Bruker D2 Phaser is satisfactory and suitable for providing precise and accurate peak positions.

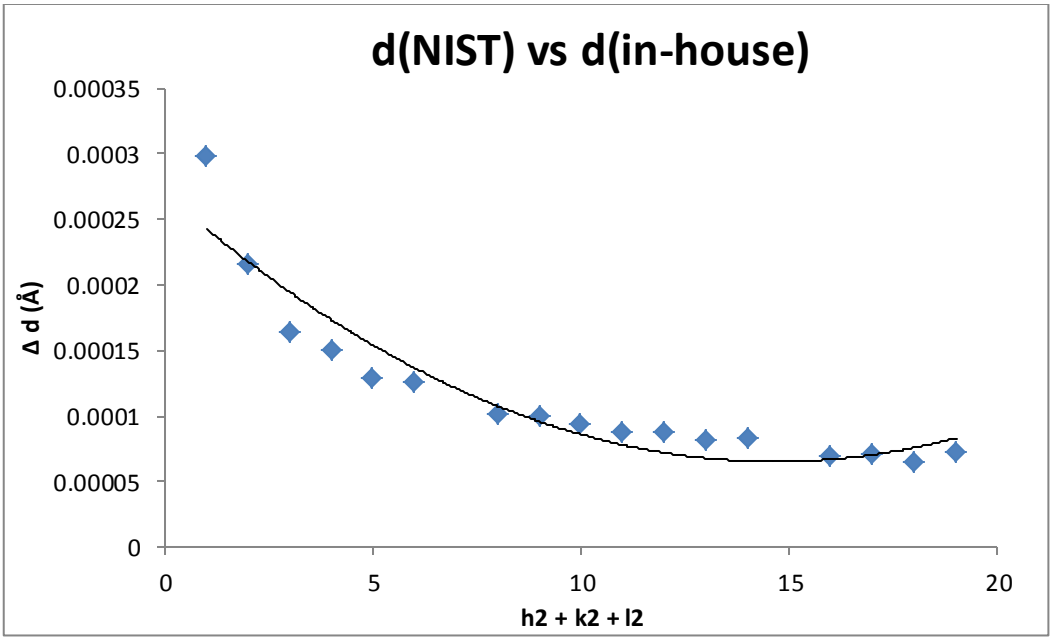


Figure A1.3: Difference in d-spacing from the NIST vs in-house Bruker D2 Phaser data for SRM 660a.

A1.2.2: Line shape evaluation

The full width at half maximum (FWHM) as a function of 2θ of the LaB_6 sample was determined in order to evaluate the instrument peak broadening, as shown in figure A1.4. The FWHM values were found by fitting each peak with a split-Pearson VII function. The observed increase in line broadening effects as a function of Bragg angle is a known phenomena [6]. This increase was described by a second order polynomial. Therefore, the FWHM vs 2θ (figure A1.4) serves as a calibration curve for the instrumental contribution to the line broadening.

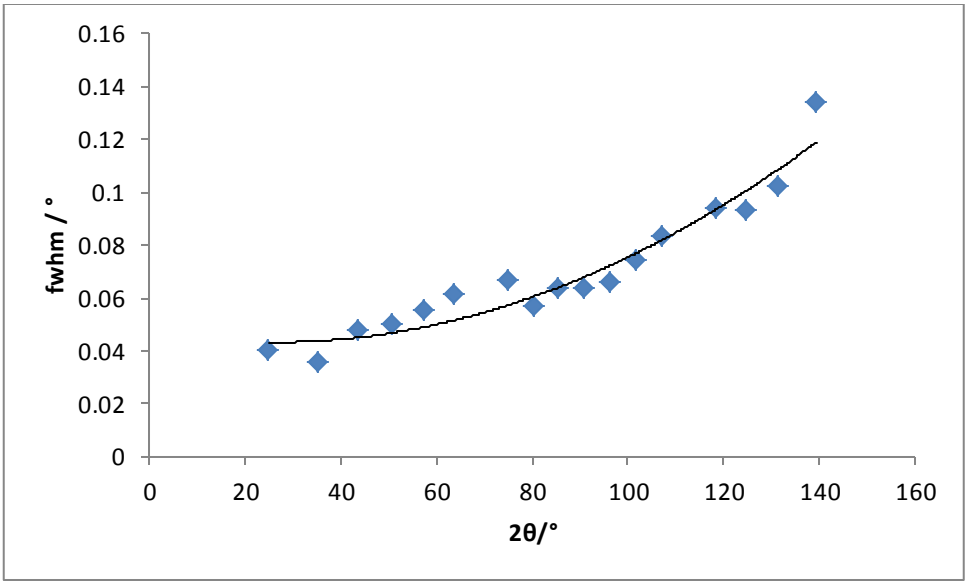


Figure A1.4: FWHM vs 2θ for SRM 660a evaluated on the in-house Bruker D2 Phaser.

A1.3: References

[1] V.K. Pecharsky, P.Y. Zavalij, Fundamentals of powder diffraction and structural characterization of materials. Springer, 2009.

[2] D.B. James P. Cline, Donald Windover, Robert B. Von Dreele, Ryan Winburn, Peter W. Stephens, James J. Filliben, Albert Henins, Accuracy in Powder Diffraction IV, NIST - Gaithersburg, MD, 2013.

[3] J. Cline, R. Deslattes, J. Staudenmann, L. Hudson, A. Henins, R. Cheary, *NIST, Gaithersburg, MD* (2000).

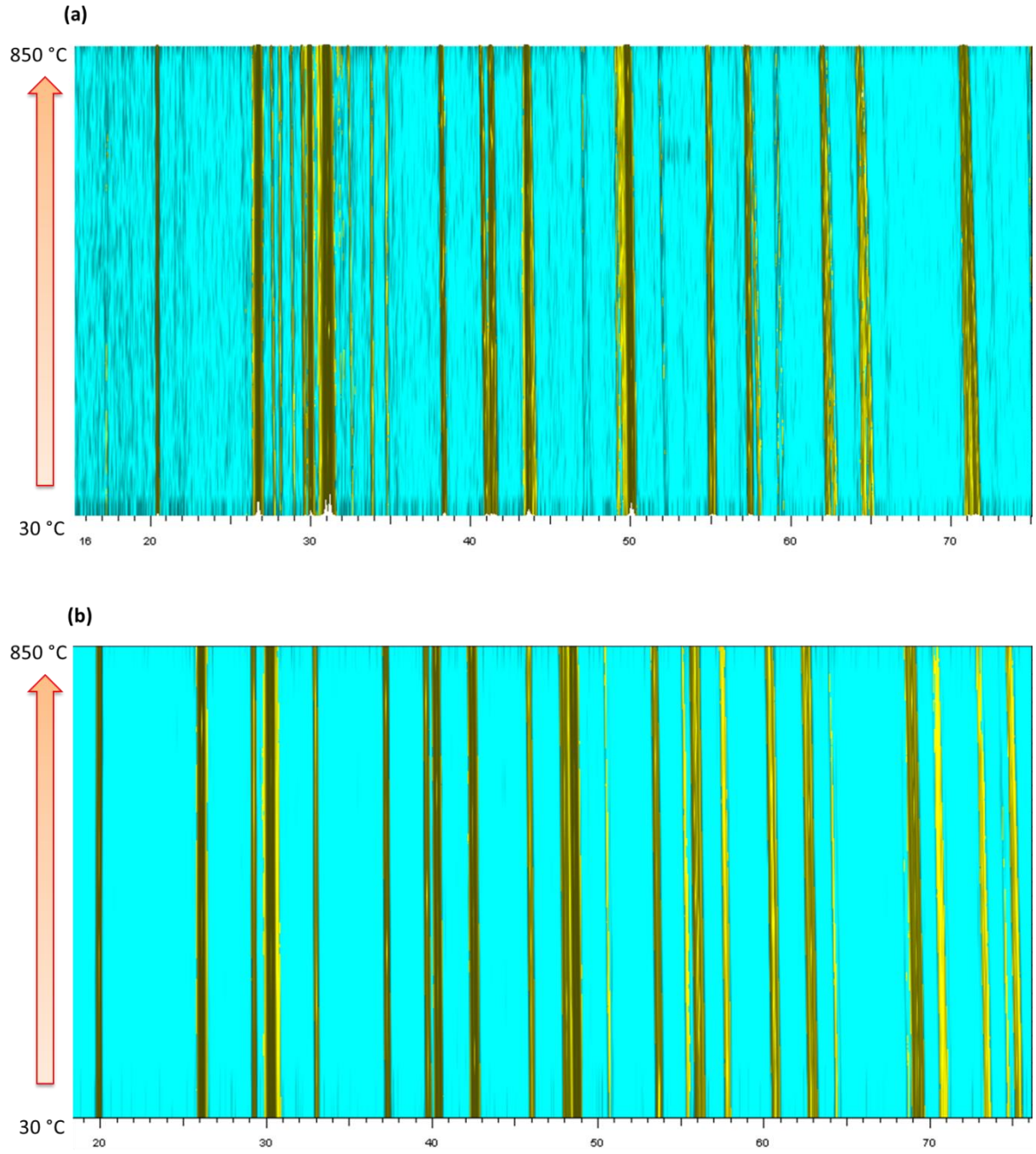
[4] R.W. Cheary, A. Coelho, *Journal of Applied Crystallography* 25 (1992) 109-121.

[5] J. Bergmann, R. Kleeberg, A. Haase, B. Breidenstein, *Materials science forum, Trans Tech Publ* (2000) pp. 303-308.

[6] A. Clearfield, J.H. Reibenspies, N. Bhuvanesh, *Principles and applications of powder diffraction*. John Wiley and Sons, Ltd., 2008.

Appendix 2: Supplementary material

A2.1: Chapter 3



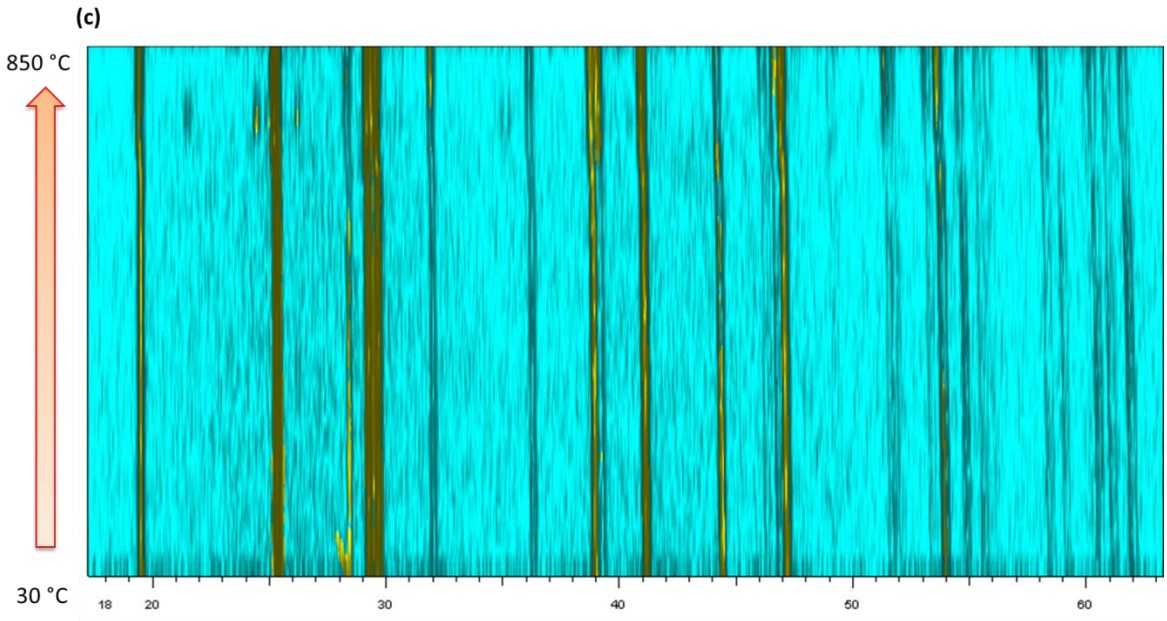
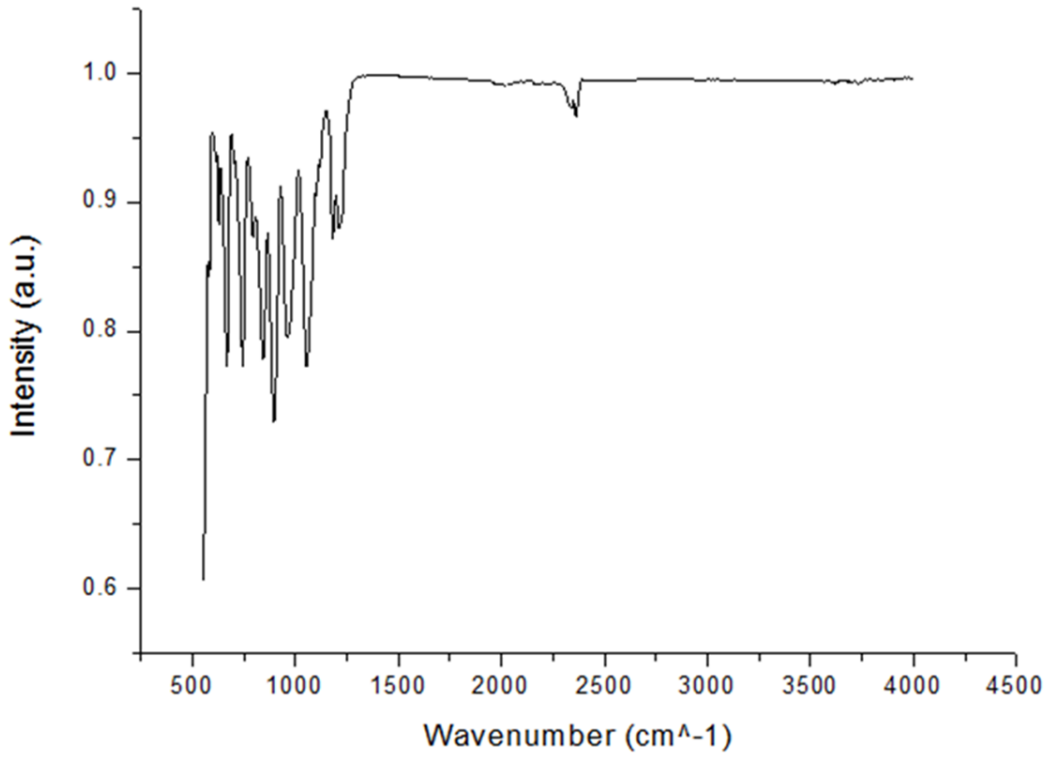
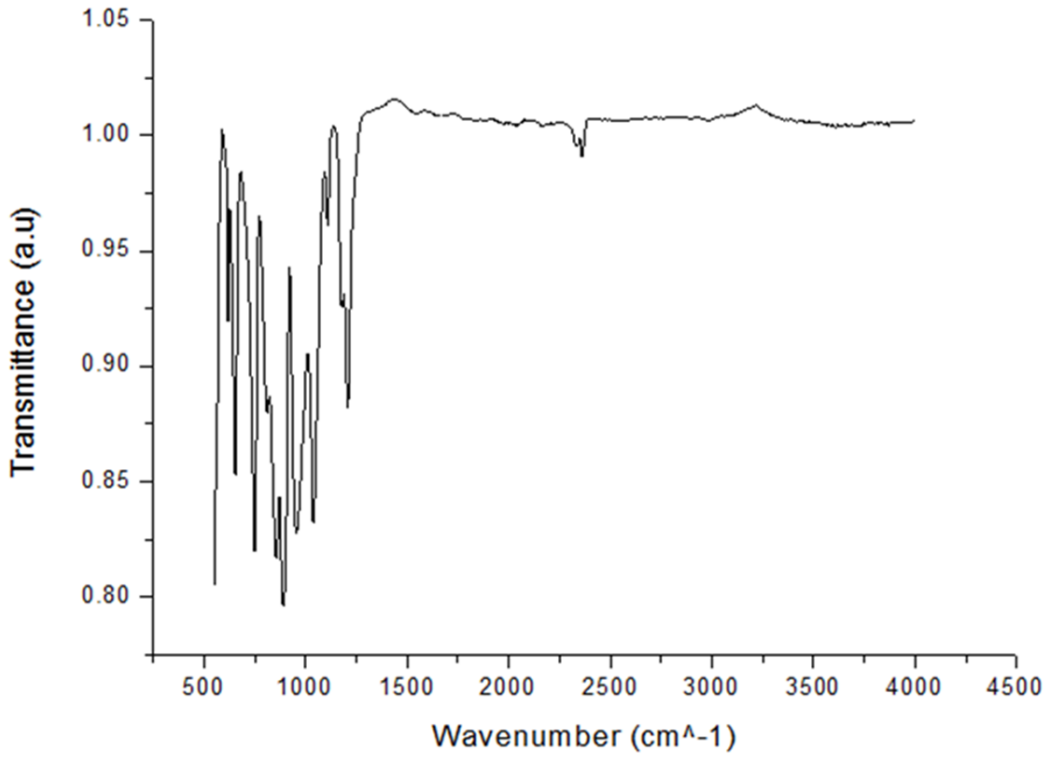


Figure A2.1: Topographical/2 dimensional view (with colour levels) of variable temperature powder X-ray diffraction (VT-PXRD) patterns of (a) $CaBPO_5$, (b) $SrBPO_5$, (c) $BaBPO_5$. In all plots two colour levels were created: Background (turquoise colour) and peaks/reflections (yellow colour).

(a)


Intensity (a.u.)
1.0
0.9
0.8
0.7
0.6
500
1000
1500
2000
2500
3000
3500
4000
4500
Wavenumber (cm^-1)

(b)


Transmittance (a.u)
1.05
1.00
0.95
0.90
0.85
0.80
500
1000
1500
2000
2500
3000
3500
4000
4500
Wavenumber (cm^-1)

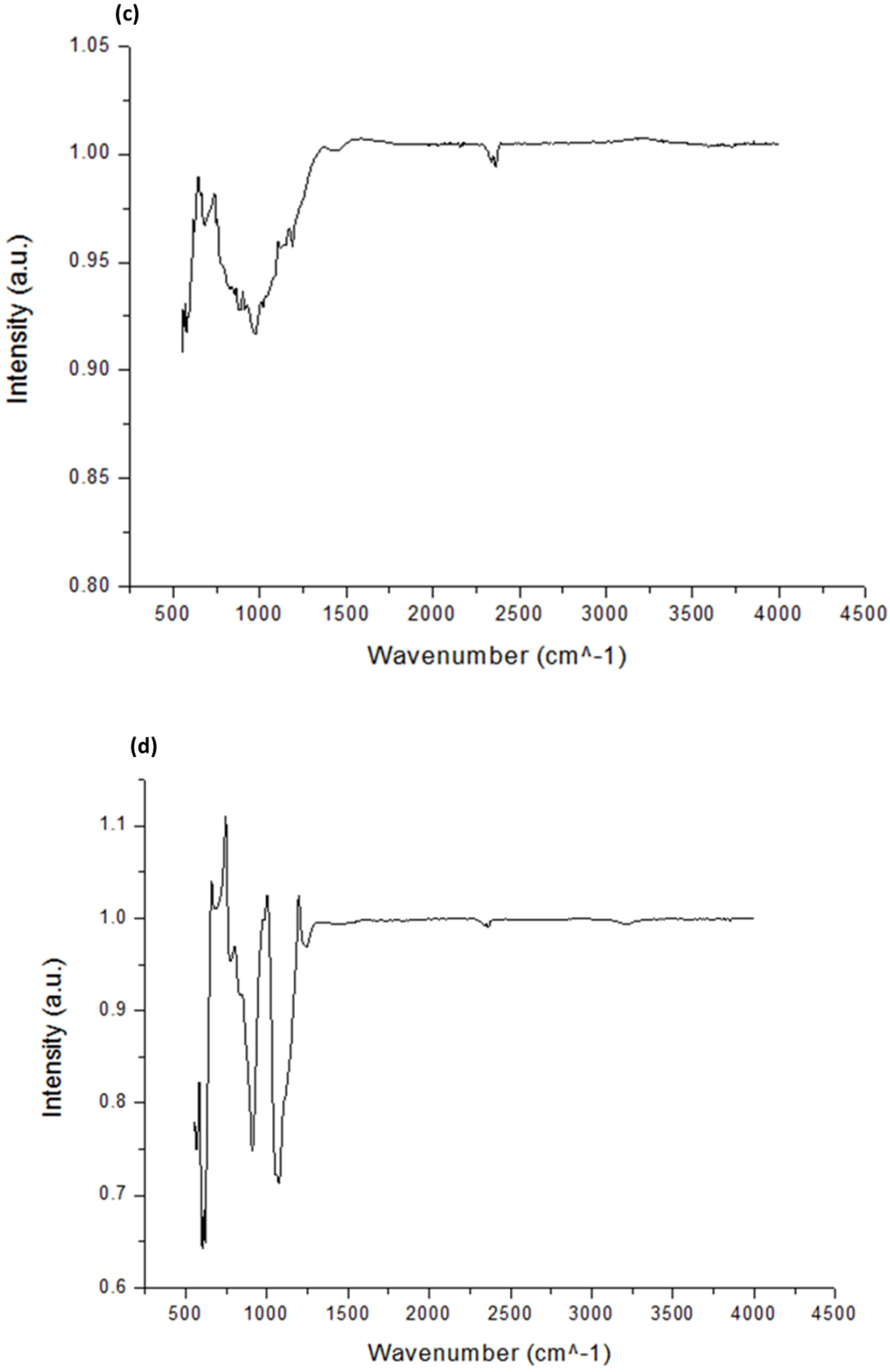
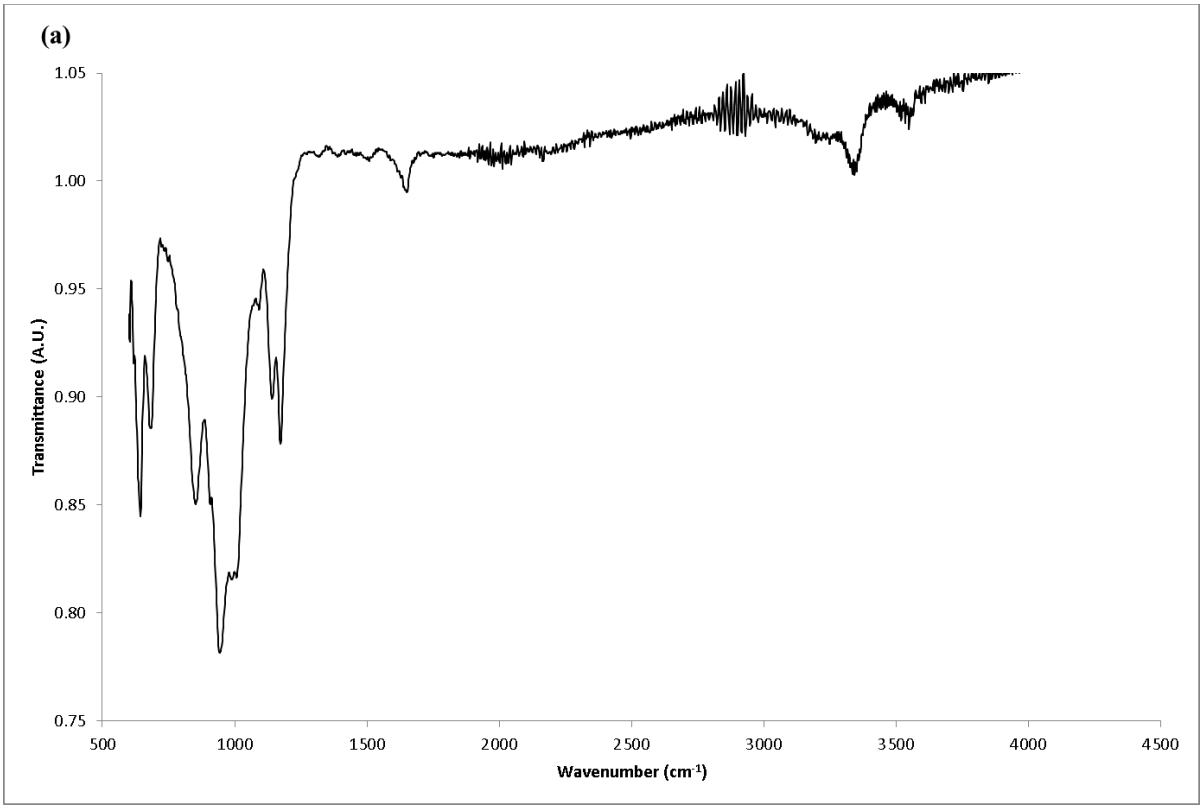
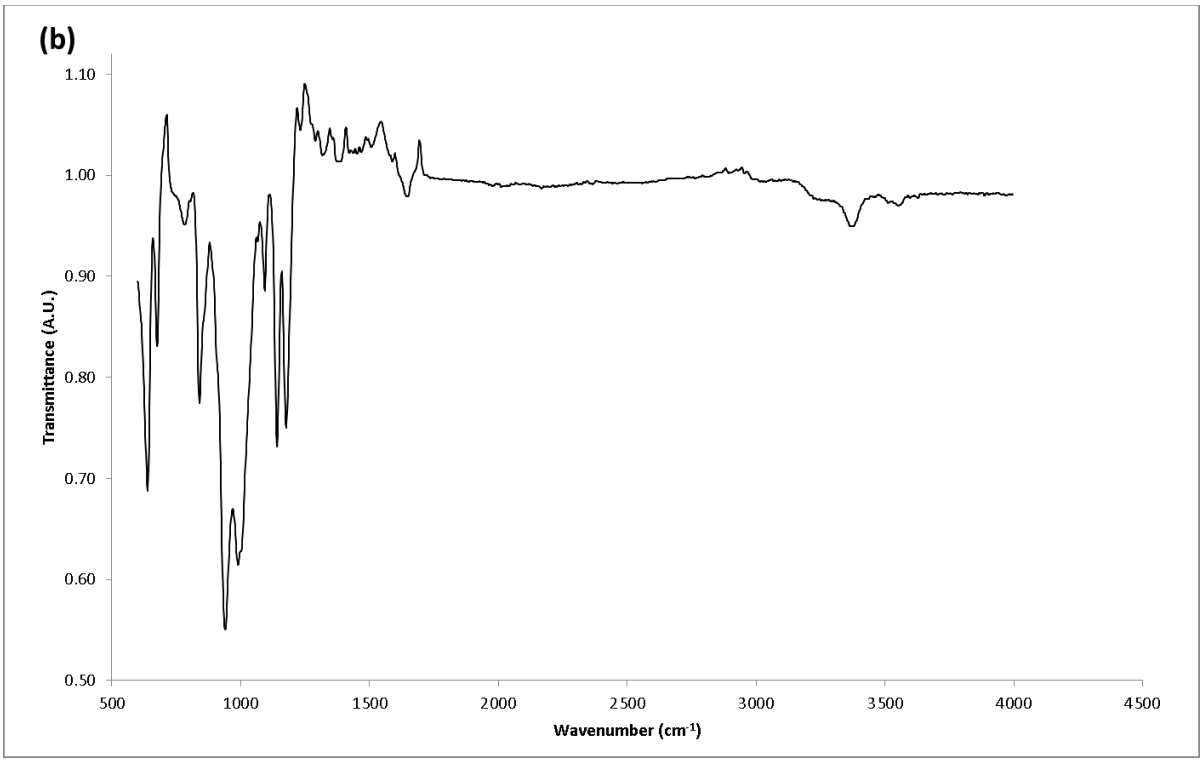


Figure A2.2: FTIR spectra of (a) $CaBPO_5$, (b) $SrBPO_5$, (c) $BaBPO_5$ and (d) BPO_4.

A2.2: Chapter 4





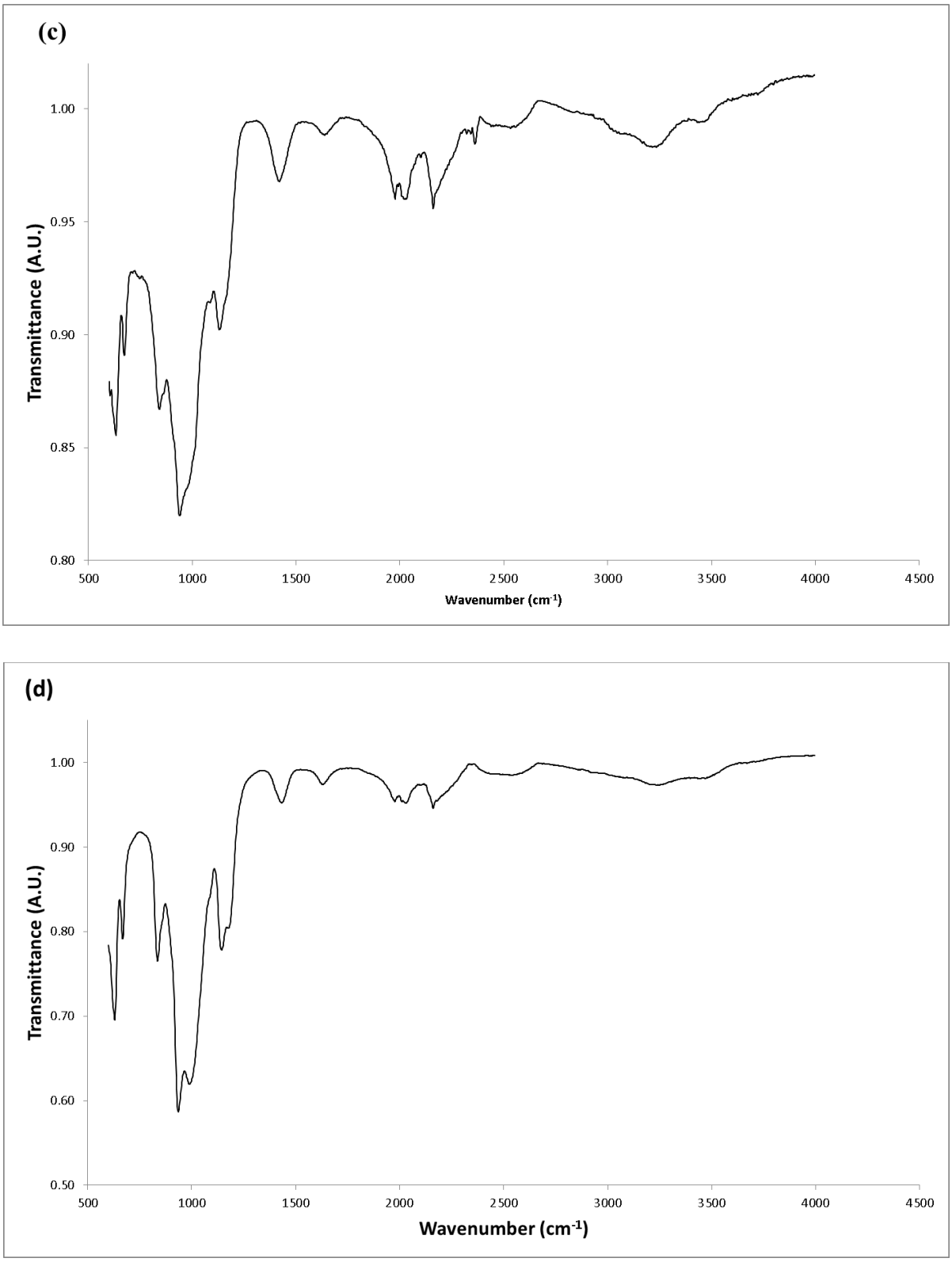


Figure A2.3: FTIR spectra of (a) sample **I**, (b) sample **II**, (c) sample **III** and (d) sample **IV**.

A2.3: Chapter 5

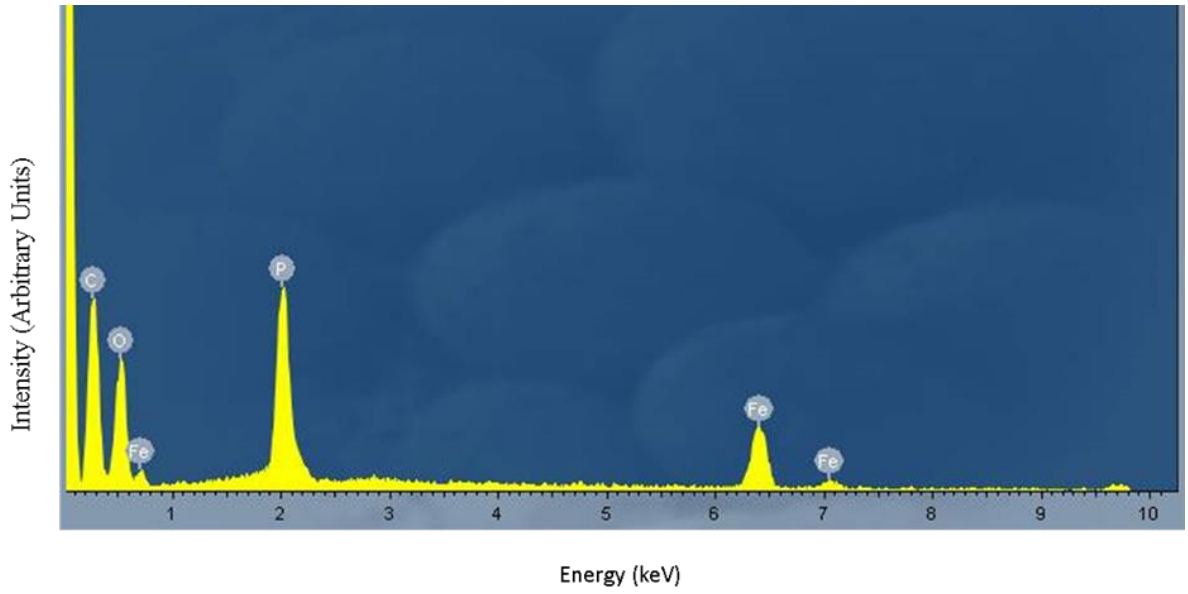


Figure A2.4: EDS of $NH_4Fe[BP_2O_8(OH)]$.

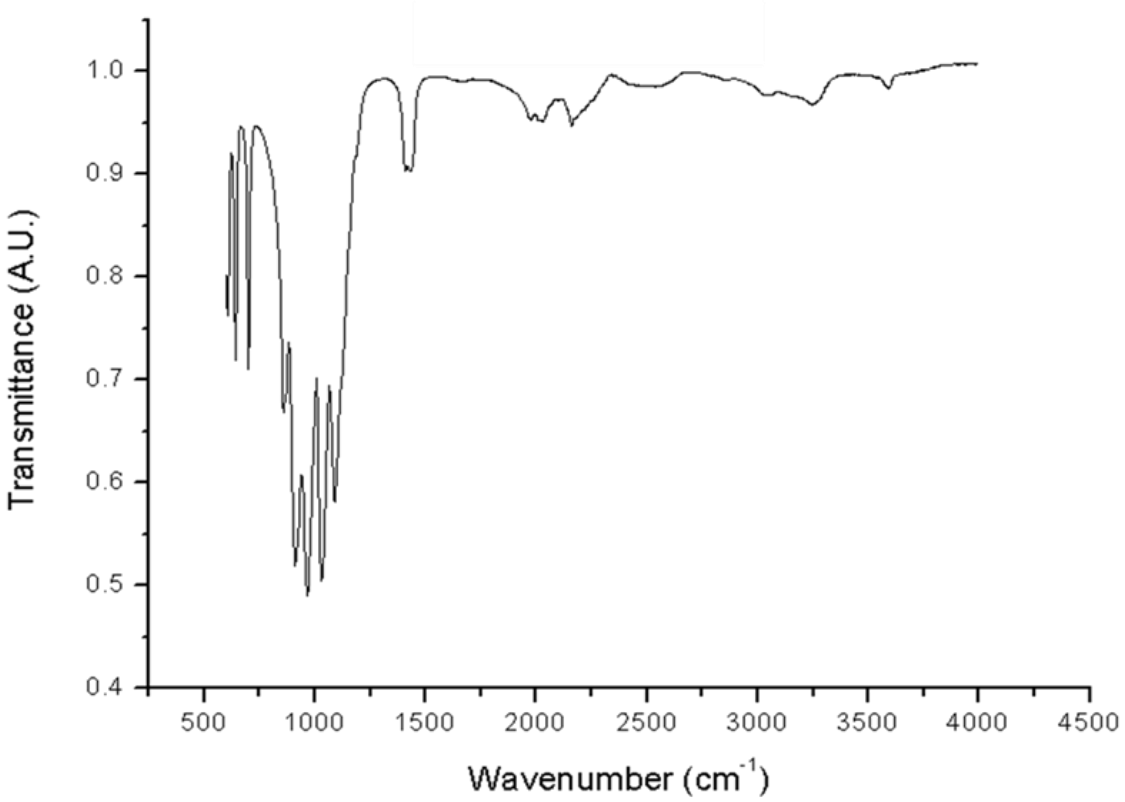


Figure A2.5: FTIR spectrum of $NH_4Fe[BP_2O_8(OH)]$.

A2.4: Chapter 6

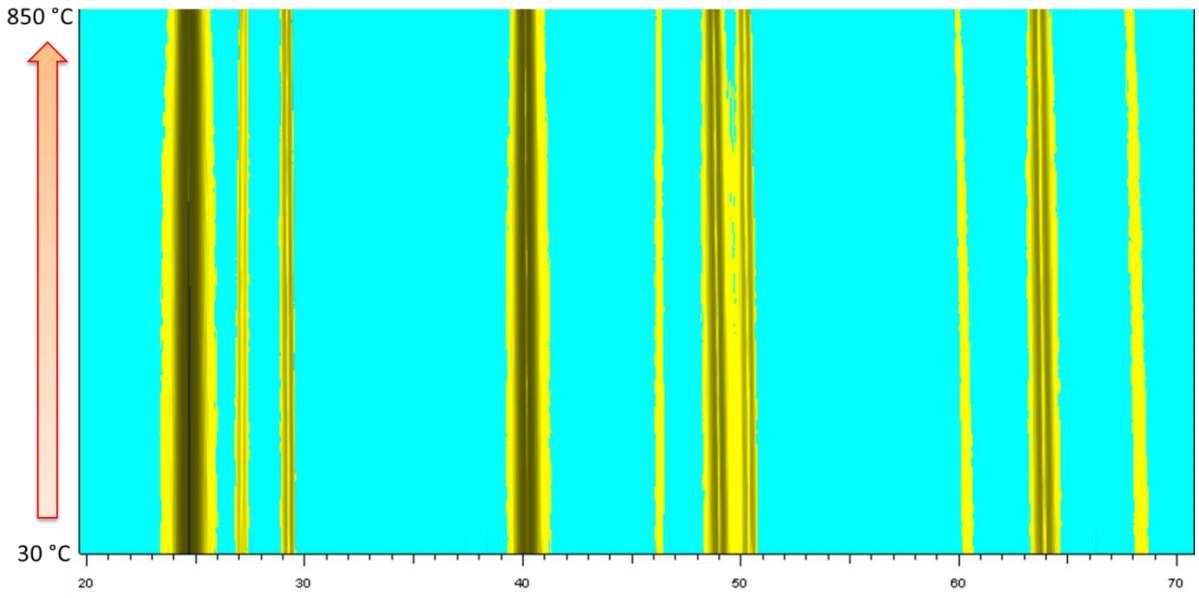


Figure A2.6: Topographical/2 dimensional view (with colour levels) of the variable temperature powder X-ray diffraction (VT-PXRD) pattern of BPO_4. Two colour levels were created: Background (turquoise colour) and peaks/reflections (yellow colour).

Appendix 3: Guide to the electronic appendix

All of the files used below can be found in CD-R attached to this PhD thesis.

Chapter (section)	Compound	Description	File type	Filename
3	$CaBPO_5$	VT-PXRD data	Bruker AXS measurement data	d8_01159.raw
		Sequential Rietveld refinement	Input file	CaBPO5.inp
		Sequential Rietveld refinement	Input file	CaBPO5_Original.inp
		Execute sequential Rietveld refinements	Batch file	CaBPO5_VT.bat
3	$SrBPO_5$	VT-PXRD data	Bruker AXS measurement data	d8_12_173.raw
		Sequential Rietveld refinement	Input file	SrBPO5.inp
		Sequential Rietveld refinement	Input file	SrBPO5_Original.inp
		Execute sequential Rietveld refinements	Batch file	SrBPO5_VT.bat
3	$BaBPO_5$	VT-PXRD data	Bruker AXS measurement data	d8_13_32.raw
		Sequential Rietveld refinement	Input file	BaBPO5.inp
		Sequential	Input file	BaBPO5_Original.inp

		Rietveld refinement		
		Execute sequential Rietveld refinements	Batch file	BaBPO5_VT.bat
4	I-$NaCo(H_2O)_2[BP_2O_8](H_2O)$	Room temperature diffraction data (Co-source)	Bruker AXS measurement data	d2_15_595_RoomTemp.raw
		Room temperature diffraction data (Cu-source)	Bruker AXS measurement data	d8_15_92_RoomTemp.raw
		VT-PXRD data	Bruker AXS measurement data	d8_15_92_VT.raw
		Room temperature Rietveld refinement	Topas project file	I-NaCo(H2O)2[BP2O8](H2O)_RoomTemp_D2Phaser.pro
		Room temperature Rietveld refinement	Topas project file	I-NaCo(H2O)2[BP2O8](H2O)_RoomTemp_D8.pro
		Crystallographic information file	cif	I-NaCo(H2O)2[BP2O8](H2O)_RoomTemp.cif
4	II-$NaMn(H_2O)_2[BP_2O_8](H_2O)$	Room temperature diffraction data (Co-source)	Bruker AXS measurement data	d2_15_594_RoomTemp.raw
		VT-PXRD data	Bruker AXS measurement data	d8_15_69_VT.raw
		Room temperature Rietveld	Topas project file	II-NaMn(H2O)2[BP2O8](H2O).pro

		refinement		
		Crystallographic information file	cif	II-NaMn(H2O)2[BP2O8](H2O)_RoomTemp.cif
4	III-$(NH_4)_{0.5}Co_{1.25}(H_2O)_2[BP_2O_8].(H_2O)_{0.5}$	Room temperature diffraction data (Co-source)	Bruker AXS measurement data	d2_15_596_RoomTemp.raw
		VT-PXRD data	Bruker AXS measurement data	d8_14_71_VT.raw
		Room temperature Rietveld refinement	Topas project file	III-(NH4)0.5Co1.25(H2O)2[BP2O8].(H2O)0.5.pro
		Crystallographic information file	cif	III-(NH4)0.5Co1.25(H2O)2[BP2O8].(H2O)0.5.cif
4	IV-$(NH_4)_{0.5}Mn_{1.25}(H_2O)_2[BP_2O_8].(H_2O)_{0.5}$	Room temperature diffraction data (Co-source)	Bruker AXS measurement data	d2_15_626_RoomTemp.raw
		VT-PXRD data	Bruker AXS measurement data	d8_15_3_VT.raw
		Room temperature Rietveld refinement	Topas project file	IV-(NH4)0.5Mn1.25(H2O)2[BP2O8].(H2O)0.5.pro
		Crystallographic information file	cif	IV-(NH4)0.5Mn1.25(H2O)2[BP2O8].(H2O)0.5.cif
5	$NH_4Fe[BP_2O_8(OH)]$	Room temperature diffraction data (Cu-source)	Bruker AXS measurement data	d8_15_53_RoomTemp.raw

		Room temperature Rietveld refinement	Topas project file	NH4Fe[BP2O8(OH)]_RoomTemp.pro
		Crystallographic information file	cif	NH4Fe[BP2O8(OH)]_RoomTemp.cif
		VT-PXRD data	Bruker AXS measurement data	d8_15_53_pure.raw
		Sequential Rietveld refinement	Input file	Fe_[0062].inp
		Sequential Rietveld refinement	Input file	Fe_[0062]_Original.inp
		Execute sequential Rietveld refinements	Batch file	Fe_[0062].bat
6 (6.2.1)	BPO_4	VT-PXRD data	Bruker AXS measurement data	d8_13_28.raw
		Sequential Rietveld refinement	Input file	BPO4.INP
		Sequential Rietveld refinement	Input file	BPO4_Original.INP
		Execute sequential Rietveld refinements	Batch file	BPO4_VT.bat
		Parametric Rietveld refinement (parameterization of cell parameter)	Input file	BPO4_Parametric_Script_Eqn3.inp
6 (6.2.2)		Parametric Rietveld	Input file	BPO4_Parametric_Script_Polynom.inp

		refinement (parameterization by low order polynomials)		
6 (6.2.3)		Rigid body sequential Rietveld refinement	Input file	BPO4_RGD.inp
		Rigid body sequential Rietveld refinement	Input file	BPO4_RGD_Original.inp
		Execute sequential Rietveld refinements	Batch file	BPO4_RGD_VT.bat
		Rigid body Parametric Rietveld refinement	Input file	BPO4_Parametric_Script_Rigid_RX_Rz.inp